Evaluation of a switched reluctance motor for solar vehicle application

J Maré

orcid.org/0000-0002-4970-6106

Dissertation accepted in fulfilment of the requirements for the degree *Master of Engineering in Electrical and Electronic Engineering* at the North-West University

Supervisor:	Dr MG Botha
Co-supervisor:	Dr JJ Bosman
Co-supervisor:	Mr JD Human

Graduation:	August 2023
Student number:	27000729

ABSTRACT

The impact of global warming forces the world to develop environmentally sustainable solutions. Common practices for sustainable machines include renewable energy sources and biofuels. The automotive industry is determined to combat environmental problems by investing significantly in the research and development of electric vehicles. The development of electric vehicles using renewable energy sources are promoted by various universities competing in solar races.

Solar racing uses vehicles powered from the sun to propel the vehicle. Solar energy is used as an alternative fuel source to charge a battery that provides energy for the electric motor. The first solar race was the Tour the Sol in Switzerland held in 1985 which led to several similar races. Today, solar racing is a highly competitive sport entered by universities to develop the engineering and technological skills of their students.

The North-West University frequently competes in the Sasol Solar Challenge; therefore, this study aims to evaluate a switched reluctance motor for solar vehicle application. The switched reluctance motor is believed to be a possible candidate for the next-generation traction motor in electric vehicles. Although the switch reluctance motor originated in the 1850s, the 20th century brought revival to the switched reluctance motor with the improvements made in power electronics, power switches, magnetic materials, and various electric motor design simulation tools and methods.

In this study, an un-optimised exploratory development model of a modular switched reluctance motor was designed instead of evaluating an off the shelf switched reluctance motor. The idea of using a modular structure instead of a conventional structure was chosen on the basis of performance and efficiency. The exploratory development model of the modular switched reluctance motor was simulated using numerical simulation software. Using the numerical simulation software, an efficiency map was constructed to evaluate the motor model using a drive cycle.

The drive cycle was constructed to typically represent a solar race. The drive cycle consisted of a closed-loop route, in which the traction motor propelled the solar vehicle for eight hours using only the energy from the sun. Solar energy was extracted from the sun using a photovoltaic array. By driving the solar vehicle through the drive cycle, the total driving distance was evaluated for the eight-hour operating period.

To justify the switched reluctance motor as a possible candidate for solar vehicle application, a brushless direct current motor, currently used as the traction motor in the solar vehicle of the North-West University was evaluated as the expected reference point for motor performance. When comparing the switched reluctance motor with the brushless direct current motor, the switched reluctance motor managed a total driving distance of 375.98 km, 23 km less than the total driving distance achieved by the brushless direct current motor. Therefore, the switched reluctance motor operated at lower efficiency. Thus, more energy was used by the switched reluctance motor to maintain the same torque and speed operations as the brushless direct current motor.

Although the modular switched reluctance motor did not improve the travelling distance set by the brushless direct current motor, the proposed switched reluctance motor has future potential. The modular switched reluctance motor can be designed for optimised efficiency when modifying the construction, geometric parameters or magnetic materials. Another method is to use a motor controller, designed to work with the modular switched reluctance motor that can improve efficiency over its operating range.

In the conclusion of this study it was shown that an un-optimised exploratory development model of a switched reluctance motor used as a traction motor for solar vehicle application is justified for future development studies. Optimising and improving the exploratory development model of the switched reluctance motor will improve its torque, speed and efficiency, such that the achievable total driving distance could be equivalent or extended when compared to the brushless direct current motor. Only after a design is obtained that shows improved efficiency compared to the brushless direct current motor shall the manufacturing of a prototype be justified.

Keywords: Switched reluctance motor, Motor efficiency, Solar vehicle, Drive cycle

TABLE OF CONTENTS

LIST OF FIGURES

LIST OF TABLES

ABBREVIATIONS AND ACRONYMNS

2D	Two Dimensional
3D	Three Dimensional
AC	Alternating Current
AIAA	American Institute of Aeronautics and Astronautics
ASC	American Solar Challenge
AWG	American Wire Gauge
BLDC	Brushless Direct Current Motor
BWSC	Bridgestone World Solar Challenge
CCC	Chopped Current Control
CFD	Computational Fluid Dynamics
CPU	Central Processing Unit
CSIRO	Commonwealth Scientific and Industrial Research Organisation
DC	Direct Current
DCC	Dependent Current Control
E	East
EMF	Electromotive Force
EU	European Union
EV	Electric Vehicle
FD-TD	Finite-Difference Time-Domain
FEA	Finite Element Analysis
FTP-72	Federal Test Procedure-72

GHG	Green House Gasses
GPU	Graphics Processing Unit
HEV	Hybrid Electric Vehicle
HWFET	Highway Fuel Economy Test
ICE	Internal Combustion Engine
IDC	Indian Driving Cycle
IEC	International Electrotechnical Commission
IEEE	Institute of Electrical and Electronics Engineering
IM	Induction Motor
ISO	International Organization for Standardization
MEC	Magnetic Equivalent Circuit
MMF	Magnetomotive Force
MoM	Method of Moments
MOT	Marching-On-in-Time
MSRM	Modular Switched Reluctance Motor
NEDC	New European Driving Cycle
NWU	North-West University
PMSM	Permanent Magnet Synchronous Motor
PM-SRM	Permanent Magnet Assisted Switched Reluctance Motor
PV	Photovoltaic
R&D	Research
RAM	Random Access Memory
RMS	Root Mean Square

S	South
SA	South Africa
SESC	Somabay Egyptian Solar Challenge
SPC	Single Point Control
SRM	Switched Reluctance Motor
SSC	Sasol Solar Challenge
Std	Standard
SynRM	Synchronous Reluctance Motor
UN	United Nations
V&V	Validation and Verification
WCED	World Commission on Environmental and Development
XDM	Exploratory Development Model

SYMBOLOGY

a	Acceleration, [m/s^2]
A	Frontal area of a vehicle, [m^2]
$A_{conductor}$	Cross sectional area of a conductor, [mm^2]
A_{ss}	Slot area, [mm^2]
b	Tyre pressure bar, [bar]
B	Magnetic flux density [T]
B_s	Stator flux density, [T]
B_{max}	Maximum flux density, [T]
C_d	Aerodynamic drag coefficient, [-]
C_H	Coil height, [mm]
D_c	Damping coefficient, [-]
D	Electric flux density, [T]
d_s	Stator pole length, [mm]
D_{ro}	Rotor outer diameter, [mm]
D_S	Inner stator diameter, [mm]
E_f	Electric field density, [V/m]
E	Energy, [Wh]
$E_{balance}$	Energy balance, [Wh]
$E_{available}$	Available energy, [Wh]
E_{used}	Used energy, [Wh]
E_{Mech}	Mechanical output energy, [Wh]

F	Force, [N]
F_a	Acceleration force, [N]
F_{drag}	Aerodynamic drag force, [N]
F_{slope}	Slope force, [N]
$F_{Traction}$	Traction force, [N]
F_{tyre}	Tyre friction force, [N]
FF	Fill factor, [%]
g	Air gap length, [mm]
g_a	Gravitational acceleration, [m/s^2]
H	Magnetic field strength, [A/m]
I	Current, [A]
I_{RMS_coil}	RMS current of coil, [A]
$I_{RMS\_conductor}$	RMS current of a single conductor, [A]
I_p	Maximum peak current, [A]
J	Current density, [A/mm^2]
J_{rotor}	Rotor inertia, [kgm^2]
L	Inductance, [H]
L_s	Stator total length, [mm]
L_{s1}	Upper stator pole length, [mm]
L_{s2}	Middle stator pole length, [mm]
L_{s3}	Lower Stator pole length, [mm]
M	Mass, [kg]

N	Number of conductor turns, [-]
N_b	Base speed, [rpm]
N_{rp}	Number of rotor poles, [-]
N_r	Rotor speed, [rpm]
P	Power, [W]
P_{cu}	Copper loss, [W]
P_H	Pole height, [mm]
P_{out}	Output power, [W]
P_{in}	Input power, [W]
P_{f+w}	Friction and windage losses, [W]
P_{steel}	Iron losses, [W]
q	Number of phases, [-]
r	Radius, [m]
R	Resistance, [Ω]
r_{ro}	Rotor outer radius, [mm]
r_{sh}	Shaft outer radius, [mm]
r_{so}	Stator outer radius, [mm]
t	Time, [h]
T_b	Rated torque, [Nm]
T_s	Period, [s]
T_L	Load torque, [Nm]
v	Vehicle speed, [m/s]

V	Voltage, [V]
W_c	Co-energy, [-]
W_e	Input energy, [W]
W_m	Mechanical work, [W]
W_{losses}	Energy losses, [W]
W_{m2}	Magnetic field energy, [-]
W_s	Stored magnetic energy, [-]
y_r	Rotor yoke width, [mm]
y_s	Stator outer yoke width, [mm]
∇	Nabla, [-]
$\nabla \times$	Curl operator, [-]
$\nabla \cdot$	Divergence operator, [-]
μ_0	Permeability of a vacuum, [H/m]
μ_r	Relative permeability, [H/m]
μ	Absolute magnetic permeability, [H/m]
M_p	Permanent magnetisation, [A/m]
T_s	Switching time, [s]

Greek and special symbols

β_r	Rotor pole arc angle, [˚]
β_s	Stator pole arc angle, [˚]
ε	Step angle, [˚]
ε_b	Back EMF, [V]

η	Efficiency, [%]
θ_s	Angle of slope, [˚]
θ	Rotor position, [˚]
λ	Flux linkage, [Wb]
ρ	Air density, [kg/m^3]
ρ_c	Charge density, [C/m^3]
τ	Torque, [Nm]
τ_e	Electromagnetic torque, [Nm]
τ_r	Rotor pole width, [mm]
τ_s	Stator pole width, [mm]
ω	Angular velocity, [rad/s]
ω_f	Angular frequency
ω_b	Base speed, [rad/s]
ω_p	Peak speed, [rad/s]
$\emptyset$	Equivalent flux, [Wb]
$\mathcal{F}$	Magnetomotive force, [AT]
$\mathcal{R}$	Reluctance, [AT/Wb]
σ	Conductivity, [S/m]

CHAPTER 1 INTRODUCTION

"The switched reluctance motor is a potential contender for the next generation electric vehicle traction motor due to its low cost, high efficiency, and ability to operate at higher temperatures and in other harsh environments" [1].

The invention of the tyre, that made travel and movement easier led to the development of a steam engine and internal combustion engine, able to propel a vehicle. However, these developments brought a few unwanted features, i.e., carbon emissions. Thus, the concern for an electric and hybrid vehicle is brought forth.

The 21st century is progressively searching for improved technology in conventional electric motors to use in electric vehicles. With all the technological improvements made, it is considered a suitable time to use a special electric machine, namely a switched reluctance motor [2].

1.1 Environmental sustainability

There are many interpretations of the meaning of sustainability. In the most likely sense, sustainability refers to the ability of something to maintain or "sustain" itself over time [3]. The interpretation of environmental sustainability according to the United Nations (UN) and World Commission on Environment and Development (WCED) stated that environmental sustainability is about acting in such a manner that ensures future generations have natural resources available to live an equal, if not better, way of life as current generations [4, 5].

The definition of environmental sustainability leads to question what part people should play, i.e., as evolutionary species. Thus, in what way must humans change the way they live and develop science and engineering on this planet to assure the environmental sustainability for future generations? [6]

Since ecological conditions as well as economic and social systems differ in each country, there is no single proposal for how sustainability must be implemented. Each country has to propose and execute its own strategy to ensure that sustainable development is performed as a worldwide objective.

Due to the impact of global warming, glaciers and polar ice are melting at rates two to three times higher than the last century. The earth is going through one of the largest biodiversity losses of unforeseen and unpredictable impact. The human-caused rate of extinction is hundreds of times higher than the natural rate in the past. As the situation turns out, it could be a thousand times higher in the near future. Therefore, environmental sustainability is one of the main areas of

attention for researchers, academicians, scholars, governments, and nongovernmental organisations that involve individuals, communities, countries, continents, and the world [7].

Some issues that pose major environmental sustainability complications listed in [8] include:

- The destruction of living environments from native species.
- The discharge of polluting chemicals and materials into the environment.
- Emissions of greenhouse gasses (GHG) into the atmosphere causing climate changes.
- Depletion of oil and fossil fuels.

These environmental sustainability problems are combatted by promoting sustainable environmental practices, i.e., moving to renewable energy sources, biofuels, and reducing waste. The transport sector is responsible for 27% and 14% of all fossil fuel emissions in the European Union (EU) and South Africa (SA) [9, 10, 11]. With the determination to combat the abovementioned environmental sustainability problems, the automotive industry is a sector that has significant investments in research and development (R&D). Electric vehicles (EVs) have tremendous potential to drastically minimise emissions, which is a tactical path for environmental sustainability growth.

> **Definition 1 (Automotive):** *Automotive pertain to the design, operation, manufacture, or sale of automobiles.*

> **Definition 2 (Automobile):** *The automobile, also called a motorcar, is usually a four-wheeled vehicle designed primarily for personal or passenger transportation.*

1.2 Electric vehicles

The Benz patent *motorwagen*, built in 1885 by Karl Benz, is widely regarded as the first true automobile. However, unlike other major inventions, the original idea of the vehicle cannot be attributed to a single individual. The idea of a self-propelled vehicle was first formulated in the 13th century by the English philosopher Roger Bacon. In his letter '*De mirabile potestate artis et natura*' ('On the Marvellous Power of Art and Nature'). Roger Bacon wrote the following: "It is possible that a car shall be made which will move with inestimable speed, and the motion will be without the help of any living creature" [12]. Likewise, Giovanni Fontana and Leonardo da Vinci were the first to introduce a design of a vehicle. Around 1420, Fontana drew a self-propelled vehicle in his technological treatise '*Bellicorum instrumentorum liber*' ('Book on the instruments of war'), while Leonardo da Vinci drew a self-propelled vehicle around the year of 1478 that can be found in his '*Codice Atlantico'* ('Atlantic Codex').

During the Renaissance period, the word '*Disegno*' that translates to ‘design’ was only an 'Idea', and therefore it was not essential to build the invention. For this reason, most inventions, such as the case of the automobile or vehicle as referred to in this dissertation, remained on paper. It was not until the 19th century, when the development of the internal combustion engine (ICE) took place, that the idea of a self-propelled vehicle started to development [13, 14]. Today, a vehicle is propelled mostly by an ICE, an electric motor or a combination of both.

Research and development of electric vehicles started in 1827 when a Slovak-Hungarian priest Ányos Jedlik built the first crude but viable electric motor. The electric motor was using a stator, rotor, and commutator. Robert Anderson of Scotland is reported to have constructed a crude electric carriage in 1832 but it wasn't until the 1870s that EVs became somewhat practical. In 1873, Robert Davidson built an electric vehicle that is referred to as the first working electric road vehicle. Inventors have explored many ways to improve the technology of EVs. For example, Ferdinand Porsche developed the P1 in 1898, the world's first hybrid vehicle powered by electricity and gasoline. In 1914, Henry Ford partnered with Thomas Alva Edison to explore options for low-cost EVs [14].

At the beginning of the 20th century, almost a third of American automobiles were electric, as it offered attractive selling points such as instant self-starting, silent operation, minimal maintenance, and higher reliability than the ICE. However, Henry Ford's mass-produced Model T dealt a blow to EVs. This was the cause of Charles Kettering, who introduced the electric starter for the ICE. Simultaneously, ICE vehicles became more reliable and comfortable [14, 15].

The ICE is recognised as one of the greatest inventions of the 20th century and remains popular for the same reason that it became a success, namely, high power density, low cost, rapid refuelling, convenience, high speed operation and long travelling distances [16]. Though, the combustion of fossil fuels is the primary contributor to carbon dioxide production. Carbon dioxide is believed to contribute to climate change, and transport systems alone have doubled the contribution to climate change since 1970 [17].

Technological advances have been made to reduce GHG emissions. In 1980 the catalytic converter was introduced. In the early 2000s, European vehicle manufacturers switched to diesel-powered engines to reduce emissions, although it was later proven that diesel is not more climate-friendly than petrol [18]. Re-evaluation of EVs began at the end of the 20th century.

The start of the 21st century brought revival to EVs for many of the same reasons they were first popular, namely, quiet operation, easy to operate, and no pollution. The interest in reviving EVs is said to originate from the introduction of the Toyota Prius in 2000 and the Tesla Roadster in 2008 [15]. The world’s first mass-produced hybrid electric vehicle was the Toyota Prius. The Tesla

Roadster was the first-ever high-end, all-electric, highway-legal vehicle that could travel more than 320 km on a single battery charge, a range unprecedented for a production EV at that time [19, 20]. The achieved travelling distance persuaded many other vehicle manufacturers to accelerate work on their electric vehicle line-ups. The European Union suggested an effective ban on the sale of new petrol and diesel vehicles from 2035 onwards. The ban on ICE vehicles effectively forces vehicle manufacturers to invest in alternative energy sources.

Along with the development of electric vehicles, the quest to develop an everlasting, cleaner, and environmentally friendly fuel is never ending to progress the development of environmental sustainability. The best alternative to current fuels are renewable energy sources such as the wind, tides, the sun, hydropower, and biomass. The cleanest sustainable energy for the longest time is solar energy. The dream of driving a vehicle without environmental sustainability problems would come true at the time we drive solar powered [21].

1.3 Solar vehicle races

The Tour de Sol in Switzerland was the first race for solar powered vehicles. The first class of vehicles was powered exclusively by direct on-board solar power. The second class of vehicles was allowed direct human power with attached pedals in the vehicle. The race winners were regarded as those who have travelled the least amount of time for the set course each day. The course was on undisclosed roads where drivers were obliged to obey all traffic rules and speed limits [22].

Today, these solar challenges include the Bridgestone World Solar Challenge (BWSC, Australia), the Somabay Egyptian Solar Challenge (SESC Egypt), the American Solar Challenge (ASC, America), the Sasol Solar Challenge (SSC, South Africa) and many more [23]. Even though many solar challenges exist globally, the South African based Sasol Solar Challenge is a notoriously challenging race. This race provides varying weather conditions and extreme landscape topographies such as severe road gradients along the entire route.

Solar racing is a highly competitive sport and a test arena for tomorrow's renewable energy applications. The competitive nature leads teams to design solar vehicles for efficiency rather than practicality under the imposed race regulations [24]. These rules limit the energy used to only the energy extracted from solar radiation, although starting with a fully charged battery. Energy consumption is a vital part of the design when striving to improve race performance. It is not uncommon to see teams design solar vehicles with similar aerodynamic characteristics in order to reduce energy consumption [23, 24].

Solar vehicles rely on a photovoltaic (PV) cell array to convert solar radiation into electrical energy. Electrical energy is stored in the battery and used by the electric motor to propel the vehicle,

similar to an EV. In this instance, the electric motor, called a traction motor, converts the electrical energy into mechanical energy to overcome rolling resistance, aerodynamic drag, and slope resistance during hill climbs.

> **Definition 3 (Traction motor):** *A traction motor is an electric motor used for the propulsion of a vehicle, such as an electric locomotive or electric roadway vehicle* [25].

1.4 Traction motors

A wide range of electric motors exists, but only a few are used as traction motors. The most common electric motors used as traction motors in EVs are the induction motor (IM), permanent magnet synchronous motor (PMSM), switched reluctance motor (SRM), brushless DC motor (BLDC) and direct current (DC) motor. The DC motor is the oldest type of traction motor. The other named electric motors became available as traction motor options in the past four decades. This is due to advancements in electric motors, power electronics, microelectronics, and control strategies. The PMSM, IM, and SRM are listed as the three most popular electric motors employed in EVs and heavy electric vehicles (HEVs) [26]. These traction motors exhibit the following qualities: high efficiency, high power density, effective regenerative braking, robustness, and good reliability.

Each electric motor features different operating principles. The difference in operating principles can be either an advantage or disadvantage in EV applications. The following sections provide background to each traction motor by; a basic description, efficiency of the motor, EV use, the expected torque and speed of the motor and the cost associated with the electric motor.

1.4.1 Direct current motor

The DC motor works on the principle of Faraday's law, whereby the current-carrying conductor, when placed in a magnetic field, will experience a torque and tend to move, or in this case, rotate.

The efficiency of a DC motor is expected to be around 80%. Motor losses is predominantly in the rotor, known as copper loss. The copper loss occurs as a result of current flow in the windings, as in the case of other electric motors. The copper losses of a DC motor are categorised into three parts, armature loss, field winding loss and brush contact resistance loss.

Controlling the DC motor is straightforward. The DC motor does not require complex power electronics and allows the motor to be coupled directly to a battery. However, showing low efficiency, low power density, and the risk of premature wear and tear of the brushes make the DC motor no longer a choice as a traction motor [27, 28].

The DC motor was a good solution as an electric motor up to the 1990s, before power electronics became affordable. Since then, AC electric motors are preferred in the industry.

1.4.2 Induction motor

The IM is a commonly used alternating current (AC) motor. Torque is produced by the reaction between a rotating magnetic field generated in the stator windings and the current induced in the coils of the rotor. No induced current will result at synchronous speed; therefore, the IM rotates slower than the magnetic field in the stator windings. Thus, the IM is also referred to as an asynchronous motor.

> **Definition 4 (Coil):** *The coil in an electric motor is one or more turns, usually cylindrical, of current-carrying wire that is designed to produce a magnetic field or to provide electrical resistance or inductance.*

> **Definition 5 (Winding):** *A winding in an electric motor is the connection of several coils, either in parallel or in series.*

Assuming that the stator copper loss is negligible and the rotational loss is zero, the IM efficiency under ideal conditions operating at 5% slip can theoretically have an efficiency of 95% [29]. Shahria Sharifan *et al.* obtained a simulated efficiency of 86% for an IM drive that included both the motor and motor controller [30]. David Dorrel *et al.* designed an eight-pole, 48-slot IM that achieved efficiencies of 83.1% and 95.2% at speeds of 1500 rpm and 6000 rpm [16]. Nasser Hashernnia and Asaei Behzad state that an IM is usually considered the best candidate for EV applications even though an IM is usually larger and heavier than a PMSM [31]. The Tesla Model S and Mahindra Revo e2o use an IM as the traction motor.

T Selvathai *et al.* chose an IM instead of an PMSM despite the advantages offered by an PMSM [32]. The primary decision to choose an IM was that the flux weakening operation is better controlled since no permanent magnets are in an IM. Therefore, allowing for higher overload capability. The IM requires little to no maintenance with the advantage of using matured technology, making the IM inexpensive compared to other electric motors [33].

1.4.3 Permanent magnet synchronous motor

The PMSM is an AC synchronous motor. The field excitation is provided by the permanent magnets in the rotor and has a sinusoidal back electromotive force (EMF). When the rotor synchronises with the rotating magnetic field in the stator windings, synchronous speed is obtained.

The efficiency of the 2004 Toyota Prius hybrid EV achieved an efficiency of 91.3% and 96.1% at speeds of 1500 rpm and 6000 rpm. It has been stated that PMSMs, compared to IMs of the same size, have higher efficiency [16]. Permanent magnets eliminate field excitation losses and enable the motor to be designed to be more compact and lighter [34]. However, a PMSM operating with poor thermal dissipation poses a risk of demagnetising the permanent magnets in the motor that would result in a decrease of performance [35]. Operating at high temperature influences the magnetic properties of the magnetic material which in turn reduces the maximum output torque of the motor. This adds to the already reduced performance of demagnetised permanent magnets [36].

Permanent magnet synchronous motors are serious competitors against IMs. They are widely used by automotive manufacturers and are the traction motor choice in the Formula E motorsport series [37, 38].

The PMSM have faster acceleration, greater efficiency-torque-speed characteristics and higher power density compared to an IM [30]. When the construction of a PMSM is considered, the axial flux PMSM, compared to the radial flux PMSM, has the benefit of a higher power-to-weight ratio, less noise, and less vibration [39]. However, the PMSM does not allow for the overload capability of an IM but offers quite an extensive torque overload capability over a wide speed range when flux weakening methods or custom control algorithms are used under the thermal limitations of the permanent magnets [28].

The cost of PMSM is steadily increasing with the reduced availability of permanent magnets. Thermal prediction is also an important part of the design to avoid irreversible demagnetisation that would result in decreased motor efficiency and performance [34, 40].

1.4.4 Brushless direct current motor

The BLDC motor is an electrically commutated DC motor with the exclusion of brushes. Like the PMSM, the field excitation is provided by the permanent magnets in the rotor, but the BLDC motor has a trapezoidal back EMF instead of a sinusoidal back EMF [41]. Another difference is that concentrated windings are used in BLDC motors, and lap wave windings are used in PMSMs.

The efficiency of a BLDC motor is typically within the range of 85% to 90%. In 2009 a research group from Tokai University achieved efficiency in the range of 93% to 96% under various operating conditions. When comparing a BLDC motor against an SRM in [42], the BLDC has only a 1% efficiency improvement compared to the SRM. It should be noted that both motors were designed for the same output power and same outer diameter.

Similar to the PMSM, the BLDC motor is preferred in EVs. Their power-to-volume ratio makes them a popular choice in Japan, with their small, lightweight, and more compact vehicles [44].

From the comparison between a BLDC motor and a PMSM in [45], it is concluded that the BLDC has a lower power and torque density than a PMSM. For both these permanent magnet motors, an outer rotor radial flux motor is the preferred choice in high-power and torque-density applications.

As in the case of the PMSM, the BLDC motor is expensive and risks demagnetising the permanent magnets when operating above the thermal limitation.

1.4.5 Switched reluctance motor

The SRM is a double salient pole motor with phase coils wound on the stator poles. An inherent advantage of the motor is that there are no windings or magnets on the rotor. The rotor consists only of stacked laminated magnetic material. The SRM operates on the principle of magnetic reluctance between the aligned and unaligned pole positions.

The efficiencies of 85.2% and 88.2% are achieved at speeds of 1500 rpm and 6000 rpm in [16]. By comparing the efficiency with the efficiency of the IM and PMSM, it is observed that the efficiency is almost 7% lower than the PMSM. A 12/26 SRM simulated in [42] shows an efficiency of 90.4%, only 1% lower than the compared BLDC motor of the same output power. Concluded in [46], the implementation of a dependent current control (DCC) strategy at low speeds and high torque operation can increase efficiency. Motor losses are significantly reduced, along with heat generation and overall weight, since no windings or permanent magnets are in the rotor.

The SRM is making a prominent role in appliances, industrial equipment, commercial and vehicular applications in the 21st century, even though the SRM was developed in the 1800s. Optimum operation depend on relatively sophisticated control. Control of an SRM is made possible by the advent of improved switching devices and power electronics [47]. Tesla and Holden already use a permanent magnet-assisted SRM (PM-SRM) in their electric vehicle line-up [42, 48]. The SRM is gaining major attraction given its simple, robust, and inexpensive construction. Control of an SRM is more complex than three-phase sinusoidal excitation [35]. Due to the complexity of the control strategy, the cost of the motor often increases to the range of other electric motors. Another disadvantage of an SRM include torque ripple, vibrations, and strong acoustic noise [49, 27, 44]. M. Yildirim *et al*. has the state that torque ripple and acoustic noise are not considered a crucial problem in traction motors [50]. This is not always the case, as torque ripple is considered a crucial issue in SRMs that leads to vibrations, premature wear and ultimately failure of the drivetrain system [48]. Therefore, many mitigations methods have to be incorporated when designing or controlling a traction motor.

Comparing an SRM to other electric motors, i.e., BLDC and PMSMs found that an SRM offer a wider speed range when operating at constant power. When comparing torque of an SRM, an SRM typically has less torque when operating at low speeds, though more torque at higher speeds when compared to an IM and PMSM.

With the absence of rotor windings and permanent magnets, the SRM is inexpensive compared to other electric motors. The absence of the windings and permanent magnets provides a simpler, more rugged rotor that provides high reliability and enables the electric motor to continue operation under open-circuit fault conditions [28, 32].

1.5 Purpose of the research

The Sasol Solar Challenge is the South African solar race. The goal of the Sasol Solar Challenge is to maximise the driving distance each day. Efficiency is the pillar of solar vehicle design. Traditionally, design improvements have focused on reducing mass and aerodynamic drag. The next attempt to improve efficiency of a solar vehicle is to use or design an improved traction motor.

1.5.1 Research problem

A traction motor is an essential part of a solar vehicle. Currently, the North-West University (NWU) and competitors in solar races have the option of buying a traction motor, specifically designed for solar racing from two manufacturers. Each of the two manufacturers, namely, Mitsuba and Marand offer a permanent magnet type motor. Marand offer a single motor whilst Mitsuba offer a motor with a list of modification options to improve its performance. However, these traction motors are expensive and bought standard off the shelf.

From the opinion of Nir Vaks and Nyah Zarante in [1], the SRM is a potential candidate for the next-generation traction motor in EVs. But the problem is that no SRM is available as a traction motor for solar vehicle application, since no SRM has been adequately evaluated against a PMSM. Since no SRM has been adequately evaluated against a permanent magnet motor (BLDC or PMSM), the research problem manifests that the potential of an SRM for solar vehicle application should be justified by evaluating an SRM as a traction motor in a solar vehicle.

1.5.2 Research scope

To evaluate an SRM for solar vehicle application, a suitable SRM for the solar vehicle of the NWU is required. Therefore, an SRM should be designed. The design specifications for the SRM are obtained by evaluating the Mitsuba M2096-DII BLDC, currently the traction motor in the solar vehicle of the NWU. The SRM design follows the same procedures found in [51, 52, 53]. To justify the use of an SRM for solar vehicle application, the scope of this study is limited to a first

experimental development model (XDM) and does not follow an iterative design process to find the most optimised motor design. Thus, the most optimised SRM design will not be evaluated for solar vehicle application.

Thus, the designed SRM, however not optimised, can be evaluated and provide sense to the hypothesis "*The SRM is a potential contender for the next generation traction motor in EVs* ". Note that the motor controller is not part of the scope of the study, although a motor controller circuit is required during transient simulations. Therefore, an optimised motor controller or design is not used to simulate the SRM. The conclusion of the evaluated SRM will justify future development and studies to provide an optimal SRM design that can be developed as a manufactured prototype.

> **Definition 6 (Exploratory development model):** *The exploratory model is an experimental research-based system development method used to develop and redesign a system or product. The exploratory model is based on planning and reviewing potential scenarios and approaches until the one that appears to be optimal is selected. However, this method is essentially a form of educated guesswork.*
>
> *The exploratory model is a type of prototyping model, but it is much more open-ended and less formal than other systems. As such, there is a risk that the results of the exploratory model will be less than optimal* [54].

1.5.3 Research limitations

The following research limitations were imposed or identified:

- Manufacturing and financial constraints: Manufacturing an electric motor is expensive. Due to the financial costs involved with manufacturing, the switched reluctance motor in this study is modelled using finite element analysis (FEA) software rather than manufacturing the electric motor.
- Validation and verification constraints: the validation process cannot be performed on a physical electric motor since the switched reluctance motor is modelled rather than manufactured. Validation and verification are mainly performed by simulating a similar motor to ensure the correct setup and modelling process is followed when analysing an SRM. This requires motor and experimental data from a similar SRM.
- Computer resource constraints: Simulations of finite element analysis require extensive computing resources. The simulations of the study were limited to two computers with the following hardware:
    - Computer 1: Intel i7-5500 CPU, 8GB RAM, NVIDIA GeForce 840M GPU
    - Computer 2: AMD Ryzen 7-3700X CPU, 64GB RAM, Quadro P2200 GPU

- Software constraints: Many numerical simulation software are used in the industry. Thus, many software is available to analyse electrical machines, listed in §3.1.2, p.49. The simulation software is expensive. However, the NWU has licenses to the simulation software of Ansys®.
- Simulation accuracy constraint: An engineering project is based on financial limitations. In this study for a Master of Engineering degree, the limitations can be divided between time and energy, therefore, limiting the degree of accuracy when simulating. A trade-off between simulation time and the model accuracy is necessary.
- Design constraints: The study is not based on the design of an SRM but on the evaluation of an SRM. Design is not part of the scope of the study. However, a random SRM cannot just be evaluated. Thus, some design, based on the specifications of the solar vehicle is necessary. The design is not the best or an optimised design, but merely an un-optimised XDM, as explained in §1.5.2.
- Drive cycle constraints: The scope of this study does not focus on the accurate setup of a drive cycle to evaluate a traction motor. A simplified drive cycle does not provide the most accurate evaluation of a traction motor, but uses the procedure to evaluate different traction motors for comparison against each other.

1.5.4 Research assumptions

- It is assumed that the magnetic material properties and characteristics provided in the material database of Ansys® are accurate and correct.
- The drive cycle setup assumes assumptions of solar radiation and road and route conditions. An accurate setup of the drive cycle is not part of the scope of this study. Therefore, assumptions were made to simplify and demonstrate the evaluation process. All assumptions are set out in chapter 6.
- Following the definition of an XDM during the design process, the switched reluctance motor design in chapter 5 is assumed from previous research and literature, i.e., the efficiency of an SRM design is based on the static flux linkages.

1.6 Dissertation outline

The dissertation consists of seven chapters, a bibliography, and four appendices. All chapters are provided in logical order. However, during the study, the work is not completed in the particular order of the chapters.

Chapter 1 is an introduction. A background on solar races and traction motors used for EVs is discussed, providing an overview of the research topic. The purpose of the research is provided, which includes the research problem, scope, limitations, and assumptions.

Chapter 2 provides a literature review on topics related to the research. Relevant background on the SRM and the operating principles of an SRM is provided. Thereafter, the chapter focuses on design considerations of an SRM, including geometrical structures that improve the performance and efficiency of an SRM. Following the conclusion, an SRM is proposed as an XDM.

Chapter 3 provides a literature review on the topics of numerical simulations. Relevant background on the numerical simulation methods used in Ansys® Maxwell is discussed. The literature review provides a better understanding of the different types of solvers, solutions, and setups during the analysis of an electromagnetic machine, i.e., an electric motor or transformer. This chapter also summarises different electromagnetic simulation software.

Chapter 4 validates the FEA method for analysing a modular switched reluctance motor (MSRM). Replicating the MSRM of Wen Ding *et al.* is used to validate the FEA methods. Replicating a model instead of comparing data against experimental data is due to financial limitations that prohibit the manufacturing of a switched reluctance motor. The experimental tests of the Mitsuba M2096-DII BLDC used to create an efficiency map for evaluation purposes would have been perfect to validate the FEA method. However, because of the difference in operation by flux production and excitation methods, it is suggested to validate an SRM instead of a BLDC.

Chapter 5 presents the steps to design the proposed SRM. Design specifications are obtained by analysing the operating points of the Mitsuba M2096-DII when evaluated using the drive cycle. Design analysis of the geometric structure, windings, and thermal considerations and the constructed efficiency map are provided.

Chapter 6 provides an evaluation of an SRM for solar vehicle application. This chapter also evaluates the Mitsuba M2096-DII as a reference. A drive cycle is constructed to evaluate a traction motor. The conclusion compares the results of the proposed SRM with those of the Mitsuba M2096-DII. Evaluating the Mitsuba M2096-DII was completed before starting with chapter 5 to specify performance requirements the design should adhere to.

Chapter 7 provides the conclusion of this study. Recommendations for further work and possible design alterations that could improve the proposed SRM are identified for future development studies.

The appendices consist of the following:

- A methodology to experimentally test a traction motor.
- Additional FEA data obtained from the validation study (chapter 4).
- Thermal validation and analysis of an MSRM.
- Analysis data of the drive cycle evaluation.

CHAPTER 2 THE SWITCHED RELUCTANCE MOTOR

Today, almost every automotive manufacturer has an EV or HEV in their fleet. The European Union suggested an effective ban on the sale of new ICE vehicles from 2035 onward. The ban on ICE vehicles forces automotive manufacturers to invest in alternative energy sources. As such, electric motors will be used in transport systems at an increasing rate. The largest consumer of electrical energy is electrical motors and therefore an electrical motor plays a vital part in the growing market of electrification. Switched reluctance motors are becoming an exceptionally attractive choice for use in the industrial, residential, commercial, and transportation sectors [55].

This chapter discusses the overview and principles of an SRM. Furthermore, designs of SRMs with similar specifications to the Mitsuba M2096-DII are reviewed. Subsequently, the most important design considerations when designing an SRM are discussed. The design considerations are followed by a review of modular SRM structures that provide improved motor efficiency. This chapter concludes with a summary and a proposed SRM design for evaluation.

2.1 Overview

The SRM represents one of the oldest electric motor designs. This motor design originated around the 1830s to the 1850s. The origin of the motor lies in the horseshoe electromagnet of William Sturgeon in an attempt to convert the “once only” attraction of an iron armature into an oscillatory or continuous motion.

A piece of soft magnetic material is fastened to a lever and placed near an electromagnet, as shown in Figure 2-1a. The force of the electromagnet tends to attract the piece of magnetic material. The attraction force is divided into a radial and a tangential component. The tangential force attempts to move the piece of magnetic material into the so-called aligned position, shown in Figure 2-1b. With the lever fastened at some central point, the tangential force creates torque, and rotation of the magnetic material occurs.

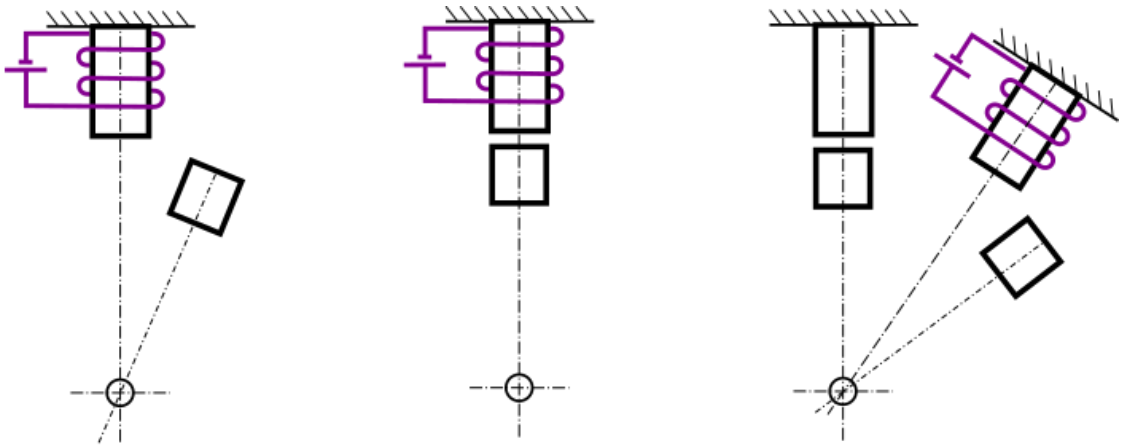

(a) *(b)* *(c)*

Figure 2-1: Attractive forces between an electromagnet and magnetic material in the: (a) Unaligned position; (b) Aligned position; (c) Continuous motion

The rotation of a piece of magnetic material around the centre is based on the principle of mechanical construction. There should always be at least one electromagnet per piece of magnetic material in the unaligned position, as shown in Figure 2-1a. For continuous rotation, a pair of electromagnets must be energised sequentially according to a prescribed energising pattern. The anticlockwise rotation of the magnetic material piece shown in Figure 2-1c is achieved by energising the electromagnet when the magnetic material piece is near and on the right-hand side of the electromagnet. After the de-energisation of the electromagnet, the next electromagnet is energised, similarly, the next phase and so forth. For anti-clockwise rotation, a clockwise excitation pattern is followed. The basic operation highlights that current polarity has nothing to do with the direction of rotation but is determined instead by the excitation sequence of the electromagnet coils [56].

The direct ancestor of the SRM, or the so-called ‘electromagnetic engine’, patented by WH Taylor in 1838, was based on the principle of the horseshoe electromagnet. However, the SRM required mechanical switches that were inefficient that resulted in the SRM suffering from torque pulsations and low reliability. The SRM lost all attention and was soon replaced by DC and AC motors. With the improvement in power electronics, power switches, and advancements in magnetic materials and motor design principles, the SRM was brought into the variable speed market.

2.1.1 Mathematical model of an SRM

The SRM is a non-linear control structure and therefore it is vital to develop a relevant model. An elementary equivalent circuit, as shown in Figure 2-2 can be derived when neglecting the mutual inductance between the phases as follows [57]:

The instantaneous voltage, according to Faraday's law, is equal to the sum of the resistive voltage drop and the flux linkage derivative as a function of rotor position and the current, provided as [58]:

$$V = IR + \frac{d\lambda(\theta, I)}{dt} \tag{1}$$

Where V is the phase voltage, I the phase current, R the phase resistance, θ the rotor position, and λ the flux linkage per phase given by:

$$\lambda = \lambda(\theta, I) \tag{2}$$

The flux linkage is a function of the rotor position and phase current and by neglecting magnetic saturation in the equivalent circuit, flux linkage is redefined as:

$$\lambda = L(\theta, I)I \tag{3}$$

Where L is the dynamic winding inductance dependent on the position of the rotor and the phase excitation current. Differentiating equation (1), the instantaneous voltage equation is:

$$V = IR + \frac{\partial\lambda(\theta, I)}{\partial i}\frac{dI}{dt} + \frac{\partial\lambda(\theta, I)}{\partial\theta}\frac{d\theta}{dt} = IR + L(\theta, I)\frac{dI}{dt} + I\frac{dL(\theta, I)}{dt}\omega \tag{4}$$

Where ω is the angular velocity. In this equation, the third term on the right-hand side represents the back EMF, ε_b, and is obtained as:

$$\varepsilon_b = I\frac{dL(\theta, I)}{dt}\omega \tag{5}$$

Note that the back EMF is dependent on the operating point and is obtained at the rated torque-speed operating point.

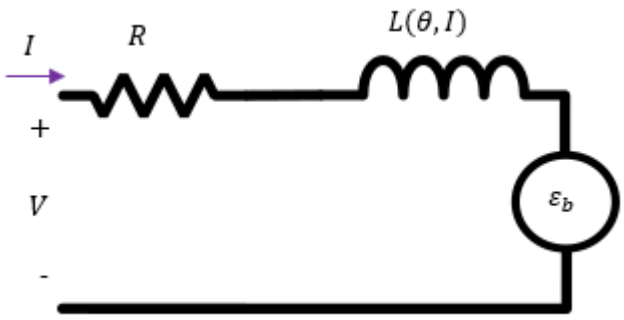

Figure 2-2: Equivalent circuit of an SRM

Furthermore, the power conversion process of an SRM can be derived by multiplying both sides of equation (4) with the phase current.

$$V = I^2R + L(\theta, I)I\frac{dI}{dt} + I^2\frac{dL(\theta, I)}{dt}\omega \tag{6}$$

Assuming the SRM is operating in the magnetic linear region, the second term on the right-hand side can be expressed further using the product rule for differentiation.

$$IL(\theta, I)\frac{dI}{dt} = \frac{dI}{dt}\left(\frac{1}{2}L(\theta, I)I^2\right) - \frac{1}{2}I^2\frac{dL(\theta, I)}{dt}\omega \tag{7}$$

Substituting equation (7) into equation (6), the power equation of an SRM is calculated as:

$$P = VI = I^2R + \frac{dI}{dt}\left(\frac{1}{2}L(\theta, I)I^2\right) + \frac{1}{2}I^2\frac{dL(\theta, I)}{dt}\omega \tag{8}$$

It can be seen that the input electrical power on the left-hand side is converted, respectively, to electrical, magnetic, and mechanical power on the right-hand side. The electrical power on the right-hand side is dissipated as heat in terms of copper losses. The magnetic power is stored in the magnetic field energy of the magnetic core and the mechanical energy is in terms of torque production. The torque production (τ) in the linear region is given by:

$$\tau = \frac{I^2}{2}\frac{dL(\theta, I)}{dt} \tag{9}$$

It is seen that the direction of torque is independent of current polarity, due to the square of the current. The next section will demonstrate how the torque equation of an SRM is derived using co-energy. Co-energy is a non-physical quantity used in extensively in the analysis of non-linear systems, such as electrical machines and electromechanical devices [55].

2.1.2 Principle of operation

An SRM is identified by the number of stator poles and number of rotor poles. As shown in Figure 2-3, an SRM with 6 stator poles and 4 rotor poles, called a 6/4 SRM is shown to describe the basic principles of an SRM. Figure 2-3 shows a 6/4 conventional SRM in its aligned position, misaligned position, and unaligned position with respect to the coils [59]. The following parameters are shown in Figure 2-3: pole height, pole arc, and pole pitch, which applies to both the stator and the rotor. Also, a non-magnetic spacer shown, explained in §2.1.4 is used to minimise windage losses.

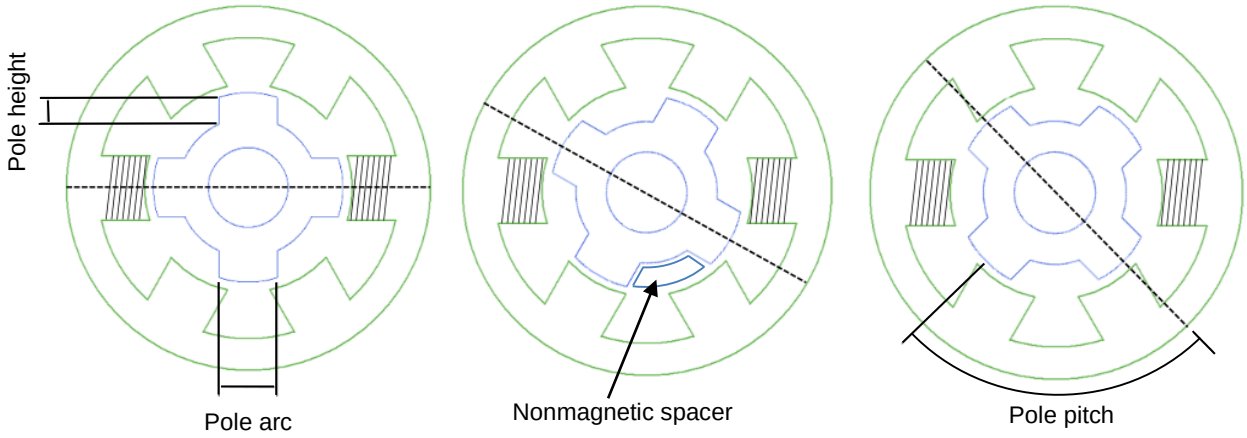

Figure 2-3: A 6/4 SRM in the: (a) Aligned position; (b) Misaligned position; (c) Unaligned position

The operation of a motor relies on torque production to achieve the desired rotational speed. Torque production is a function of inductance in an SRM. Inductance is derived from the magnetomotive force (MMF), $\mathcal{F}$, in a magnetic circuit [29]. MMF is given by:

$$\mathcal{F} = \emptyset\mathcal{R} = NI \tag{10}$$

Where N is the number of conductor turns, I is the current, $\mathcal{R}$ is the magnetic reluctance, $\emptyset$ is the equivalent flux and is given by:

$$\emptyset = \frac{\lambda}{N} \tag{11}$$

Where λ is flux linkage, given by $\lambda = LI$, with L as inductance.

Rearranging the equations, we can obtain the following:

$$L = \frac{N^2}{\mathcal{R}} \tag{12}$$

Thus, the phase inductance of a coil is inversely proportional to the magnetic reluctance in the magnetic circuit of an SRM. The three relative positions of an SRM described by inductance and reluctance are as follows:

- An aligned position where the rotor poles are aligned with the stator poles. During this instance, the phase inductance of the winding is at a maximum and the magnetic reluctance at a minimum.
- A misaligned position where rotor poles are not fully aligned with the stator poles, nor unaligned with two stator poles. Moving from the unaligned position to the aligned position, the phase inductance of the winding is gradually increasing, and the magnetic reluctance gradually decreases. When moving from the aligned position to the unaligned position, the phase inductance of the winding is gradually decreasing, and the magnetic reluctance gradually increasing; and
- An unaligned position where the rotor poles are exactly between two stator poles. During this instance, the phase inductance of the winding is at a minimum and the magnetic reluctance at a maximum.

A magnetic circuit, similar to an electrical circuit can be used to analyse an SRM. The biggest difference in the analogy is that a resistor in an electric circuit dissipates electrical energy, whereas reluctance stores magnetic energy as discussed in the operating principles of an SRM. The operating principles of an SRM for torque production are described in the following sections. The operating principles of an SRM are divided into its electromechanical energy conversion and its torque production.

2.1.2.1 Electromechanical energy conversion

Electromechanical energy conversion is the consecutive transformation of electrical energy into magnetic energy and magnetic energy into mechanical energy, or mechanical energy into magnetic energy and magnetic energy into electrical energy. An SRM is a single electromechanical system in which the electrical energy is converted into mechanical energy [60, 55]. Non-linear analysis of an SRM takes into account the saturation of the magnetic circuit to fully understand the electromagnetic energy conversion for motor operation. To understand the electromechanical energy conversion process of a non-linear system, a non-linear magnetisation curve is used, shown in Figure 2-4.

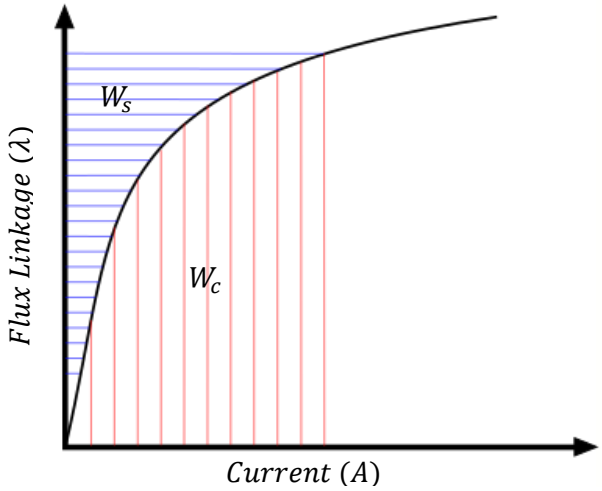

Figure 2-4: Magnetic characteristic relationship between energy (W_s) and co-energy (W_c)

The magnetisation curve in Figure 2-4 plot the flux linkage versus current for a fixed rotor position of the SRM, shown in Figure 2-4. The magnetisation curve shows the stored magnetic energy, W_s, and the magnetic co-energy, W_c. The stored magnetic energy and co-energy is given by equations (13) and (14) respectively:

$$W_s = \int I d\lambda \tag{13}$$

$$W_c = \int \lambda dI \tag{14}$$

When the rotor reaches the turn-on position, the phase switches are turned and the phase voltage starts to build up phase current. A part of the energy is stored in the magnetic field at this stage, called the magnetic field energy. The magnetic field energy will increase with the rotating rotor until the position where the current excitation, known as the turn-off position is reached and the phase winding switches are turned off [61]. The other part of the input energy, W_e, is dissipated by mechanical work, W_m , and losses, W_{losses}. Thus, the energy conversion is given by:

$$W_e = W_s + W_m + W_{losses} \tag{15}$$

The flux linkage of an SRM during operation is not constant, as shown in Figure 2-5. Nevertheless, a uniform flux distribution is crucial to obtain smooth torque. Note that the conversion of electromagnetic energy is explained on the basis of constant supply voltage and fixed rotor speed.

The mechanical work produced during the magnetisation process is known as the co-energy in the electromechanical energy conversion. The input energy starts at the turn-on position, taken as the unaligned position and stops at the turn-off position. The turn-off position, is some time

before the aligned position. Once the turn-off position is reached, the magnetic energy at that moment is $F + W_{m2}$. At this stage, the magnetic field energy, W_{m2} is converted into mechanical work and losses [61]. The surplus of field energy, F, are fed back to the power source.

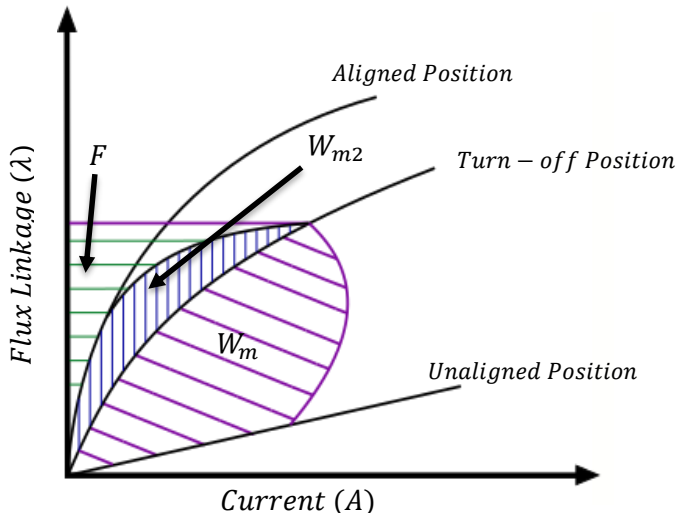

Figure 2-5: Magnetic characteristics of an SRM under operation

The aligned position of an SRM in saturation has higher stored energy than an SRM not in saturation for the same current magnitude. Significant magnetic saturation of a motor has an influence on the torque producing capability and power factor, equal to about twice that of a motor not in magnetic saturation [55]. The degree of saturation influences the choice of motor and inverter design. Thus, magnetic saturation is a desirable characteristic for SRM operations but must be localised to the pole tips since electromagnetic energy conversion occurs in the air gap [62].

2.1.2.2 Torque production

The torque production of an electric machine is mainly of two types; electromagnetic torque and reluctance torque [56]. Electromagnetic torque is produced with the interaction of the magnetic fields between the stator and rotor poles and the reluctance torque is produced by the variable air gap between the stator and rotor poles. The torque of an SRM can be calculated by applying the principles described in the previous section.

Using the flux linkage curve of Figure 2-5, the electromagnetic torque of a non-linear magnetic system can be calculated in terms of the co-energy [55, 58]. The electromagnetic torque equation is given by:

$$\tau_e(\theta, I) = \frac{\partial W_c(\theta, I)}{\partial \theta} \tag{16}$$

Rewriting equation (14), the co-energy can be expressed at any rotor angle, θ, as given by:

$$W_c = \int_0^I \lambda(\theta, I) dI \tag{17}$$

If a linear magnetic model is assumed, the co-energy and torque equations, using the relationship between flux linkage and current can be rewritten as:

$$W_c = \int_0^I L(\theta) I \, dI \tag{18}$$

$$W_c = \frac{I^2}{2} L(\theta) \tag{19}$$

$$\tau_e = \frac{I^2}{2} * \frac{dL}{d\theta} \tag{20}$$

The absolute value of $\frac{dL}{d\theta}$ contribute to the amount of mechanical torque, and therefore SRM designs require large $\frac{L_{max}}{L_{min}}$ ratios, hence the large absolute value of $\frac{dL}{d\theta}$ to obtain the high torque.

The equation of motion torque for an SRM is given by:

$$\tau = J_{rotor} \frac{\partial \omega}{\partial t} + D\omega + T_L \tag{21}$$

Where J_{rotor} is rotor inertia, D_c is the damping coefficient and T_L is the load torque. Angular velocity can be written as a function of the rotor speed, N_r, as:

$$\omega = 2\pi N_r \tag{22}$$

In this section, it is shown that a simple equivalent circuit, as shown in Figure 2-2 cannot be used to represent an SRM. However, an equivalent circuit can only be used under the assumption of unsaturated, linear operating conditions and is only an approximation of reality. To accurately predict the characteristics of an SRM, the saturation and non-linear effects should be included. Therefore, FEA software is used to consider all these effects when analysing an SRM [63]. §3.1.2, p.49, offers a review of the different FEA software for electromagnetic systems.

2.1.3 Motor operation

Depending on the applications, an electric motor can operate under different load conditions. For an industrial motor, some priority is given to the operating region. An industrial motor operates more frequently near a single operating point than the rest of the points in its torque-speed profile. However, for traction, its operating region is constantly changing [61]. Therefore, a traction motor must meet all operating requirements. Obtaining a better understanding of motor usage and operational changes under different driving cycles will be required. A driving cycle is used to assess the performance of a vehicle, refer to chapter 6. The expected operating regions when using an SRM as a traction motor are mapped by its torque-speed characteristics as shown in Figure 2-6.

2.1.3.1 Torque-speed characteristics

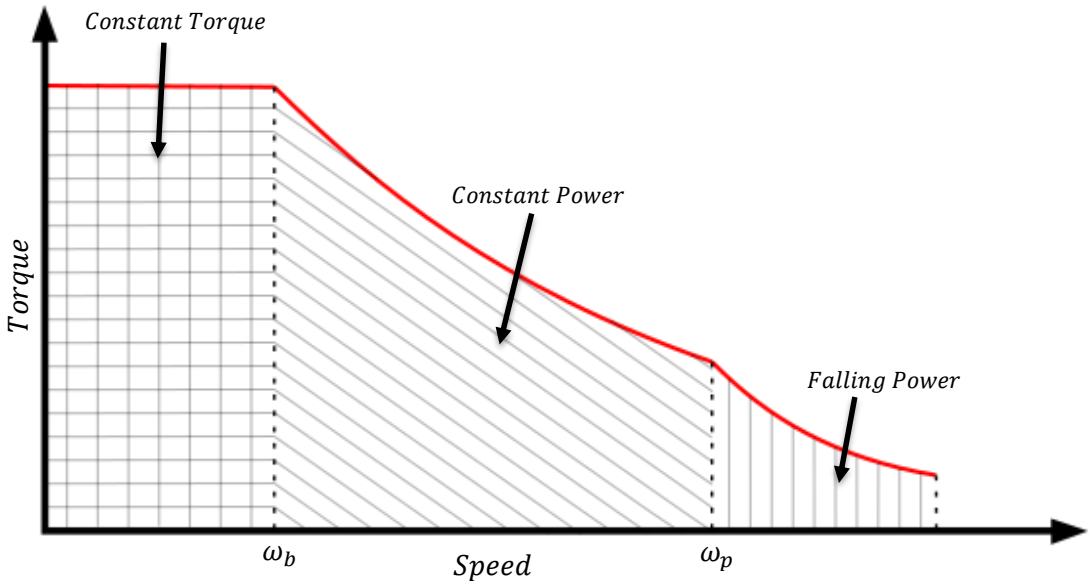

Figure 2-6: Desired torque-speed characteristics of an SRM

The typical torque-speed characteristics of an SRM are shown in Figure 2-6. Torque-speed characteristics can be divided into three visible operating regions. The three operating regions are the constant torque, constant power, and falling power regions. The constant torque operation occurs between the zero speed and the base speed (ω_b). The base speed is the maximum speed at which the current rises almost instantly as the generated voltage is higher than the back EMF. The current should be limited to achieve constant torque.

An increase in back EMF also occurs at speeds above the base speed. At speeds above the base speed, the conduction angle of the motor should be increased to reach the desired current level before the motor reaches an aligned position. In the region of constant power, the torque

decreases with the increase of speed until the maximum speed of constant power, ω_p, is reached. At speeds beyond the maximum speed of constant power, the conduction angle cannot be increased, such that the torque decreases more rapidly with the increase of speed. This is known as the region of falling power. In the falling power region, constant power is no longer achievable [61]. A motor control strategy is used to operate in each of these three operating regions.

2.1.3.2 Control strategies

To operate an SRM a certain amount of control and power electronics is necessary, unlike an IM or DC motor which can run directly from a DC or AC power supply. Torque of an SRM is produced in impulses, flux is built from zero and has to return to zero in each stroke. The orthogonality of the flux and current as found in DC machines or employed in AC machines is not present in an SRM. As torque is produced in impulses, a certain amount of control and power electronics is necessary to control an SRM. For the operation of an SRM, only one phase should be excited at a time. Another phase is then activated and so forth to generate continuous torque. The switching of a three-phase SRM is shown in Figure 2-7.

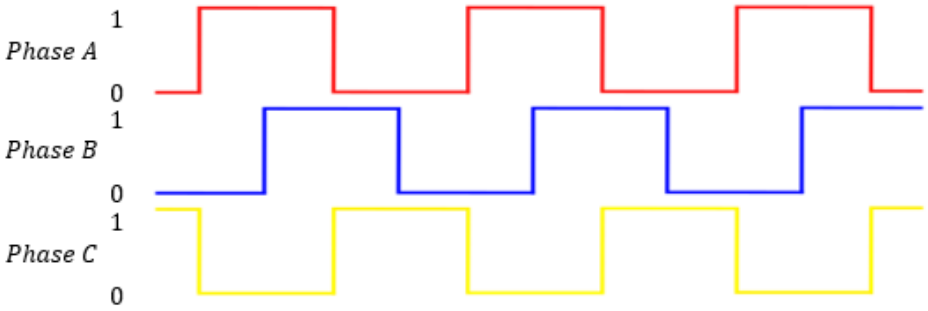

Figure 2-7: Phase excitation of a three-phase SRM

The different operating regions shown in Figure 2-6 are usually controlled by different motor control strategies. The control strategies are current control and single-point control (SPC). The back EMF is very small at low speeds; therefore, the phase current rapidly increases. A hysteresis band is used to maintain the current within a reference value. The current is maintained within the hysteresis band of the reference value, and the semiconductor switches act as a current chopper. This control strategy is known as chopped current control (CCC).

The conduction angle (turn-on and turn-off angles) usually stays constant for CCC unless the motor is optimised for efficiency, torque ripple, or acoustic noise. SPC is used to operate the SRM above its base speed. For constant torque operations, the conduction angles are adapted to their torque and speed requirements until the conduction angles can no longer be adapted, therefore

staying constant and operating in the falling power region [64]. The control operation of an SRM is summarised in Table 2-1.

Table 2-1: Control strategies of an SRM

Control	Operation	Variables	Constants
CCC	Constant torque	Reference current	Conduction angle
SPC	Constant power	Conduction angle	Supply voltage

2.1.4 Losses

In §2.1.2.1, the review of electromagnetic energy conversion, copper loss in the windings, core losses in the iron core, and mechanical losses in the rotor are neglected. When considering the losses in an electrical motor, the energy balance can be categorised as shown in Figure 2-8 [55].

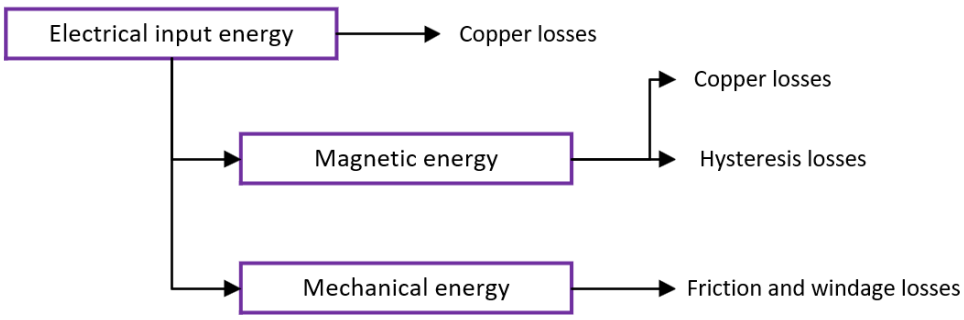

Figure 2-8: Losses in an SRM

When all losses are subtracted from the input power, the mechanical output power is obtained. Mechanical output power divided by the electrical input power gives efficiency. In an electric motor, efficiency is considered an important aspect during the development process to maximise the amount of output power when providing a set amount of input power [65].

The mechanical loss of an electric motor originates from the bearing friction and wind resistance opposing the rotor. Bearing losses depend mainly on the bearing load, bearing type, bearing lubricant, and lubricant characteristic properties.

When the rotor of an SRM is rotating, the rotor work like a fan, which generate windage loss. To reduce the windage losses, the air gap between the rotor poles and the rotor structure, referred to as the back iron should be a cylindrical shape obtained by filling epoxy resin or using non-magnetic spacers, creating a smooth rotor surface, as shown in Figure 2-3. These mechanical

losses often present much higher losses at high speeds, since the mechanical losses are a cubic function of rotor velocity, rather than a linear function [66].

Electrical losses of an electric motor are divided into two categories. The two categories are copper losses and iron losses. Copper losses is used to describe the resistance in the wire used to wind a coil, which means that even conductors made of aluminium account for copper losses, or more specifically resistive losses. Copper losses in an SRM are due to the electrical resistivity of the stator windings and are usually the most significant energy loss of the motor, predominantly active at low-speed and high-current operating conditions. Copper is relatively heavy, therefore in the development of an electric motor, as little as possible copper usage is desired to minimise motor mass. However, minimising the cross-sectional area of copper in the motor leads to an increase in resistance and therefore an increase in copper losses [67]. Thus, a trade-off between motor mass and motor performance is expected when limited by constraints.

Iron losses, also known as core losses, consists of eddy current losses and hysteresis losses. The eddy current losses are produced by parasitic current through the magnetic core of an electric motor and are dependent on the lamination thickness, motor operating frequency, flux density, and material resistivity. The hysteresis losses are the resistance to a directional change from the magnetisation, frequency or flux density in the magnetic core and are mainly dependent on the hysteresis loop of the material [68, 69].

Determining core losses in an electrical motor is a significant part of the development process of an electric motor. However, it is a complicated process to accurately predict the core losses in an SRM when following an analytical approach. The difficulty of the analytical approach is a consequence of the flux linkage waveforms and flux densities that differ in each part of an SRM [55, 70]. An analytical procedure often does not account for the difference between the flux linkage and the flux densities in the motor. Due to distorted and non-sinusoidal flux and magnetic saturation in different parts of the stator and rotor, calculating core losses is very complicated [71]. Analytical models and lookup tables are a fast approach to determine losses, however have reduced accuracy. Empirical formulas are usually considered in core loss estimation, but are insufficient for SRMs [72]. Therefore, the best alternative method to accurately determine core losses is to use FEA [73].

2.2 Propulsion of electric vehicles

Traction motors play a crucial role in an EV. The purpose of an electric motor is to propel the vehicle using energy extracted from the battery. The purpose of this study is to evaluate an SRM for solar vehicle application. A suitable SRM should be selected to evaluate. In this section, four SRM designs found in literature, exhibiting similar power ratings as the Mitsuba M2096-DII were

reviewed as the Mitsuba M2096-DII is currently used as the traction motor in the solar vehicle of the NWU. However, per the scope of this study (§1.5.2, p.9), an SRM best suited for the solar vehicle characteristics would need to be designed to justify the use and future development of an SRM for solar vehicle application.

Nikunj Ramabhai Patel *et al.* designed a 12/16 C-core radial flux modular SRM [74, 75]. The motor is designed to propel a vehicle, having a total mass of 120 kg, 0.6 m^2 frontal area, and 0.7 drag coefficient. These vehicle characteristics resulted in the motor specifications of 26 Nm at a rated speed of 600 rpm when considering acceleration of 0-50 km/h in 20 seconds and speeds of roughly 60 km/h.

The design process is divided into three steps. The first is to derive the required torque and power using vehicle dynamic equations. The second part is to fulfil the three basic SRM conditions using the feasibility triangle (refer to §2.3.4, p.32). The third part was to calculate the excitation parameters and torque using magnetic analysis and Ansys Maxwell to analyse the static and dynamic characteristics. When comparing the analysis results against a 12/16 conventional SRM, Nikunj Ramabhai Patel *et al.* concluded that when comparing magnetic characteristics of a conventional radial flux SRM and the designed C-core radial flux modular SRM, that less magnetic material was required for the C-core design [74, 75]. The C-core radial flux modular SRM offered higher torque and efficiency than the conventional SRM at rated current and at the rated operating condition.

This C-core radial flux modular SRM proved a viable contender to use for evaluation purposes based on its rated operating condition. However, not enough information was provided to construct and verify the design using Ansys Maxwell. Also, the study did not provide an efficiency map for the designed motor that could be used for evaluation purposes.

Jeanin Lin designed a 6/10 conventional SRM [56]. The motor was designed to propel a bicycle, with total mass of 100kg (mass of the cyclist and the bicycle), 0.5 m^2 frontal area, and 0.5 drag coefficient. These characteristics resulted in motor specifications of 9.5 Nm at a rated speed of 500 rpm. Using a reduction gear ratio of 3:1 and a wheel radius of 0.33 m, 500 rpm equalled 20 km/h as the rated speed.

The configuration of an electric bicycle system was constraint by the legislation of Ontario, Canada, which limits the output power of electric bicycles to be within 500 Watt with the maximum speed not exceeding 32 km/h while the bicycle is only propelled by the electric motor. The design process started with the requirements obtained by analysing a typical velocity profile of an electric bicycle. SPEED PC-SRD, a commercial machine design software was used to assist in SRM

geometry analysis, where after Flux 2D from Magsoft was used to obtain a detailed design analysis.

Jeanin Lin concluded that the motor exhibits higher torque compared to a conventional 6/4 SRM, and that an alternate pole configuration (NSNSNS) compared to a traditional pole configuration (NNNSSS) in an SRM proved to have higher and more consistent output torque. It was concluded from experimental testing that the difference between 2D FEA and test results showed that the end winding effects needs to be considered for small thickness machines.

This SRM design lacked performance characteristics, not only when compared to the Mitsuba M2096-DII (§6.2.1, p.136), but also when considering the design constraints as the motor was only designed to assist the cyclist when pedalling.

Saurabh Prakash Nikam *et al.* designed a conventional SRM [43]. The motor was designed for a two-wheeler vehicle with a total mass of 120 kg (mass of the driver and the vehicle). The maximum speed of 30 km/h and an acceleration target of 0 to 20 km/h in 5 seconds was required. The characteristics resulted in motor specifications of 36 Nm at rated power of 500 W whilst using a gear ratio of 6:1.

Both a three phase 6/4 pole SRM, a three phase 6/8 and a four phase 8/6 pole SRM was considered during the design process. The rotor poles were increased from four to eight for the three phase motor to reduce the magnetic flux paths. However, with the rotor poles close to one another, the motor exhibited low field weakening capabilities. Therefore, a four phase 8/6 pole SRM was proposed to improve the field weakening capabilities, that could lead to increased efficiency.

Even though the different designs were discussed, the studies did not discuss the design processes. Considering the motor specifications, the motor designed by Saurabh Prakash Nikam *et al.* without the gear ratio will be rated for a torque of 4 Nm, and speed of 1200 rpm. These characteristics were not sufficient to propel the solar vehicle.

Vandana Rallabandi and Baylon Godfrey Fernandes designed a 12/26 segmented rotor SRM [76]. The motor was designed for direct drive applications with the performance characteristics of 24 Nm and 600 rpm for maximum torque and speed.

The motor was chosen as a 12/26 segmented rotor SRM to demonstrate tight torque, low speed and high efficiency operations. The effects of the number of rotor poles, pole arc angles and the geometric dimensions of the stator was analysed using FEA. Flux 2D, developed by Cedrat is used to analyse this SRM design.

Comparing the design with that of a 6/10 SRM and 12/16 segmented rotor SRM with equal dimensions, it was shown that the design exhibited significantly higher efficiency and a higher torque to weight ratio. Efficiency was 2 to 4% higher, whilst the torque to weight ratio was roughly 1 Nm/kg more than the other SRMs. The increase in efficiency was due to lower copper losses, with copper losses almost a third to half the losses compared to the other two SRMs.

This design exhibited good performance characteristic, however, the maximum performance characteristics of this design was roughly the required rated performance characteristics for evaluation purposes.

The four SRM designs were briefly discussed in order of their designed performance characteristics, design process, modelling tool, results and a quick summary. Though, none of these motor designs offered the required performance ratings, as specified in §5.1, p.89.

If an SRM was found with the required performance characteristics and enough data to replicate the design using FEA software and thereafter validate the design to provided experimental data (i.e. torque-speed characteristics, efficiency map, operating currents), the SRM design could have been used for evaluation purposes in this study. Thus, as no design was found with the required performance characteristics, an XDM of an SRM was required, as per the scope of this study (§1.5.2, p.9).

2.3 Design considerations

The geometric dimensions of an SRM are the main contributing factor to its magnetic characteristics, and therefore its electromagnetic energy conversion as reviewed in §2.1.2.1. Specifying the desired performance characteristics, such as the torque-speed profile, the SRM design can begin. The design considers the aspects of geometric dimensions, pole configurations, and the winding parameters as discussed in this section.

Anas Labak has shown that an SRM with increased reluctance improves the magnetic flux characteristics. A significant improvement in the aligned position of magnetic flux is seen when observing the magnetic flux characteristics. This improvement in magnetic flux relate to improved dynamic torque operations, resulting in higher output performance. Assuming the input power is constant, an SRM of high efficiency can roughly be estimated during the design stage using magnetic flux characteristics. However, magnetic flux characteristics are not always a guarantee of an optimal and high efficient SRM design [55, 77]. The motor controller and conduction angles, shown in §2.1.3, p.22 and §5.3.3, p.117 also have a major effect on the performance and efficiency of an SRM [55, 78].

2.3.1 Structure

Switched reluctance motors fall into three classifications based on the direction of flux through the air gap. The three classifications are the transverse, axial, and radial flux motors [55]. The basics of the radial and axial flux directions are explained from the coordinate system in Figure 2-9. Both the radial and axial flux motors lie centralised around the z-axis, also called the axial direction. As observed in Figure 2-9, the axial flux motor is where the magnetic flux path in the air gap is parallel to the axis of rotation and the radial flux motor is where the magnetic flux path in the air gap is perpendicular to the axis of rotation. The transverse-flux motor has the magnetic flux path predominantly tangential to the relative axis of rotation. A transverse flux motor is complex and very rarely found [79]. The basic principles of the transverse flux motor are further discussed in §2.4.4.

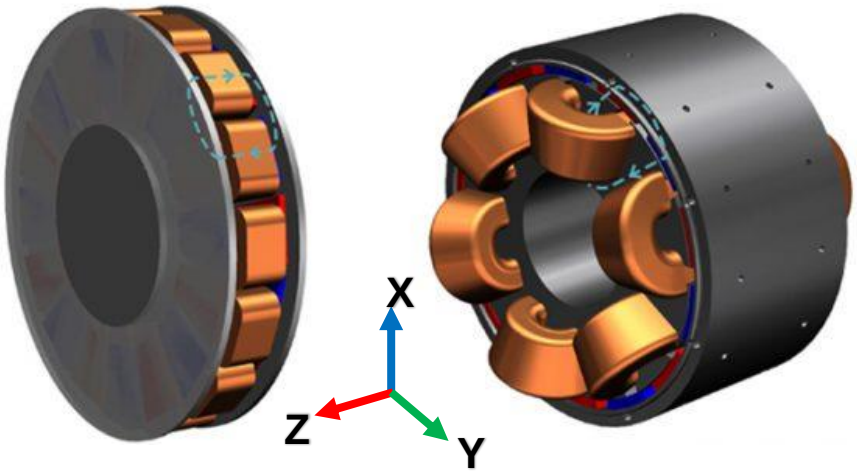

Figure 2-9: SRM structures: (a) Axial flux; (b) Radial flux [80]

An axial and radial flux SRM is compared in [81]. Both the axial and the radial flux motors consist of the same volume, resulting in the radial flux motor offering more torque. This is mainly due to the fact that magnetic flux crosses the air gap twice in a radial flux motor compared to four times in the double-sided axial flux motor. To obtain the same torque as the radial flux motor, the diameter of the axial flux motor has to be increased beyond the diameter of the radial flux motor. It is often difficult to obtain the same amount of torque when the diameter is constrained. Manufacturing an axial flux motor is also a difficult process. Another method to manufacture an axial flux motor is shown in [82], where the complex structure is machined from a block of soft magnetic material instead of laminations.

An outer rotor radial flux SRM is an appealing choice when mounting the rim of the wheel directly to the traction motor, commonly referred to as an in-wheel traction motor [55, 83]. An outer rotor configuration offers higher torque capability due to its extended air gap diameter and larger rotor

inertia. An outer rotor motor can be coupled directly to a wheel rim, eliminating the use of mechanical gears, and can reduce the overall drive efficiency by around 20-30%. Due to the larger inertia of the rotor, the torque ripple is damped, making for smooth and stable low-speed operation [55].

Quite a few topological variations of SRMs have emerged over the years to improve their performance. The main considerations include the number of phases, pole configurations, pole and winding designs, and the magnetic material. However, segmented pole configurations offered an alternative way to improve motor performance. These performance improvements are reviewed in §2.3.8.

2.3.2 Phases

Common industry practice is to use a three-phase motor [55]. For an electric motor, at least two phases are needed to maintain torque and rotational capability. In an SRM, increasing the number of phases reduces the root mean square (RMS) current of each phase for the same amount of torque capability. However, increasing the number of phases also adds to the reliability of the motor, so that when one phase fails, the other phases will still allow the motor to operate at a lower performance rating.

Increasing the number of phases also has its drawback. The major drawback of increasing the phases is the increase of electronic switches and converters in the motor controller. In low and medium-power motors, the increase in switches and converters significantly increases the cost of the motor drive system [84]. Also, a higher number of phases requires a higher number of poles. A larger number of poles will reduce the available space for coils if the outer diameter of the motor is constrained. Therefore, increasing phases is not always a practical solution [55].

During the design of an SRM, the following factors are usually the deciding factors when specifying the number of phases [85]:

- The starting capability of the motor
- The directional capability of the motor
- The reliability of the motor
- The cost of the motor
- The power density of the motor
- The efficiency of the motor

Efficiency is a crucial aspect of an electric motor and is enhanced by reducing losses. For an SRM, the decrease in the number of stator phases and the number of phases switching per revolution reduces the core losses at high-speed operations. Therefore, three phases are

preferred over four phases in an aircraft starter/generator with the requirement of very low losses [85]. This is because the starter/generator of small size requires a reduction in losses to maintain thermal robustness when operating at high speeds.

2.3.3 Pole configuration

An SRM is identified by the number of stator poles and the number of rotor poles. The number of poles has a significant effect on the operational and performance requirements of the motor. The pole configuration requires a correct selection during the design process so that the condition of balanced operation is satisfied. Balanced motor operation is obtained by symmetry of the electrical angle between stator poles and the number of stator pole to rotor pole combinations [86, 59]. The well-known SRM combinations are as follows:

- Three-phase SRMs: 6/2; 6/4; 6/8; 6/14; 12/8; 18/12; 24/16
- Four-phase SRMs: 8/6; 8/10; 16/12; 24/18; 32/24;
- Five phase SRMs: 10/4; 10/6; 10/8; 10/12.

Note that at a set rotational speed, the increase of a rotor poles will cause the excitation frequency to increase. For an SRM, the phase excitation frequency is determined by the time it takes for one rotor pole to move from one phase to an adjacent phase. The phase excitation frequency can be calculated using equation (46), p.108.

Also, when the outer diameter of the motor is a constraint, an increase of poles will reduce the width of the stator teeth and slot areas. A small slot area might be difficult to wind the specified winding, reduce the copper losses, and achieve the required current density. Furthermore, if the width of the stator pole decreases, the core might oversaturate when operating at peak current, which can lead to reduced torque production capability [55]. However, it is known that the torque production of an SRM is improved when operating in the saturation region of its magnetic material.

Comparing a 12/16 three-phase SRM with a 12/8 three-phase SRM of the same geometry and magnetic material, it is determined that the 12/16 SRM offers more static torque over its electrical period [86]. The 12/16 SRM has a smaller mechanical angle for its respective electrical period. The 12/16 pole configuration exhibits a good static torque to rotor position shape and is concluded to be advantageous to use for EVs.

A 6/10 three-phase SRM is compared to a 6/4 three-phase SRM in [87]. The outer diameter, stack length, and air gap were kept constant between the two motors. The 6/10 SRM configuration showed a significant increase in torque during the comparison. However, it should be noted that, for comparative cases, the stator and rotor arc angles, phase windings, current ratings, and

switching frequencies differ. Thus, the comparison between motors is not a direct comparative case.

These studies proved that an SRM with a high ratio of stator to rotor poles has higher efficiency, lower torque ripple, and a high torque to weight ratio. Note that the studies focus on inner rotor, radial flux SRMs and not on outer runner SRMs. Furthermore, the losses depend on the electrical frequency and could be intensified at the same operating speed given a higher ratio of poles [55].

2.3.4 Pole embrace

Pole embrace is regarded as a satisfactory performance requirement. The importance of pole embrace is to satisfy the requirements of self-starting, high output torque, and low torque ripple in an SRM [55]. Pole embrace, illustrated in Figure 2-10 is defined as the ratio of the pole arc to pole pitch angle and can be expressed as:

$$Embrace = \frac{pole\ arc}{pole\ pitch} \tag{23}$$

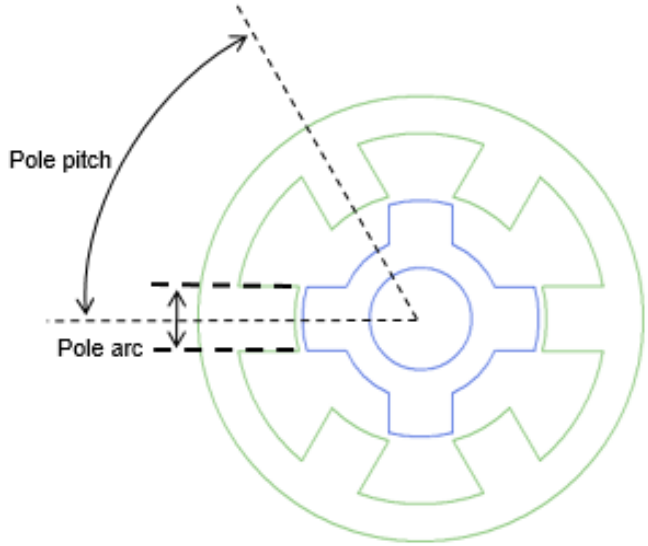

Figure 2-10: Illustration of pole embrace

Thus, pole arc angles have a significant effect on the operation of the motor. The stator and rotor arc angles are easily obtained from the feasibility triangle, shown in Figure 2-11. The feasibility triangle is constructed for a three-phase, 6/4 SRM that adheres to the requirements of self-starting, high output torque, and low torque ripple.

To satisfy the requirement of self-starting capability, the stator arc angle should be greater than the stroke angle, obtained by the following:

$$\varepsilon = \frac{2\pi}{qN_{rp}} < \beta_s \tag{24}$$

Where ε is the step angle, q is the number of phases, N_{rp} is the number of rotor poles, and β_s is the stator pole arc angle. Keeping the ratio of aligned to unaligned inductance as high as possible is to improve torque production, as discussed in §2.1.2.1, p.18. The stator pole should be smaller than the interpolar arc angle of the rotor, obtained by:

$$\frac{2\pi}{N_r} - \beta_r > \beta_s \tag{25}$$

Where β_r is the rotor pole arc angle. To further reduce torque ripple, the positive slope of the inductance curve should not overlap the negative slope of the previous shape. Thus, the rotor pole arc angle should be equal to or slightly larger than the stator pole arc angle, shown as:

$$\beta_r \geq \beta_s \tag{26}$$

Traditionally, the stator and rotor pole arcs are chosen approximately the same to avoid zero torque zones centred at the aligned position. Choosing the rotor pole arc angle equal to the stator pole arc angle is an effective way to extend the positive torque zone.

From these three constraints shown in equations (24), (25) and (26), the stator and rotor pole arc angle possibilities satisfying the three requirements are easily obtainable [88]. However, the use of the feasibility triangle requires the number of phases and pole configuration of the SRM to be known.

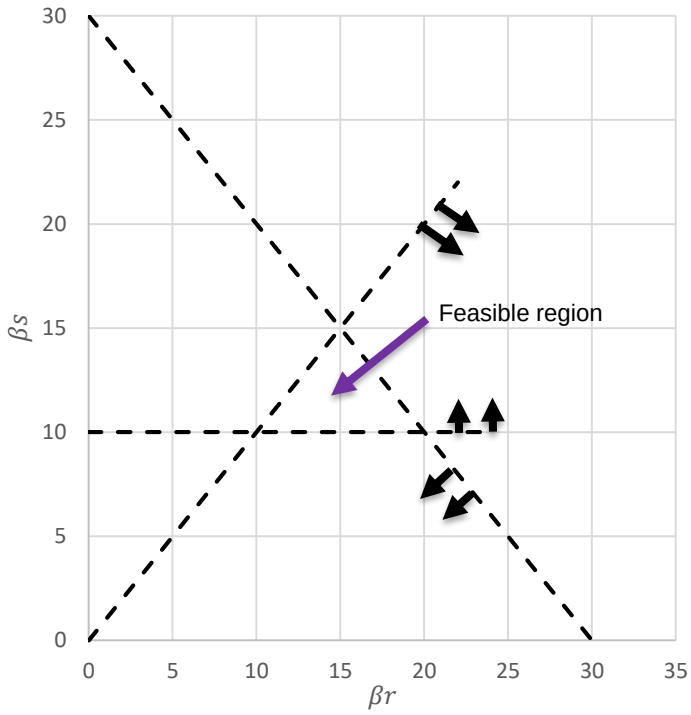

Figure 2-11: Feasibility triangle of a 6/4 SRM

A study of the effect of the pole embrace was carried out in [89]. The pole embrace ranged from a ratio of 0.2 to 0.5. The pole embrace of the stator was kept the same as that of the rotor. The findings showed that an increase of the stator pole arc angle resulted in a lower torque ripple due to minimum inductance at the unaligned position. Another study ranged the pole embrace between the ratio of 0.45 to 0.6 [90]. The results showed that the highest peak torque was obtained at a pole embrace combination of 0.45 for the rotor and 0.5 for the stator. The lowest torque obtained was at a pole embrace combination of 0.6 for the rotor and 0.45 for the stator. It was concluded that the output torque decreased when the rotor embrace increased for the same stator embrace. Thus, the pole embrace by considering the stator and rotor pole arc angles is among the most important geometrical parameters of an SRM [55].

2.3.5 Pole height

The height of the stator pole in an SRM is the height of the coil, as seen in Figure 2-3. Some space at the pole tip must be left for the pole shoe and pole wedge, which ensures that the coil remains in place during operation. If the pole tips are too long, the rotor poles operate like a fan which, in turn, along with the stator poles, generates windage losses, vibrations, and acoustic noise. In critical motor applications, the gaps between poles are filled with epoxy to minimise windage losses [55].

Analysis of pole heights results in the conclusion that an increase in stator pole heights decreases the motor torque. This is because the diameter of the rotor is decreased to satisfy the constraint of the outer diameter of the motor. Therefore, the distance between the air gap and the shaft is decreased [55]. Note that the SRM under investigation is a conventional SRM of the inner rotor structure, as shown in Figure 2-3. In addition to windage losses, a longer pole height increases the amount of magnetic material that has to be saturated, thus affecting the magnetic flux characteristics [55].

2.3.6 Wire and slot factor

Enamelled copper wire, also known as magnet wire is widely used in motor windings and exists of two components, namely the copper strand coated with a very thin layer of insulation material. The insulation material around the bare copper allows the wires to touch each other without causing an electrical short circuit [55].

Magnet wire is standardised and categorised using the American Wire Gauge (AWG). These are different categories of wire classification, but AWG is the most widely known. When winding the magnet wire around a pole, the amount of wire is limited to the available slot area. This restriction is known as the fill factor. The copper fill factor is the amount of copper that can be used in the available slot fill factor. Theoretically, the fill factor is 71.3%, however, in practice, the fill factor is around 35 to 60% and for hand-wound coils, the fill factor is between 35 and 40% [55]. The fill factor is an important parameter for an SRM, given the restrictions in manufacturability, cost, torque density, and thermal considerations. A further review of the fill factor is discussed in §5.2.3.1, p.109.

2.3.7 Magnetic material

In contrast to copper losses in low-speed operations, iron losses are predominantly active in high-speed operations. The selection of the magnetic material used for an electric motor can reduce iron losses. The magnetic characteristics are a fundamental characteristic of an SRM as no permanent magnets are used in an SRM. Thus, for an electric motor, the correct choice of magnetic material can achieve characteristic traits of high efficiency or high torque [55].

High power and torque density and low loss standard grade (EN 10106) magnetic material are usually used in traction motors. Some electric steel manufacturers provide specific magnetic materials with characteristics intended for EVs. ArcelorMittal offers its iCARe® range, with low loss levels, high torque, and speed-specific uses [91]. Cogent Power offers its Hi-lite range of advanced thin gauge electrical steel with a specific design to improve the performance of an energy-efficient application system [92]. Thyssenkrupp offers its Powercore® range consisting of magnetic material grades for e-mobility and high frequencies that are ideal for use in highly

efficient traction motors [93]. These magnetic materials are offered in very thin lamination sheets to reduce eddy current losses and increase motor efficiency [94].

2.3.8 Stacking factor

Stacking factor of an SRM is defined as the ratio of the total thickness of the lamination sheets to the axial length of the iron core [55].

For an electrical machine, the stacking factor is always less than 100%. The stacking factor typically varies between 80% and 95%. For laminations of 0.1 mm thickness, the stacking factor is around 89.6%, while for 0.2 mm thickness, the stacking factor is around 92.5%. For a lamination thickness of 0.5 mm, the stacking factor is around 95.8%. Thus, as the lamination thickness increases, the stacking factor increases [55].

2.4 Performance Improvements

Various methods are investigated to improve the performance of an SRM. These methods to enhance the performance of an SRM are ultimately divided into two feasible approaches: modifying the magnetic structure or implementing a sophisticated motor controller [1]. The motor controller can significantly affect efficiency. The scope of this study does not include the motor controller; however, because the motor controller can significantly affect efficiency, the effect of the motor controller was briefly shown in §5.3.3, p.117. For the performance improvements of an SRM, this section focused on the magnetic structure of an SRM.

Loránd Szabó stated that electrical machines were pushed to their limits by a high market demand in the last decade. As a response to the demanding challenges and high market demands of electric motors, improvements were to made to the design and manufacturing of an electric motor [95]. One of the technology solutions introduced for the magnetic structure of an SRM was the modular structure. The modular structure allowed for fast and easy repairs. The principles of modular construction tend to increase efficiency. This is due to the reduction of magnetic flux paths which tend to minimise iron losses, as well as copper losses, because less magnetisation is needed to operate at certain output power [55]. The different modular constructions and other alternative methods to improve the performance of an SRM are discussed.

2.4.1 Modular construction

The modular construction of an SRM is a method to reduce the flux path length. The concept of modular construction initially came as a response to increase the safety and reliability requirements of an electrical motor [64]. For an SRM, modular construction is an approach to increase performance and efficiency [57].

A modular switched reluctance motor (MSRM) eliminates the long magnetic path in the back iron of the stator when a phase is excited. In addition, the modular construction eliminates magnetic flux reversal in the back iron. When flux reversal in the back iron is eliminated, the phase flux linkage is enhanced and the flux leakage is reduced, leading to a reduction of hysteresis losses [96].

When an MSRM is compared to a conventional SRM, performance advantages can be expected [97]. For comparison, a 16/18 four-phase MSRM is compared with a 16/18 four-phase SRM. The MSRM is designed for short flux paths to minimise iron losses without compromising high-power capability. Thus, by comparison, the following advantages are listed [98, 99].

- The flux path is independent of the diameter of the rotor, providing the designer with the ability to increase the output torque by increasing the diameter of the rotor. An increase in the diameter of the rotor increases the output torque without increasing the flux paths between the stator and rotor.
- The modular construction provides an independent magnetic circuit for each individual phase, unlike a conventional SRM. In a conventional SRM, one magnetic circuit is shared with other phases; and windings of two adjacent phases fitted together in one slot contribute to mutual coupling between phases. Since each phase of an MSRM is separated, the mutual coupling is almost entirely removed.
- The flux direction in the back iron of the start and rotor core is always in the same direction. Thus, no flux reversal occurs in an MSRM compared to a conventional SRM. Having no flux reversal in the back iron reduces hysteresis losses as residual magnetism in the back iron is eliminated.
- The modular construction allows for an enlarged winding slot space. A larger winding slot space allows for design flexibility in the winding turns, gauge, and coil type.
- The modular construction of the rotor allows for lower rotor inertia that allows for high-speed operations. Also, the modular construction of either the stator or rotor provides the benefit of reduced weight and, therefore, costs are reduced as less magnetic material is used.
- Greater heat dissipation in the motor structure can occur in a modular structure due to open winding structures compared to a conventional SRM where windings are packed together in slots.
- A modular structure allows for easy replacement of an individual stator or rotor core when the core is damaged.

The purpose of the comparison by Anas Labak *et al.* was mainly to provide a solution to improve the torque ripple of an SRM [98]. However, the modular construction approach was found to lead

not only to the improvement of torque ripple, but also to increased motor efficiency compared to the conventional SRM. Ultimately, various MSRM structures that consist of segmented stator cores, segmented rotor cores, or both offer a range of advantages when compared to a conventional SRM. Not only is the performance of the motor improved, but also costs are reduced as less magnetic material is used [100].

2.4.1.1 Segmented stators

The simplicity of an SRM allows for modular construction. A modular structure allows easy manufacturing methods [64]. However, the main challenge of a modular structure is to find an effective way to join the modules while maintaining the necessary robustness of the conventional SRM structure [64].

Modular switched reluctance motors of segmented stators usually employ a C-shaped or E-shaped stator segment called a stator core. Segmented stator cores are joined together by plastic fixtures or other non-magnetic permeability materials [101]. As in the case of a conventional SRM, the stator can be placed in the inner or outer region of the motor, as seen in Figure 2-12. However, these figures demonstrate segmented stator cores in a conventional structure. Figure 2-12a represents an E-core and Figure 2-12b represents a C-core MSRM where only the stator cores are segmented.

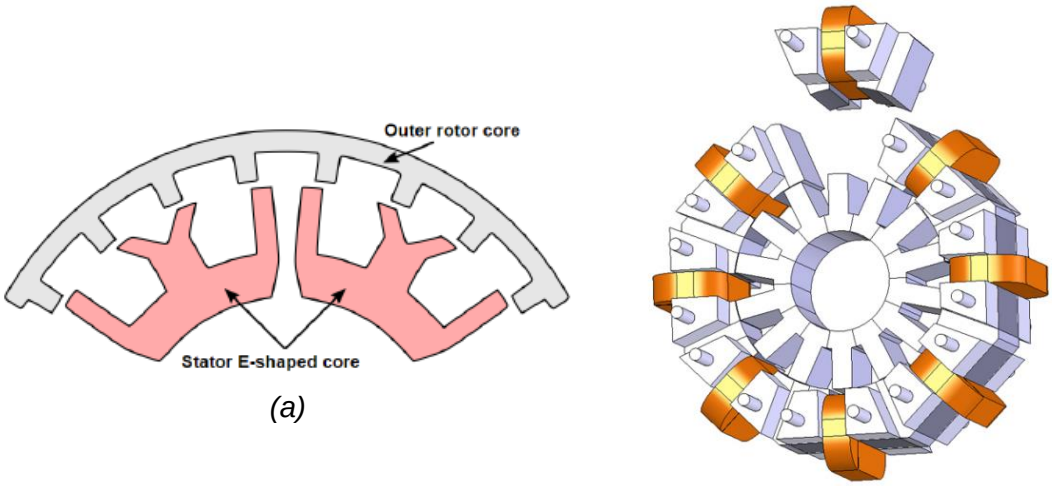

Figure 2-12: Segmented stator MSRM of (a) Outer rotor of E-core stator segments; (b) Inner rotor of C-core segments [101]

When comparing the E-core-shaped stator MSRM against a conventional MSRM, it is found that the E-core-shaped MSRM produces 20% higher torque. Furthermore, the same performance as the conventional SRM can be obtained using less iron and copper [102, 103]. The C-core shaped stator MSRM, shown in Figure 2-12b consists of 18 C-shaped stator cores. A coil is wound around

the yoke of two stator cores, and adjacent stator core modules are separated with a non-magnetic spacer. The non-magnetic spacer ensures adequate magnetic saturation between the flux paths of phases and stator cores [101].

An MSRM of segmented stator cores offers inexpensive and easy manufacturing methods, low iron losses, high efficiency, and fault-tolerant operation with the benefit of easy stator core replacement if a stator core is damaged [64].

2.4.1.2 Segmented rotors

The inspiration behind segmented rotor cores in an SRM was taken from the synchronous reluctance motor (SynRM) [95]. The development of a SynRM focuses on the magnetic circuit of the rotor. Identical axial laminations of different sized non-magnetic material sheets are interleaved between the core segments as an approach. This approach of a segmented rotor increased the torque output as the magnetic utilization of the magnetic flux carried in the magnetic circuit is enhanced [42].

An SRM with segmented stator cores is shown in Figure 2-13. The 12/8 three-phase SRM is a modified SRM, where the stator has excitation and auxiliary poles along the segmented rotor [104]. The auxiliary stator poles provide a flux return path; therefore, they are not wound. The approach to auxiliary poles in an SRM provides short magnetic paths for one excitation sequence, as two adjacent auxiliary poles form one magnetic circuit, as shown below.

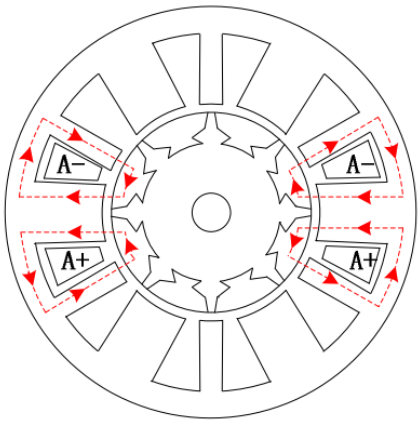

Figure 2-13: Magnetic flux path of phase A in a segmented rotor MSRM [104]

An MSRM of segmented rotor cores offers increased torque performance compared to a conventional SRM. For the example shown in Figure 2-13, the magnetised stator poles are doubled. Thus, the torque output is increased as the attractive radial force on the rotor is dispersed among the poles. Given its circumferential flux direction, the electromagnetic forces are lower than those of a conventional SRM [105].

2.4.1.3 Double segmentation

As mentioned above, an MSRM can consist of segmented stator or rotor cores. However, an MSRM can also consist of a double segmented construction, meaning that the MSRM can consist of both a segmented stator and a segmented rotor.

Anas Labak developed an axial flux MSRM consisting of double-segmented cores. The stator of the MSRM has 15 C-cores, each having a concentrated coil wound around its yoke. The rotor poles were embedded in non-magnetic material, as shown in Figure 2-14a [77]. Nikunj Ramanbhai Patel *et al.* developed a similar MSRM, where the motor was compared to a conventional SRM of the same dimensions. When the two motors were compared, it was evident that the C-core MSRM produced more torque than the conventional SRM for the same current. It was concluded that the MMF in the C-cores had increased, resulting in the reduction of coil length, increased torque, lower current use, and therefore lower copper losses that result in higher efficiency [74]. Additionally, the space available for a coil on the C-core allowed for thicker conductors to be used, which will reduce the copper losses even further as the winding resistance is reduced. Thus, an MSRM allows for a considerable amount of design flexibility [64, 95].

These modular stator and rotor segments allow for design alterations between a radial flux and an axial flux structure, as shown in Figure 2-14. As seen in Figure 2-14b, an MSRM allows a phase winding, depicted by green, yellow, and red coils, to be connected in series or parallel, depending on the performance requirements. With a segmented rotor and stator core, the magnetic characteristics of the entire motor can be generated by analysis of a single stator and rotor core. This analysis of its magnetic characteristics is due to the MSRM symmetry [75, 106].

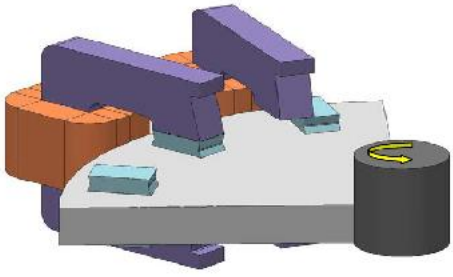

(a)

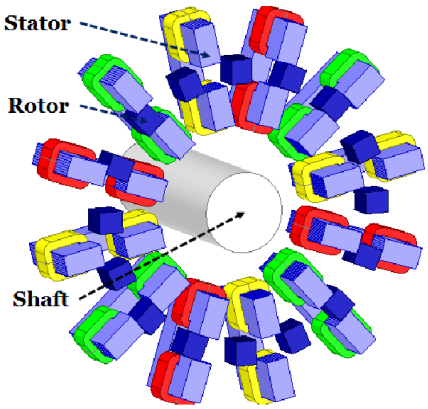

(b)

Figure 2-14: Double-segmented MSRMs of C-core stators. (a) Axial flux motor; (b) Radial flux motor [77, 74]

Comparing the 12/16 radial flux MSRM, shown in Figure 2-14a with a conventional motor, the design structure was found to offer minimal axial length, short and independent magnetic flux paths, good heat dissipation and an increase in performance. The torque was increased by 12%, the efficiency by 5% and the magnetic material of the motor was decreased by 20% [74].

A C-core MSRM can easily be augmented by cascading several c-cores on each other for more power [99]. This variant was proposed by Wen Ding *et al.*, consisting of E-cores as shown in Figure 2-15 [96, 97, 107, 108, 109, 110, 111]. Comparing the MSRM with a conventional SRM structure of the same pole configuration, diameter, and axial length, it was found that the MSRM produced higher torque and power. Furthermore, the MSRM had the lowest mass between the two motors, as a result of a segmented stator and rotor.

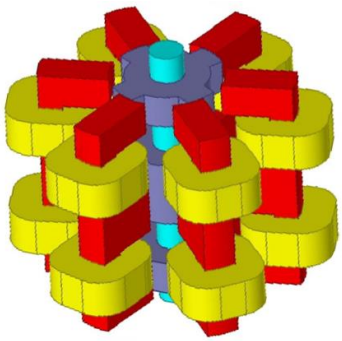

Figure 2-15: Double-segmented MSRMs of E-core stators [96]

Wen Ding *et al.* concluded that such an MSRM can be an outstanding competitor for traction motor applications. Consequently, an MSRM offers excellent performance suitable for in-wheel implementations of EVs [96].

2.4.2 Multilayer construction

The multilayer construction of an SRM is a method of reducing torque ripple. However, this approach uses segmented rotors and stators in the axial direction, as shown in Figure 2-16. The multiplayer SRM shown in Figure 2-16 consists of three independent rotor stacks, each identical to one another. However, each rotor stack is placed at a 15˚ mechanical shift to one another.

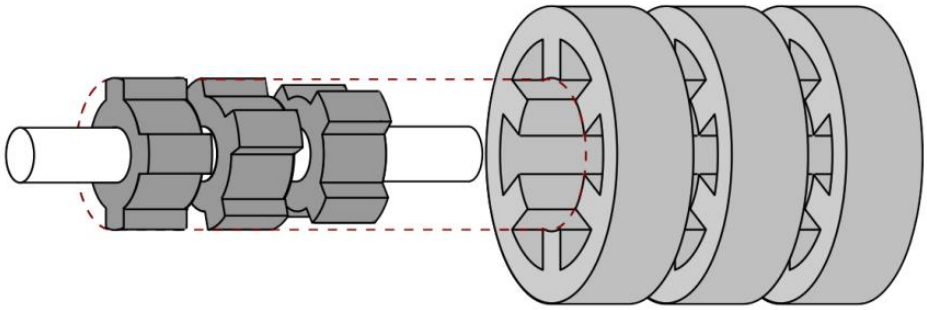

Figure 2-16: Multilayer SRM with rotor stack rotation [112]

The multilayer construction significantly reduces torque ripple, which was proven to have the same effect as a skewed rotor. For a multilayer SRM, each rotor pole arrives at the aligned position at different instances. Therefore, three control circuits are required to operate a motor stack. By analysis of the multilayer SRM, it was found that efficiency was improved by almost 10%. The efficiency improvement was due to the reduction of torque ripple and the reduction of eddy current losses [112].

2.4.3 Hybrid construction

The hybrid construction of an SRM aims to increase the power density. The approach to increase the power density is to add permanent magnets to the excitation poles. The simplest way to introduce permanent magnets to the motor structure is to replace the non-magnetic spacers in stator-segmented MSRMs. Adding a permanent magnet to the excitation pole increases MFF. As a result of higher MMF, higher power than a conventional SRM is achieved as the magnetic flux is improved in the motor [113].

Figure 2-17 shows a conventional SRM structure modified as a hybrid construction. Figure 2-17a represents a pole-assisted SRM where the permanent magnet is placed in the excitation pole. Figure 2-17b represents the yoke-assisted SRM where the permanent magnet is placed in the back iron of the SRM [113]. Placing the permanent magnets inside the back iron of the motor provides the benefit of longer, larger, and less thick permanent magnets to be used. Therefore, permanent magnets larger than the pole-assisted SRM can be used.

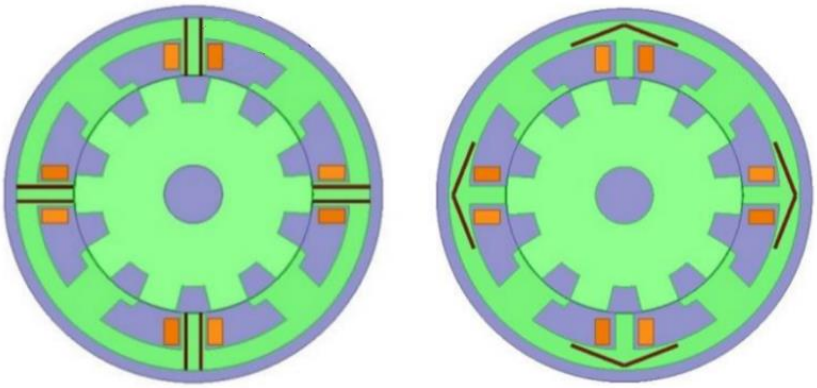

(a) *(b)*

Figure 2-17: Conventional SRM with (a) Pole permanent magnets; (b) Yoke permanent magnets [113]

Wen Ding *et al.* designed and analysed a 12/10 hybrid SRM. The SRM consisted of a segmented stator that contained six C-cores [108]. Each C-core was wound with concentrated coils and a permanent magnet placed between the poles, as shown in Figure 2-18. The permanent magnet enclosed the flux path within the core when the coil was not excited, as shown in Figure 2-18a. When the coil was excited, the flux generated by the permanent magnet added to the flux of the coil. Thus, two flux paths occurred during excitation, as shown in Figure 2-18b.

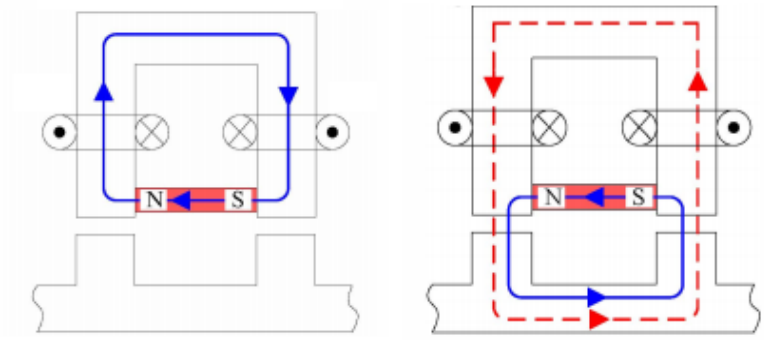

(a) *(b)*

Figure 2-18: C-core MSRM with permanent magnet-assisted poled in the aligned position under; (a) No excitation current; (b) Excitation current [108]

Comparing the hybrid C-core SRM with a conventional SRM of the same dimensions, it was concluded that the hybrid SRM were less likely to saturate under the same excitation currents. Therefore, the hybrid SRM achieved higher torque production [108].

2.4.4 Transverse construction

The transverse construction of an SRM has one toroidal coil for a single phase, as shown in Figure 2-19. The MM generated by the toroidal coil is homopolar, and the flux path is in a transverse direction. This provides the transverse SRM with high torque density, high efficiency, and low copper losses as end-turn effects are fully eliminated.

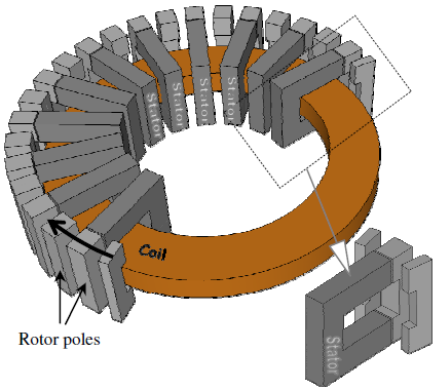

Figure 2-19: Single stack of a transverse SRM [114]

From fundamentals, a transverse construction requires a modular approach due to its complex flux paths. The flux path occurs in a 3D domain, similar to the double-segmented construction shown in Figure 2-14. Unlike the double segmented SRM, the transverse SRM offers an increase in the stator and rotor segments without reducing the MMF [114]. However, considering a three-phase transverse SRM, the motor would consist of three stacks, as shown in Figure 2-16 joined together. Thus, the axial length of the motor would be three times that of a stack, almost similar to multilayer SRMs.

2.5 Summary of the literature

From the literature, the overview of an SRM was discussed. This overview included the basic mathematical model and operating principles of an SRM. The operating principles of an SRM clarified how toque was produced from the electromagnetic energy conversion process. Thereafter, the torque-speed characteristics of an SRM were discussed, accompanied by two control strategies used to obtain the constant torque, constant power and falling power torque-speed characteristics.

Various SRM designs that could possibly be used to evaluate an SRM for solar vehicle application was reviewed. The SRM designs does not produce the same amount of performance characteristics as the Mitsuba M2096-DII, currently used in the solar vehicle of the NWU. Not enough information was provided to replicate the design successfully. Therefore, an un-optimised

XDM of an SRM was designed to justify the development and use of an SRM for solar vehicle application.

To design an XDM, the design considerations of an SRM was reviewed. From the design considerations it was found that an SRM of an outer rotor radial flux structure is an appealing choice for in-wheel traction motor applications. Many considerations could be made for the amount of phases in the motor, but increasing the amount of phases increases the overall costs. A three-phase motor is preferred over a motor with more phases.

The pole configuration of an SRM can have an effect on the operational and performance characteristics of an SRM, along with the pole arc angles. Once the pole configuration was chosen, a feasibility triangle could be used to evaluate the acceptable pole arc angles adhering to self-starting, high output torque and low torque ripple requirements.

High power and torque density and low loss standard grade (EN 10106) magnetic material are usually used in traction motors which are stacked together. The typical stacking factor can range between 80% to 95% depending on the lamination thickness.

After the review of the design considerations, the design review was broadened by a review of geometrical variations of an SRM to improve the performance characteristics. These design variations include modular, multilayer, hybrid and transverse constructions. The modular construction offered the best performance improvements without extending the axial length of the motor or adding permanent magnets, which adds thermal limitations to the operating capability.

Thus, the literature review provided a broad overview of an SRM, such that an un-optimised XDM of an SRM could be designed for evaluation purposes. Using the design considerations, aspects for the XDM of an SRM could be proposed.

2.6 The proposed switched reluctance motor

To evaluate an SRM as a traction motor for solar vehicle application, a suitable SRM should be selected. In this case, as discussed in §2.2, p.25, an SRM should be designed for the required specifications. An MSRM was proposed as the selected XDM. An MSRM was selected to eliminate long flux paths and flux reversal to reduce losses and increase motor efficiency.

It was proposed to use a 12/16 pole configuration, similar to the design of Nikunj Ramanbhai Patel *et al.* [74]. However, an outer rotor motor was proposed for use as a direct drive motor. A segmented E-core stator was selected instead of a C-core. Xinglong Li and Ernest Mendrela found that an E-core in a transverse linear SRM has a higher force-to-mass ratio than a C-core [115]. Winding turns, pole area, and air gap are kept constant in the study. Applying the principle

of a linear motor around an axis, a rotary motor was formed. Thus, the torque-to-mass ratio of an E-core MSRM was expected to be higher than that of a C-core MSRM.

As stated by Shang-Hsun Mao and Mi-Ching Tsai, C-cores can be mounted on top of each other to increase their power [99]. However, the axial length, winding turns, and input power increases. Considering that short flux paths, as in an MSRM, have high losses, an additional research question was formed. The research question of the flux paths is whether a C-core with a winding is less efficient than an E-core with the same axial length and winding turns. However, the winding constitutes two coils, and the sum of the coil turns is the winding turns.

The axial length and winding change are shown in Figure 2-20, where a C-core is changed to an E-core and the E-core to a four-pole stator core (IIII-core). C_H is the coil height and P_H the pole height, which is used to demonstrate the geometric effect when more poles are added to a core while keeping the axial length and winding turns constant. Note that the sum of the pole heights and coil height remains the same no matter the number of poles.

This research question is not within the scope of the study. However, the effect of pole changes on the core was analysed in §5.2.1.1, p.97 to gain an understanding of whether more poles on a core may lead to a more efficient motor. A future study is recommended to gain a comprehensive understanding of this research question.

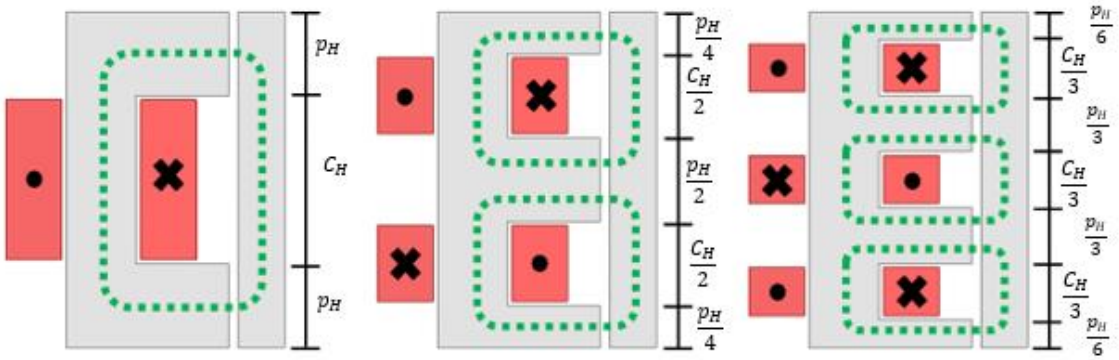

Figure 2-20: Flux paths of a C-core, E-core, and IIII-core

A selection of magnetic material will be limited to lamination thickness of around 0.5 mm, to steel losses and maximising the stacking factor, as a stacking factor of 95.8% was expected for material of a 0.5 mm lamination thickness.

When considering the proposed MSRM, an efficiency map was essential to evaluate the proposed motor. An expected efficiency map of an SRM is shown in Figure 2-21. Figure 2-21a shows an efficiency map of an inner rotor double U-core SRM, provided by ePower Motors [116], and Figure 2-21b shows an efficiency map of a three-phase inner rotor 6/4 SRM designed to propel a scooter. Efficiency values are indicated by the legends, which range from a dark blue indicating 75% and 0% efficiency to a yellow and dark red indicating 100% efficiency.

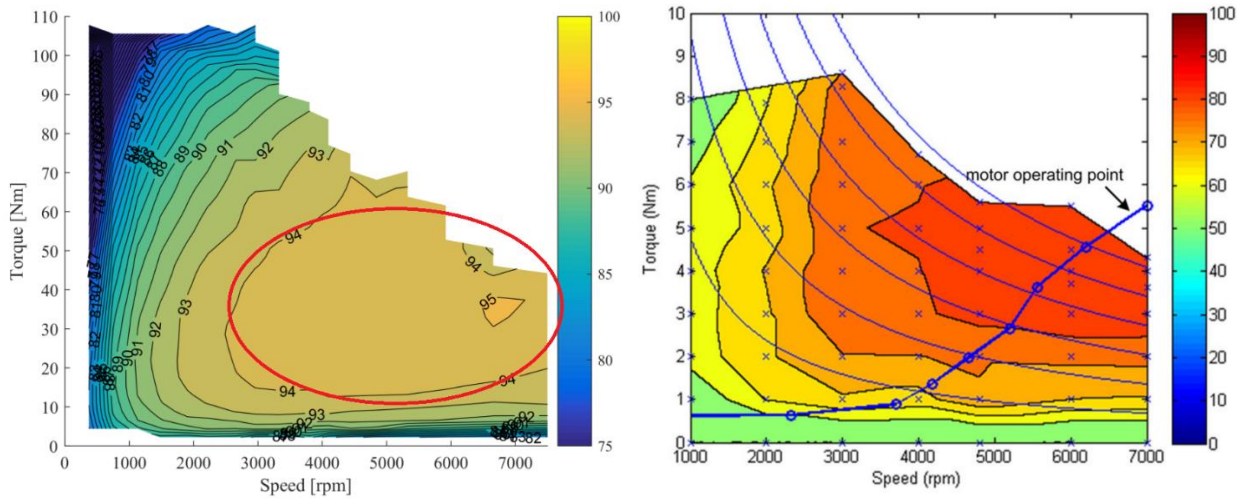

(a) *(b)*

Figure 2-21: Efficiency map of an SRM [116, 117]

It is unknown whether a similar efficiency map can be expected for the proposed MSRM. Similarity of the efficiency maps is unknown due to the lack of literature providing no efficiency map of an MSRM. An efficiency map of a conventional SRM was rarely obtained, and if an efficiency map was obtained, very little information about the SRM was provided. Therefore, a comparative analysis between the efficiency map of a conventional SRM and an MSRM is proposed as a future study. However, the construction of the proposed MSRM efficiency map will provide some indication of the similarity between the efficiency maps. Furthermore, the verification and validation of the efficiency map are proposed by manufacturing a prototype of the proposed MSRM.

To conclude, a 12/16 E-core MSRM was proposed as an un-optimised XDM, which is used to justify future development and utilisation for solar vehicle application. The proposed XDM was designed according to the specified power characteristics and design constraints, listed in Table 5-2, p.95 and Table 5-1, p.90.

CHAPTER 3 ELECTROMAGNETIC MODELLING

The electromagnetic modelling method is reviewed in this chapter. This chapter focused on the FEA method used to design or analyse an electrical motor. Finite element analysis is a popular solution for electromagnetic modelling. An overview of the simulation software used in this study, Ansys® Maxwell, is presented in this chapter.

Ansys® Maxwell is an industry standard electromagnetic modelling software utilised by most designers to analyse an electrical motor, as seen throughout the literature review on the design articles and journals. There is various other simulation software, but in this study, the software is limited to Ansys® Maxwell, as the NWU has license access.

3.1 Electrical machine analysis

An electrical machine's design and step-by-step optimisation is often a trial-and-error process. The design and construction of the electrical machine require expensive prototypes to be manufactured. Having to build an iteration of prototypes is time-consuming and expensive, such that numerical methods are suggested to replace the iterative design stage. The same numerical analysis procedure can be used to analyse an electrical machine [118].

Numerical methods became necessary in many electromagnetic applications where the electrical machine operates in the saturated region. The most popular method to solve an electromagnetic problem is the use of FEA [119]. This chapter focuses on the FEA approach in Ansys® Maxwell.

Compared to numerical methods, the analytical methods can significantly reduce computational complexity without solving high-dimensional matrixes such as FEA. The magnetic equivalent circuit (MEC) method is popular for electromagnetic analysis. However, the task to solve the MEC is to find as many assumptions, simplifications, and empirical factors as possible, which cannot always be satisfied [118]. The background and solving principle of an MEC are described in [29].

In PMSMs, the permeability of a permanent magnet is close to the permeability of air, allowing the assumption of linear material characteristics. The SRM have non-linear characteristics, and the assumption does not hold when analysing an SRM. Additionally, the flux topology of the SRM changes with the rotor angle. Thus, the MEC structure of an SRM is empirical, and different assumptions on the magnetic flux path, especially the areas and lengths of fringing/ leakage reluctance in the air region that are non-linear, have to be made for the different rotor positions. The assumptions should be based on previous experiences with FEA results, which confine the accuracy and generality applied to the analysis of SRMS with arbitrary geometries. The accuracy of an analytical approach decreases when the machine operates in the saturated region, and

even if the MEC considers magnetic saturation using an iterative approach, the solution is not as generic as a numerical solution. Therefore, this study uses a numerical approach of FEA to analyse an SRM. An extended review of analytical methods is not discussed further in the study.

3.1.1 Modelling methods

Electromagnetic modelling is the process of modelling the interaction of electromagnetic fields between a physical object and the surrounding environment (e.g. air, vacuum). The process typically involves software to compute the solutions of Maxwell's equations. The computational numerical technique can overcome the inability to derive closed-form solutions when an analytical method is not solvable. This makes electromagnetic modelling a critical "tool" in the design and analysis procedure of an electrical machine.

Any electromagnetic problem can be described using integral and/ or partial differential equations derived from Maxwell's equations (§3.2.1). Typical problems involve either time-stepping through the equations over the domain of each instant, a matrix inversion when modelled by FEA, or matrix products when using the transfer matrix method, calculating integrals using the method of moments; or using the fast Fourier transform method. The most commonly used numerical methods are shown in Table 3-1 and discussed below:

Table 3-1: Numerical methods used to solve electromagnetic problems

	Time-Domain	**Frequency-Domain**
Partial differential equation formulation	Finite-Difference Time-Domain (FD-TD)	Finite Element Analysis (FEA)
Integral formulation	Marching-On-in-Time (MOT)	Method of Moments (MoM)

The different numerical methods used by the simulation software to solve electromagnetic problems are not discussed in detail in this study. More information on the numerical methods can be found in [120, 121, 122]. In this study, FEA is used to analyse an SRM.

3.1.2 Simulation software

With the application of highly efficient numerical algorithms running on high-performance computers, it is possible to rapidly design and analyse an electrical machine. At the same time, these numerical algorithms enable the development of ever more complex machine designs. The advanced software offered today can effectively analyse and characterise electrical machines. The software makes solving an electrical machine by its respective equations no longer a challenging, time-consuming process. Quite a number of commercially available simulation

software is available for electromagnetic modelling. A non-exhaustive list with relevant web links of the most popular software used to analyse electrical machines is listed below:

- Ansys® Maxwell [123];
- Altair Flux [124];
- Simcenter Magnet [125];
- JMag [126];
- COMSOL Multiphysics [127];
- FEMM [128];
- Elmer FEM [129];

The software license, required to use the electromagnetic simulation software are very expensive. Thus, not just any simulation software is readily available for use in this study. As the NWU has license access for students to use Ansys® Maxwell, this study is limited to Ansys® Maxwell. Therefore, Ansys® Maxwell is used to analyse the magnetic characteristics of an SRM in this study.

Ansys® Maxwell is compared to Cedrat in [130]. Cedrat was an electromagnetic simulation software acquired by Altair in 2016. The comparison between the simulation software concluded that Maxwell is a convenient choice for young engineers using FEA software for the first time, while Cedrat is more suited for those who desire a more realistic solution. However, the multidisciplinary simulation environment offered by Ansys®, i.e., coupling Ansys® Maxwell to Ansys® Fluent or Ansys® Mechanical, makes it the best solution for professional engineers wanting to analyse the mechanical, structural, and thermal characteristics of an electrical machine whilst the electromagnetic interaction of the machine occurs.

3.2 Finite element analysis

The finite element analysis comprises of two fields, namely mathematics and engineering. The first record of differential equations in a surface with a minimum area confined by a closed curve in space was in Schellenbach's study, 1851. In 1943, Courant developed the FEA to what it is known today. In the 1950s, engineers in the aeronautical field made progress in their designs and structural analysis using FEA. During this time, the key contributors to the analysis method were Ton Turner, John Argyris, and Ray Clough with Ray Clough coining the term "finite element" in 1960. Since then, the analysis method spread to all engineering fields [131].

The FEA provides mesh elements to cover the entire solution domain, making the solution process adaptable to any complex or irregular machine geometry. The FEA provides an accurate magnetic field distribution solution with inhomogeneous properties, i.e., the laminated cores with non-linear permeability. Regardless of the adaptations of the model, the solution process remains

the same. Additionally, FEA provides an iterative approach to the solution, and using computational resources provides a faster solution time than an analytical approach [132]. Maxwell's equations define the solution of the electromagnetic field.

3.2.1 Maxwell's equations

The study of electromagnetic field phenomena has been developed since the 19th century. Formulations were proposed by scientists like Gauss, Ampère, Faraday, and Lenz, but only completed in 1862 when James Clerk Maxwell added an extra term to Ampere's law. The added addition to the equation allowed for a complete description of electromagnetic field phenomena [131, 133, 134]. The four fundamental equations that define the electromagnetic fields are as follows:

Ampère's circuital law $$\nabla \times H = J + \frac{\partial D}{\partial t} \quad (27)$$

Faraday's law of induction $$\nabla \times E_f = -\frac{\partial B}{\partial t} \quad (28)$$

Gauss's law $$\nabla \cdot D = 0 \quad (29)$$

Gauss's law for magnetism: $$\nabla \cdot B = 0 \quad (30)$$

In these equations, J represents the current density, H the magnetic field strength, E_f the electric field density, B the magnetic flux density, D the electric flux density, and $\nabla \times$ and $\nabla \cdot$ the curl and divergence operators.

Equation (27) describes Ampère's circuital law in differential form and can also be represented by the integral form, shown in equation (31). The equation states that the line integral of the magnetic field, H, in a closed path, dl, is equal to the current enclosed in that path.

$$\oint \mathrm{H} \cdot \mathrm{dl} = \mathrm{I} \quad (31)$$

The time variation section of Ampère's circuital law represents the displacement current effect. The current effect produces a time-varying, non-steady magnetic field as an adequate flow of electrical charges, as proposed by the equation of electrical continuity [133].

$$\nabla \cdot \mathrm{J} = -\frac{\partial \rho_c}{\partial \mathrm{t}} \quad (32)$$

Where ρ_c is the charge density. The four fundamental equations are linear and may appear relatively easy to solve analytically. However, complex geometries and boundary conditions of an electromagnetic problem make these equations difficult to solve. Therefore, numerical analysis software is used to solve such machines, i.e., an electrical machine.

3.2.2 Ansys® Maxwell

Ansys® Maxwell is a low-frequency electromagnetic field simulation solution that uses finite element analysis to solve static, frequency domain, and time-varying electromagnetic and electric fields. When solving an electromagnetic model, the procedure, adapted from the documentation provided by Ansys® in [133], shown in Figure 3-1, is followed.

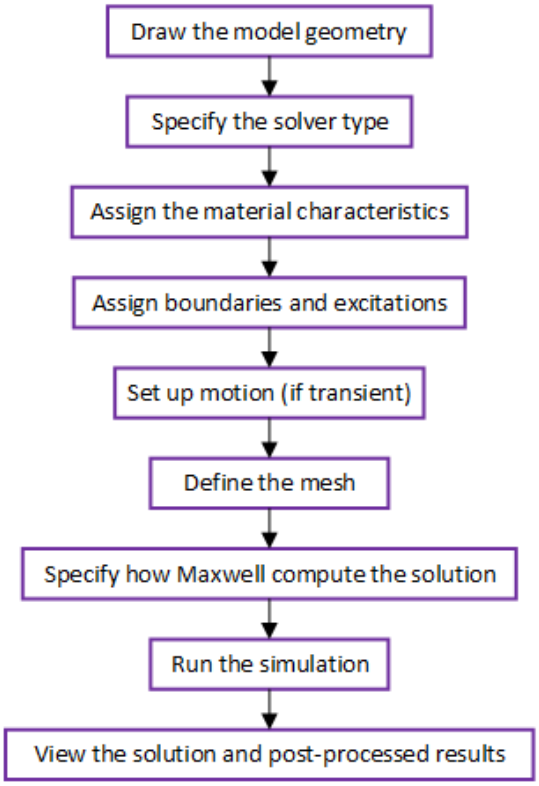

Figure 3-1: Analysis Procedure in Ansys® Maxwell

The process of formulating and solving an electromagnetic solution is used in chapter 4 to validate the electromagnetic modelling method of an MSRM. The necessary information about some of the processes is discussed in this section.

3.2.3 Geometry

Ansys® Maxwell offers 2D and 3D model analysis. A 3D model analysis holds an advantage when exploring the electromagnetic field distribution around a complex domain. When analysing an electric motor, the magnetisation direction of the magnetic field is in the same plane as conventional motor topologies. When ignoring end winding effects, often the case for well established, conventional radial flux motors, Maxwell 2D can obtain an accurate solution. The advantage of a 2D approach is a decrease in mesh elements, allowing for faster simulations [131, 133]. However, the end winding effect considerably influences solution accuracy when modelling electric motors of complex winding distributions, such as an axial flux motor, transverse flux motor, or an MSRM [135]. In the case of an MSRM, the end winding has a winding ratio of roughly 1:1, while the end winding of a conventional SRM is usually around a ratio of 1:8. Thus, the end winding of a conventional SRM constitutes only a tiny fraction of the whole winding when simulated in a 2D domain [52]. A 2D and 3D simulation comparison of an MSRM is shown in Appendix B, p171.

Thus, analysing an MSRM (chapter 4 and chapter 5) that utilises a unique magnetic path, field distribution, and magnetic field effects requires Ansys® Maxwell 3D. The consequence of using a 3D solving domain is that a larger number of mesh elements need to be solved. A larger number of mesh elements results in slower simulations [136, 137]. When using a 3D solving domain and restricted by a time constraint, the user is limited to the number of simulations in the study if an accurate motor solution is to be obtained. Therefore, if limited time is available, the user will either use all of the available time for a single simulation, should only a single point of operation be analysed, or the user will split the time for various simulations setups, should different operation points be analysed.

3.2.4 Domain partitions

The discretisation of the domain is the stage in which a great number of tetrahedra elements define the model. The assembly of all tetrahedra is referred to as the finite element mesh of the model or simply the mesh. The mesh setup defines the accuracy of the solution by providing a better simulation resolution of the field distributions. Therefore, there is a trade-off between the size of the mesh, the desired level of accuracy, and the number of available computing resources [131].

The precision of the solution depends on the size of each tetrahedron, shown in Figure 3-2. To generate a precise description of the magnetic field quantity, each tetrahedron should occupy a sufficiently small region. A sufficiently small region for the magnetic fields is necessary to adequately interpolate from the nodal values [133]. For the tetrahedron:

- The magnetic field component, tangential to the element's edges, is explicitly stored at the vertices.
- The magnetic field components that are tangential to the face of an element and normal to an edge are explicitly stored at the midpoint of the selected edges.
- The value of a vector field at the interior point is interpolated from the nodal values.

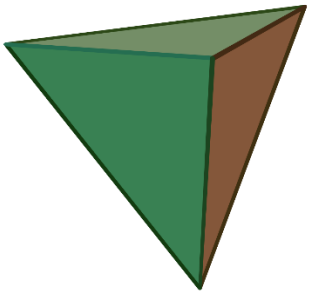

Figure 3-2: The tetrahedron as a finite element

Definition 7 (Tetrahedron): *A tetrahedron (plural: tetrahedra or tetrahedrons) is a polyhedron with four faces, six edges, and four vertices, in which all faces are triangles. A regular tetrahedron has equilateral triangles. Therefore, all its interior angles measure 60°* [138].

The desired field in each element is approximated by the second order quadratic polynomial, shown in equation (33).

$$\mathrm{H}_X(x,y,z) = a_0 + a_1x + a_2y + a_3z + a_4xy + a_5yz + a_6xz + a_7x^2 + a_8y^2 + a_9z^2 \qquad (33)$$

Solving a magnetic field solution involves the inverting of a matrix with approximately the number of elements of the tetrahedra nodes. For a mesh setup of many tetrahedra elements, inversion of the matrix requires a significant amount of computing resources. Therefore, it is desirable to use a mesh setup that is refined enough to obtain an accurate solution but coarse enough not to overwhelm the available computing resources [133].

The mesh setup used to analyse an MSRM is explained in §4.3.1.3 and §4.4.1.3, using the magnetostatic solver and the transient solver.

3.2.5 Magnetic solvers

Ansys® Maxwell offers three independent solving approaches to analyse electrical machines related to magnetic magnitudes. The three magnetic solvers include the magnetostatic, eddy-current, and transient solvers.

The two solver approaches chosen to validate the model of an electric motor are the magnetostatic solver and the transient solver. The three solvers in a 3D domain are presented in this section. From the documentation of Ansys ® Maxwell, it is clear that the eddy current solver is also a static solver, but is primarily used when analysing electrical transformers [133].

3.2.5.1 Magnetostatic

The magnetostatic solver computes static magnetic field simulations where the source of the static magnetic field is one or more of the following:

- DC currents in conductors
- Permanent magnets
- Static external magnetic fields represented by the boundary conditions

The quantities which the magnetostatic solver solves are the magnetic field, H, the current density distribution, J, and the magnetic flux density, B. These fundamental field quantities are used to calculate the force, torque, energy, and inductance. Note that no time variation effects are included in magnetostatic solutions, as the objects are considered stationary. Therefore, the transformation of energy in a magnetostatic solution is only due to ohmic losses associated with currents flowing in real (non-ideal) conductors [133]. Thus, the heating effect is acknowledged in the solver, though the effect of heating has no influence on the simulated. To simulate the effect of heating, the simulation has to be coupled with a temperature simulation.

The solution process of the magnetostatic solver is very automated. Once the problem is fully defined, Maxwell automatically runs through several stages of the solution process, as shown in Figure 3-3. When performing domain discretisation, the solver follows an iterative process that involves adaptive mesh refinement (§4.3.1.3, Figure 4-3, p.68) until the maximum number of mesh refinement passes is reached or the solution has converged [133, 139].

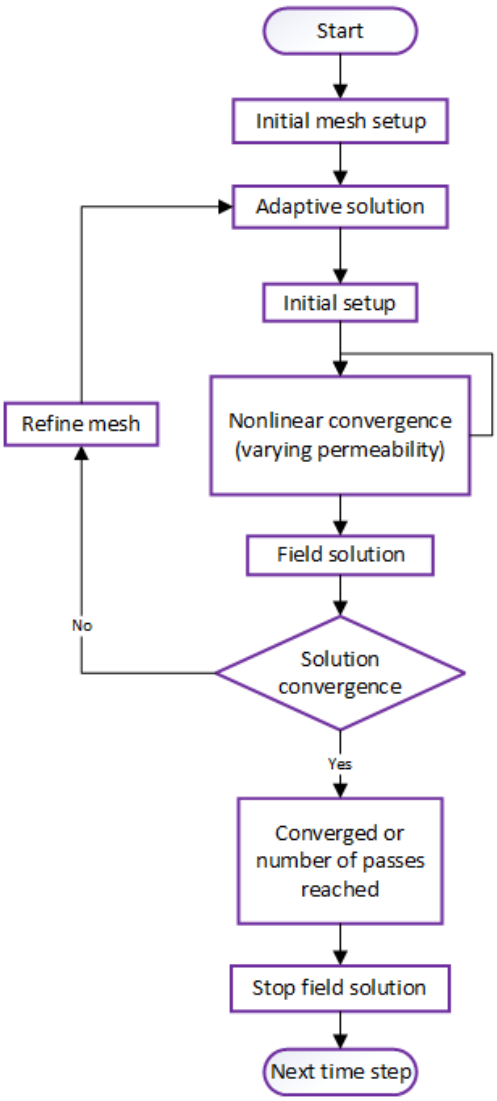

Figure 3-3: Magnetostatic solver diagram

During the solution process, the magnetostatic solver solves the following two Maxwell equations [63]:

$$\nabla \times H = J \tag{34}$$

$$\nabla \cdot B = 0 \tag{35}$$

The following constitutive (material) relationship is also applicable:

$$B = \mu_0(H + M) = \mu_0 \cdot \mu_r \cdot J + \mu_0 \cdot M_p \tag{36}$$

Where H is the magnetic field strength, B is the magnetic flux density, J is the conduction current density, M_p is the permanent magnetisation, μ_0 is the permeability of a vacuum, and μ_r is the relative permeability.

3.2.5.2 Eddy current (static)

The eddy-current solver computes electromagnetic field simulations in the frequency domain where the source of the electromagnetic field is one or more of the following:

- AC currents in conductors
- Time-harmonic external magnetic fields represented by boundary conditions

The quantities which the eddy current solver solves are the magnetic field, and the magnetic flux density, B. Force, torque, energy, and inductance are calculated at the solution frequencies from these fundamental field quantities. The solver assumes that all electromagnetic fields pulse at the same frequency. Note that the eddy-current solver does not allow moving objects or permanent magnets, and that magnetic materials are assumed to be linear. Solutions of non-linear material are based on the fundamental components of B and H at the specified frequency as an approximation [133].

Like the magnetostatic solver, the solution process of the eddy current solver is automated. Once the problem is fully defined, Maxwell automatically runs through several stages of the solution process, as shown in Figure 3-4. When performing the domain discretisation, the solver follows an iterative process involving adaptive mesh refinement, similar to the magnetostatic solver.

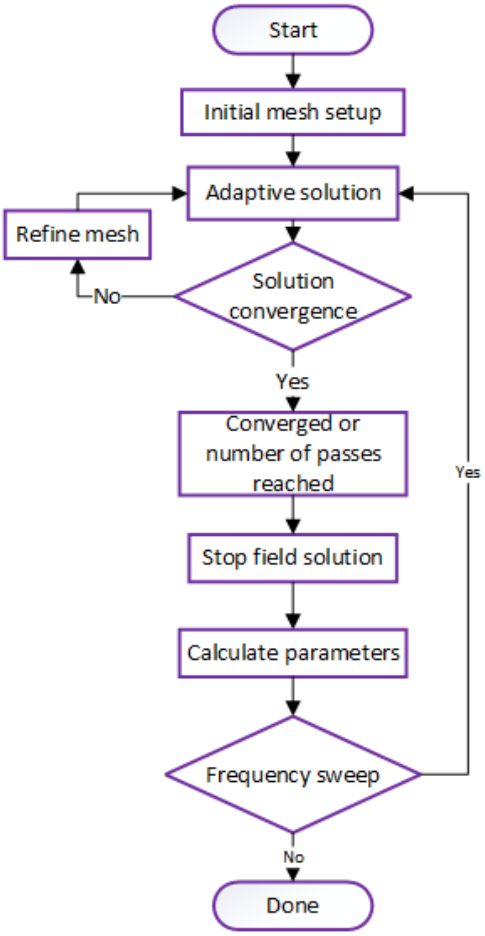

Figure 3-4: Eddy-current solver diagram

During the solution process, the eddy current solver solves the magnetic field equation [63]:

$$\nabla \times \left(\frac{1}{\sigma + j \cdot \omega_f \cdot \epsilon} \nabla \times H \right) = -j \cdot \omega \cdot \mu \cdot H \qquad (37)$$

Where ϵ is the absolute permittivity, ω_f the angular frequency at which all quantities oscillate, σ the conductivity, and μ the absolute magnetic permeability. j indicates an imaginary part of the complex number.

3.2.5.3 Transient

The transient solver computes the time-domain magnetic field where the source of the magnetic fields is one or more of the following:

- Moving or non-moving time-varying currents and voltages
- Moving or non-moving coils and/ or permanent magnets
- Moving or non-moving external circuit coupling

The quantities which the transient solver solves are the magnetic field, H, the current distribution, J, and the magnetic flux density, B. The quantities of force, torque, energy, speed, position, winding flux linkage, and winding induced voltage are calculated from these fundamental field quantities [133].

In the 3D transient solver, the solver uses the $T-\Omega$ formulation. The formulation $T-\Omega$ is said to be a powerful method to solve low frequency electromagnetic problems [133]. This is the only formulation used in Ansys® Maxwell. The solution process is shown in Figure 3-5. For simulations involving rotational motion, i.e., the rotor of a motor, a "sliding band" approach is followed, and thus no re-meshing is done during the simulation. Note that the transient solver does not use adaptive refinement like the above mentioned solvers, and therefore a mesh needs to be defined by the user [133].

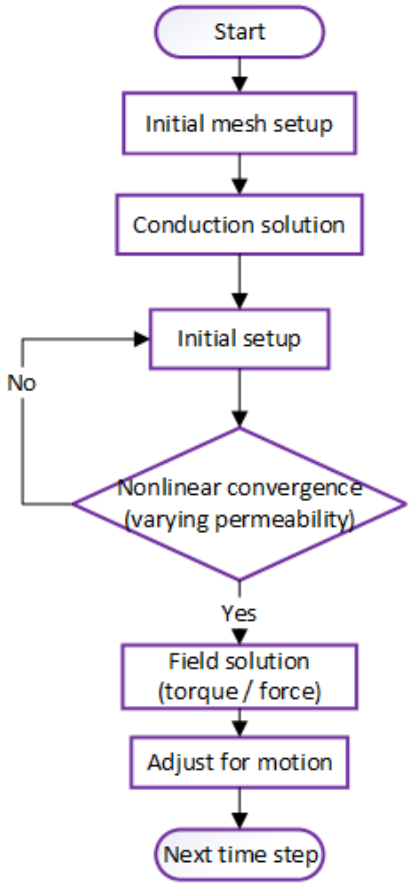

Figure 3-5: Transient solver diagram

During the solution process, the transient solver solves the following Maxwell equations:

$$\nabla \times \frac{1}{\sigma} \nabla \times H + \frac{\partial B}{\partial t} = 0 \tag{38}$$

$$\nabla \cdot \mathrm{B} = 0 \tag{39}$$

Note that, even though the transient solver is used in Ansys® Maxwell, the motion setup offers either a transient or a steady-state solution. When a transient simulation is set up, the solution is automatically set to a steady-state solution. However, if a transient response simulation is required, the mechanical transient selection should be selected in the motion setup before starting the simulation [133]. Thus, for the remainder of this study, when referring to transient simulations, the simulations will provide steady-state solutions. This imply that motor start-up shall not be observed in the simulations. Only steady-state simulations are required to construct an efficiency map, needed to evaluate an SRM through the drive cycle, provided in chapter 6.

3.2.6 Post-processing

Post-processing is the last step of the solution. At this step, it is possible to analyse the solution based on the solution data, convergence, mesh statistics, and plot reports of a parameter [133]. The output parameters used to evaluate the results during simulations are summarised as follows:

- Solution data: The solution data provide information about the solution process, containing info about the software performance, simulation time, and the computational memory utilised during the simulation. The data can be checked during the simulation process.
- Field Overlays: The field overlay is one of the main demonstrative tools to represent the model graphically. The field plot contour or vector plot is used to show the magnetic flux density, magnetic field, current density, and electric field.
- Plot reports: The report plotting tool is helpful when analysing graphs of time-varying parameters, such as the current and torque of a transient solution.

3.3 Summary of electromagnetic modelling

In many instances, studying a real system can be too complex, expensive, or even dangerous if exposed to electrical hazardous conditions. For this reason, simulation software using FEA (Ansys® Maxwell) is an appropriate solution that can be conducted within cost constraints and without injury. An electromagnetic simulation can be helpful when the machine does not yet exist or is not fully understood.

However, a good simulation can ultimately yield wrong solutions, especially when the simulation or simulation method is difficult to understand and implement. This chapter provided a basic understanding of the numerical methods, mainly FEA, used to analyse an electrical machine. The FEA method of Ansys® Maxwell was reviewed to understand the solution process of the software.

For this study, in conjunction with the manufacturing & financial constraints (§1.5.3, p.10), validation of the simulation method was finalised before the proposed MSRM was designed. Thus, both the validation of an MSRM and the design of the proposed MSRM form part of the electromagnetic analysis discussed in this chapter.

CHAPTER 4 ELECTROMAGNETIC SIMULATION VALIDATION AND VERIFICATION

The validation and verification (V&V) of an MSRM in this chapter is based on an E-core MSRM designed by Wen Ding *et al.* [96, 110, 109, 97, 107, 111]. The simulation and experimental results were compared to the modelled MSRM, using numerical simulation software. The numerical simulation software used to set up and model the MSRM was Ansys® Maxwell.

Usually, validation is completed after the prototype is built. In this study, due to limitations (§1.5.3, p.10), no prototype could be manufactured. The design of the E-core MSRM was to be validated following the same procedures as provided in the articles. Following the same procedures, the magnetostatic and transient solution data were used to validate the setup and modelling method of an MSRM.

These publications were chosen for validation purposes, not only because an MSRM is analysed, but because the publications offer experimental data. Experimental data for MSRMs, throughout the literature review, were rarely found, and if found the motor analysed constitutes an axial flux SRM.

In these publications, it is noted that the E-core MSRM designed by Wen Ding *et al.* differ in terms of the structure (inner vs outer rotor) and flux path (different rotor segmentation) when compared to the proposed MSRM (§2.6, p.45).

In [97], Wen Ding *et al.* compared the segmented rotor to a conventional rotor. The conventional rotor had four short flux paths, similar to the proposed MSRM, but due to the inner rotor topology, still a yoke on the rotor, that is removed when compared to the I shaped rotor segments of the proposed MSRM. Wen Ding *et al.* found that the two rotor structures had similar winding flux linkage and electromagnetic torque characteristics. It was also found that the segmented rotor had higher torque density power density and accelerated faster at start-up. Though this was due to the conventional rotor structure having more magnetic material and therefore weighing more.

Thus, the flux paths of the E-core MSRM designed by Wen Ding *et al.* will have no significant influence on operations compared to the flux path of the proposed MSRM. Also, the difference between inner and outer rotor structures will only have an effect on the overall size of the motor and output torque if the air gap diameter differs. When using a double segmented MSRM, flux path is independent of the diameter of the rotor and the structure, i.e., inner or outer rotor. As some difference might have an effect between the two motors, it is proposed as a future study to validate the proposed MSRM against experimental data once a prototype is manufactured.

4.1 Validation and verification

Many interpretations exist for the meaning of V&V. Some of the interpretations include the IEEE Std 1012, 1998 AIAA, and the ISO/IEC 17027:2019 [140, 141, 142]. The V&V definitions used in this study are adapted from [143].

Definition 8 (Validation): *Validation is the process of ensuring that a model, when integrated together with other models, gives the expected behaviour for the application environment it is used in. If the validation process has been finished for a model with no anomalies, then the model has a validated status.*

Definition 9 (Verification): *Verification is the process of making sure that a model has been implemented correctly. If the verification process has been finished for a model with no anomalies, then the model has a verified status.*

There are many ways of performing V&V, as described in [140]. In this study, the following methods for V&V are applied:

- Hand-checking that the calculations used for the drive cycle implementation was correct, i.e. the excel spreadsheet used to calculate the power use at each time iteration.
- Analysing an alternative approach to arrive at the expected results of the models and integrated models, i.e. using other simulation software like the 2D simulation model provided in Appendix B, §B.1, p.171
- Comparisons to literature, i.e., comparing the model results to published results.
- Comparisons with well-defined criteria, i.e., experimental data or other simulation models that have been validated.

Ansys® Maxwell provide quality assurance by V&V both existing and new program functions. Both internal and external quality audits were conducted to ensure the software fulfils the requirements of the ISO 9001:2015 standard [144]. Normally, the validation of an electrical motor is performed after the design is finalised. However, due to manufacturing & financial constraints (§1.5.3, p.10), a prototype cannot be built to validate the design. Therefore, the numerical modelling method of an MSRM was validated and verified to ensure that the correct procedures are followed when evaluating the design options and criteria of an MSRM.

§4.2 to §4.4 contains the setup of the E-core MSRM described by Wen Ding *et al.* in [96, 110, 109, 97, 107, 111]. This SRM was simulated using the magnetisation and transient solvers in Ansys® Maxwell to V&V the simulation model setup, simulation methods and simulation post-processed results

4.2 Geometry of the validation model

The MSRM designed by Wen Ding *et al.* consists of six independent modular E-shaped stator cores and a segmented rotor, shown in Figure 4-1. The rotor consists of three rotor cores as shown in Figure 4-1a, thus called a segmented rotor. Figure 4-1a and Figure 4-1b shows the magnetic paths of the MSRM when one phase is excited. It is observed that there are two magnetic paths in this MSRM, and the two paths are in the same direction in the middle pole. Unlike a conventional SRM, each phase has independent magnetic paths. Thus, there is no mutual coupling between phases through cross-slot leakage flux [110].

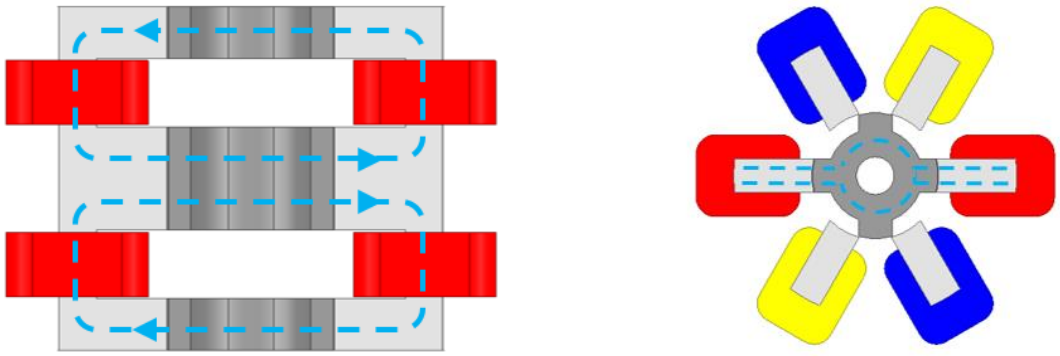

(a) *(b)*

Figure 4-1: Basic structure of the MSRM. (a) Cut front view of one-phase and (b) Top view of the three-phase MSRM

The physical parameters and characteristics of the stator and rotor are defined in Figure 4-2a and Figure 4-2b. The geometric parameters are summarised in Table 4-1. Two coils are wound around each stator core and connected to the diametrically opposite stator coils in a series-parallel combination, shown in Figure 4-2c. The four connected coils form one phase winding.

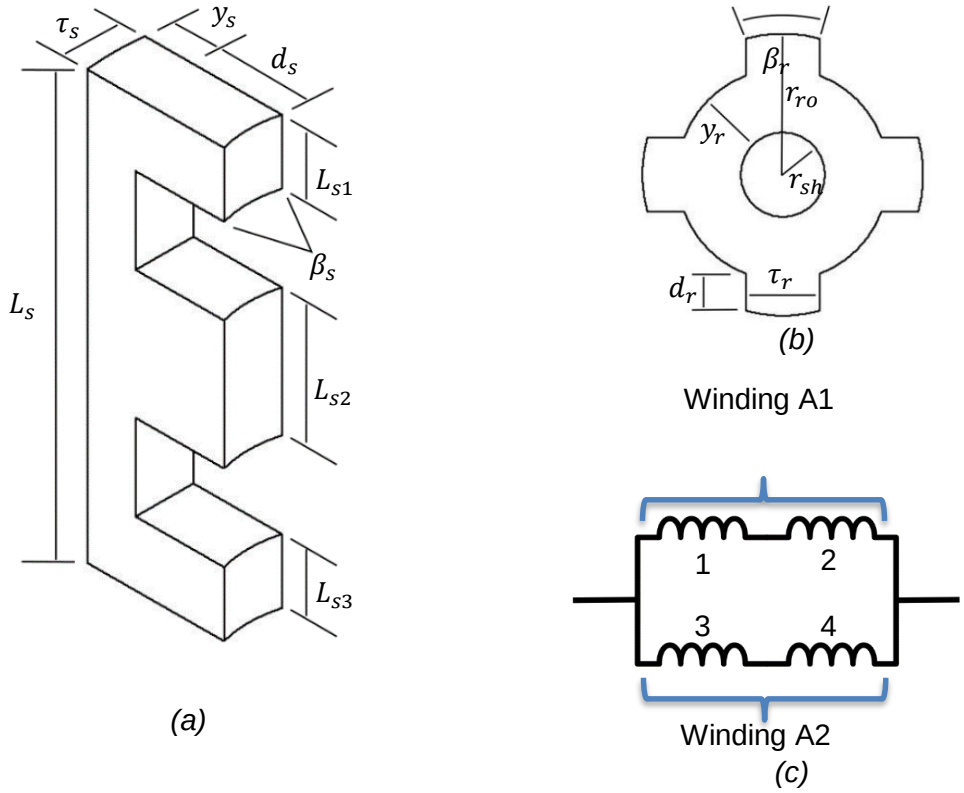

Figure 4-2: Geometry parameters of the MSRM: (a) One stator core; (b) The rotor core (top view); (c) The winding connection of one phase.

The magnetic material, specified by Wen Ding *et al.* for the stator and rotor was the non-oriented silicon steel DW540-50. All material characteristics were used as provided from the material database of Ansys®. This material database is maintained by Ansys® Granta, providing a broad coverage of material types and key property data for analysis.

At the time of publishing articles [109, 110, 111] in 2014, Ansys® Maxwell 2013 was the latest version available. Ansys® Maxwell 2013 required manual allocation of the magnetic material DW540-50. The magnetic material properties and characteristics could differ from the material database of Ansys®. Thus, the simulation results of the motor model might differ from the published results. It was assumed that the magnetic material characteristics provided by Ansys® was correct, thus no difference between the simulated results and experimental data were expected.

Table 4-1: Geometry parameters of the MSRM.

Geometry Parameters of the SRM (unit: mm)

Stator outer radius, r_{so}	45	Shaft outer radius, r_{sh}	6
Rotor outer radius, r_{ro}	20	Stator total length, L_s	80
Stator yoke width, y_s	9	Upper stator pole length, L_{s1}	12
Rotor yoke width, y_r	9	Middle stator pole length, L_{s2}	24
Stator pole arc, β_s	32˚	Lower stator pole length, L_{s3}	12
Rotor pole arc, β_r	32˚	Stator pole width, τ_s	10.73
Air gap length, g	0.25	Rotor pole width, τ_r	10.60

4.3 Magnetostatic validation

The magnetostatic solver of Ansys® Maxwell was used to obtain the magnetostatic characteristics of the E-core MSRM, described in §4.2. The magnetostatic characteristics of the MSRM involves the flux linkage, static torque, and winding inductance. The magnetostatic characteristics were obtained over half an electrical period when the rotor moves from the unaligned position to the aligned position, similar to results provided by Wen Ding *et al*. Refer to Figure 2-3, p.17 for the unaligned and aligned positions of an SRM.

Owing to the independent magnetic structure of each motor phase, the magnetostatic structure of one phase was selected as the solving domain. Only two E-shaped stators and the segmented rotor were modelled, as shown in Figure 4-1a.

4.3.1 Magnetostatic simulation setup

The model setup should be finalised for the numerical simulation to be solved. The magnetostatic setup involves the excitation, boundary conditions, mesh and the magnetostatic solution and analysis setup, in that particular order.

4.3.1.1 Excitation setup

Excitation of the phase winding is done in the following process. Each coil is assigned a current excitation that sets the conduction path. The stranded type wire is selected in the current excitation settings, and the coil number is set to 300 turns. The direction of the current flow is changed to indicate the winding direction of the coil, such that the flux path, shown in Figure 4-1a and Figure 4-7, is achieved. The flux path in the stator is easily known by using Fleming's right-hand rule. Note that in the magnetostatic solver, the MMF is used as the value of current excitation.

4.3.1.2 Boundary setup

Before a boundary condition is assigned, a solving domain is created. The solving domain involves the construction of a volumetric region around the motor model. The magnetostatic solver automatically assigns two boundary conditions. The boundary conditions are the Neumann and the natural boundary conditions.

Neumann boundaries are assigned to the outside surfaces of the solving domain. Natural boundaries are assigned to surfaces between objects, i.e., between the stator and the coils. Additionally, verification of the conduction paths between the coils and the stator cores is applicable. Otherwise, an insulating boundary must be assigned to the coil to exclude excitation interference between the coil and the stator.

4.3.1.3 Mesh configuration

An explicit mesh configuration is not applied to the magnetostatic model, but rather an adaptive mesh refinement. The magnetostatic solver customarily uses the adaptive mesh refinement described by the flow chart in Figure 4-3a. The magnetostatic solver creates an initial mesh. The solver then analyses the model. The solution is then analysed by calculating the energy error in each mesh node. When the energy error in certain areas is higher than the specified criteria (§4.3.1.4), the mesh is refined for these areas of unsatisfied energy errors. This refinement process continues until the total energy error is smaller than the specified energy error, or the maximum refinement iterations have been reached. Under ideal conditions, the energy value would be exactly zero, but is not plausible due to some amount of residual current density in FEA solutions.

The adaptive mesh refinement allows for mesh independence. Mesh independence means that the mesh is refined until the obtained solution converges. Any further refinement of the mesh would only waste valuable computational time without improving the accuracy of the simulation.

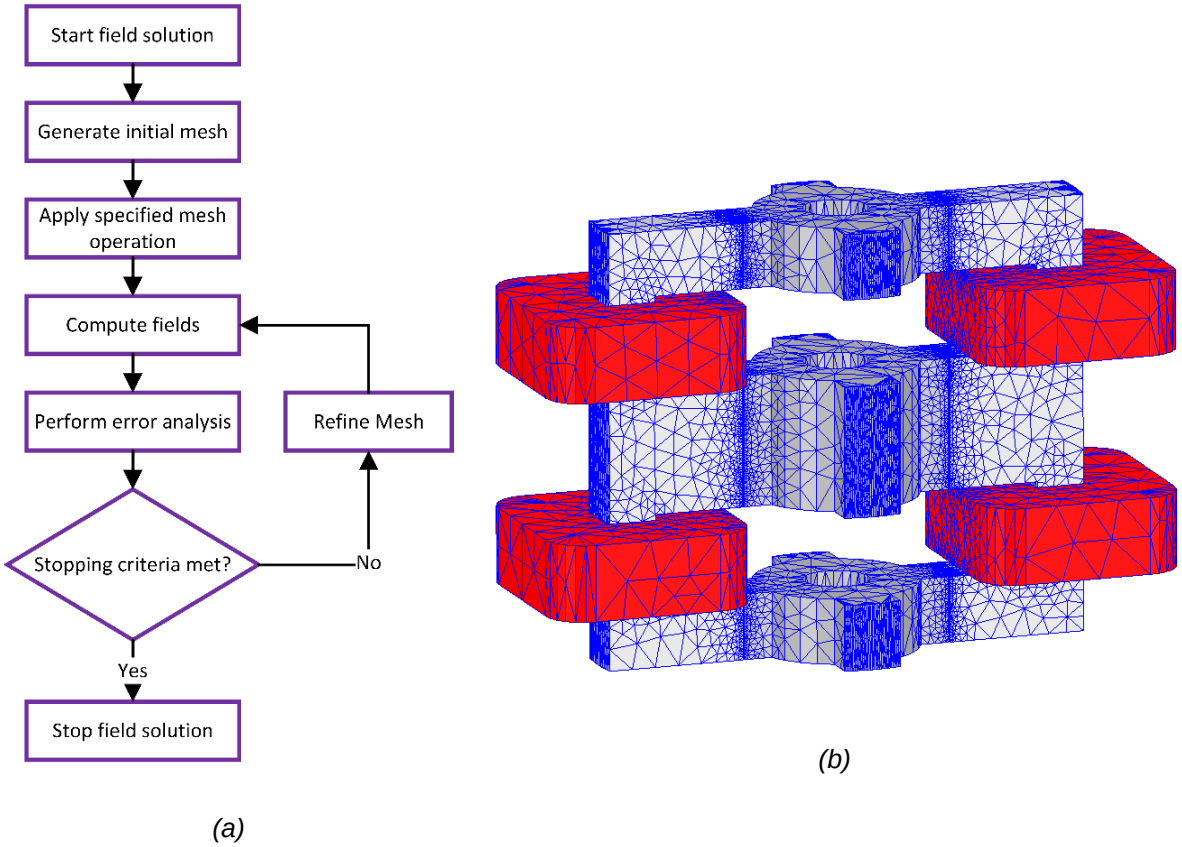

Figure 4-3: (a) The adaptive mesh method used by Ansys®; (b) 3D FEA mesh model.

4.3.1.4 Solution and analysis setup

Before simulations can be performed, the magnetostatic solution parameters have to be set. The parameters of the magnetostatic solver with their respective values are:

- The maximum number of mesh refinement iterations is set to 10.
- The maximum percentage error acceptable in the nodes is set to 1%.
- The mesh refinement per iteration is set to 35%.
- The minimum converged iterations are set to 2.

The solution and analysis setup means that a maximum of 20 mesh refinements will be made before the simulation is stopped without obtaining a solution. Each iteration will refine the mesh by 35%, as per the method explained in §4.3.1.2. If a solution with more than 1% energy error is obtained in the nodes, the solution has to undertake another iteration to confirm convergence and stop the simulation. The converged answer is then taken as the solution.

The mesh, energy error, and mesh refinement information provided by Ansys® Maxwell is shown in Figure 4-4. This information is provided during a magnetostatic simulation of the E-core MSRM.

Energy error is the error energy as a percentage of the total energy calculated at each node. The delta energy is the percentage difference in total energy calculated from the previous simulation.

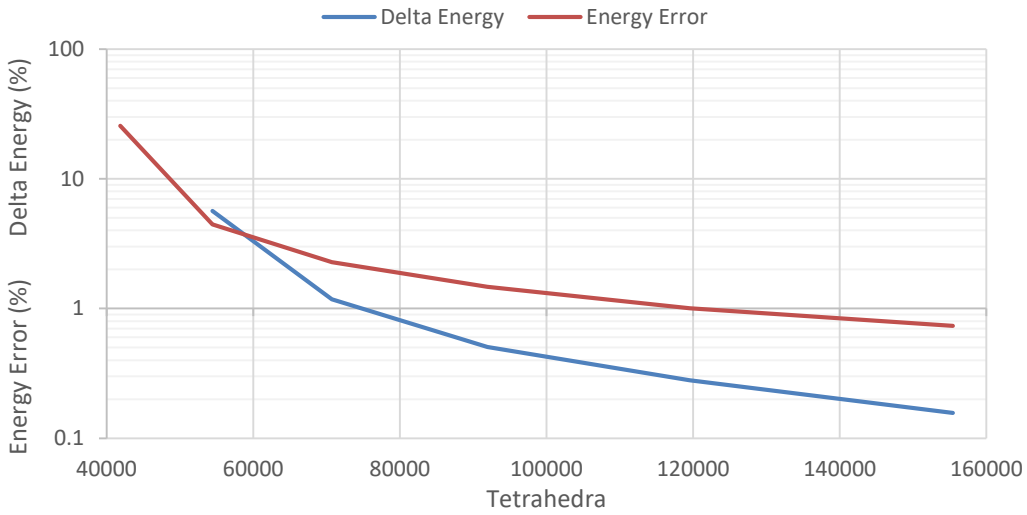

Figure 4-4: Typical monitoring of a solution convergence provided by Ansys® Maxwell.

4.3.2 Magnetostatic simulation procedure

Obtaining the magnetostatic characteristics from the unaligned position to aligned position requires many simulation setups. These setups require the change of rotor position and excitation current. Thus, a parametric sweep is used to allow the rotor position and excitation current to be swept through a range of values. The rotor position is defined by the angle from the values ranging from 0˚ to 45˚ in steps of 3˚. The excitation current is set to values ranging from 0 to 3.5 A in steps of 0.5 A. The parametric sweep accounts for 128 simulated solutions.

Wen Ding *et al.* provided both experimental data and FEA data in the articles, that was used to validate the magnetostatic simulation method. The experimental data of flux linkage characteristics and the winding inductance were obtained from [96] and [110]. These experimental data were compared to the FEA data, provided in [110]. The experimental data of the two articles and the FEA is shown in Figure 4-5. No experimental data on the static torque characteristics were provided in any of the listed articles (§4, p.63). However, FEA data were provided in [96] and [110], as shown in Figure 4-6. The static torque is shown at excitation currents of 0 to 3 A in steps of 0.5 A.

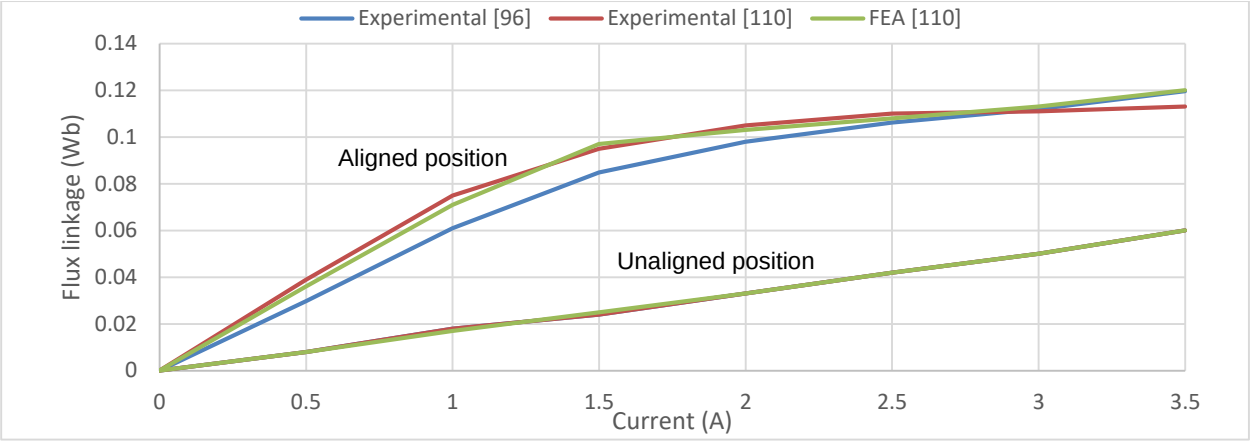

(a)

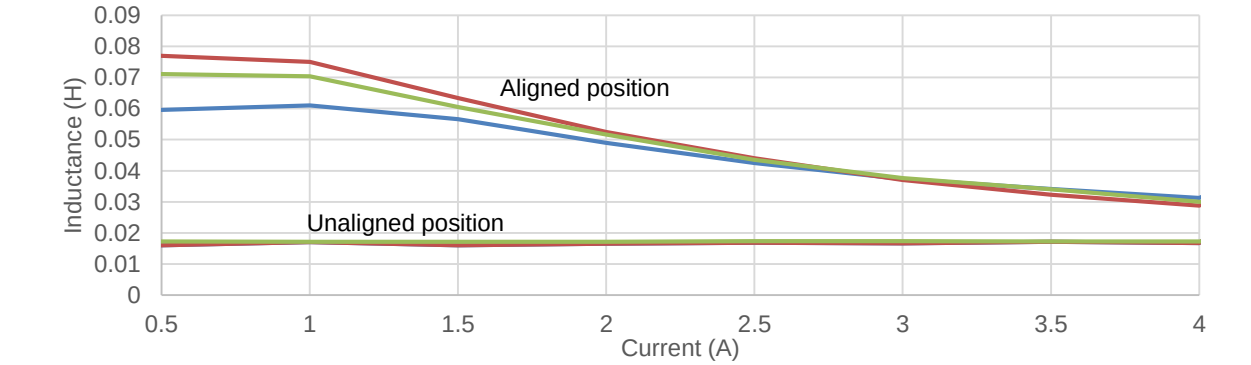

(b)

Figure 4-5: Magnetic characteristics for validation: (a) Flux linkage; (b) Winding inductance.

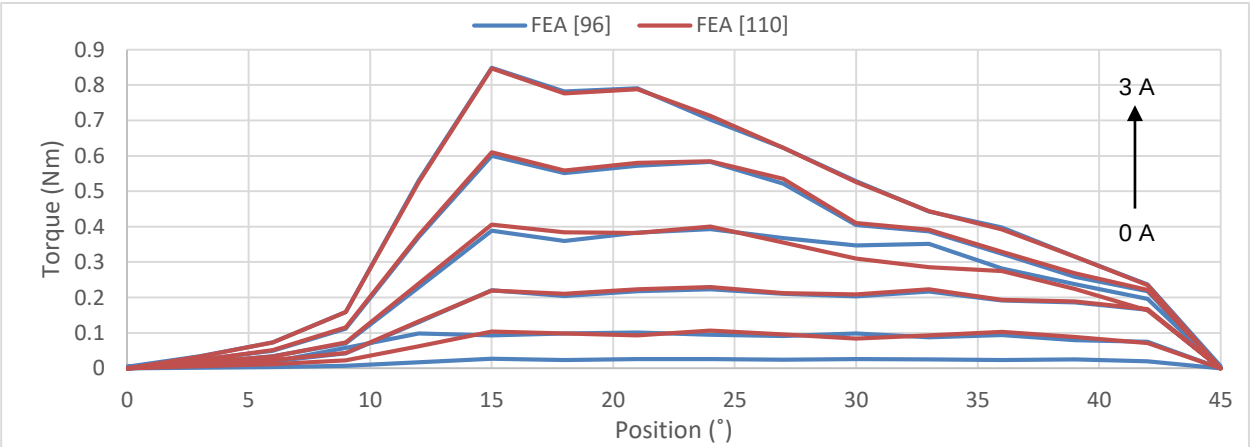

Figure 4-6: Static torque characteristics for validation.

Observing the flux linkage and winding inductance graphs in Figure 4-5, a contradiction is observed between the experimental data from [96] and [110]. Furthermore, by observing Figure 4-6, the static torque shows some deviation from the FEA data provided in [96] and [110]. These contradictions posed the problem that the experimental test method was not properly

implemented between tests or that the information about the data was incorrectly implemented during the writing of the article. However, the articles listed (§4, p.63) provide the most information on a radial flux MSRM by FEA data and experimental data.

The sequence of validating the magnetic characteristics is set out below.

1. The articles do not provide various geometric parameters of the MSRM model (§4, p.63). Therefore, five geometric parameters are chosen to evaluate. It is necessary to evaluate these parameters' degree of accuracy with respect to the magnetostatic characteristics. The degree of accuracy is achieved by varying the parameters of:
    a. The cross-sectional coil area.
    b. The stacking factor of the rotor and stator cores.
    c. The rotor and stator pole width.
    d. The radius of the coil fillet when modelling.
    e. The coil shapes. (From a square to rectangular shape when viewed from the top view. The top view is in reference to Figure 4-2b.)
2. Simulating the flux linkage at each rotor position and excitation current. The results are compared with the experimental data and the FEA data (Figure 4-5).
3. Simulating static torque at each rotor position and excitation current. The results are compared with the FEA data (Figure 4-6). Unfortunately, the static torque characteristics of the MSRM cannot be compared with the experimental data. This is due to the static torque characteristics limited to FEA data in the articles (§4, p.63).

It was stated by Wen Ding *et al.* in [96] that the error margin between FEA and experimental flux linkage at aligned and unaligned positions was 12% and 3.2%. Error margins were said to be within a reasonable amount of error. The error is justified by the B-H characteristics of the material in the FEA software, showing a 5-10% deviation in practice. In addition, there may have been a subtle deviation in the air gap length in the manufactured prototype, which contributed to this error deviation.

4.3.3 Magnetostatic simulation results

A series of magnetostatic simulations was constructed for the selected geometric parameters (§4.3.2). Each of these parameters was assigned a variable value, allowing the parametric sweep to account for the variation of these parameters during the simulations.

The 3D flux distribution of the hybrid magnetic flux paths in the MSRM can be seen from the simulated solutions. The 3D flux distribution of the MSRM is shown in Figure 4-7. In this simulation, a current excitation of 2.5 A was used. The MSRM is seen to produce around 1.6 T to 2.0 T at an aligned rotor position under current excitation of 2.5 A.

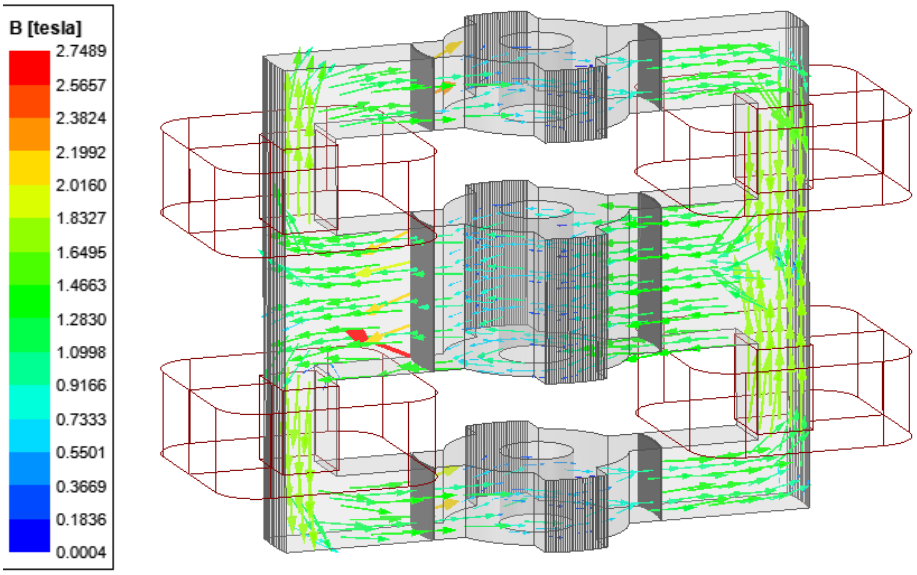

Figure 4-7: Flux distribution at the aligned position when one phase is excited.

The simulated flux linkage and static torque characteristics, following the procedures in §4.3.2, were compared to the FEA data and the experimental data (Figure 4-5 and Figure 4-6), as obtained from the articles (§4, p.63).

The magnetic characteristics by *variation of the cross-sectional coil area* are compared in Figure 4-8. The width of the coil was changed to change the cross-sectional area, keeping the coil height constant. Note that the legend indicates the coil width value, 'FEA' indicates the FEA data simulated by Wen Ding *et al.* and 'Experimental' indicate the experimental data obtained by Wen Ding *et al.* When the flux linkage is analysed, a 5% deviation occurred between the simulated and experimental data. Observing the static torque graph, a similar shape occurs from 15˚ onward, but the simulated data do not have the same trend between 10˚ and 15˚. It was concluded from the flux linkage that the cross-sectional coil area does not have a major effect on the simulation results due to all the simulating points deviating within 5% from the comparative data. For static torque, a minimal variation is shown, with the exception between 10˚ and 15˚.

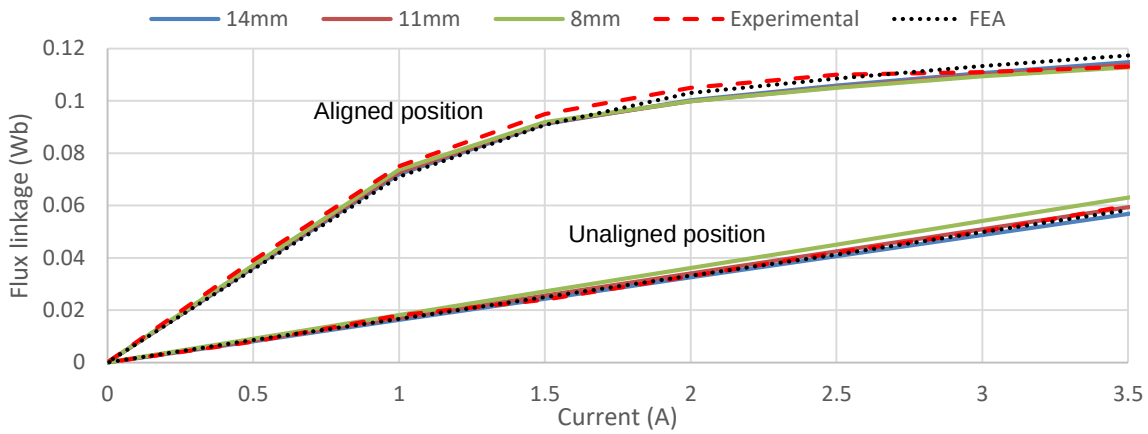

(a)

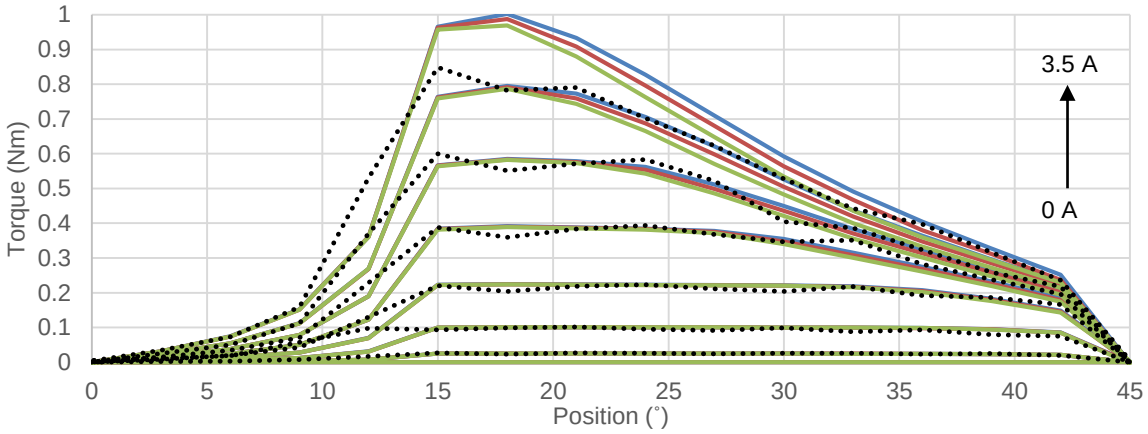

(b)

Figure 4-8: Magnetic characteristics by variation of the cross-sectional coil area: (a) Flux linkage; (b) Static torque.

The magnetic characteristics by *variation of the stacking factor* are compared in Figure 4-9. The stacking factor of the rotor and stator were changed in 5% intervals. Note that the stacking factor of the rotor and stator was the same stacking factor value when doing a simulation. When the flux linkage was analysed, a 5% deviation occurred for the aligned position between simulations. A 3% and 5% deviation occurred when compared to the simulation with a 95% stacking factor. Observing the static torque graph (only graphed at current excitation of 0,1,2 and 3 A), the same shape occurrence is seen as in Figure 4-8b. Comparing the static torque data to the FEA data provided by Wen Ding *et al.*, it is visually observed that the static torque with 95% stacking factor have a minor error margin with an excitation current of 3 A. Hence, a stacking factor of 95% with reference to §2.3.8, p.36 can be assumed for the MSRM. Thus, it is clearly seen that the stacking factor of an MSRM have an influence on the magnetostatic results.

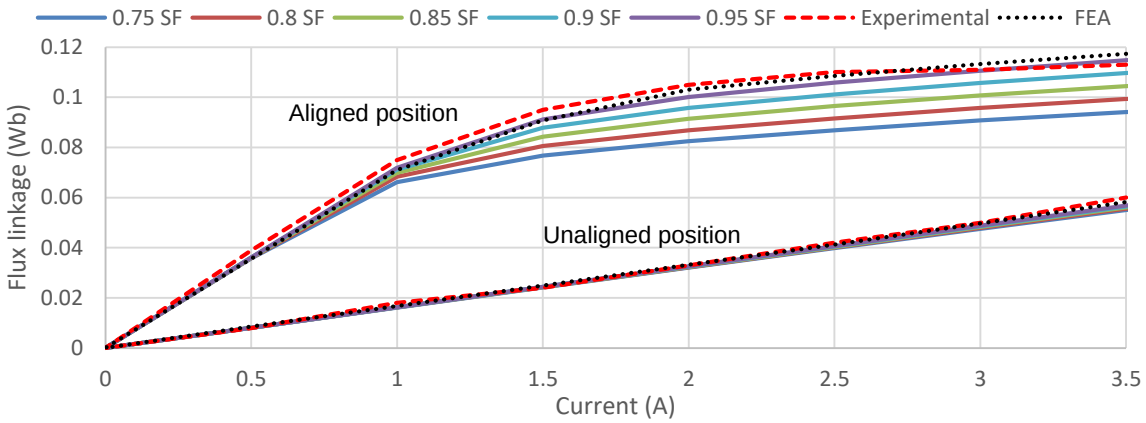

(a)

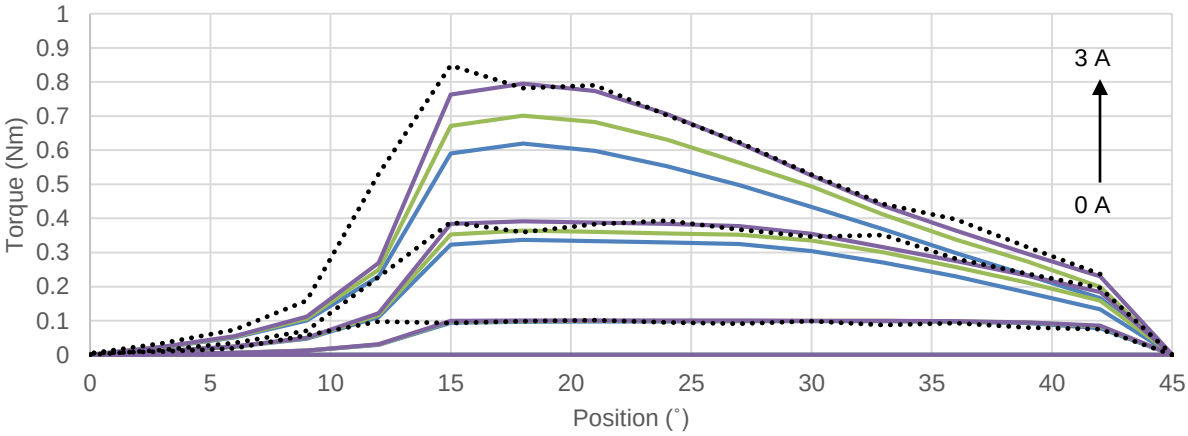

(b)

Figure 4-9: Magnetic characteristics by variation of stacking factor: (a) Flux linkage; (b) Static torque.

The magnetic characteristics by *variation of the pole width* are compared in Figure 4-10. The rotor and stator pole widths were changed, thus increasing their pole arc angle. Note that the legend refers to the width value of the stator pole. The same ratio changes the width of the rotor pole. The ratio relates to the width value of the pole divided by the original width value of the pole (Table 4-1). By analysing the flux linkage, a 5% deviation occurred between the simulated, experimental, and FEA data. Observing the static torque graph, it is seen that the torque increases more rapidly between 10˚ and 15˚. When excluding the static torque between 10˚ and 15˚, less of a variation between simulated static torque and FEA data is observed. Therefore, it was concluded that pole width has the most influence on static torque when the rotor rotates from an unaligned position to an aligned position. This was most likely due to the magnetic flux path between the stator and rotor cores occuring at an earlier rotor rotational angle. The magnetic flux path started to occur at an earlier rotor rotational angle due to the wider core poles.

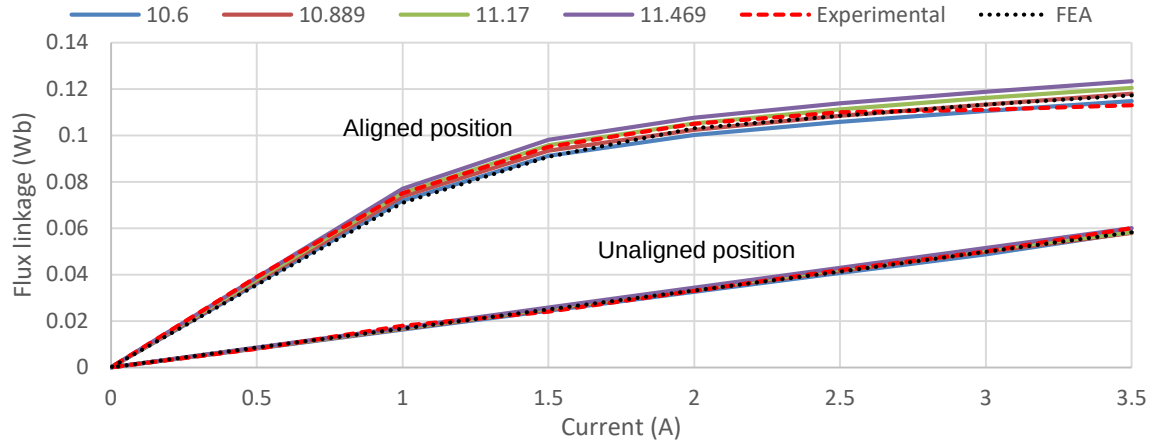

(a)

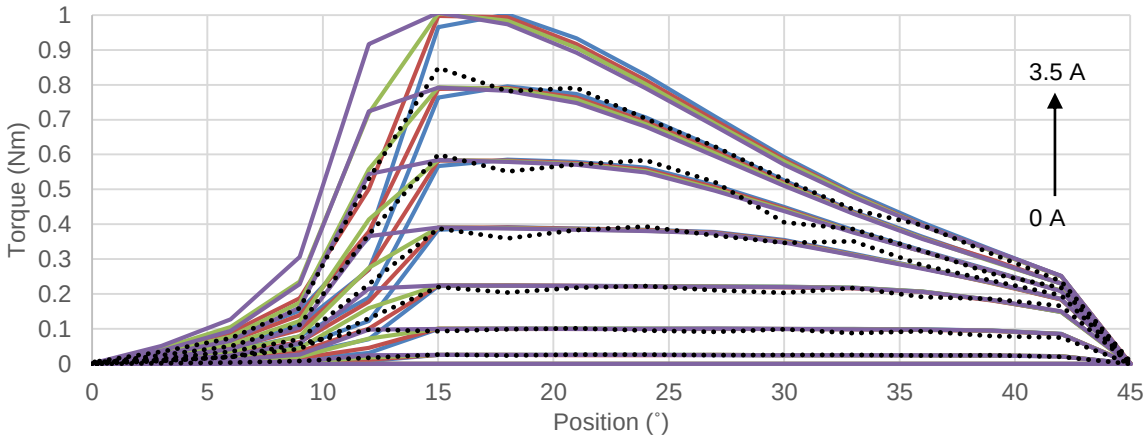

(b)

Figure 4-10: Magnetic characteristics by variation of pole width: (a) Flux linkage; (b) Static torque.

The magnetic characteristics by *variation of the coil shape* and *variation of the coil fillet* had no significant effect on the magnetic characteristics. By analysing the flux linkage, a 1% deviation occurred between the simulated, experimental, and FEA data. The simulated data are provided in Appendix B, §B.2, p.173.

4.3.4 Magnetostatic simulation summary

The magnetostatic process to replicate the magnetostatic characteristics of the MSRM was provided in §4.3.1 to §4.3.3. The parameters of the cross-sectional coil area, rotor and stator core stacking factor and coil shape were not provided by Wen Ding *et al.* in [96, 110, 109, 97, 107, 111]. The replication procedure was analysed by a parametric sweep simulation of the geometric parameters to observe the effect on the magnetostatic characteristics.

The flux linkage compared well to the experimental data when a stacking factor of 95% was used. This stacking factor coincides with that found in the literature for magnetic material laminations of

0.5 mm thickness (§2.3.8, p.36). The effect of pole width and coil cross-sectional area had an effect on the solution, and it should be remembered that a manufactured prototype was not produced to the precise dimensional specifications. Thus, there will be some deviation from the prototype.

Comparing the simulated static torque to FEA data, provided by Wen Ding *et al.*, a torque characteristic difference was seen when the rotor was between the angles of 10˚ and 15˚. Unfortunately, no experimental data was provided to confirm the correct static torque characteristic graph. Torque production for an SRM, during motoring operation was produced and calculated in terms of co-energy, using a flux linkage curve (§2.1.2.2, p.20). Therefore, the flux linkage characteristics are considered the most important aspect of the magnetostatic simulation. This is because the flux linkage characteristic can be used to calculate the electromagnetic torque of an SRM.

4.4 Transient validation

The transient solver of Ansys® Maxwell was used to obtain the dynamic behaviour of the MSRM. The dynamic behaviour observed in this study was the motor speed, shaft torque, phase current, and phase voltage to calculate motor efficiency. The dynamic behaviour was simulated for the amount of time it took one electrical period to complete at the specified motor speed. For an SRM, the mechanical degrees were calculated by dividing the degrees of an electrical period with the number of rotor poles and multiplying the answer by two. Thus, simulating this 4/6 MSRM of Wen Ding *et al.* over an electrical period resulted in the rotor rotating 90˚ mechanical degrees. Only one electrical period was needed to simulate the motor at steady-state. The post-processed result could then be multiplied to obtain the result over multiple electrical periods.

Unlike the magnetostatic validation, the whole motor was constructed for the transient validation. This was because each phase winding was excited one after the other with the dynamic behaviour of a motor. For transient simulations (§4.4.3, p.81), the upper and lower coils of the opposing stators were divided into two windings connected in parallel to form one phase, shown in Figure 4-2.

4.4.1 Transient simulation setup

The model setup should be finalised for the numerical simulation to be solved. The transient setup contains the excitation, boundary conditions, mesh, and the transient solution and analysis setup. The setup is discussed in the order listed.

4.4.1.1 Excitation simulation setup

Excitation of the phase windings is provided in the following process. Each coil in a phase winding is assigned an excitation. The external excitation method is selected, the stranded coil type is selected, and the number of turns is set to 300. The stranded coil type is selected for the excitation method, otherwise the simulation assumes a solid piece of material for the coil geometry. The direction of the current flow is changed to the desired position, so that the flux path of the phase, shown in Figure 4-7, is achieved. The external excitation method is used so that an asymmetric half-bridge circuit can be coupled to the simulation to drive the electric motor.

The asymmetric half-bridge converter, shown in Figure 4-11, is one of the most flexible and versatile switching circuits used in SRM drives. Each phase winding is controlled independently and allows three modes of operation, as discussed [55, 58]:

1. Magnetisation mode: The upper and lower switches of a phase are turned on together, exciting the phase by the current flow.
2. Freewheeling mode: Only one pair of the switches is turned on, and the phase winding is not connected to the DC source. Thus, there is no energy flowing back to the DC source.
3. Demagnetisation mode: When both switches are turned off, the current flows through the diodes, transferring trapped magnetic energy from the phase winding back to the DC source. Demagnetisation and magnetisation of the two phases occur simultaneously.

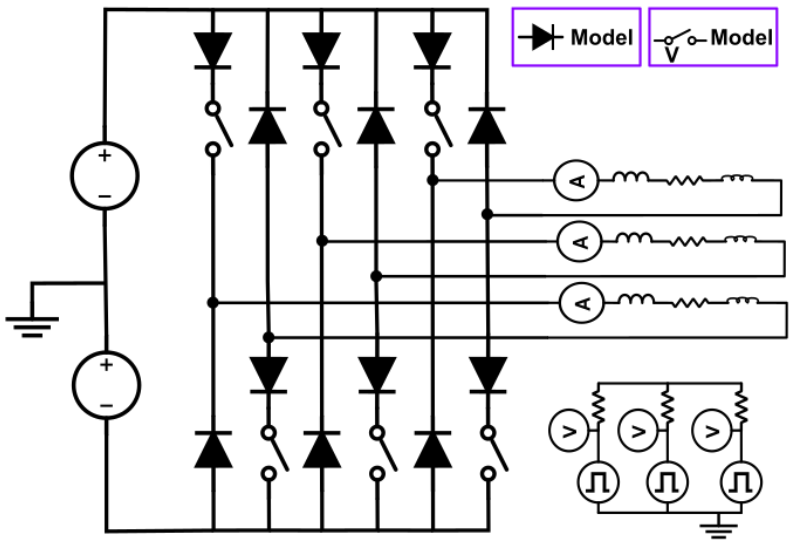

Figure 4-11: Drive circuit for three-phase SRM.

The asymmetric half-bridge converter is set up in the Ansys® Maxwell circuit. The switches in the circuit are operated by position control, meaning that the switch is turned on and off on the basis

of the angle of the rotor during rotation. The turn-on and turn-off angles vary at different motor speeds, as found in §4.4.2.

Finalising the asymmetric half-bridge converter requires the winding resistance of each phase. A winding resistance of 1.15 Ω is used to validate the MSRM. The value of 1.15 Ω was obtained using the equation of copper loss in a three-phase motor. Note that the phase resistance is the same as the individual coil resistance due to its series-parallel connection.

Copper loss: $$P_{cu} = 3I^2R \quad (40)$$

Here, I is the root mean square (RMS) current and R is the winding resistance.

4.4.1.2 Boundary setup

Before a boundary condition is assigned, a solving domain is created. The solving domain consists of two volumetric cylinder regions. The first cylinder is constructed such that the cylindrical area is in between the rotor and stator pole areas. This region is known as the 'Band' and is used as a reference for the motion setup. The motion setup is set to the rotational type and the specified angular velocity (speed in Table 4-2) is assigned. Note that the mechanical transient selection is not selected in the motion setup. Thus, a steady-state solution will be obtained using the transient solver, as discussed in §3.2.5.3, p.58. The second cylinder is constructed around the motor model. The solver automatically assigns natural boundary conditions while an insulating boundary is considered, refer to §4.3.1.2.

Transient 3D FEA consumes significant computational time [131]. The motor model is divided into four symmetric quadrants to reduce simulation time. When dividing the motor model into sections, a master and slave symmetry boundary is assigned to the motor model. Thereafter, the motor symmetry is set to the inverse of the modelled section value. Dividing the model saves significant computational time [133, 145]. Verifying the symmetry setup, a full, half, and a quarter motor model was simulated using identical simulation setups, and the results were equivalent whilst saving significant computational time.

4.4.1.3 Mesh configuration

The transient solver does not use the adaptive meshing technique. Therefore, manual mesh specifications are required to define the mesh in the important regions of the motor model to achieve the accuracy of the results. The mesh setup is a relatively important aspect when FEA is done. Therefore, the sensitivity to the mesh setup is performed in §4.4.3, following the procedure in §4.4.2.

The mesh generated in Ansys® Maxwell of half of the motor model is shown in Figure 4-12. Note that the setup of a rotary region around the rotor automatically assigns a cylindrical gap mesh to the 'band' (§4.4.1.2).

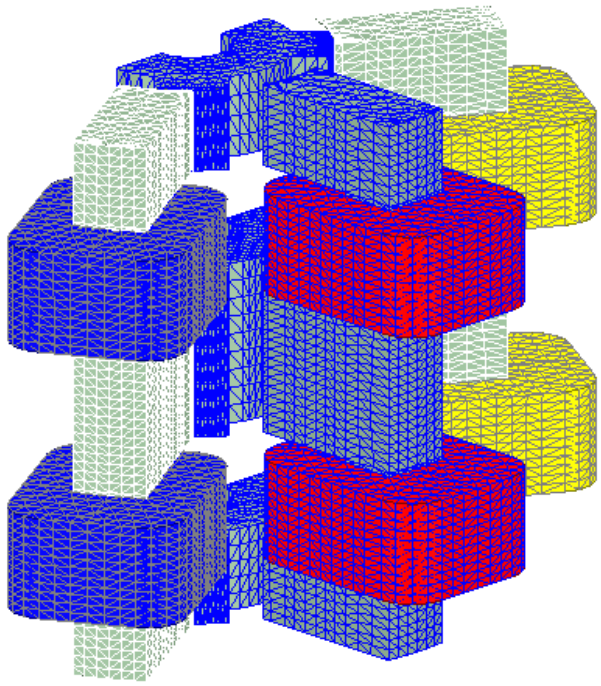

Figure 4-12: 3D FEA mesh model of the transient solution.

The mesh setup assigned to validate the transient behaviour of the MSRM in §4.4.3 consists of the following mesh selection for each geometric aspect:

- Band
  - Cylindrical gap mesh with clone mesh mapping angle assigned at 0.5˚
  - Inside selection length-based mesh of 5 mm
- Rotor core segments
  - Inside selection length-based mesh of 5 mm
  - Clone mesh density of 15 layers
- Stator core segment
  - Inside selection mesh of 5 mm
  - Clone mesh density of 15 layers
- Coils
  - Inside selection length-based mesh of 4 mm

4.4.1.4 Solution and analysis setup

Before a simulation can be performed, the parameters of the transient solution must be set. The parameters of the transient solver are as follows:

- The simulation stepping time is set to 0.055 ms, chosen from the sensitivity analysis in §4.4.3.
- The simulation stopping is set to the time it would take the motor to rotate 90˚ at the specified speed, shown in Table 4-2. This means that the simulation performs one complete electrical period.
- The non-linear residuals of the transient solver are set to 0.0001, and the option of a smooth B-H curve is selected to improve the accuracy of material characteristics during a simulation.
- The second-order potential solver is selected as the standard used in the transient solver.
- The rotational speed, DC source voltage and conduction angles (turn-on and turn-off angles) are assigned for three simulations, shown in Table 4-2.

Table 4-2: Transient solution setups.

Speed (rpm)	DC voltage (V)	Turn-on; Turn off angles	Stop time (s)
1500	35	0˚; 33˚	0.01
1000	25	5˚; 35˚	0.015
700	40	0˚; 30˚	0.02143

4.4.2 Transient simulation procedure

Minimal experimental data of dynamic operation were provided in the articles (§4, p.63). However, the articles provided most experimental data when considering other MSRMs found in literature. Therefore, the transient solutions were compared with the FEA and experimental data obtained from the articles. Comparing the solution data to experimental data ensured that the transient setup and procedures were performed correctly.

Confidence in using the transient magnetic solver will be obtained when the transient solution is replicated within an acceptable error margin of the article data.

The sequence of validating the transient operation is set out below.

1. The complete setup of the transient operation is not provided in the articles (§4, p.63). The data not provided in the articles include the mesh setup and the solution setup. Therefore,

it is necessary to determine the influence of these parameters. The influence of these parameters is called a sensitivity analysis.

The solver time steps and mapping angles of the cylindrical gap mesh are chosen as the two most important parameters [133, 137]. Both the phase current and torque solutions are compared as indications of the parameter effects. These simulations of the sensitivity analysis consist of:

a. The variation of time steps with no clone mesh mapping angle is assigned.
b. Assigning a clone mesh mapping angle under the variation of time steps.
c. Keeping the time steps constant under a variety of mapping angles, and
d. Keeping the exact setup and only changing the stacking factors of the cores between 95% and 100%.

2. Simulating the MSRM at steady-state speeds of 700, 1000 and 1500 rpm. Simulations are carried out for a single electrical period. The solution data for each electrical period are equivalent. Thus, saving valuable computational time. The post-processed results, including the phase currents and shaft torque, are compared with the experimental and FEA data.

Note that all simulations were based on single-phase excitations. This is credible because the magnetic poles of an SRM can be generated with non-coupled coil configurations. Therefore, the mutual coupling between phases becomes negligible, and the flux linkage characteristics for a single phase can be used to model the other phases. Additionally, during commutation between phases, two phases are conducting simultaneously. This is mutual coupling, but since it occurs very briefly in each cycle, the effect can be neglected when modelling an SRM [55]. If adequate spacing between any two spaces is provided, the mutual coupling in an MSRM is negligible [146].

4.4.3 Transient simulation results

A series of transient simulations were conducted to conclude the sensitivity analysis. Each of these parameters was evaluated during the sensitivity analysis to understand and set up a transient simulation in order to obtain the best post-processed solution data. An in depth understanding of all equations, methods, processes and procedures can be found in [133].

As observed in Figure 4-16, the post-processed torque and current data of the simulations represented graphically better than those shown in Figure 4-13. Note that the torque and current graph colours are represented by the legend on the right-hand side.

The transient results by *variation of time steps with no clone mesh mapping angles* are compared in Figure 4-13. The time steps of the simulations were changed between 0.555 ms, 0.111 ms, and 0.055 ms. It is observed from Figure 4-13 that the visual waveform of torque increased with

the decrease of time steps. This was due to more simulations being carried out within the same simulation time period when rotating between 0˚ and 70˚. Thus, smaller simulation stepping times resulted in more simulations, therefore increasing simulation time but also the accuracy of the post-processed results. The elapsed simulation time for each of these simulations ranged between 3 to 8 hours, depending on the simulation setup and computer resource availability.

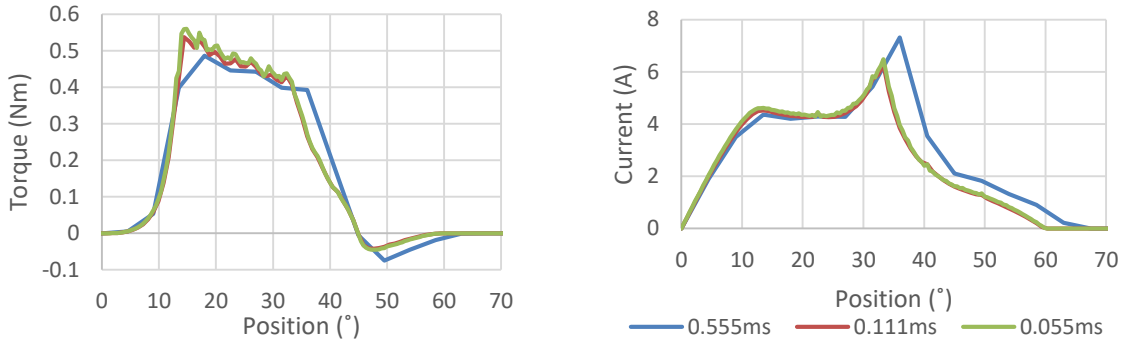

(a) *(b)*

Figure 4-13: Sensitivity analysis with no clone mesh mapping angle: (a) Phase torque; (b) Phase current.

The transient results by *variation of time steps with a 1˚ clone mesh mapping angle* are compared in Figure 4-14. The time steps of the simulations were changed between 0.222 ms, 0.111 ms, and 0.055 ms. The waveform resolution was observed to increase with decreasing time steps, as observed in Figure 4-14. When comparing the waveforms (0.055 ms and 0.111 ms) of no clone mesh mapping angles with the waveforms of a 1˚ clone mesh mapping angle (0.055 ms and 0.111 ms) in Figure 4-13, it is visually observed that the use of a clone mesh mapping angle improves the current post-processed results. However, the torque waveform still shows acoustical noise at the top of the torque waveform.

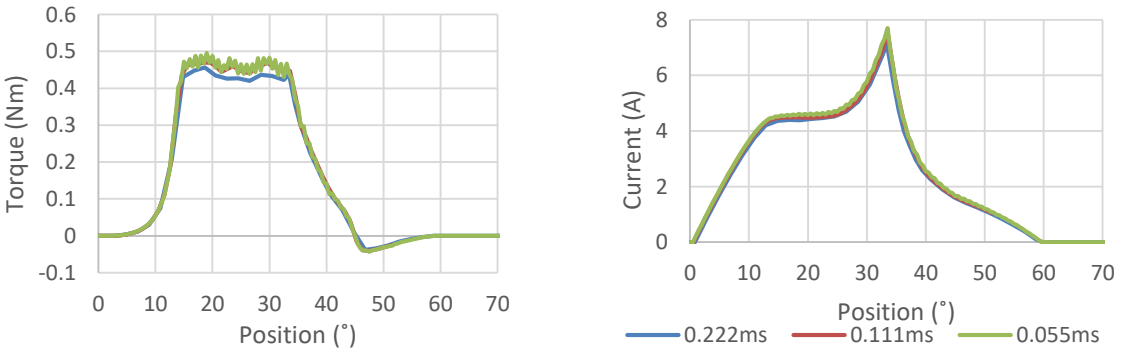

(a) *(b)*

Figure 4-14: Sensitivity analysis of 1˚ mapping angle: (a) Phase torque; (b) Phase current.

From the above simulation results, it was chosen to use 0.055 ms time steps for further sensitivity analysis. Note that the torque shapes in Figure 4-13 and Figure 4-14 differ from one another. This was because the torque simulations shown in Figure 4-13 were simulated using a stacking factor of 100% and the torque simulations in Figure 4-14 were simulated using a stacking factor of 95%. The effect the stacking factor has on the torque and current waveforms are shown in Figure 4-16.

The transient results by *variation of mapping angles with 0.055 ms time steps* are compared in Figure 4-15. The clone mesh mapping angles were changed between 0.5˚, 1˚ and 2˚. The waveform resolution is observed to increase with the decrease of the mapping angle, as observed. Decreasing the mapping angle would increase the simulation time and the visual accuracy of the post-processed simulation results as the acoustic noise is eliminated.

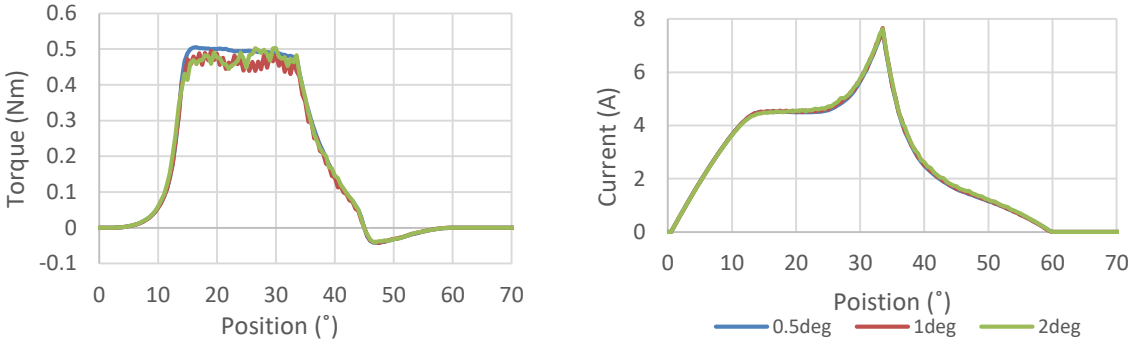

(a) *(b)*

Figure 4-15: Sensitivity analysis of mapping angle at a 0.055 ms time step: (a) Phase torque; (b) Phase current.

The transient results by *variation of the stacking factor with 0.055 ms time steps and a 0.5˚ clone mesh mapping angle* are compared in Figure 4-16. It is observed that the torque shape differs. For solid cores, the torque shape rises to a peak and descent faster than cores with a 95% stacking factors, as observed between Figure 4-13 and Figure 4-14. It is also observed that more current is drawn when cores of a 95% stacking factor are used. Thus, it was concluded that the use of the highest stacking factor in an electrical motor was to minimise losses, as the excitation current would be less and therefore less copper losses can be expected in the motor.

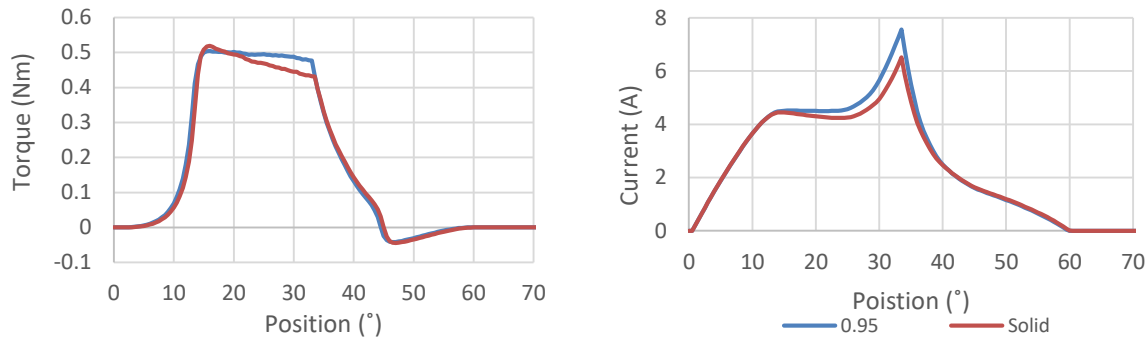

(a) *(b)*

Figure 4-16: Sensitivity analysis of the stacking factor: (a) Phase torque; (b) Phase current.

In finalising the sensitivity analysis, it was concluded that different setup options affect the post-processed results. Setup values that result in the best post-processed solutions were applied to the simulations to finalise the transient validation.

Steady-state transient solutions of 700 rpm and 1500 rpm were compared to FEA data, and the solution of 1000 rpm was compared with experimental data obtained in the articles (§4, p.63). Note that the experimental data of the MSRM were conducted under closed-loop control. The turn-on and turn-off angles were assumed to be the same as those of the 1000 rpm simulation in [110]. However, the provided simulation used a 24 V DC source, as specified by Wen Ding *et al.* in the articles and does not provide further solution data.

The post-processed solution data of 700 rpm and 1500 rpm are shown in Figure 4-17. The difference in shaft torque and phase current was due not only to the difference in speed but also to the different control methodology used by the motor controller. At 700 rpm, the motor uses current chopping control and at 1500 rpm, the motor uses single pulse control, as explained in §2.1.3, p22. Both the shaft torque and phase torque are represented in the torque waveforms. The shaft torque is indicated by the solid line and the phase torque is represented by the dotted lines, often times overlapped by the shaft torque.

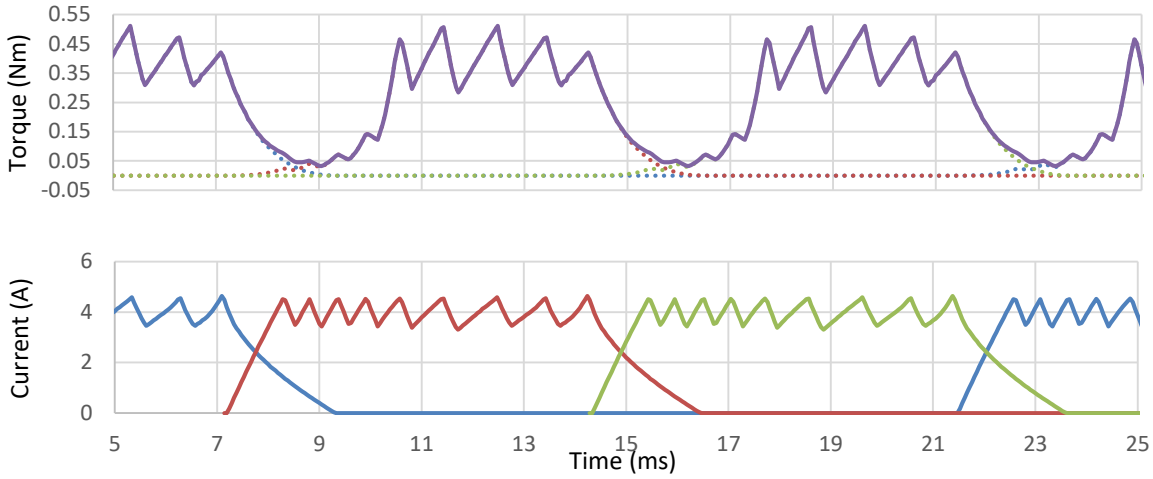

(a)

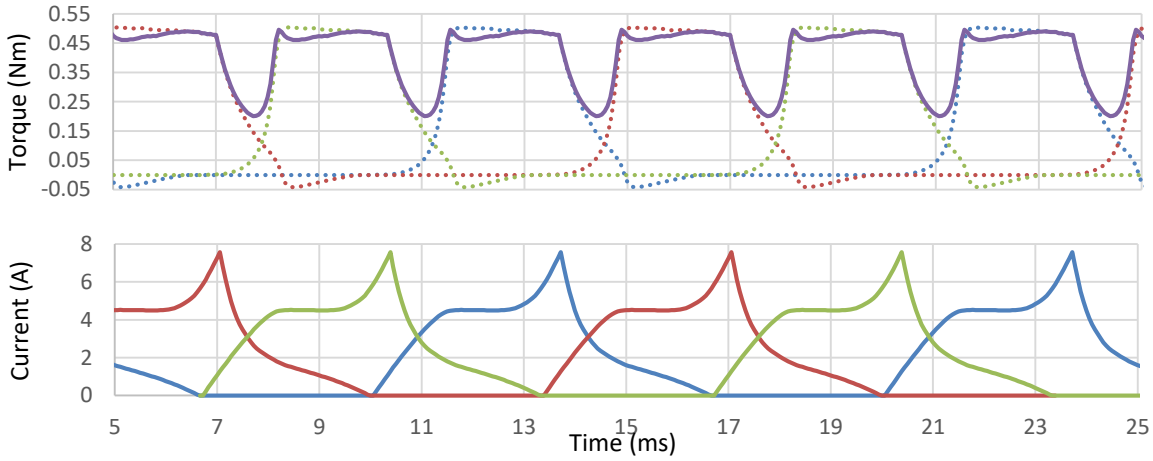

(b)

Figure 4-17: Simulated steady-state torque and phase current waveforms: (a) Current chopping control operation at 40 V and 700 rpm (b); Single pulse control operation at 35 V and 1500 rpm.

A comparison between the post-processed simulation data and the FEA data provided in the articles is summarised in Table 4-3. It is shown that the simulated solution has a deviation of 13.45% for the copper loss at 1500 rpm. As per equation (40), the copper loss is a function of the RMS current and winding resistance. Phase current is subject to winding resistance and magnetic core stacking factor, as seen in Figure 4-16.

The stacking factor was shown to be around 95% in §4.3.3, p.71, and supported from literature (§2.3.8, p.36). The coil resistance was calculated using the provided copper loss and RMS phase current. Since these parameters, along with the mesh setup was not provided by Wen Ding *et al.*, an error margin was expected between the comparisons of the simulated and provided FEA data.

Table 4-3: FEA comparison of dynamic performance.

	Simulated	FEA data	Error (%)		Simulated	FEA data	Error (%)
Speed (rpm)	700	700	-		1500	1500	-
RMS phase current (A)	1.83	1.89	2.89		2.11	1.98	6.52
Maximum phase current (A)	4.68	-	-		7.56	6.85	10.38
Average torque (Nm)	0.26	0.26	1.94		0.410	0.43	5.72
Maximum torque (Nm)	0.51	0.48	5.58		0.496	0.53	7.61
Copper loss (W)	11.65	7.61	7.00		15.44	13.61	13.45

The error differences at the solution of 700 rpm were smaller than those at the solution of 1500 rpm. An explanation for this phenomenon is that more simulations were conducted in an electrical period at slow speed than in high-speed operation because of the solution and analysis setup. Thus, acquiring a lower solution error in high-speed simulation requires smaller time steps in the solution setup, therefore allowing the same number of simulations during an electrical period.

The steady-state transient solution of 1000 rpm was compared to the experimental data obtained in the article [109]. The motor simulation used single pulse control, a 25 V DC source and turn-on and turn-off angles of 5˚ and 35˚. A 25 V DC source voltage was chosen for the simulation of a 1000 rpm, as provided by Wen Ding *et al.* in [109]. Figure 4-18 shows the shaft torque and phase current waveforms compared to the experimental data.

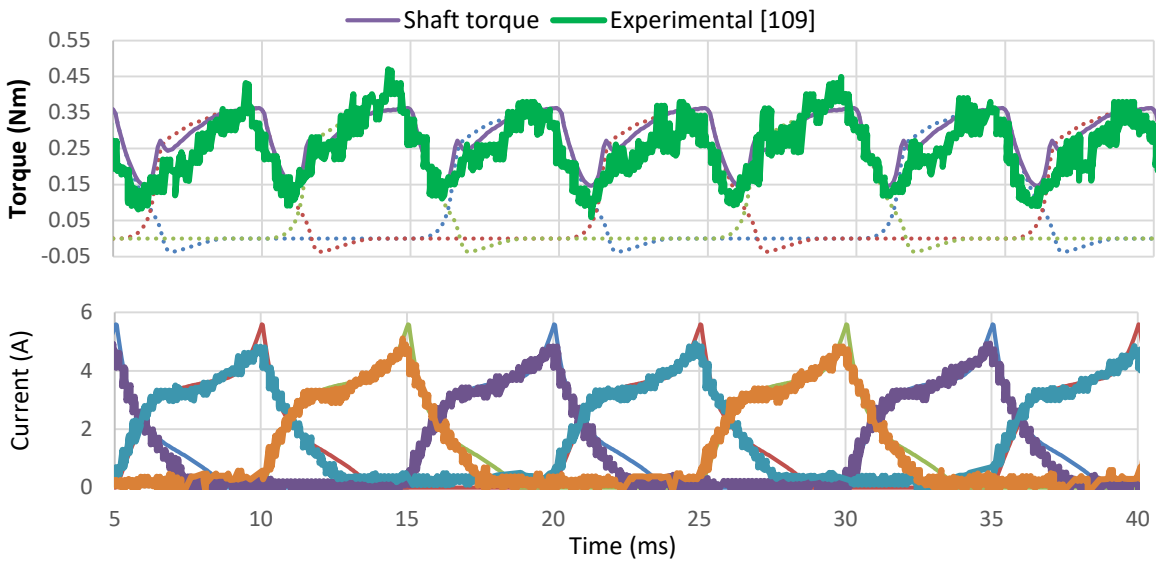

Figure 4-18: Simulated steady-state torque and phase current waveforms compared to experimental data using single pulse operation at 25V and 1000 rpm.

The post-processed solution data are summarised in Table 4-4. Note that only the average torque and maximum phase current of the experimental data are provided in the article.

Table 4-4: Experimental comparison of dynamic performance.

	Simulated	Experimental data	Error (%)
Speed (rpm)	1000	1000	-
RMS phase current (A)	1.637	-	-
Maximum phase current (A)	5.604	5.108	9.71
Average torque (Nm)	0.285	0.328	13.11
Maximum torque (Nm)	0.362	-	-
Copper loss (W)	9.243	-	-

The simulated solution has a deviation of 13.11% for the average shaft torque and a deviation of 9.73% for the maximum phase current. This deviation could be due to numerous factors the simulation had compared to the experimental motor, i.e., the stacking factor, the motor controller, geometric deviation, material characteristic deviations, measuring equipment accuracy, and operating conditions. A quick solution to improve the accuracy of the solution was to increase the

stacking factors of the magnetic cores. However, increasing the stacking factor was not very practical as the maximum stacking factor for thin gauge silicon steel is 97% [147].

4.4.4 Transient simulation summary

The transient process to replicate the dynamic behaviour of the MSRM was provided in §4.4. The replication procedure was analysed by performing a sensitivity analysis of the post-processing solutions. The sensitivity analysis included the solution time steps, the clone mesh mapping angle, and the stacking factor. During the simulations, the coil resistance and stacking factors were unknown. The resistance obtained by equation (40) and the stacking factor of 95% were used, provided from the magnetostatic validation summary of the stacking factor (§4.3.4, p.75).

The predicted performance of the simulations compared well with the FEA data and the experimental data provided in the articles (§4, p.63). Given the unknown resistance of the coil and the stacking factor of the magnetic material, a maximum deviation of 13.11% and 12.884% occurred for the experimental data and the FEA data. Provided a more refined mesh, solution setup, or exact parameters were used during a simulation, the maximum deviation was expected to decrease. However, this might not always be the result for FEA.

4.5 Summary of the electromagnetic simulation validation

The process to set up, construct, and analyse an electromagnetic model of an MSRM was accomplished following the procedures in this chapter. Following the procedures, both the magnetostatic and transient behaviour of the MSRM was validated. The MSRM was replicated within a 5% and 13% deviation from the experimental data. The articles state a 7.5% maximum deviation between the FEA and the experimental data.

Given the unknown motor parameters of the stacking factor, coil resistance, mesh and simulation setup that was not provided in the article data, along with the possibility of different material characteristics between Maxwell 2013 and Ansys® Maxwell 2021 and time and computing power limitations (§1.5.3, p.10), the simulation accuracy was limited. Therefore, the deviation of the solution data was considered acceptable when demostrating the simulation methods. Thus, the same simulation methods could be used to design an MSRM. For future studies, it is proposed to validate the MSRM using different simulation software, i.e. JMAG or Altair Flux, listed in §3.1.2, p.49.

CHAPTER 5 DESIGN OF A SWITCHED RELUCTANCE MOTOR

This design of a three-phase MSRM, proposed in §2.6, p.45, is provided in this chapter. The conceptual diagram of the proposed MSRM is shown in Figure 5-1. The stator comprises of 12 E-cores with a coil wound on the upper and lower yoke of each core. Eight coils are connected in series to form a phase winding, shown in Figure 5-1 as blue, red, and yellow.

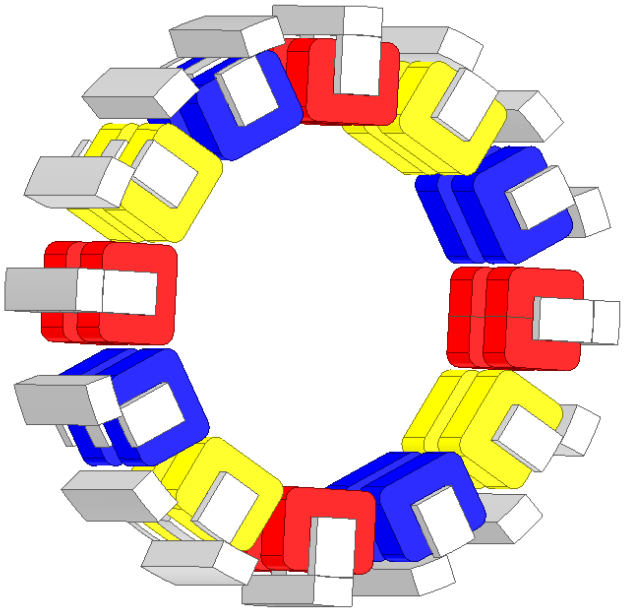

Figure 5-1: The proposed MSRM

This chapter focused on an electromagnetic design using FEA, as the manufacture of a prototype is unfeasible due to financial limitations (§1.5.3, p.10). The electromagnetic design of the proposed MSRM used the design principles of Vanessa Siqueira De Castro Teixeira *et al.* [51], Nikunj R Patel *et al.* [75, 106, 74, 53], and Anas Labak [52, 57] with the addition of the literature review (chapter 2) to construct an XDM. The MSRM was designed according to the specified power characteristics. Thereafter, an efficiency map of the proposed MSRM was constructed for use in the drive cycle. Refer to chapter 6 for the evaluation of a traction motor.

5.1 Motor specifications

The design specifications of AC machines are usually provided in terms of their torque-speed characteristic curve. The designed motor is expected to provide constant torque below rated speed and constant power above rated speed [148]. The torque-speed characteristic curve of the proposed MSRM was determined in this section while considering the motor size before the design of the proposed MSRM commenced.

The MSRM, proposed in §2.6, p.45 was constrained to the parameters listed in Table 5-1. The outer diameter of the motor, considering that the proposed MSRM is a direct drive motor, is constrained by the rim of the solar vehicle. The axial length of the motor was restricted to ensure that the motor uses minimal space. The design of the mechanical housing for the motor is not part of this study, therefore the mechanical housing will increase the axial length of the motor to some extent. In this study, the focus was only on the electromagnetic design of the motor, as provided in this chapter.

The maximum peak current was restricted by the battery of the solar vehicle, and a three-phase motor is specified, keeping to the most commonly used industry practice of using a three-phase motor. Furthermore, specifying a three-phase SRM ensures that electric switches and converters do not increase, thus keeping the cost of the motor controller minimal if it should be considered to manufacture a prototype of the proposed MSRM in the future.

Table 5-1: Design constraints

Motor structure	Radial flux
Rotor outer diameter, D_{ro}	$D_{ro} \leq 14"\ (355.6\ mm)$
Inner stator diameter, D_S	$D_S > D_{shaft}$
Axial length, L_s	$L_s \leq 150\ mm$
Maximum peak current, I_p	$I_p < 80\ A$
Phases, q	$q = 3$

5.1.1 Motor sizing

The proposed MSRM is a direct drive motor, similar to the Mitsuba M2096-DII. For a direct drive motor, the diameter is limited to the size of the tyre. Thus, a tyre incorporates a rim and therefore sets the constraint of the outer diameter of the motor, such that the outer diameter cannot be selected as an optimised parameter [149].

The overall dimensions of a direct drive motor are limited to the space available inside a rim. Due to of the profile of a rim cross section, shown in Figure 5-2, only 80% of the rim diameter is available to insert the motor. Generally, for lightweight vehicles that use tyre size R13 (330.2 mm) and R14 (355.6 mm), an outer diameter of 290 mm is used as a design constraint. Keeping the diameter constraint in mind, the rules of thumb are followed to size the proposed MSRM [83].

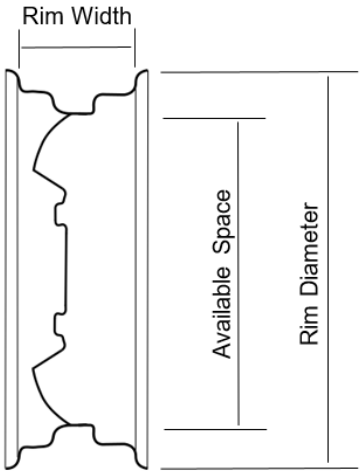

Figure 5-2: Cross-sectional view of a wheel rim

Generally, a given air gap at the greatest radius will produce the greatest torque. Similarly, the torque will require lower field strength when the air gap is at a larger radius, and energising the windings will therefore require less current. Lower current will provide lower thermal losses, better efficiency, and greater continuous performance in a traction motor [55]. Thus, the consideration can be represented by the following.

$$Torque \propto (Diameter_{AG}^2 * Length) \tag{41}$$

Where $Diameter_{AG}$ is the average air gap diameter. For the rule of thumb to size an electric motor, the difference between the inner and outer air gap diameter is negligible. From equation (41) it is observed that by doubling the diameter of the air gap, both the distance of the tangential forces and the air gap shear area are doubled. This results in doubling the tangential forces and therefore quadrupling the torque. If only the length of the motor is doubled, only the air gap shear area is doubled, and therefore the torque is only doubled [83]. Assuming a cylindrical machine, the equation is provided as:

$$Volume_{cylinder} \propto (Diameter_O^2 * Length) \tag{42}$$

Where $Diameter_O$ is the outer diameter of the machine. By accepting that $Diameter_O = Diameter_{AG}$ for an outer rotor radial flux machine, dividing equation (41) by equation (42) gives the following approximate relationship:

$$\frac{Torque}{Volume_{cylinder}} \propto \sim constant \tag{43}$$

Fundamentally, no matter what parameter of a cylindrical, outer-rotor, radial flux machine is altered, the machine will still require the same amount of volume to produce the required torque. However, energising the air gap requires only a certain radial depth. Thus, once the motor reaches a diameter where the inner diameter of the stator is large enough, the motor can essentially take on a toroidal form, and the rules that govern the occupied volume significantly change [83].

Assuming that the radial depth is constant and the diameter and length are free to scale, the volume of a toroid is proportional to that shown in equation (44).

$$Volume_{toroid} \propto (Diameter_{AG} * Length) \tag{44}$$

The approximate relationship of a toroidal motor, provided in equation (45) is obtained when dividing equation (43) by equation (44).

$$\frac{Torque}{Volume_{toroid}} \propto \sim Diameter \tag{45}$$

Thus, as the outer diameter of the motor increases, the motor can transition from a cylindrical motor shape to a toroidal motor shape, and the torque per volume performance changes from an essentially constant value to an approximately linear proportion to the diameter of the motor, as demonstrated in Figure 5-3.

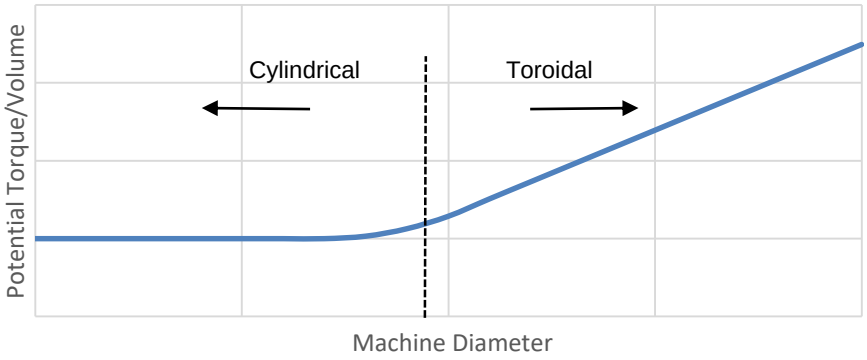

Figure 5-3: Demonstration of the 'breakpoint' of the motor diameter where the torque/ volume increases

From these approximate scaling factors, a large diameter, short axial length, toroidal shaped motor will most likely meet the performance requirements. However, the large diameter of the motor is limited by the rim. The constraint allows for a maximum diameter of 370 mm, measured inside the rim of the solar vehicle. This will allow future considerations where the outer rotor is

used as a rim hub for the tyre, similar to the case of the Commonwealth Scientific and Industrial Research Organisation (CSIRO) motor, implemented by the Aurora and Nuna solar teams [150].

5.1.2 Motor performance

The required performance characteristics of the proposed MSRM were obtained by evaluating the Mitsuba M2096-DII in §6.2.2, p.138 as the current traction motor of the NWU solar vehicle after following a similar approach as discussed by Amir Ahmed and Dikki Bhutia in [151]. Evaluating the Mitsuba M2096-DII was carried out using the drive cycle developed in §6.1.1, p.125. Using the evaluated data, a scatter plot of instantaneous torque and speed throughout the drive cycle is plotted in Figure 5-4. The instantaneous torque and speed are known as the operating points, plotted as blue dots. A similar approach as in [151] was used to specify the performance parameters of the proposed MSRM. This approach is discussed in this section.

The transient torque-speed characteristics of a motor are constructed from the rated torque-speed parameters. However, the transient torque-speed characteristics of a motor are greater than the continuous operating capability. Thus, the operating capability of an electric motor can be extended for a period of time. The operating time beyond the transient limits, otherwise known as the overload torque-speed characteristics, is a function of thermal constraints.

Effective thermal management of an electric motor will improve its performance and ensure reliable operation, while poor thermal management will result in performance degradation and accelerated machine wear that may eventually cause motor failure. The SRM, compared to other electric motors, does not have additional losses generated in the rotor by windings or permanent magnets. Therefore, concerns of demagnetisation of permanent magnets or excessive thermal heat are non-existent in SRMs. Thus, an SRM is only limited by the thermal limits of the stator windings and therefore offers the highest temperature operation capacity [55].

Following a similar approach to the one used in [151], the rated torque-speed characteristics and the overload torque-speed characteristics were chosen. The rated torque-speed characteristics were chosen where the power under evaluation (the operating points) is constant with the increase of speed. However, it was observed from the power-speed operating points that the torque falls linearly above 525 rpm. This was due to the torque-speed characteristics of the Mitsuba M2096-DII, which cannot be operated at extended torque for high speeds. Given the torque-speed characteristics of an SRM, a decreasing power-speed relation will likely not be the case. The approach in [151] did not include an overload torque-speed characteristic. Thus, the approach was altered to include both the rated torque-speed characteristics and the overload torque-speed characteristics, as shown in Figure 5-4.

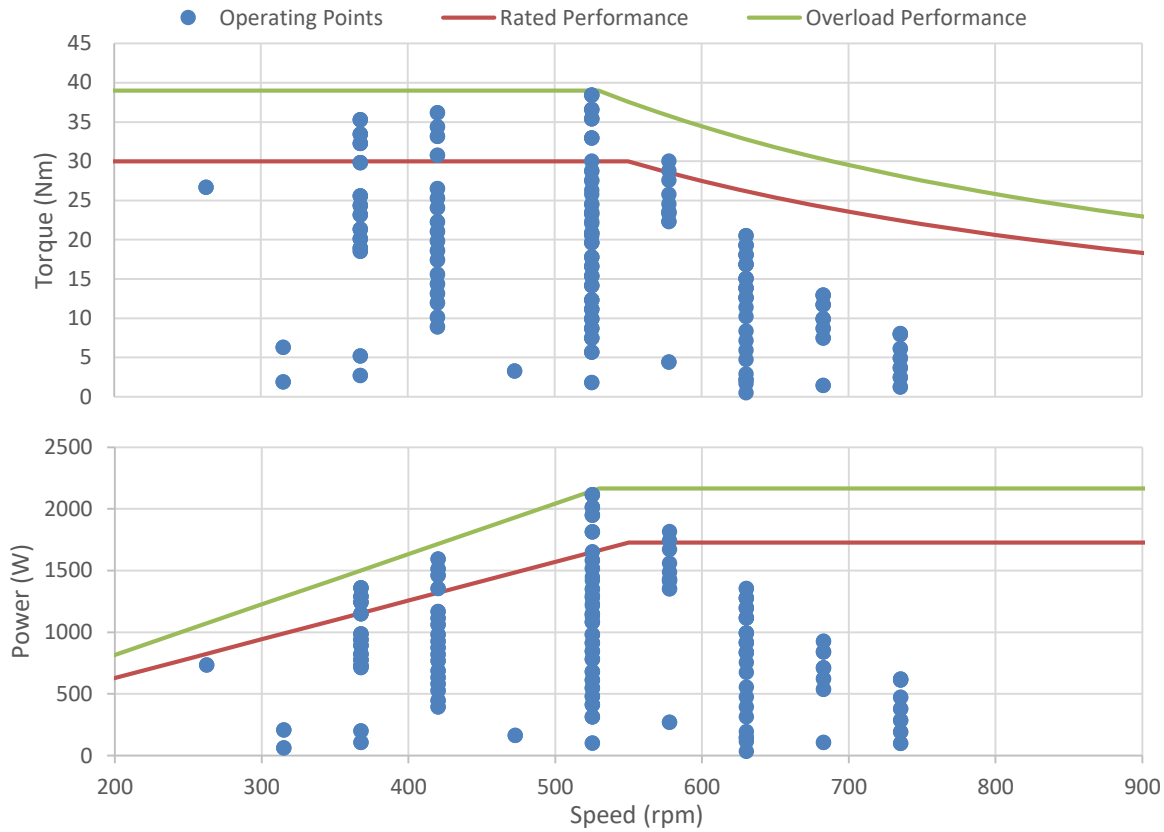

Figure 5-4: The anticipated torque-speed characteristics and power-speed characteristics of the proposed MSRM

The rated torque-speed characteristics were chosen to include the most frequent operating points of the Mitsuba M2096-DII, according to the evaluation of the Mitsuba M2096-DII (§6.2.2, p.138). A minor number of operating points was excluded from the rated torque-speed characteristics. The excluded operating points will be achieved under overload operations. Thus, the torque-speed characteristics were chosen at 30 Nm and 550 rpm, which equate to an output power of 1.73 kW. The overload parameters offer an output power of around 2.1 kW.

5.2 Motor design

The objective of the design was to provide an XDM of an SRM. The XDM was evaluated for solar vehicle application to justify the use of an SRM as a traction motor in solar vehicle races. The required design characteristics of the proposed MSRM are summarised in Table 5-7. Some margin for the speed specification was provided. The margin was provided as the intersection between the operating regions from constant torque to constant power that is not a definite point, as observed in Figure 5-22. Wen Ding *et al.* showed the difference when constructing the torque-speed characteristics of an MSRM in [97].

Table 5-2: Design specifications

Rated Torque, T_b	$30\ Nm \leq T_b \leq 35\ Nm$
Base speed, N_b	$500\ rpm <\ N_b\ < 600\ rpm$

The outer diameter of the MSRM is set to the maximum allowable value within the constraints listed in Table 5-1 to provide the maximum electromagnetic torque in the air gap of the motor.

The rotor and stator cores are segmented so that the flux path length is minimised. Thus, high efficiency is achievable [77, 74].

The performance of an SRM depends mainly on the dimensions of the stator and rotor core, pole configuration, pole arc angles, and its phase windings [148]. The design of the proposed MSRM was divided into three sections namely: geometry, magnetic material, and windings. These sections were intertwined with each other during the design and was not a straightforward process. A flow diagram summarising the design procedures is shown in Figure 5-5.

The flow diagram shows the iterative design procedure between the start and end of the design process. After the design is completed, the flow diagram continues with additional procedures. These extra procedures were included to indicate the process of evaluating the designed motor. Note that after the construction of the efficiency map, the flow splits into two with different coloured arrows. In this study, the red arrow was followed to evaluate the proposed MSRM. Evaluation of the proposed MSRM is done in §6.3, p.140.

The green arrow indicates the design process when the most efficient SRM is desired. However, this process is a time-consuming design process, as each motor design has to be analysed on the basis of its efficiency map. The construction of an efficiency map required a lot of simulation time and computer resources. Note that this is the idealised design process to obtain an SRM for the solar vehicle of the NWU. However, due to time and resource constraints (§1.5.3, p.10), this design process could not be accomplished.

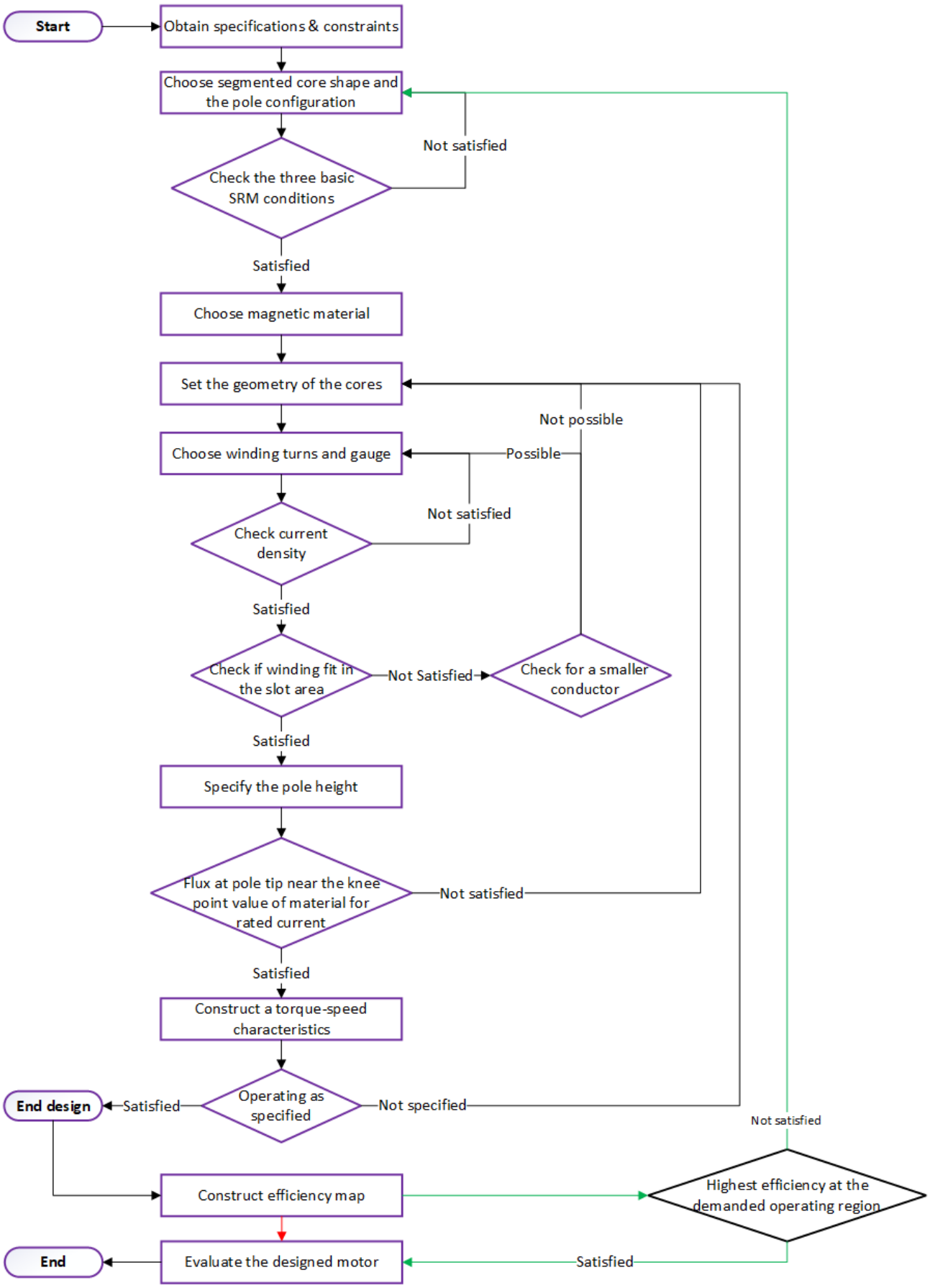

Figure 5-5: Flow diagram of the design procedure

5.2.1 Geometry

Following the design procedures shown in Figure 5-5, the geometry of the proposed MSRM was defined. An MSRM of segmented stators and rotors was proposed because of its short flux paths. The proposed MSRM allows for a large diameter motor with short flux paths to increase motor efficiency. This section discusses the geometric design procedures, where the design variables corresponding to the geometry have the following parameters:

- Stator pole width, τ_s
- Rotor pole width, τ_r
- Stator pole length, $L_{s1} = \frac{L_{s2}}{2} = L_{s3}$
- Stator total length, L_s

Note that because an E-core-shaped stator was used, the stator consisted of three poles. The middle pole is twice the volume of an outer pole to carry the flux density of both, as graphically shown in Figure 5-18, p.114. Thus, the total length of the stator was not equal to the sum of the three lengths of the poles. In a conventional SRM, the pole length would be the length of the stator, also known as the axial length.

The initial geometry values used are those of a C-core MSRM, designed by Anas Labak [77], and Nikunj Ramanbhai Patel *et al.* [53]. The C-core MSRM was designed for a rated performance of 28 Nm and 600 rpm. The C-core MSRM, although an axial flux motor was easily modifiable to use as a radial flux motor, while obtaining the same rotor diameter.

5.2.1.1 Core shape

The stator pole shape of the proposed MSRM consists of an E-core. An E-core was chosen on the basis of the study of Xinglong Li and Ernest Mendrela [115]. Xinglong Li and Ernest Mendrela found that an E-core has a higher force-to-mass ratio than a C-core linear SRM [115]. Applying the principle of a linear motor around an axis, a rotary motor can be formed. Thus, a higher torque-to-mass ratio can be expected for an E-core MSRM.

During the proposal of the SRM in §2.6, p.45, a research question was formed from the literature. The research question formulated the idea that a core with more poles while keeping the core length, width, and winding turns constant will result in higher efficiency as the flux paths are shorter. The research question was based on Figure 2-20, p.46, showing the flux paths and parameters of a C-core, E-core, and IIII-core. The C-core consists of two poles, the E-core consists of three poles, and the IIII-core consists of four poles. The poles of these cores are otherwise known as pole teeth [152]. Even though the research question did not form part of the

scope of this study, the effect of the core shapes was analysed using magnetostatic and transient simulations to justify selecting an E-core over a C-core and to gain a basic understanding of the effect of having more poles on the core.

The C-core, E-core and IIII-core MSRM geometry parameters consist of a total core length of 80 mm, pole arc angle of 9° and a total of 80 winding turns. Note that with the addition of poles, the pole height and winding height decreased. However, the sum of pole heights and winding heights remained constant.

The magnetic flux characteristics of the C-core, E-core, and IIII-core MSRM are shown in Figure 5-6. It is observed that the magnetic flux characteristics (aligned and unaligned flux linkage curves) of each core shape differ from each other. As discussed in §2.1.2.1, p.18, the core shape with the highest energy area will produce the highest amount of torque given a constant excitation current. However, in a transient operation, the excitation current will not be a constant variable. Thus, a transient simulation is required.

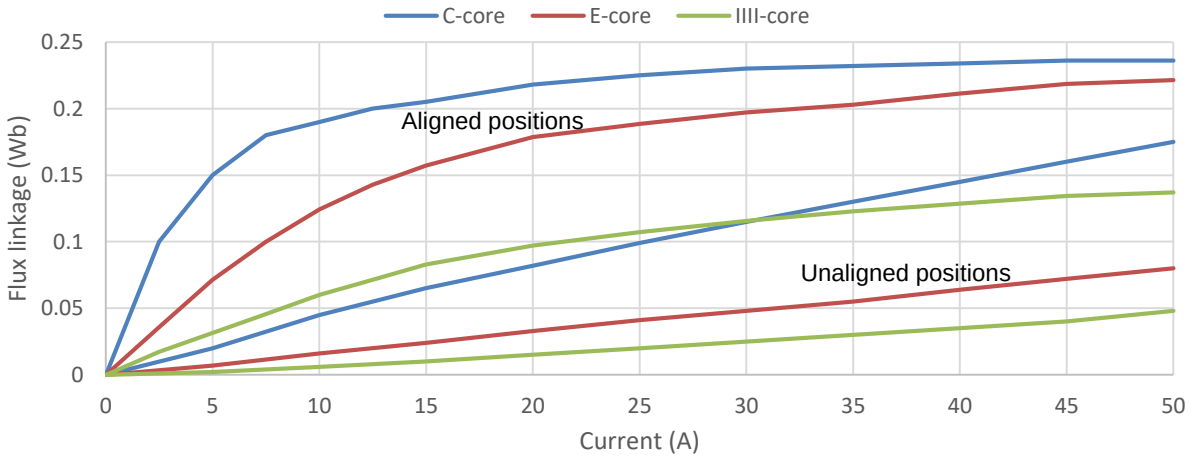

Figure 5-6: Magnetic flux linkage characteristics of a C-core, E-core, and IIII-core MSRM

Steady-state transient solutions of 550 rpm and 800 rpm of each core shape were completed. These simulations used a 100 V DC source voltage and turn-on and off-angles of 0˚ and 6˚. Figure 5-7a shows the shaft torque and phase current waveforms at a steady-state speed of 550 rpm. It is observed that the C-core operated with SPC, while the E-core and the IIII-core operated with CCC. Thus, both the C-core and the E-core operated in the constant torque region, while the IIII-core was already operating in the constant power region.

Figure 5-7b shows the shaft torque and phase current waveforms at a steady-state speed of 800 rpm. It is observed that the C-core and E-core were operating with SPC while the IIII-core was

still operating with CCC. Thus, the IIII-core was still in the constant torque operating region, whereas both the C-core and the E-core operated in the constant power region.

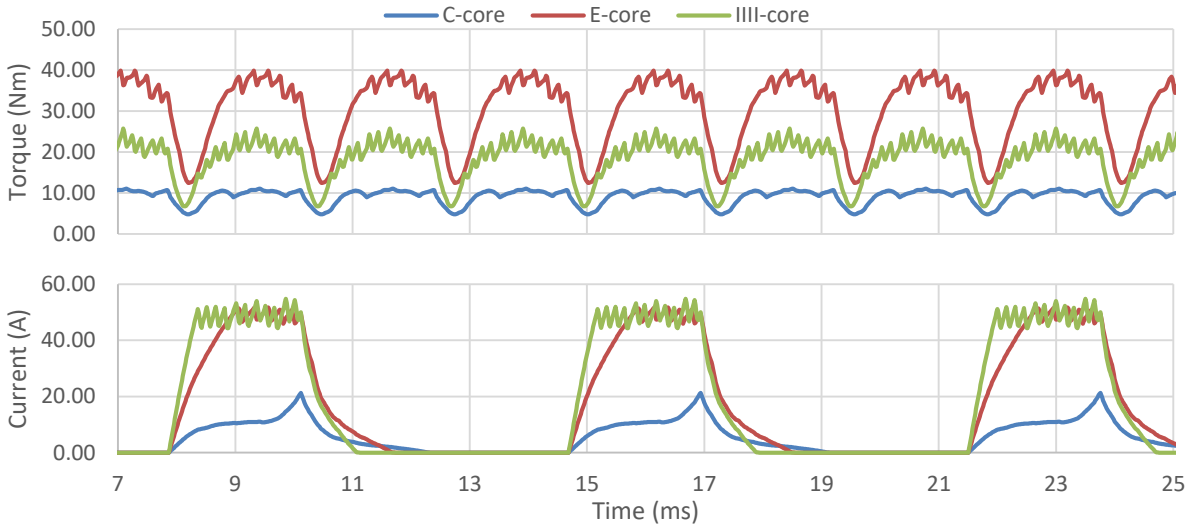

(a)

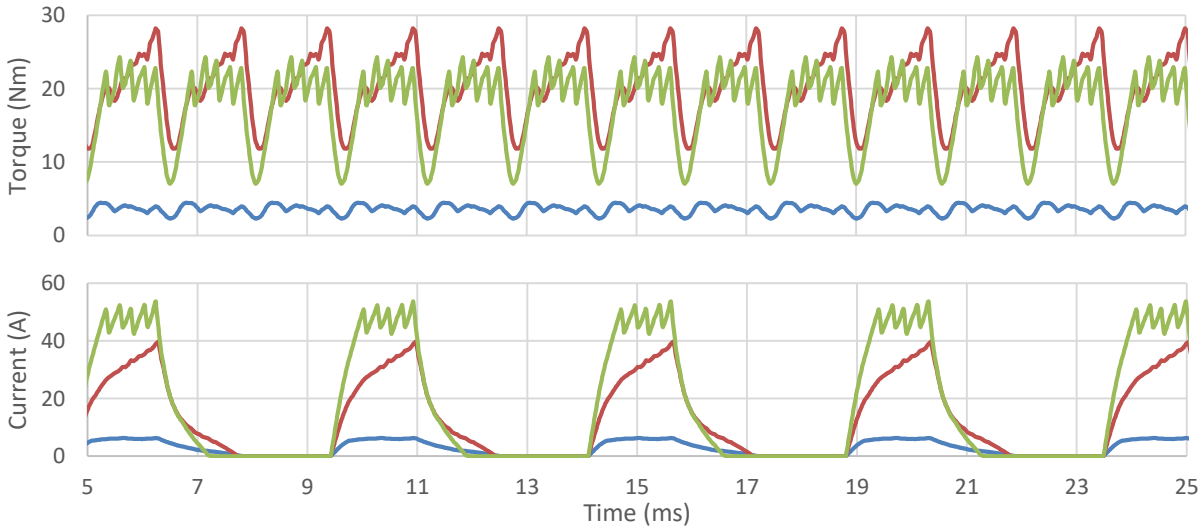

(b)

Figure 5-7: Simulated steady-state torque and phase current waveforms for speeds of (a) 550 rpm; (b) 800 rpm

The post-processed solution data are summarised in Table 5-3. The post-processed torque-speed operating points of the simulations are plotted and the predicted torque-speed characteristics of each core shape are graphed, as shown in Figure 5-8.

Observing the torque-speed characteristics of the core shapes, it was seen that the torque-speed characteristics of the C-core are not on the same constant power curve, as expected from

literature (§2.1.3.1, p.22). Thus, the operating point at 800 rpm was expected to already be in the falling power region. Therefore, a faster torque decrease was expected. However, as discussed in §5.4.1, p.120, this was due to the use of the same conduction angles at different operating speeds. To obtain a torque-speed characteristic with a constant power region, optimal conduction angles should be used at each operating point.

The operating point in which both the C-core and the IIII-core transition from a constant torque to a constant power region is unknown from these simulations. However, the difference in the torque-speed characteristics shows a difference between the core shape operations.

Table 5-3: Dynamic performance of a C-core, E-core, and IIII-core MSRM

	C-core		E-core		IIII-core	
Speed (rpm)	550	800	550	800	550	800
Average torque (Nm)	9.15	3.565	30.46	20.234	18.50	17.663
Output power (W)	527.28	298.65	1754.2	1695.1	1065.7	1479.7
RMS phase current (A)	7.253	3.603	25.478	18.017	27.283	25.759
Copper loss (W)	3.8089	1.892	13.379	9.461	14.327	13.527

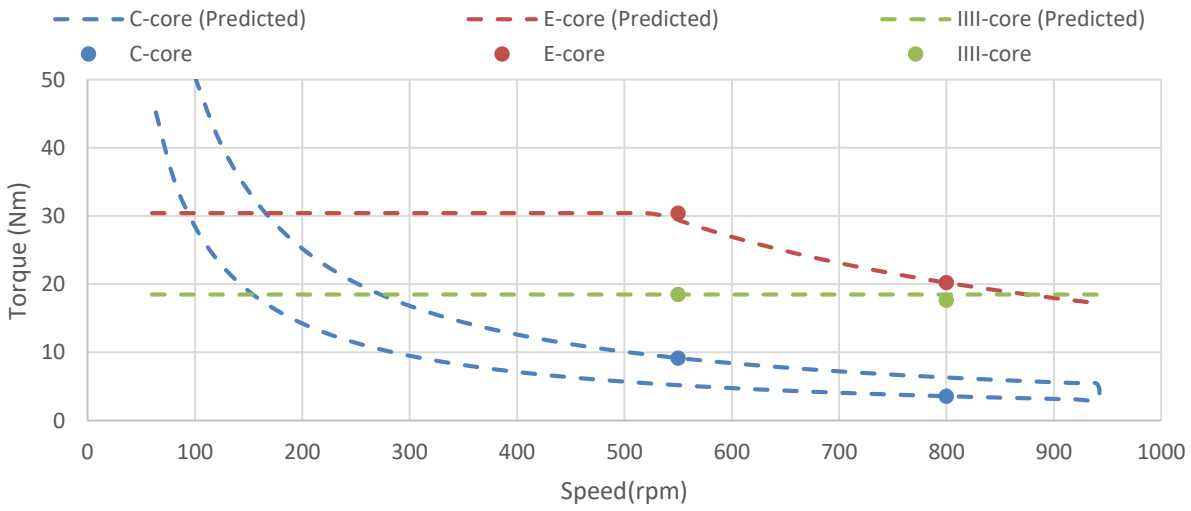

Figure 5-8: Predicted torque-speed characteristics of a C-core, E-core, and IIII-core MSRM

The three core shapes are not a direct comparison. Therefore, a conclusive assessment was not necessary for the purpose of the research question. However, it is still unknown whether one core shape is more efficient than the other, even though a core with more poles has shorter flux paths. For a conclusive evaluation of motor efficiency, the torque-speed characteristics have to be

similar. This research question is proposed as a future study to fully understand the efficiency effect when having a core with more poles while keeping the core length, width and winding turns constant.

5.2.1.2 Pole configuration

Two pole configuration options were considered for the proposed MSRM. A 12/16 and 12/20 pole configuration was considered. From literature, it is known that an SRM with more rotor poles exhibits higher static torque over an electrical period and produced more torque during operations, which is advantageous for EVs. However, maintaining the rotor and stator diameter, the pole arc angles and phase winding turns differ between the comparative SRMs. Thus, this section compares a 12/16 MSRM to a 12/20 MSRM, keeping all dimensions and operating conditions equal.

A 12/16 and 12/20 MSRM consisting of the same geometric parameters, magnetic material, and winding turns were analysed. The only difference between the configurations of the comparative motors was the rotor poles. Note that the number of rotor poles required the conduction angles of the motor controller to be different. The difference in conduction angles was demonstrated by the ideal inductance-rotor angle graph in Figure 5-9. The difference in the inductance profile was due to the rotor pole pitch. The 12/16 MSRM has a pole pitch of 22.5° and the 12/20 MSRM has a pole pitch of 18°. The respective step angle, calculated using equation (24), p.33, was applied as the conduction angle during simulations. The phase winding of the 12/16 MSRM was excited every 31.5°, and the 12/20 MSRM was excited every 20°.

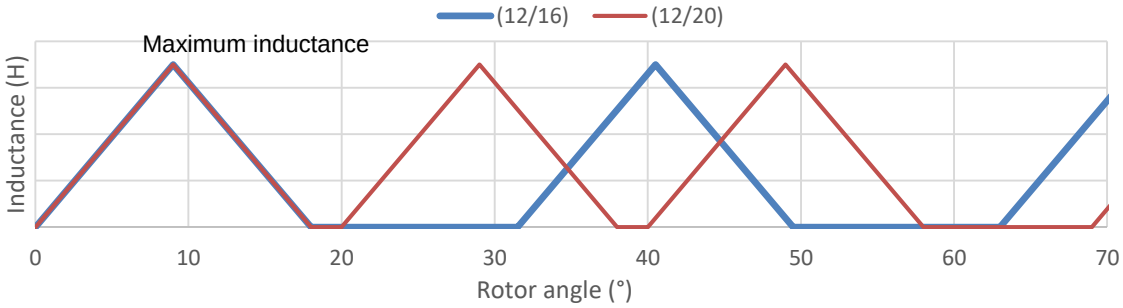

Figure 5-9: Idealistic inductance-rotor angle profile of a 12/16 and 12/20 MSRM

The magnetic flux characteristics of the two MSRM configurations are shown in Figure 5-10. It is observed that both configurations have the same characteristic curve for the aligned position. However, at the unaligned position, the 12/16 MSRM has less flux linkage per current than the 12/20 MSRM. Therefore, from the literature (§2.3.3, p.31), the 12/16 MSRM should produce more torque than the 12/20 MSRM during steady-state operations.

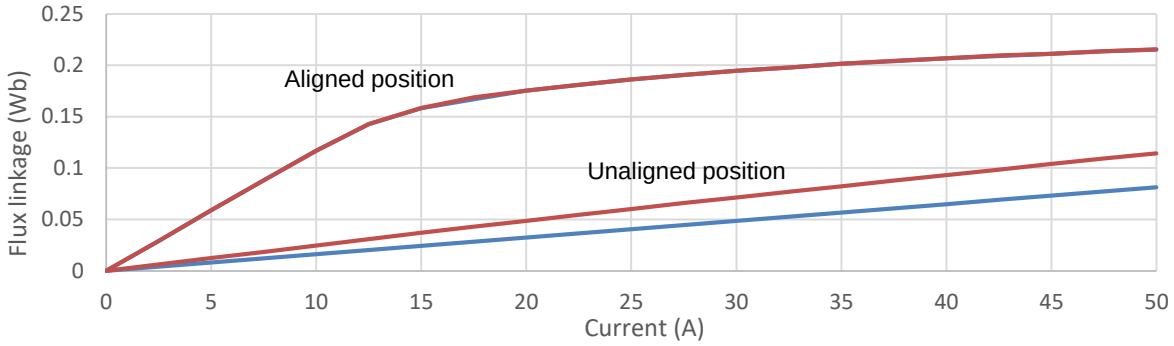

Figure 5-10: Magnetic flux linkage characteristics of the 12/16 and 12/20 MSRM

Steady-state transient solutions of 400 rpm, 550 rpm, and 750 rpm are provided in Table 5-4. Post-processed solution data from the MSRM operating at 550 rpm are shown in Figure 5-11. From Figure 5-11 it is observed that the torque waveform of the 12/20 MSRM takes longer to rise and does not stay at maximum torque as long. This was due to the phase current rising slower when operating using SPC, unlike the 12/16 MSRM operating for longer time using CCC. Note that the turn-on and turn-off angles do not occur at the same time. This is due to the different conduction angles used to operate the two configurations, as shown in the ideal inductance profile in Figure 5-9.

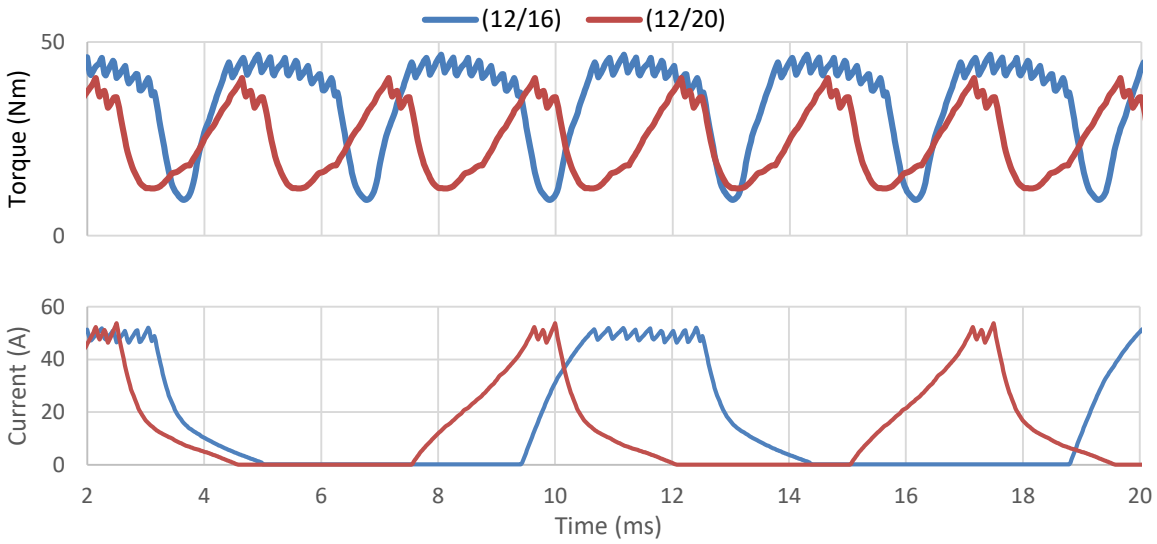

Figure 5-11: Simulated steady-state torque and phase current waveforms of the 12/16 and 12/20 MSRMs

Observing the torque waveforms, it was visually represented that the 12/20 MSRM produces less torque than the 12/16 MSRM, provided the same geometry, magnetic material and winding turns were used. Therefore, as perceived from the magnetic flux linkage characteristics in Figure 5-10,

the 12/16 MSRM configuration will provide more torque at each set speed, as summarised in Table 5-4. Provided the same DC source voltage is used, as in these simulations, the torque-speed characteristic graph of the two motors will differ.

Table 5-4: Dynamic performance of a 12/16 and 12/20 MSRM

Pole configuration	12/16	12/20	12/16	12/20	12/16	12/20
Speed	400	400	550	550	750	750
RMS phase current (A)	26.255	20.47	22.997	11.18	13.213	7.19
Average torque (Nm)	34.83	24.30	29.47	10.59	13.02	4.83

Having more rotor poles in an SRM does not provide more torque as discussed in literature (§2.3.3, p.31). From the simulations, it was seen that torque decreases for a motor with more rotor poles, provided the geometry, material and windings are kept constant. However, conclusive assessments are recommended as a future study to verify the torque production of SRM pole configuration where every design aspect is kept constant.

To improve the 12/20 MSRM and matching the torque-speed characteristics to the proposed MSRM, design iterations of the motor geometry, material, windings, and/ or motor control should be considered. These different design considerations constitute a new MSRM design from scratch, following the same design procedures shown in Figure 5-5.

5.2.1.3 Pole embrace

The pole embrace, defined in §2.3.4, p.32, ensures the requirements of self-starting, high output torque, and low torque ripple in an SRM. Therefore, the stator and rotor pole arc angles must be defined. Pole pitch was defined from the chosen pole configuration. For the chosen 12/16 MSRM, the pole pitch of the stator and rotor is 30° and 22.5°. To ensure the three requirements of self-starting, high-output torque and low torque ripple were obtained for an SRM, a feasibility triangle was used to obtained the stator and rotor pole arc angles. The feasibility triangle, shown in Figure 5-12 was constructed using equations (24), (25) and (26). Refer to p.33 for the equations.

The triangle formed from the three equations shows the possible stator and rotor pole arc angles, provided that the number of poles and phases is known. For the proposed MSRM, the pole arc angles were restricted to the overlapped feasibility triangles of a three-phase 12/16 and 12/20 SRM, as shown in Figure 5-12.

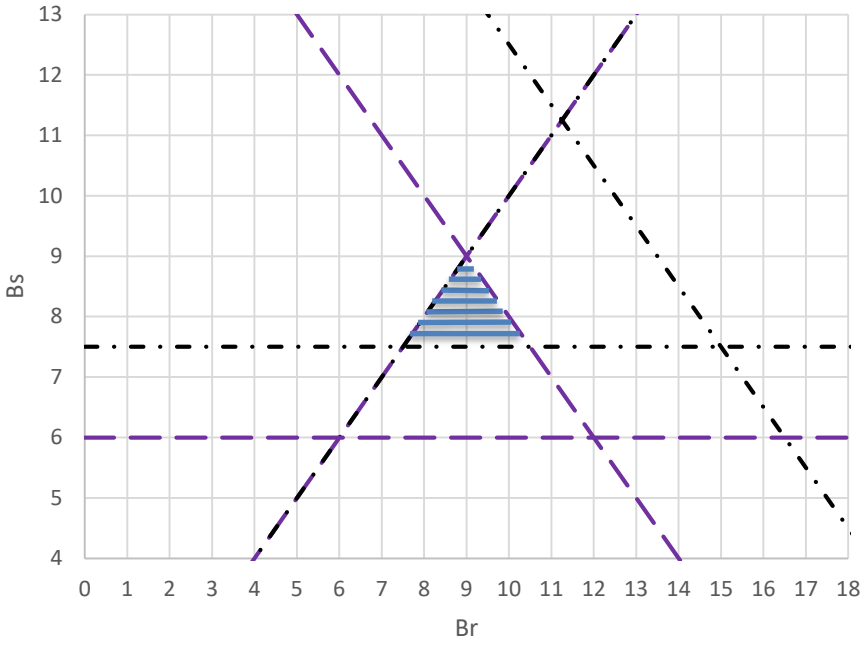

Figure 5-12: Feasibility triangle of the proposed MSRM

However, the feasible region was still quite large to decide on the correct choice of rotor pole arc and stator pole arc angles. R. Pohl suggested that the rotor arc angle should be approximately 40% of the rotor slot pitch to maximise the inductance difference between the unaligned and aligned positions [153]. For the 12/16 pole configuration, the rotor pole pitch is 22.5°, and for a 12/20 pole configuration, the rotor pole pitch is 18°. Calculating the rotor pole arc at 40% of the rotor slot pitch, the suggested pole arc angle of the respective pole configurations should be 9° and 7.2°.

Using the overlapped feasible region, 9° was available for both a 12/16 and 12/20 three-phase SRM. Anas Labak suggests that pole arc angles should be made as large as possible to maximise aligned inductance [77]. However, a wide pole arc angle restricts the available coil space on the E-core stator cores. To obtain the same MMF, the axial length of the cores was increased to fit the same number of coil turns when the same conductor gauge was used. Therefore, to keep the axial length of the stator cores at a minimum, a 9° pole arc angle was chosen. Anas Labak states that an adequate choice of an SRM design is to have both the stator and the rotor pole arc angles equal [77]. Equal pole arc angles are an effective way to extend the positive torque zone and avoid zero torque zones at the aligned position [106].

The pole arc angle sets the pole width of the proposed MSRM, such that the respective pole height and the winding space conclude the geometry of the segmented E-core stator. Thus, for

the proposed MSRM, a pole embrace of 0.4 and 0.5 was obtained for the respective 12/16 and 12/20 pole configurations.

5.2.1.4 Pole area

The E-core consists of three poles. The pole width was already defined from the pole arc angle. Thus, the remaining parameter was the pole heights. The middle pole of the E-core is twice the height of the two outer poles as shown in Figure 2-20, p.46, keeping the magnetic flux density in each pole the same. Thus, the flux linkage in the middle pole is the sum of the flux linkages in the two outer poles. The purpose of the pole height was to obtain a pole area that operates at the required flux density. The flux density in the poles was defined as the knee point of the selected magnetic material. The required flux density in the core should be obtained at rated current.

The pole heights were analysed using the magnetostatic solver. An excitation current, equal to the rated current, was applied to the windings, and the flux linkages in the core were graphically analysed. The analysis was conducted at the aligned position, as this is the position where the flux linkages in the core will be at the maximum. Note that during transient simulations, the flux linkage will be somewhat lower, as the excitation shall stop before reaching the aligned position. The graphical representation of the flux linkages in an E-core is shown in Figure 5-18.

For the analysis of the pole heights, the winding turns and conductor gauge were kept constant. Thus, by increasing the pole height, the total length of the core increased, otherwise referred to as the axial length of the core. The pole heights were started at a value of which the total length of the core was equal to 100 mm. Pole heights were increased for each simulation, although they were restricted by the total length, as per §5.1. The pole height was chosen such that the flux linkage in the pole was equal to the knee point of the magnetic material while the winding was excited with the rated current. However, the pole height was chosen as the minimum while ensuring the required flux. This ensured that the total length of the core was such that the axial length of the motor was minimal.

The minimal axial length of the motor was chosen purely to decrease motor volume and weight. It was uncertain whether an increased pole height operating at a lower flux density will provide an improved efficiency map for the proposed MSRM. Due to time constraints, a comparison between another motor with increased pole height was not accomplished in this study. Thus, analysis of pole height, with comparison to the efficiency map of the motor is recommended for future studies.

5.2.1.5 The proposed modular switched reluctance motor

The proposed MSRM consists of twelve independent modular E-shaped stator cores and sixteen I-shaped rotor cores. A single E-shaped stator and an I-shaped rotor core are shown in Figure 5-13. Two coils are wound on to each stator and connected to six other coils, as observed in Figure 5-1. The physical parameters and characteristics of the stator and rotor are summarised in Table 5-5.

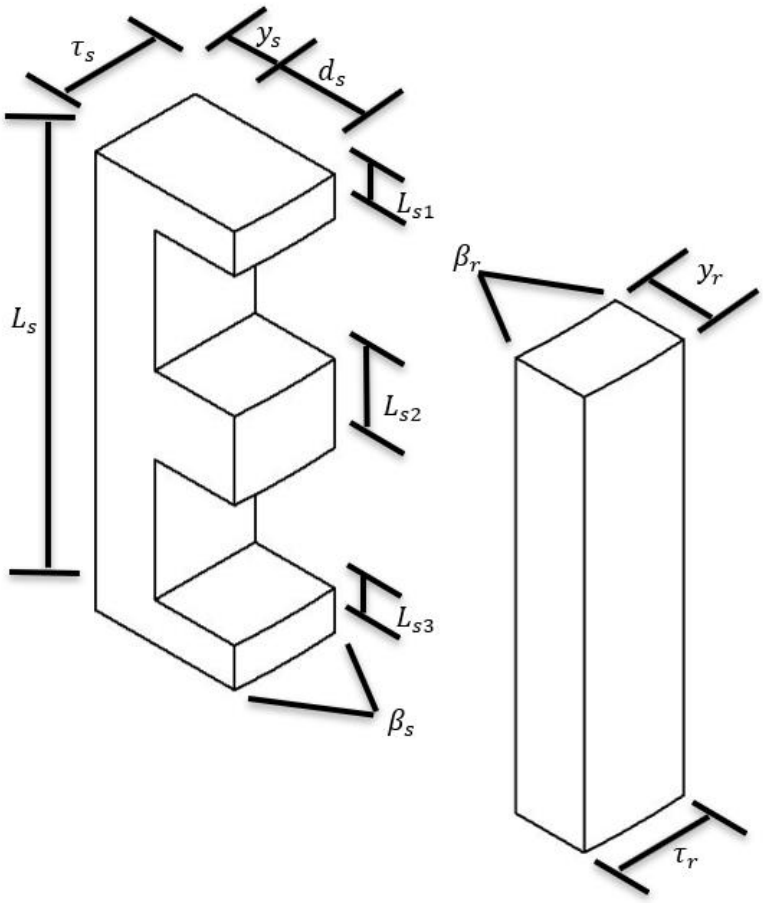

Figure 5-13: Geometry parameters of the proposed MSRM

The magnetic material of the stator and rotor is the non-oriented silicon steel M235-35A, as discussed in the next section. All the material characteristics used were provided by the material database of Ansys®. The magnetic material used to stack the stator and rotor cores is a 0.35 mm silicon steel lamination for the proposed MSRM. The ideal stacking factor of 95% is assumed and used for transient simulations based on literature (§2.3.8, p. 36).

Table 5-5: Geometry parameters of the proposed MSRM

Geometry parameters of the SRM (unit: mm)			
Stator outer radius, r_{so}	160.25	Stator pole length, d_s	20
Rotor outer radius, r_{ro}	177.5	Stator total length, L_s	110
Stator yoke width, y_s	15	Upper stator pole length, L_{s1}	12.45
Rotor yoke width, y_r	17	Middle stator pole length, L_{s2}	24.9
Stator pole arc, β_s	9˚	Lower stator pole length, L_{s3}	12.45
Rotor pole arc, β_r	9˚	Stator pole width, τ_s	25.146
Air gap length, g	0.25	Rotor pole width, τ_r	25.185

5.2.2 Magnetic material

Both the stator and rotor cores consist of the same magnetic material. Magnetic material is an important decision for electrical machine design, as reviewed in §2.3.7, p.35. For an electrical motor, the material must exhibit low hysteresis losses and high magnetic polarization properties. The standard type of magnetic material used for SRMs includes non-oriented electrical steel, which is graded according to the European standard EN 1016 [70, 154]. The shortlisted materials for the proposed MSRM, along with their magnetic properties, are listed in Table 5-6.

Table 5-6: Magnetic properties of the shortlisted magnetic material

Grade (EN10106)	Thickness (mm)	Max specific loss (mW/kg) 1.5T	H_{min} = 5000(AT/m)	H_{min} = 10000(AT/m)
M235-35A	0.35	2.35	1.6	1.7
M250-35A	0.35	2.50	1.6	1.7
M270-35A	0.35	2.70	1.6	1.7
M300-35A	0.35	3.00	1.6	1.7
M250-50A	0.5	2.50	1.6	1.7
M270-50A	0.5	2.70	1.6	1.7
M290-50A	0.5	3.00	1.6	1.7

The Powercore® and Hi-Lite range offered by ThyssenKrupp and Cogent Power (Grade EN 10303), only offer the significant benefit of lower losses around frequencies of 400 Hz. Because SRMs operate at frequencies about ten times lower than other motor types, these magnetic materials are not considered for shortlisting.

Calculating the phase switching frequency, it was noted that the frequency of 400 Hz was only exceeded at speeds of 1500 rpm and 1200 rpm, when considering a three-phase SRM of 16 or 20 rotor poles. The phase switching frequency was determined for the time it takes one rotor pole to move from one phase to an adjacent phase, provided as:

$$T_s = \frac{2\pi}{\omega_b N_{rp}} \tag{46}$$

Considering the shortlisted magnetic materials, the material with minimum lamination thickness was considered, since thinner laminations reduce eddy current losses. The magnetic material, M235-35A is chosen for the proposed MSRM. The chosen magnetic material was one of four magnetic materials of the same lamination thickness. However, the magnetic material, M235-35A, had the lowest specific loss out of the shortlisted materials, while still exhibiting properties of great tensile strength, as provided in [93, 155].

5.2.2.1 M235-35A

The magnetic material chosen for the proposed MSRM is the M235-35A of ThyssenKrupp. The B-H magnetisation curve of the magnetic material is shown in Figure 5-14. The magnetisation curve was obtained from the materials library of Ansys® Granta.

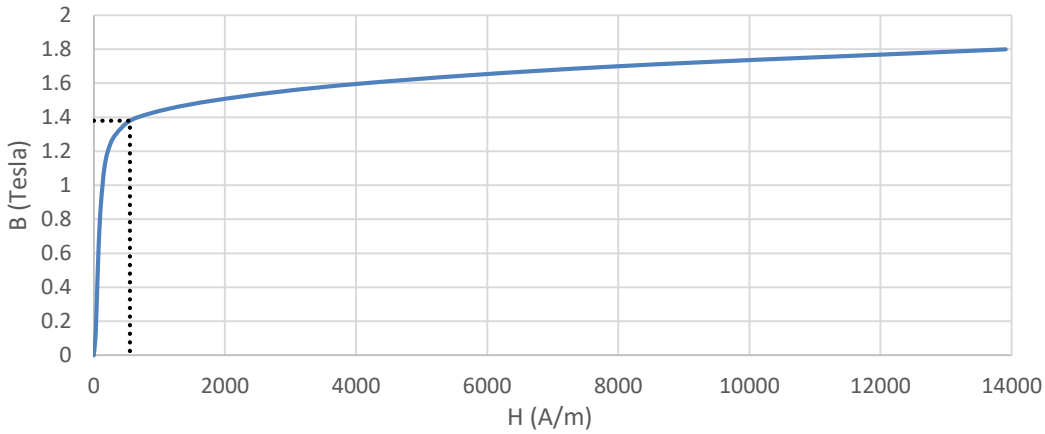

Figure 5-14: B235-35A B-H characteristics

The magnetisation curve was specifically used during the geometry design of an SRM. Motor performance depends on the maximum flux density at different parts of the motor i.e. stator and rotor yoke and poles. Note that when the flux density reaches a maximum and start to oversaturate the cores, a decrease in motor performance is expected [55]. Therefore, for an MSRM, the stator flux density, B_s is assumed to be equal to the maximum flux density, B_{max} and, therefore, operating at the knee value obtained from the B-H characteristics [53].

5.2.3 Windings

Conventional SRMs have concentrated windings around each stator pole, with each winding pair connected in series or parallel on diametrically opposite stator poles. However, as in the case of the E-core in chapter 4, the proposed MSRM has two cylindrical coils wound around a single E-core. The phase winding produces the required flux density in the air gap, owing to excitation current and result in output power of the motor. Thus, the objective of the coil design was to achieve the necessary flux density in the air gap region with minimal copper and iron losses.

The parameters of the coil design were the winding slot space, the coil dimensions, the number of winding turns, the switching frequency, the maximum permissible current density, and the thermal effect of the winding [55].

5.2.3.1 Slot space

The winding space of a coil, also known as the slot area, was defined as the rectangular cross-sectional area between two poles, as shown in Figure 5-15, with the area defined as $a * b$. The cross-sectional area of the winding was determined to enclose an area of 512 mm^2.

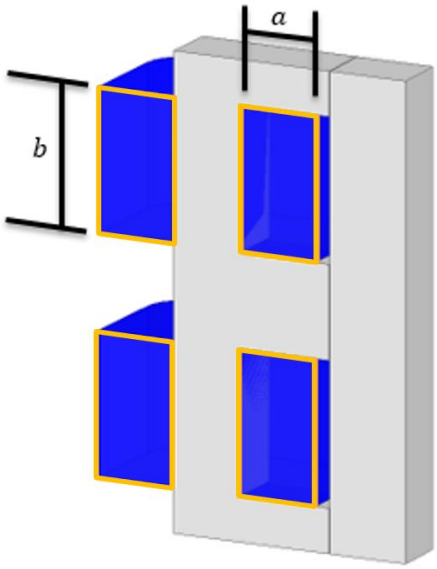

Figure 5-15: Winding slot area for a single E-core

The number of conductors that fit into the designated cross-sectional area of a winding was restricted by the fill factor (FF). For the proposed MSRM, round conductors are used instead of rectangular conductors, although more windings of rectangular conductors could fit in the given slot space. The simplest winding types are characterised by round conductors. Round conductors are also less expensive and easier to wind than rectangular conductors. Rectangular conductors

experience high mechanical stress when the conductor is bent around the corners of the stator cores. Therefore, rectangular conductors are seldom used in small or medium size SRMs.

The FF of a round conductor was derived from the ratio of a circular area to the area of a square, where the square tangentially surrounds the circle. The theoretical fill factor, when calculated, is 78.54% for a round conductor and 100% for a rectangular conductor. However, the practical fill factor for hand-wound coils was found to be as high as 40% [77]. When using specialised winding machines to wind concentrated windings, the practical fill factor is 60% [55]. Even higher fill factors can be achieved when using a pressed coil [156, 157].

5.2.3.2 Conductor gauge

In parallel design, along with defining the slot area in the section above and fitting the required number of winding turns, the conductor size should be defined. According to the current density, an important parameter in an electric motor, the conductor size should be chosen. Current density is defined as the ratio of RMS current to the bare copper area, given as:

Current density: $$J = \frac{I_{RMS\_coil}}{A_{ss} * FF} = \frac{I_{RMS\_conductor}}{A_{conductor}} \quad (47)$$

Where I_{RMS_coil} is the RMS value of the current through the coil, and $I_{RMS\_conductor}$ is the current through a single conductor when stranded wire is used. A_{ss} is the winding space, or slot area as shown in Figure 5-15 and $A_{conductor}$ the cross-sectional area of a single conductor. The cross-sectional area of a single conductor constitutes a circular area, as per the AWG size.

By design, it was chosen to accommodate the required conductors so that the current density through each coil does not exceed the maximum permissible value. Usually, a current density of 6 A/mm^2 is specified for electric motors with natural cooling [55, 158]. This current density is usually the limit of PMSMs that have the risk of demagnetisation. Therefore, no permanent magnets are employed in an SRM. Thus, higher current densities can be tolerated and the motor is mainly dependent on the thermal limits of the winding insulation [55, 77]. If the specified current density is exceeded during the design stage, either the rated current has to be minimised or the conductor gauge has to be increased.

5.2.3.3 Winding turns

The slot area, conductor gauge, and winding turns were an iterative process during the design of the proposed MSRM. Following the process, the coil was designed to obtain the rated torque at a fixed speed of 550 rpm operating under CCC. Multiple iterations were made to find the coil design that offered the required torque at a current density of 6 A/mm^2. The current density of 6

A/mm^2 was chosen as the limit of the overload torque-speed characteristics to keep copper losses at a minimum under overload conditions.

Multiple 3D FEA models of different winding numbers were simulated. For these simulations, shown in Figure 5-16, the supply voltage, the core shapes, the slot area, and the current limit were kept constant. Note that, since the slot area was kept the same, the winding numbers changed the conductor sizes and the coil resistance. Therefore, in the case of the simulations shown in Figure 5-16, a larger conductor was used when the number of windings decreased.

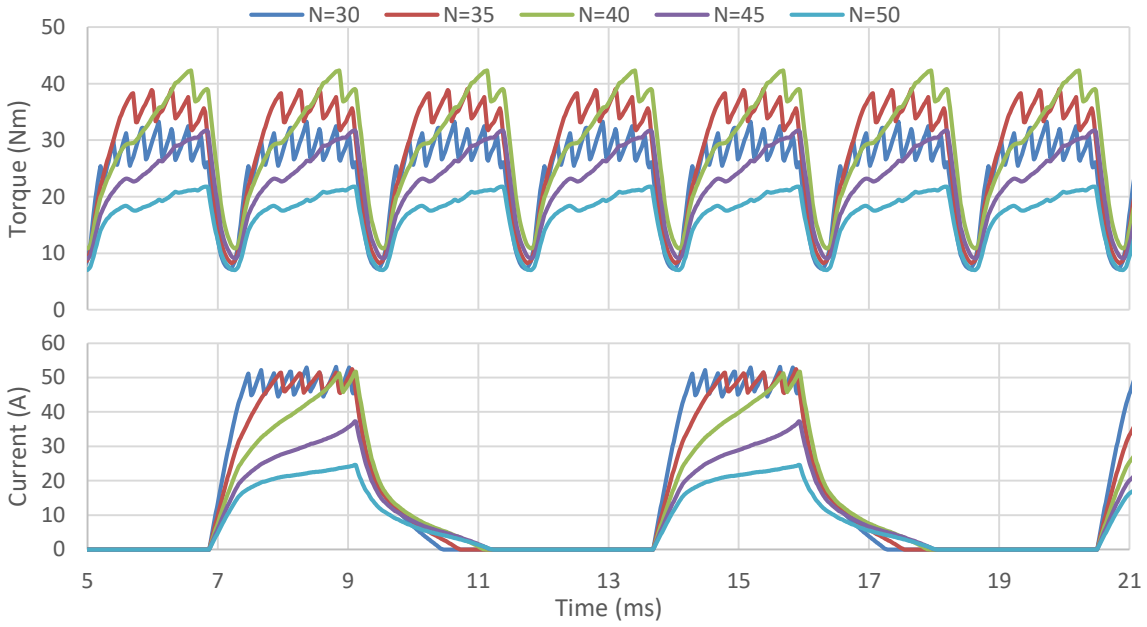

Figure 5-16: Torque and single-phase current waveforms when the number of winding turns is changed.

The coil of 40 turns was chosen for the proposed MSRM, as the torque waveform was in between the stages of constant torque and constant power operation, as observed from the torque-speed profile in Figure 5-4. Thus, for speeds lower than 550 rpm, the torque will remain constant, and for speeds above 550 rpm, the torque will decrease with the increase of speed while maintaining constant power. For a coil of 40 turns, a 10-gauge conductor seemed to be an appropriate choice for the design. For up to 2600 Hz switching frequency, it can utilise 100% of the conductor area. However, a 10-gauge conductor can be difficult to wind by hand. Alternatively, five 17-gauge conductor strands were selected for the proposed MSRM. The five stranded conductors were equivalent to the 10-gauge conductor in terms of resistance, maximum allowable ampacity, and allowed for higher switching frequencies. The five stranded 17-gauge conductors will also be easier to wind around the stator cores.

5.2.4 Thermal considerations

Thermal management is a crucial aspect of electrical machine design, as high temperature inside the motor results in higher winding resistance, and hence higher copper losses in the winding. Thermal management is also the limiting factor of overload capability. As discussed in §5.1.2, SRMs offer better overload capability than permanent magnet motors, where the thermal limits of the permanent magnet are limited by the risk of demagnetisation. The thermal limits of an SRM are limited to the winding insulation, and therefore an overload capability of 5 to 10 times the rated torque of the motor can be achieved [159]. Thus, allowing greater operational freedom under transient operations.

This section considered the thermal effects of the windings. The exact thermal behaviour of an electric motor is impossible to model due to the many variable factors of unknown loss components, airflow behaviour inside the machine and the operating cycle [160]. Various methods such as FEA and computational fluid dynamics (CFD) were proposed to model thermal behaviour. However, a certain degree of inaccuracy exists from the limitations, assumptions and boundary conditions of the modelling. Often, verification of thermal analysis by experimental testing is required to fully understand the thermal effect [160].

A thermal analysis simulation of the proposed MSRM is not within the scope of this study. Even though a complete thermal analysis was not part of the study, thermal simulations of the windings were done to ensure that the proposed MSRM operate within its temperature limits, as prescribed by the winding insulating material. These simulation results will help prove that the electromagnetic design of the MSRM can operate using the proposed conductors. The conductor considered for the proposed MSRM belongs to the thermal class of Class B, with a maximum temperature capability of 130˚C.

Thermal analysis in an electrical motor is usually accomplished by applying the rated voltage under load to ensure rated current. This ensures that the rated losses occurre continuously inside the electrical motor, and once the steady-state temperature inside the motor is reached, the measured temperature can be documented. The temperature can be measured at different locations inside the motor, most typically against the windings [77]. For an MSRM, Anas Labak used a somewhat different approach, where a continuous DC current was applied to the winding [77]. The DC current through the winding was 25% higher than the rated current. This additional amount of current was deliberately passed continuously to justify the heat that would have been generated due to iron and stray losses under transient operations [77].

A two-way steady-state thermal analysis using Ansys® Maxwell and Ansys® Fluent was used to simulate the temperature of the windings under excitation. The boundary conditions of natural convection were applied to the model with a convection film coefficient of 10 W/m^{2}K. The value of the convection film coefficient was chosen from [161], where the thermal analysis of a transformer was evaluated. The steady-state thermal analysis of the winding temperature-current curve is shown in Figure 5-17.

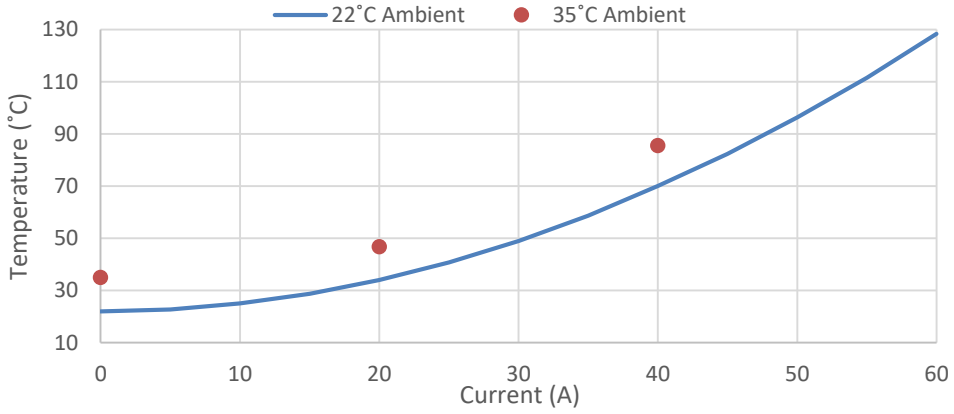

Figure 5-17: Steady-state thermal simulation

From the temperature-current curve, it was observed that an ambient temperature of 22˚C was used. This is similar to the experimental ambient temperature of the thermal analysis of an MSRM by Anas Labak [77]. Since the Sasol Solar Challenge is held in September and South Africa is known for warm weather, the ambient temperature can be much higher than 22˚C. Therefore, three steady-state temperatures of the winding were assessed when an ambient temperature of 35˚C was assumed. It is seen that the temperature-current curve maintains the same shape, though only starting from the provided ambient temperature. Thus, the current limit can be adjusted based on the ambient temperature of the location.

Assuming a winding hot spot of 20˚C higher than simulated on the outer surface of the coil, as done by Anas Labak, the maximum current at which the motor can operate safely without exceeding the thermal capacity of the winding insulation material was estimated at 55 A. Therefore, when an ambient temperature of 35˚C was expected, the motor could still operate safely at an excitation current of 45 A.

5.3 Finite element analysis

Following the design process, shown in Figure 5-5, the proposed MSRM was designed to meet the specifications set out in §5.1, p.89. The design process went through a variety of iterations to obtain the proposed MSRM, with dimensions summarised in Table 5-5. During the process, the

same numerical modelling methods, demonstrated in chapter 4 were used. This process involved the design and development of an MSRM and the analysis of its magnetostatic and transient characteristics.

As mentioned previously, validating the design by experimental testing of a prototype will be the next step. However, due to the manufacturing & financial constraints (§1.5.3, p.10), the motor was only simulated using FEA. Therefore, this section analyses the proposed MSRM using the same boundary setup, mesh setup, excitation setup, solution, and analysis setup as described in chapter 4 to provide its magnetostatic and transient characteristics. These characteristics can eventually be used for validation when a prototype is manufactured in future studies.

5.3.1 Static analysis

A 3D magnetic flux distribution of an E-core is shown in Figure 5-18a. The E-core shown is at an aligned position with an excitation of 24 A. Figure 5-18b shows an E-core at an aligned position with excitation of 40 A. It is observed that the maximum flux density at the stator poles is around 1.4 T and 1.8 T when excited. The flux at an excitation of 24 A is at the limit of the knee point value, as discussed in §5.2.2.1. An RMS current of around 23 A results in rated torque.

Note that the flux density in the stator and rotor cores will not be obtained at the aligned positions during operation. This is because the conduction angle stops the excitation at an angle before the aligned position is reached. Therefore, designing the core to operate at a flux density equal to the knee point of the magnetic material under rated current is an extremity to ensure extreme saturation does not occur during operation.

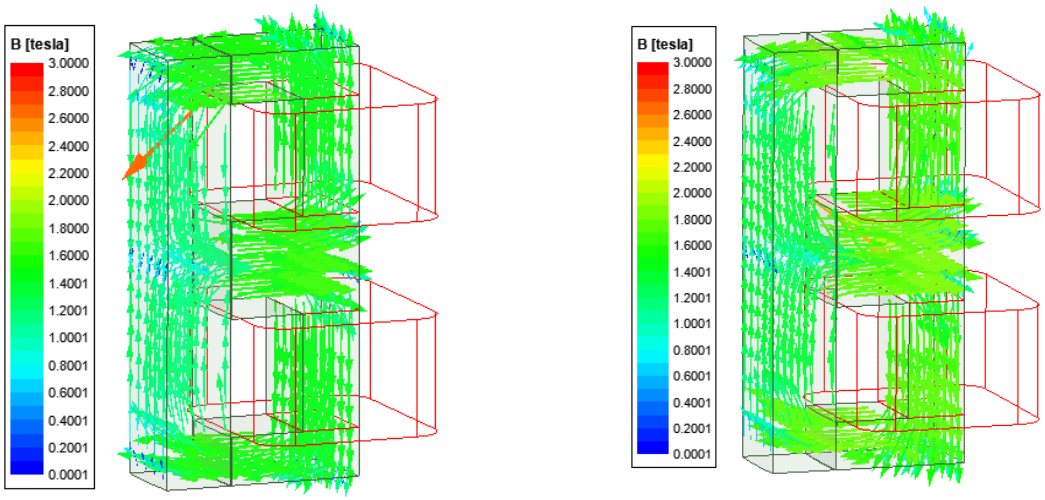

(a) *(b)*

Figure 5-18: Flux distribution in an E-core at aligned position under excitation of (a) 23 A; (b) 40 A

The flux linkage curve of a phase winding is shown in Figure 5-19a. The flux linkage is shown for both the aligned and the unaligned positions with an excitation current ranging from 0 A to 50 A, in steps of 2.5 A. The static torque of the proposed MSRM is shown in Figure 5-19b. Static torque is simulated over half an electrical period under excitation current of 10 A to 60 A, in steps of 10 A.

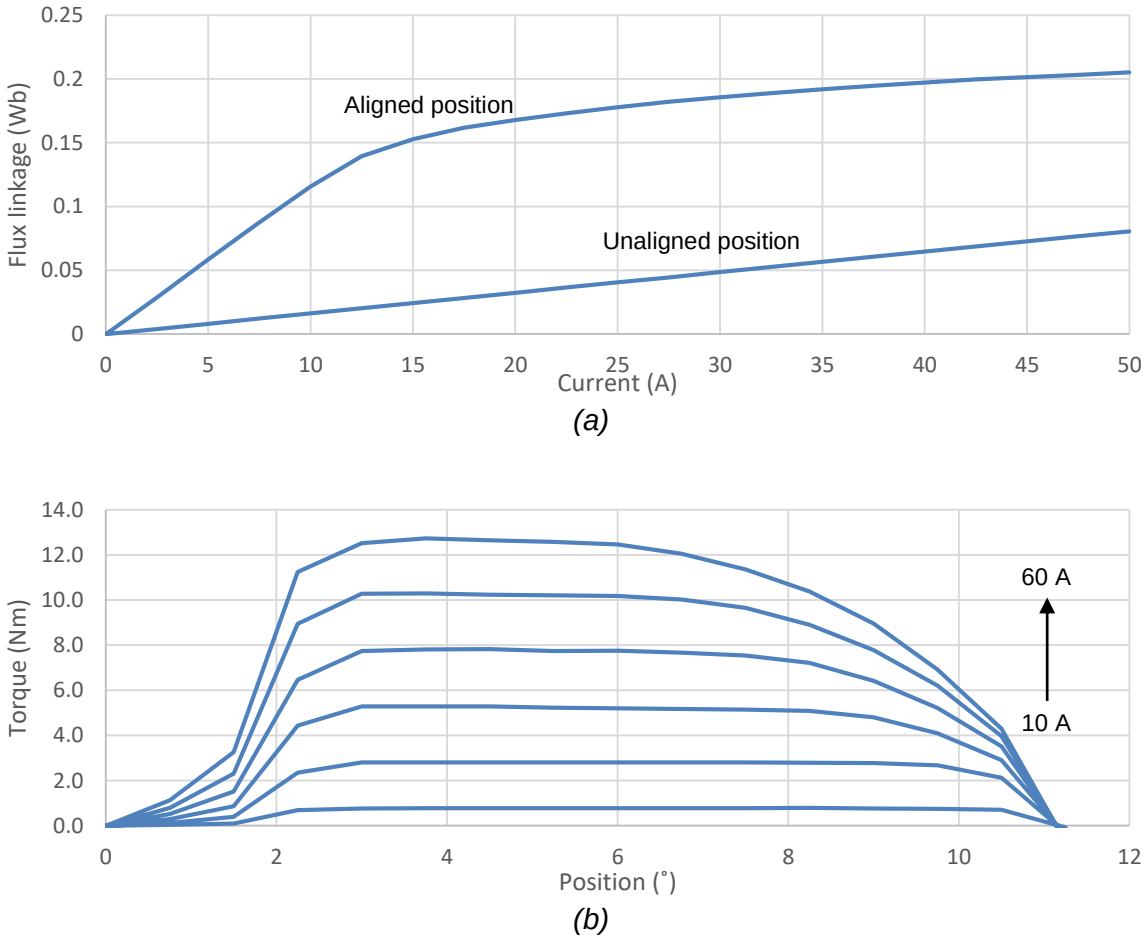

Figure 5-19: Magnetic characteristics of the proposed MSRM. (a) Flux linkage; (b) Static torque

5.3.2 Transient analysis

As stated in §5.3.1, the same setup procedure discussed in §4.4, p.76 was followed. However, a difference in the setup was where the rotary region or 'band' as it is known was considered the outer region of the motor, instead of the inner region. The difference in the band setup was due to the proposed motor consisting of an outer rotor topology and not an inner rotor topology. The MSRM validated in chapter 4 consisted of an inner rotor topology. Additionally, only the Cylindrical Gap Mesh and Clone Mesh Density were disregarded by Ansys® Maxwell during the setup of an outer rotor motor even though the same mesh setup was used as discussed in §4.4.1.3, p.78. The mesh of the proposed MSRM is shown in Appendix C, Figure C-1, p176.

The simulated steady-state torque and speed waveforms are shown in Figure 5-20. The steady-state operations shown are simulated at speeds of 400 rpm and 750 rpm. In these simulations, the DC-link voltage was 95 V and the turn-on and turn-off angles were 0° and 7.5°. Under low-speed operation, the current was restricted to 51 A, with a hysteresis band of 4 A, as shown in Figure 5-20a.

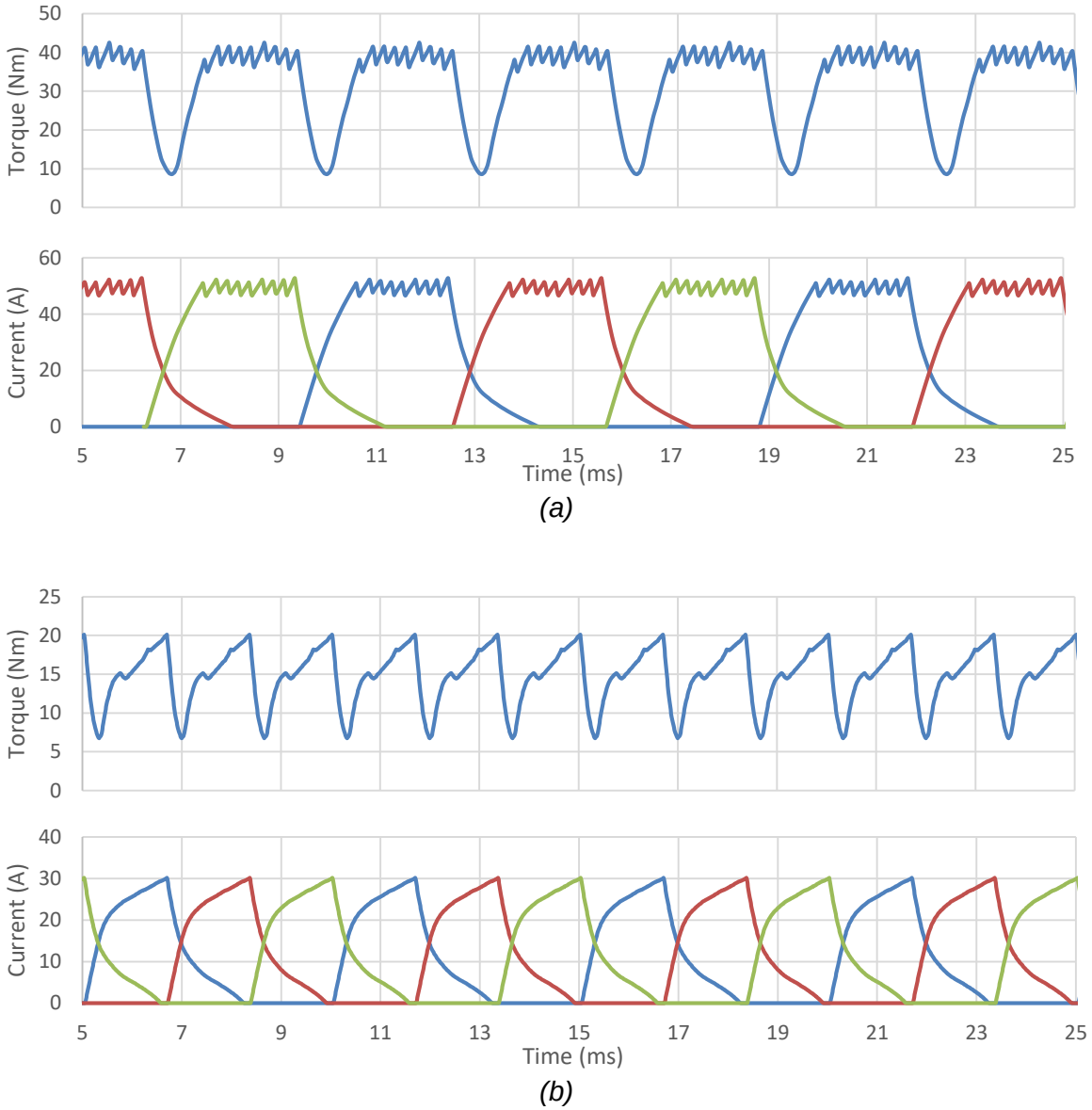

Figure 5-20: Simulated steady-state torque and phase current waveforms: (a) Current chopping control operation at 400 rpm; (b) Single pulse control operation at 750 rpm

The steady-state torque and current waveforms of 400 rpm and 750 rpm are shown, instead of the rated speed of 550 rpm. The speed of 400 rpm will be in the region of constant torque, and the 750 rpm simulation will be in the region of constant power. These speeds are chosen to

demonstrate the difference between torque and current waveforms when operating using CCC and SPC, as discussed in §2.1.3, p.22. When operating at 550 rpm, the torque and current waveform operate using both CCC and SPC. SPC will be used until the current reaches the current limit, and thereafter CCC will be used.

5.3.3 Conduction angles

Analysing the steady-state performance of the 400 rpm and 750 rpm shown in Figure 5-20, the following was observed. At 400 rpm, a torque of 32 Nm was produced resulting in mechanical output power of 1.32 kW and at 750 rpm, a torque of 14.782 Nm was produced resulting in mechanical output power of 1.16 kW. Comparing the power-speed operating points with the rated power-speed profile, shown in Figure 5-4, it is observed that constant output power was not obtained at 750 rpm. Thus, a 160 W less than the expected constant power-speed operation was obtained.

The difference in the power-speed operating point was due to the turn-on and turn-off angles as discussed in §2.1.3.2, p.23. The turn-on and turn-off angles can have a significant effect on the average torque output of an SRM, as shown in Figure 5-21. Demonstrating the effect of turn-on and turn-off angles. Two turn-on and turn-off angles were chosen to simulate. Thus, from the two turn-off angles and two turn-on angles, four conduction angles were possible, as was simulated.

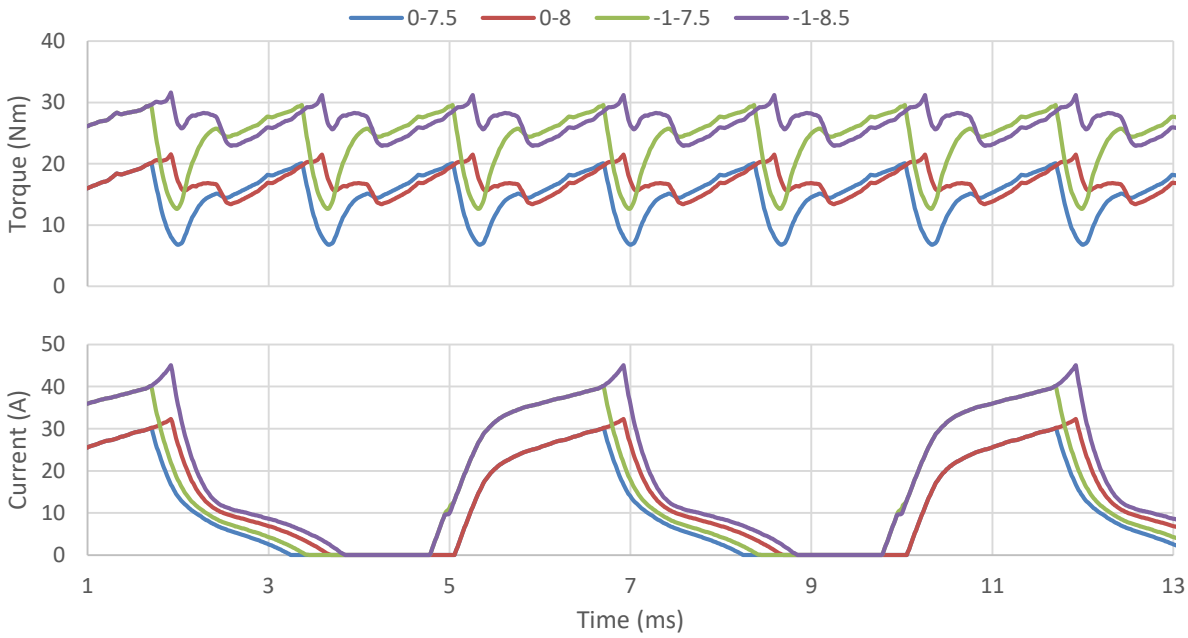

Figure 5-21: Simulated steady-state torque and phase current waveforms when changing the conduction angles at 750 rpm

Optimising the turn-on and turn-off angles form part of the motor controller. The design of the motor controller is not part of the scope of the study. Therefore, the turn-on and turn-off angles were kept constant during all steady-state simulations at all torque-speed operating points. Therefore, changing the conduction angles during the simulations shown in Figure 5-21 was merely to demonstrate the effects of the conduction angles on motor performance.

The simulated data, for the possibilities of the conduction angles were summarised in Table 5-7. From the analysis, it was seen that the combination of the turn-on and turn-off angles of -1˚ and 7.5˚ was near the specified power of the motor. The conduction angle can be optimised to obtain the mechanical output power, as per design specification. However, to achieve the specified torque-speed profile, shown in Figure 5-4, the conduction angle should be analysed at each operating speed, as the conduction angles will differ at each torque-speed operating point.

Table 5-7: Performance characteristics when changing the conduction angles at 750 rpm

Turn-on; Turn-off angles	RMS phase current (A)	Average torque (Nm)	Output power (W)
0˚; 7.5˚	14.8	14.7	1151.5
0˚; 8.5˚	16.5	16.9	1327.3
-1˚; 7.5˚	21.0	23.8	1869.2
-1˚; 8.5˚	23.2	26.6	2089.2

Note that the output power at the turn-on and turn-off angles of -1˚ and 8.5˚ produced higher output power. However, more RMS current was used for motor operation, and as a result the conduction angle combination was not necessarily more efficient.

In [117], Seubsuang Kachapornkul *et al.* studied the performance improvements of a four-phase 8/6 SRM and a three phase 6/4 SRM by adjusting the turn-on and turn-off angles in search for the turn-on and turn-off angles that provide either optimal torque or efficiency. It was found that conduction angles optimised for efficiency provided an efficiency of around 5% difference at high speeds compared to the efficiency when the turn-on and turn-off angles were optimised for torque and an efficiency difference of 10% at low speeds compared to the efficiency when the turn-on and turn-off angles were optimised for torque. For the turn-on and turn-off angles optimised for torque, it was found that the output torque of the motor was higher than the output torque obtained from the turn-on and turn-off angles optimised for efficiency. It was noted that the operating comparisons were made at fixed motor speed, but not at the same torque. Thus, this will have an influence of the torque-speed characteristic graph, rated motor parameters and the efficiency map. Therefore, a motor controller should be designed for either efficiency or torque, based on

the application the motor will be used in [1]. It is recommended that future studies design a motor controller for the proposed MSRM to maximize efficiency for the full operating range. This motor design will indicate the efficiency improvement the conduction angles have on the motor performance when comparing the same operating point, i.e., equal speed and torque.

5.4 Performance characteristics

Using the transient simulations, at different steady-state speeds, the performance characteristics of the proposed MSRM were obtained. The performance characteristics observed were the predicted torque-speed characteristics of the proposed MSRM and the efficiency map of the MSRM. The efficiency map provides efficiency at the full operating range of the motor. The efficiency map in this study was necessary to evaluate the proposed MSRM. The evaluation of the proposed MSRM is provided in §6.3.2, p.141.

The proposed MSRM ratings were obtained by multiple 3D FEA simulations, summarised in Table 5-8. The resistance of a phase winding was calculated as the resistance depends on the conductor length and gauge. The predicted torque-speed characteristics of the proposed MSRM are provided in the following section.

Table 5-8: Ratings of the proposed MSRM

The calculated phase winding resistance (Ω)	0.156288
DC-link voltage (V)	95
Rated current (A)	≈ 23.7
Rated torque (Nm)	≈ 32
Rated speed (rpm)	≈ 550
Rated power (kW)	≈1.84

From Table 5-8, it is seen that the specified power, summarised in Table 5-2, p95 was obtained for the proposed MSRM. However, this was only the rated torque-speed performance and not a full indication of the performance. Further performance evaluation is provided in the following sections.

5.4.1 Torque-speed characteristics

Observing the torque-speed characteristics of the proposed MSRM, multiple simulations were run. Each simulation was a steady-state analysis, simulated at different speeds. Once completed, the data of each simulation were analysed and tabulated to construct the torque-speed profile. The torque-speed profile, constructed from multiple FEA simulations, is shown in Figure 5-22. The torque-speed curve of the FEA simulation was compared with the design-specified torque-speed characteristic profile.

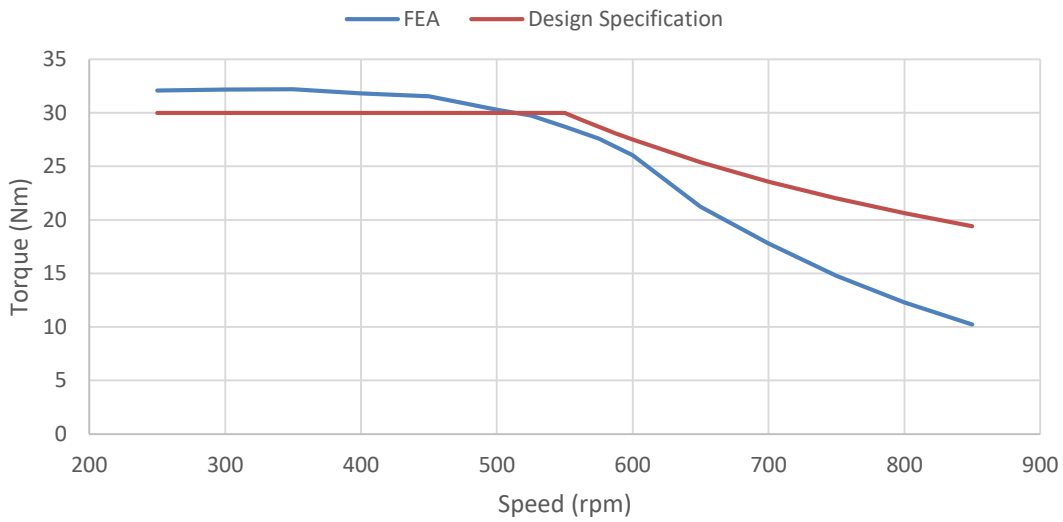

Figure 5-22: Torque-speed characteristics of the proposed MSRM

In Figure 5-22, it is observed that the torque drops rapidly beyond 550 rpm. As mentioned in §5.3.3, the simulations were conducted at constant conduction angles. Therefore, the constant power region was not obtained, but rather a falling power region, as reviewed in §2.1.3.1, p.22. For a constant power region beyond 550 rpm, the conduction angles should be suitably selected. For improved performance or efficiency, the conduction angles should be optimised.

5.4.2 Efficiency map

The efficiency map of the proposed MSRM is shown in Figure 5-23. The efficiency map was constructed from various torque-speed profiled simulations (Appendix C.3, Figure C-4, p.179). The torque-speed profiles under the rated torque-speed characteristics were simulated by employing lower source voltages and current limits. Similarly, the overload region was simulated by employing higher source voltages and current limits.

From each torque-speed profile, the output power is known at each operating point. For the same simulation, the phase voltage and phase current curves is provided by Ansys® Maxwell. Using

equation (56), p.140, the input power of each phase is calculated for each operating point that was simulated. When multiplying the input power of a single phase by three, the total input power of the motor is obtained. Thus, knowing the input power and output power at each torque-speed operating point of the simulation, an efficiency curve can be constructed. Between these efficiency curves, interpolation on the x-axis to the z-axis and on the y-axis to the z-axis was done to obtain data points in between the curves for construction of an efficiency map. The axis of the efficiency map is as follow: the x-axis represents the speed, the y-axis represents the torque, and the z-axis represents the efficiency. Using Matlab, the data of the x-axis, y-axis and z-axis are plotted using a contour plot in order visualise the 3D data using a 2D plot as shown in Figure 5-23.

The efficiency map was provided to the extent of the overload torque-speed characteristics. The rated torque-speed characteristics were provided in the efficiency plot, shown by the black striped line and the operating points of the Mitsuba M2096-DII were plotted on the efficiency map, shown by the white dots. The expected contour line with the highest efficiency in the motor is provided by the yellow curved line. This contour line was drawn based on visual representation of the efficiency contours found for an SRM in literature (Figure 2-21, p.47). The contour lines for efficiency of the proposed MSRM differ from the yellow contour line. However, the difference may be the result of an efficiency map contour of an MSRM compared to an efficiency map contour of a conventional SRM. It is uncertain what efficiency map contour can be expected from an MSRM, as no efficiency maps for an MSRM was found in literature. Thus, further studies are proposed to analyse the difference of an efficiency map between a conventional SRM and MSRM.

The construction of the efficiency map required the analysing of steady-state simulations, interpolating the data, and constructing an efficiency map as shown in Figure 5-23. However, Ansys® Maxwell offered a machine toolkit to automatically generate an efficiency map of the analysed motor. The machine toolkit will automatically simulate each operating point at the highest efficiency or torque operation, depending on how the machine toolkit is set up. Unfortunately, using the machine toolkit for SRMs was not yet functional with the release of Maxwell 2021R1 and Maxwell 2021R2.

It was unknown when the machine toolkit of an SRM will be functional. The toolkit will provide an easy and time-saving method to construct an efficiency map. Note that the elapsed simulation time of each steady-state simulation took around 3 to 8 hours. Thus, constructing an efficiency map for the proposed MSRM took a considerable amount of time. When the functionality of the machine toolkit supports an SRM, it is proposed to construct an efficiency map of the proposed MSRM and compare the result with the efficiency map constructed, shown in Figure 5-23 and, if possible, an efficiency map constructed from experimental data.

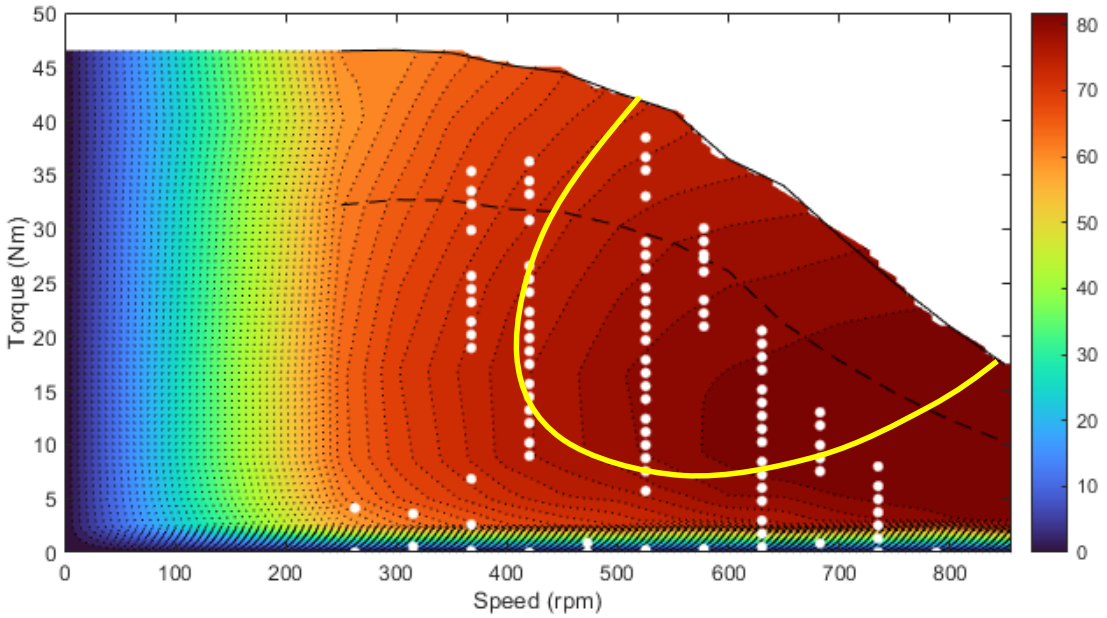

Figure 5-23: The constructed efficiency map of the proposed MSRM

To increase the motor efficiency of the proposed MSRM, a motor controller with optimised conduction angles for efficiency was proposed. However, a few mechanical design changes can also be considered. The first consideration is to design a 12/8 MSRM or 12/20 MSRM for the same torque-speed characteristics. Thereafter the efficiency map should be analysed to evaluate the effect of the pole configurations on the motor efficiency and operation.

Other mechanical considerations are to optimise the pole embrace, pole area, and winding design. Optimising the pole area will influence the effect of flux density during operation, and altering the core to an extent could decrease flux leakage between the stator and rotor poles. Minimising flux leakage will provide higher torque for the same current excitation. The winding design is included as an optimisation parameter such that a parallel connection for a design could potentially offer increased efficiency. However, various winding designs, including conductor types, should be analysed in future studies.

5.5 Summary of the motor design

A 12/16 E-core MSRM, rated at 1.84 kW was designed following the principles of Vanessa Siqueira De Castro Teixeira *et al.* [51], Nikunj R Patel *et al.* [75, 106, 74, 53], and Anas Labak [52, 57]. Power specifications were obtained by analysis of the Mitsuba M2096-DII evaluation results followed by the geometric design. The geometric design followed an iterative process, shown in Figure 5-5, p.96 to obtain the geometric parameters of an E-core with a corresponding winding design. The core, limited by geometric constraints, was designed to operate at the knee

point of the B-H characteristics of the chosen magnetic material. This was to ensure that the MSRM operates in a saturated region, although not oversaturated.

The winding design ensured that the motor operated at the required current density. The selection of the conductor gauge was made in conjunction with the geometry design. This was because the winding space, winding turns, and fill factor were each a variable of the winding design. Although the winding was designed to operate at a specified current density under rated current, thermal analysis was provided to ensure the motor operate at respectable thermal conditions.

Thermal analysis of a coil winding provided the maximum current that the coils can operate at while operating within the thermal limits of the magnetic material insulation. Operating within the thermal limits of the magnetic material ensured that the motor was not damaged while under strenuous operating conditions.

After the core and winding design, the proposed MSRM was analysed. A range of transient simulation data was used to construct an efficiency map of the proposed MSRM. The constructed efficiency map was used to evaluate the proposed MSRM in a technique identical to the Mitsuba M2096-DII. Evaluation of the proposed MSRM is provided in chapter 6.

When a prototype of the proposed MSRM is manufactured, the modular rotor segments, of rectangular shape, can be inserted into a cylinder of low magnetic permeability material. Similar materials can be used to house the stator cores in a single structure. However, the design of a motor housing would involve a comprehensive stress analysis and would most likely be coupled with a thermal and vibration analysis to ensure a complete design of the MSRM. During the electromagnetic design of an MSRM, many design aspects were ignored that include the assessment of acoustic noise levels, vibrations, bearing selections, housing design, and dynamic thermal analysis. These aspects were ignored as they extend the scope of the study, and require experience in different engineering field, i.e., aerodynamic flow analysis, thermal analysis, stress and vibration analysis, material selections and electronic design. All of these engineering fields need to be integrated to one motor design for complete finalisation. The aspects of acoustic noise levels, vibrations, bearing selections, housing design, and dynamic thermal analysis are proposed for future studies, and thereafter integrating the studies with one another to form a complete motor analysis that can be built.

CHAPTER 6 EVALUATION OF A TRACTION MOTOR

In accordance with the objective of this study, this chapter focuses on the evaluation of a traction motor for solar vehicle application. This chapter discusses a simplified drive cycle where the efficiency map of a traction motor is used to analytically propel a solar vehicle through the drive cycle using only the energy extracted from the sun. When comparing the driving distance achieved by one traction motor with another, the most efficient motor is established, provided the same variable factors are used, i.e., the weather effects, time of year, route, and road surfaces.

The chapter provides the evaluation of the Mitsuba M2096-DII, currently used as the traction motor in the solar vehicle of the NWU. The evaluation of the Mitsuba M2096-DII was used as a comparative baseline for the proposed MSRM and to stipulate the power specifications for the proposed MSRM (§5.1, p.89). Subsequently, the proposed MSRM was evaluated along the same drive cycle and input parameters as the Mitsuba M2096-DII. This chapter concludes the assessment of whether the proposed MSRM is a viable contender for solar vehicle applications.

6.1 Drive cycle as a method of evaluation

The performance of a vehicle is evaluated by performing a dyno test for various driving cycles during its development phase. The drive cycle allows the development and comparison of fuel economy, emissions, and estimated driving ranges for ICE vehicles. Similarly, the expected driving distance and energy consumption of a traction motor can be evaluated.

A driving cycle is classified as a model driving cycle or as a transient driving cycle [162, 163]. A model driving cycle consists of constant speed operation and does not represent an actual driving pattern. The model driving cycle is mainly used for specific applications, i.e., an emission test. The transient driving cycle represents an actual driving pattern that includes acceleration, deceleration, and constant speed operations. However, a significant difference between real-world applications and a transient driving cycle can still be expected.

Different driving patterns can be used in a transient driving cycle. Driving patterns are based on both city and highway driving. Common driving cycles used by automotive manufacturers include the Federal Test Procedure-72 (FTP-72), the New European Driving Cycle (NEDC), the Highway Fuel Economy Test (HWFET) and the Indian Driving Cycle (IDC) [163, 164].

In this study, a numerically simulated drive cycle is used to evaluate a traction motor for solar vehicle application. This chapter compiles the drive cycle and evaluate both the Mitsuba M2096-DII BLDC motor and the proposed MSRM for comparison against each other. Comparing these

traction motors would support the justification that the solar vehicle could benefit from using an SRM as the traction motor.

6.1.1 Construction of a drive cycle

The purpose of the Sasol Solar Challenge is to maximise the driving distance each day using only the energy extracted from the sun to charge the batteries. The team acquiring the furthest distance at the end of the 7 days is the winner of the Sasol Solar Challenge. Thus, having a traction motor that provides the best performance whilst using the least amount of energy would be beneficial for a team in these types of solar races.

Evaluating a traction motor in a drive cycle that represents the Sasol Solar Challenge, should provide an expected driving distance and energy usage. This evaluation method would significantly support the decision on which traction motor to use in the Sasol Solar Challenge. Preferably, the numerical drive cycle simulation to evaluate a traction motor should include all vehicle dynamics, weather conditions, the solar position with respect to the vehicle location, and the precise energy usage of the traction motor. Incorporating all these factors into the evaluation would accurately predict the overall distance the traction motor could reach. However, it is difficult to include all these influencing factors, and thus a simplified approach has been proposed to evaluate a traction motor. When all influencing factors are held constant between the evaluation of the different traction motors, the best traction motor can be determined.

In this section, the simplified approach of a drive cycle is constructed. The drive cycle is constructed in three sections and was interactively simulated to evaluate a traction motor for solar vehicle application. These sections consist of the following.

1. The output power required from the traction motor to propel the vehicle at a certain speed and road gradient.
2. The input power that is necessary to achieve the output power. This is the power used by the electric motor to achieve the mechanical output power.
3. The power availability during the drive cycle. This is the power extracted by the PV array.

The three sections are used interactively to evaluate a traction motor. The procedure to evaluate a traction motor is described in §6.1.2, p134.

6.1.1.1 Output power

The power used to propel the solar vehicle is known as the output power or often referred to as the mechanical output power of an electrical motor. The mechanical output power of an electric motor is the product of torque and rotational speed.

In the construction of the drive cycle, the mechanical output power required from the traction motor was obtained from a route profile and vehicle dynamic equations. The pre-defined and simplified route profile is shown in Figure 6-1, along with the route gradient at route sections.

The route chosen for the drive cycle is the R53, between Potchefstroom and Parys. The route is 47.5 km long and data at each 450 m route interval were obtained. The route data include the route altitude and the average route gradient of each section. The pre-defined route data provided in 450 m sections were obtained from plotaroute.com [165]. A simplified route of the drive cycle was created by placing the route sections in order of ascending road gradient. Thus, starting at the highest altitude of the pre-defined route, the lowest gradient is used to determine the altitude at the end of the first route section. Thereafter, the altitude for the next route section using the next road gradient is calculated and so forth.. The pre-defined route profile, simplified route profile and route gradients are shown in Figure 6-1. The route profiles show the route altitude (height above sea level). However, the altitude had no effect on the drive cycle and was only a representative of the route using the route gradient of each section.

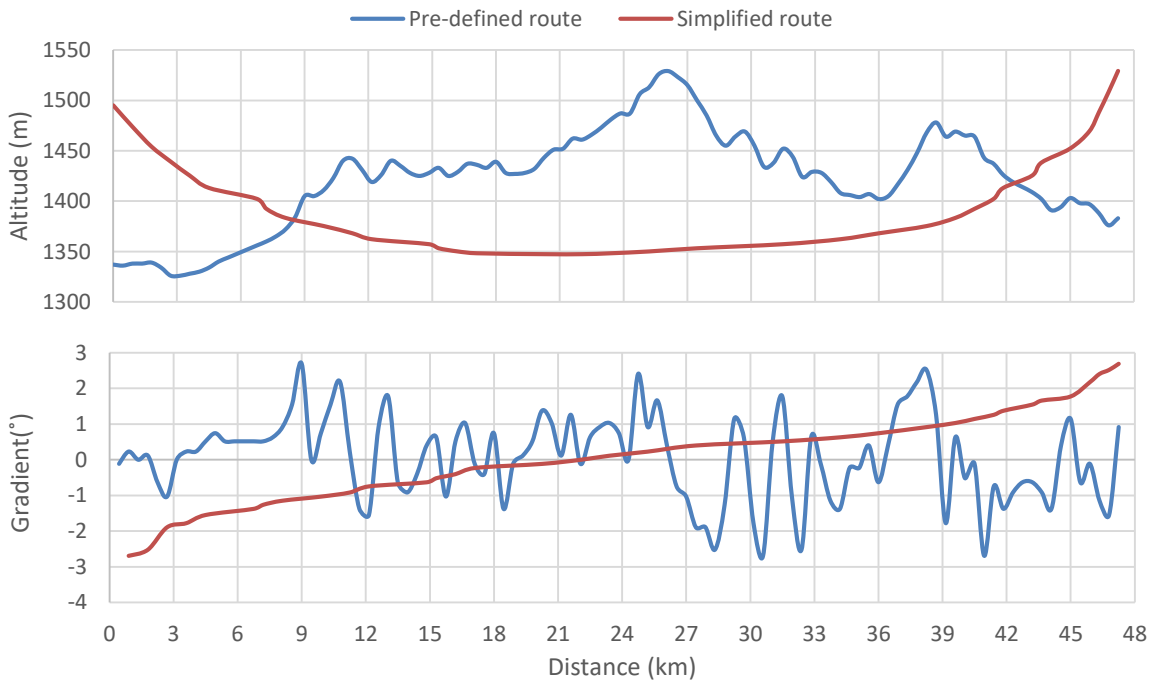

Figure 6-1: The pre-defined and simplified route profile and route gradient

The pre-defined route is typically used to evaluate a traction motor to evaluate the energy usage of the traction motor. However, the simplified route was used to demonstrate the use of a drive cycle when evaluating two or more traction motors. Even though an accurate travelling distance will not be obtained when comparing the travelling distance to experimental test data, the simplified route provides direct comparison between two traction motors. Therefore, to accurately determine the travelling distance a traction motor can propel the solar vehicle, which can also help to predict race strategies in solar races, a comprehensive drive cycle through the pre-defined route, including all external factors that have an effect on vehicle characteristics and power usage should be considered. Thus, a comprehensive drive cycle to predict race strategy for the solar vehicle is proposed as a future study.

To demonstrate the drive cycle when comparing the proposed MSRM to the Mitsuba M2096-DII, the following assumptions are made for the simplified route.

- The surface of the road is the same throughout the route. This means that water, gravel, potholes, or road friction do not play a role during the evaluation.
- The route connected as a loop is considered an oval. The oval does not have excessive road curvatures that require deceleration and acceleration. Thus, the route is almost a straight path.
- The use of momentum to climb a hill is excluded from the drive cycle.
- By law, the maximum speed of the pre-defined route is 100 km/h. The Mitsuba M2096-DII can reach a top speed of 65 km/h on level road, thus the maximum speed allowed for the drive cycle is chosen as 75 km/h for downhill sections.

Using vehicle dynamic equations, the mechanical output power required from the traction motor can be calculated at a specified velocity and route gradient. Vehicle dynamics is based on the direct application of Newton's second law for longitudinal dynamics of a vehicle, as shown in Figure 6-2.

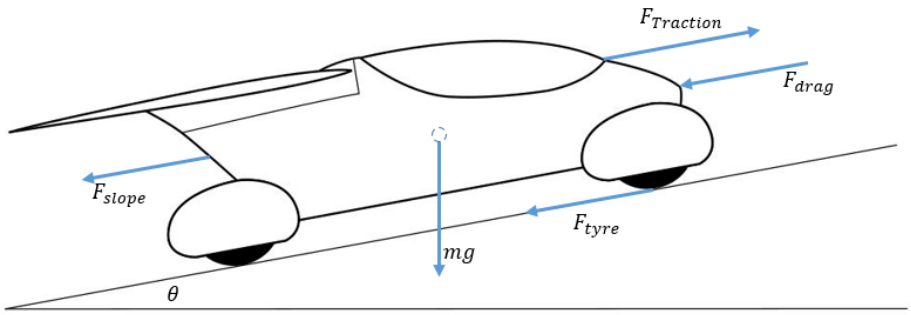

Figure 6-2: Free body diagram of the longitudinal forces acting on the vehicle

The principle of the force balance is presented in equation (48). The traction force, $F_{Traction}$, generated by the traction motor must overcome the sum of all resistive forces acting on the vehicle: aerodynamic drag, F_{drag}; slope force, F_{slope} (a component of the vehicle weight), and the friction force of the tyres, F_{tyre} [166, 167]. Finally, the traction force can be represented by the torque production of the traction motor, τ. Torque is the product of traction force and the radius of the wheel, provided in equation (52).

Force balance: $$F_{Traction} = F_{drag} + F_{tyre} + F_{slope} \quad (48)$$

Aerodynamic drag force: $$F_{drag} = \frac{1}{2} C_d \rho A v^2 \quad (49)$$

Where C_d is the aerodynamic drag coefficient, ρ is the density of air (kg/m^3), A is the frontal area of the vehicle (m^2) and v is the speed of the vehicle (m/s).

Slope force: $$F_{slope} = M g_a \sin\theta_s \quad (50)$$

Where M is the mass of the vehicle including the driver (kg), g_a is gravitational acceleration (m/s^2) and θ_s is the angle of the driving surface (°).

Tyre friction force: $$F_{tyre} = M g_a (0.005 + (\frac{1}{b})(0.01 + 0.0095 \left(\frac{3.6v}{100}\right)^2) \quad (51)$$

Where b is the tyre pressure (bar), u is the vehicle's speed (km/h).

Traction force: $$F_{Traction} = \frac{\tau}{r} \quad (52)$$

Where τ is the motor torque (Nm) and r is the radius of the wheel (m).

The solar vehicle evaluated in the drive cycle was the 2020 solar vehicle of the NWU. The main parameters, obtained from the program manager of the NWU solar vehicle are summarised in Table 6-1. The vehicle and driver mass and tyre diameter was measured in the laboratory. The aerodynamic drag coefficient and vehicle frontal area was calculated by several lecturers and students using CFD.

Table 6-1: Solar vehicle characteristics

Description	Symbol	Value
A vehicle with driver mass (kg)	M	245
Aerodynamic drag coefficient	C_d	0.156
Air density (kg/m^3)	ρ	1.225
Vehicle frontal area (m^2)	A	1.2831
Tyre Pressure (bar)	b	5
Tyre diameter (m)	r	0.505

When evaluating a traction motor using the drive cycle, the following assumptions are made for the vehicle dynamics:

- External wind forces acting on the vehicle are excluded from the drive cycle. Wind from the front or rear of the car will affect the energy usage as the vehicle requires either more or less torque to maintain a similar speed.
- The acceleration force, $F_a = Ma$, where a is the acceleration, is considered zero when calculating the force balance. For the drive cycle, a constant speed is assumed for each section of the route.

6.1.1.2 Input power

Evaluating a traction motor's energy usage in the drive cycle requires the input power to be known. The input power is defined by the summation of output power, friction and windage, copper and iron losses. However, achieving the same amount of output power by variation of speed and torque will not use the same amount of input power, thus losses is the difference between the input and output power at each operating point. The efficiency, n, of an electric motor is defined as the ratio between the output power, P_{out}, and the input power, P_{in}, with input power further divided into the sum of output power, friction and windage losses, P_{f+w}, copper losses, P_{cu}, and iron losses, P_{Fe}.

Efficiency:
$$n = \frac{P_{out}}{P_{in}} = \frac{P_{out}}{P_{out} + P_{f+w} + P_{cu} + P_{Fe}} \quad (53)$$

Identifying the input power of each operating point requires an efficiency map. An efficiency map is a contour plot of motor efficiency that indicates motor efficiency in the operating range of speed and torque of the motor. Therefore, at the required output power of each route section at a set rotational speed, the efficiency map is used to obtain the input power [168]. The input power is

the amount of power used to propel the vehicle and, therefore, in the case of a solar vehicle, extracted from the batteries.

The traction motor of the solar vehicles used in these solar races provides power in the range of 1 to 2 kW. To put this into perspective, it is almost the same amount of power as offered from by a hairdryer or kitchen kettle. Although these solar races provide a unique opportunity to showcase new technological ideas and creations, only two companies (Marand and Mitsuba) provide electric motors intended for solar racing events. Both these companies provide a BLDC motor for solar vehicles.

6.1.1.3 Available power

Per the definition of a solar vehicle, solar power is used to propel the vehicle. The energy extracted by the PV array during a solar race is stored in the batteries and the traction motor use the energy in the battery to propel the vehicle. The amount of solar power differs depending on the time of day, month, and latitudinal location. Solar energy is referred to as the available energy in the drive cycle. To save energy, solar racing teams attempt to drive ‘energy neutral’. The term ‘energy neutral’ is defined as using the same amount of energy to propel the vehicle as obtained from the PV array. Thus, no battery energy is used to propel the vehicle.

For this drive cycle comparison, it is assumed that the vehicle starts with an empty battery, and the energy extracted from the sun is stored in the battery for use, respectively, by the traction motor. This is different from the driving principle used in solar races where a vehicle will typically start the race on a fully charged battery. When the drive cycle is started on a full battery, the driving distance can be improved as there is more available energy to use for the drive cycle. However, depending on the solar race, a team will drive conservative depending on the weather.

The solar energy is extracted by the PV array obtained from the solar irradiance. Solar irradiance is based on the solar path observed throughout the year. In Figure 6-3, the solar path of Potchefstroom (lat. 26.7˚S, long. 27.1˚E, alt. 1351 m) is shown [169]. The two astronomical angles describe the solar position with respect to an observer. The solar altitude and solar azimuth are represented by circles and the cardinal directions. As observed in Figure 6-3, the solid yellow lines represent the June and December solstice. The red line represents the solar path on the 14th of September. The date is chosen as the Sasol Solar Challenge usually occurs within that period of the year.

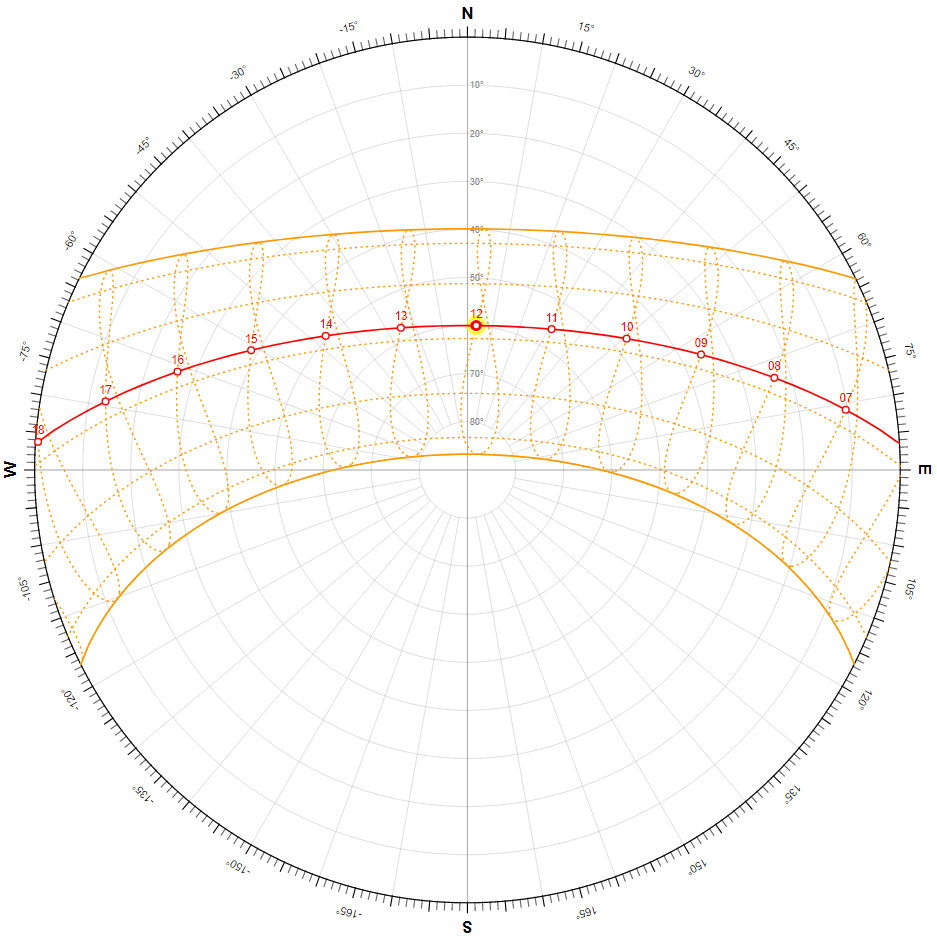

Figure 6-3: Solar path and position at Potchefstroom [169]

The extraction of solar energy is performed by a PV array on the solar vehicle. In the case of the NWU, the solar vehicle employs a single-axis rotating PV array. The rotation of the PV array allows for more energy extraction than a fixed PV array, due to the rotation improving the angle of the PV surface to the sun. The PV characteristics of the PV array used on the solar vehicle are listed in Table 6-2.

Table 6-2: Solar vehicle PV array characteristics

Description	Value
PV area (m^2)	4
PV cell efficiency (%)	24.3

To calculate the amount of energy extraction by the PV panels during the drive cycle, the following assumptions are made to simplify the setup and process:

- Solar radiation is assumed for an ideal sunshine day. Thus, no weather effect or shadows influences the energy extraction of the PV array.
- The angle of the PV surface to the sun is assumed to be a constant 80˚ during the drive cycle. Due to having only a single-axis tracking device, the PV cannot be maintained at a perpendicular angle to the sun. This is because the solar vehicle changes direction relative to the sun's angle during travel, i.e. not travelling in a north-south direction. The World Solar Challenge in Adelaide is a perfect example of how a single-axis tracking device on a vehicle can be fully exploited. This is because the solar vehicles travel in an almost constant north-to-south direction.
- The irradiance graph of a single location is assumed usable for the drive cycle as a minimal longitudinal difference between Potchefstroom and Parys exists. This allows the drive cycle over time to only consider one irradiance graph when calculating the available energy from the sun at each time period. If a longer route is chosen, different solar irradiance graphs at each time period should be used to achieve a representable drive cycle.

The energy extracted from the PV array is calculated using the solar radiance and a solar tracking PV array at the location of Potchefstroom. The tracking device is similar to a single-axis rotating PV array. Thus, a perpendicular angle between the surface of the PV array and solar irradiance could be maintained, which is known as direct radiation. As mentioned in the assumptions above, the PV array surface to the solar irradiance angle will be constant at 80˚. However, an hour before the drive cycle starts, a perpendicular angle is maintained to extract energy from the sun. This is done to have energy available at the start of the drive cycle. A perpendicular angle is used for that hour, since the vehicle can be placed at an optimum angle to accumulate solar energy an hour before the start of each day's drive in the Sasol Solar Challenge. Then the drive begins. Therefore, the simulated drive cycle is operational from 08H00 to 16H00.

Figure 6-4 shows the available solar radiation on a PV array with a 1 m^2 (red line) and 4 m^2 (blue line) area where direct radiation is maintained. The purple line indicates the extractable energy on a 4 m^2 PV array when the PV efficiency of 24.3% is included. Thus, the less than the available radiation from the sun on a 1 m^2 PV array is extracted from a 4 m^2 PV array. The extracted soar energy from radiation on the PV array of the vehicle is shown by the green line, where the maximum radiation is maintained for the charging time and thereafter the PV array is extracting energy from the sun at an 80˚ angle between the PV surface and the sun.

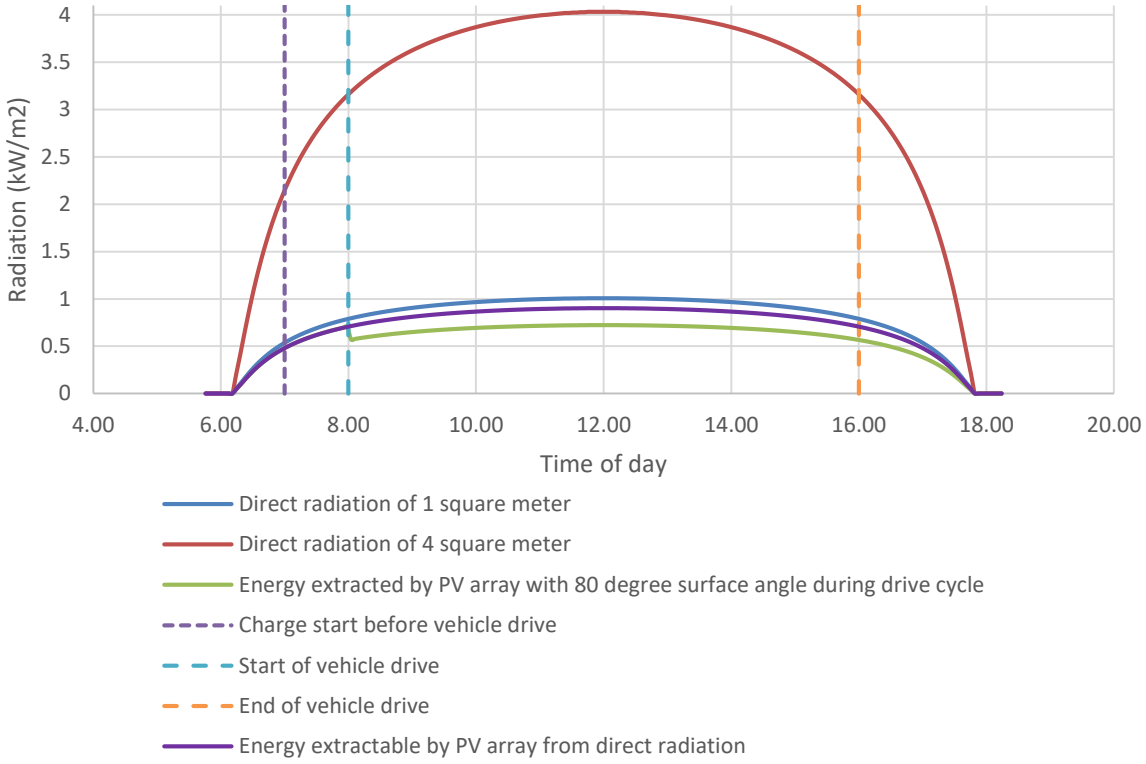

Figure 6-4: Radiation over time on the 14th September at Potchefstroom

It should be known that solar radiance is only power, as in the case of input and output power. In the drive cycle, the energy usage should be known. Energy is merely the product of power and time, as provided in equation (54). The solar energy extracted by the PV array of the solar vehicle is shown in Figure 6-5. The energy accumulation curve includes both the accumulation curve of a PV array with direct radiation at all times and a PV array perpendicular at an 80° surface to solar radiation angle.

Energy: $$E = Pt \quad (54)$$

Where E is energy (Wh), P the power (W) and t is time (h).

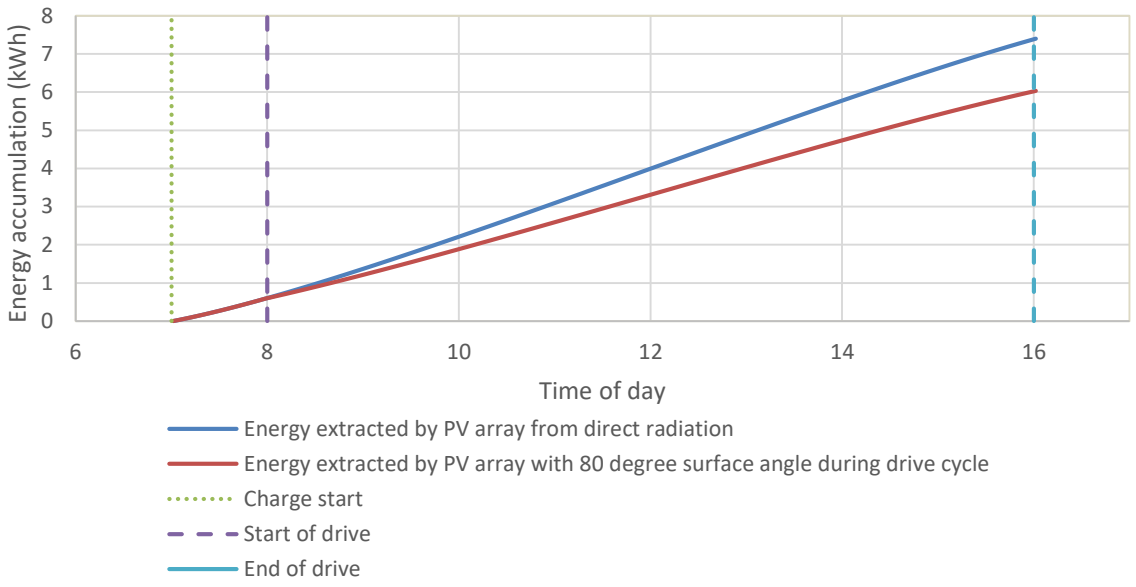

Figure 6-5: Energy accumulation throughout the day

It can be observed that around 1 kWh of energy is additionally extracted from a PV array of a perpendicular angle at all times. Thus, a solar vehicle with a rotating PV array can benefit in a solar race.

6.1.2 Drive cycle procedure

Using the simplified approach, a traction motor is evaluated when the solar vehicle is propelled through the drive cycle. The drive cycle starts at 08H00 after the initial solar energy is extracted by the PV array between 07H00 and 08H00. The available energy amounts to 582.1 Wh, at which the drive cycle begins. In this evaluation, an energy-neutral operation is used. This means that no energy is extracted from the battery, and only the energy acquired from the sun is used to propel the vehicle. During the drive cycle, a positive energy balance (equation (55)) must be obtained at all times in order for the evaluation to adhere to an energy neutral operation.

Energy balance:
$$E_{balance} = E_{available} - E_{used} = E_{available} - \frac{E_{Mech}}{\eta} \qquad (55)$$

Here, $E_{balance}$ is the energy balance, $E_{available}$ the available energy, E_{used} the used energy for propulsion and E_{Mech} the mechanical output energy for propulsion.

The procedure of the drive cycle is as follows:

- Run the traction motor through the simplified route under the operating conditions of:
    - The most efficient operating points of the traction motor per road section.
      The most efficient operating point at each road section was determined by calculating the mechanical output required to propel the vehicle at speeds of 5 km/h to 75 km/h in intervals off 5 km/h. Thus, the required output torque was calculated to achieve the desired speed. Thereafter the efficiency at the operating point was obtained using the efficiency map.
    - The operating point using the least amount of energy for the route section.
      Because the required output torque is a factor of vehicle speed, the torque requirement is not linear with speed. Therefore, the vehicle is propelled using less energy through the route section than operating at speeds of maximum efficiency. However, it takes longer to propel the vehicle through the route section.
    - some operating points use less power at lower speed than the most efficient operating point requiring higher speeds.
    - The maximum operating speed at the given road gradient; and
    - Constant speed conditions of 10 to 70 km/h in a 10 km/h interval.
- Integrate the input power, output power and available power and simulate the drive cycle between the hours of 08H00 and 16H00; using a variety of operating conditions to obtain the maximum driving distance while keeping the energy balance above zero.

It is realised that the 47 km pre-defined route could easily be driven within an hour. Therefore, the proposed drive cycle runs as a loop connecting the start and end point of the route. Employing a loop is similar to the Sasol Solar Challenge where loops are used along the main route to increase the driving distance during the race.

6.2 The Mitsuba M2096-DII

The Mitsuba M2096-DII is preferred by many solar racing teams, including the NWU. The Mitsuba M2096-DII is a BLDC motor consisting of 32 poles and 36 slots. The expected nominal power is 2 kW at 810 rpm, with a rated efficiency of 95%. By examination of the motor, it was seen that the stator poles are wound using the whole coil type, such that the three-phase circuit of the motor consists of four Wye circuit configurations, connected in parallel with one another.

Mitsuba offers several modification options for their motors. These modifications are made to improve the characteristics according to their user requirements. The modifications include a change in permanent magnets, magnetic materials, and coil configurations. These modifications

are expensive and additional to the cost of the base motor. The modifications are not a viable solution for many teams when aiming to improve the operating capability of their motor. To improve the Mitsuba M2096-DII of the NWU, the coil configurations were changed to improve the characteristics to the requirements of the solar vehicle. Thus, in this study, the changed configuration is evaluated using the drive cycle.

6.2.1 Characteristics

The Mitsuba M2096-DII characteristic graph (Appendix D, p.181) was replicated experimentally in the laboratory. The experimental procedure followed is described in Appendix A, §A.1, p.168. Figure 6-6 and Figure 6-7 show the characteristic graphs of the Mitsuba M2096-DII. The speed and efficiency characteristics of the motor are shown as the load torque increases. Both the datasheet and experimentally obtained data are shown in the torque, speed and efficiency versus DC current curves in Figure 6-6.

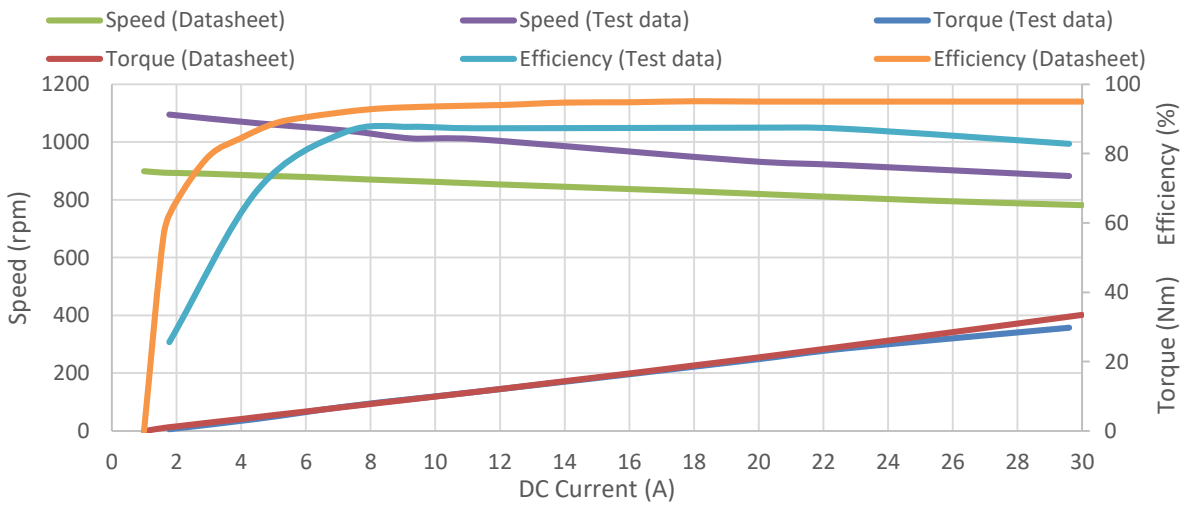

Figure 6-6: Mitsuba M2096-DII characteristics from datasheet and experimental tests

In Figure 6-6 it is observed that the motor speed is around 17% higher than expected from the datasheet, the motor efficiency is around 10% lower and efficiency starts to increase at a higher load torque than the data provided from the datasheet. This comparison concluded that the traction motor uses a lot more energy than anticipated from the datasheet. The motor was not operating at the best torque-speed characteristic requirements of the NWU solar vehicle, and therefore the coil configuration was modified in the laboratory. The coil configuration was changed from four Wye circuit configurations, connected in parallel to four Delta circuit configurations, connected in parallel. The comparison between the two coil configurations is shown in Figure 6-7.

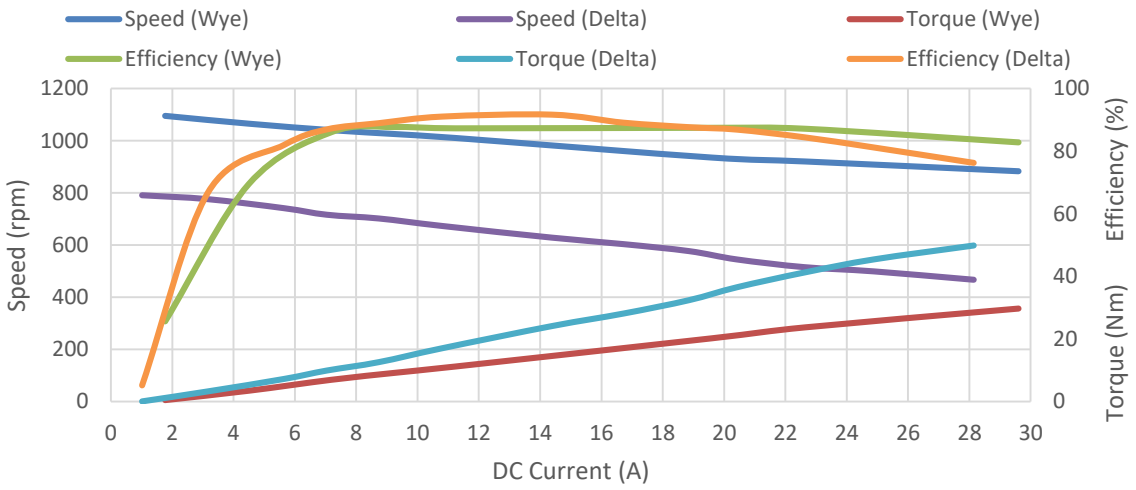

Figure 6-7: Mitsuba M2096-DII characteristics from Wye and Delta circuit configurations

In Figure 6-7 it is observed that the motor rotate at a lower speed and allows an increase in the load torque given the same amount of input current. The delta coil configuration provided a slight efficiency increase when compared to the wye coil configuration. However, it provided a better efficiency range for the required speed of the NWU solar vehicle.

These characteristic graphs provide information about the Mitsuba M2096-DII, but it quickly became apparent that the graphs do not contribute useful information about the efficiency of various operating conditions. Efficiency under various operating conditions was necessary to understand the operating capability of a traction motor. This requires an efficiency map, as mentioned in §6.1.1.2.

An efficiency map of the Mitsuba M2096-DII connected in a parallel Delta circuit configuration is shown in Figure 6-8. The efficiency map is presented by a colour contour. The efficiency value presented by colour is indicated in the legend, which ranges from a dark blue indicating 0% efficiency to a dark red indicating the maximum of 90% efficiency. The efficiency map is constructed from experimental data, using a similar method to the procedure discussed in Appendix A, §A.1, p168. Using the experimental data, various torque-speed and efficiency graphs were constructed. Interpolating between the efficiency graphs was performed to construct the efficiency map. The difference in the procedure is that a range of speeds is run at a set load torque that is documented and repeated at a different load torque.

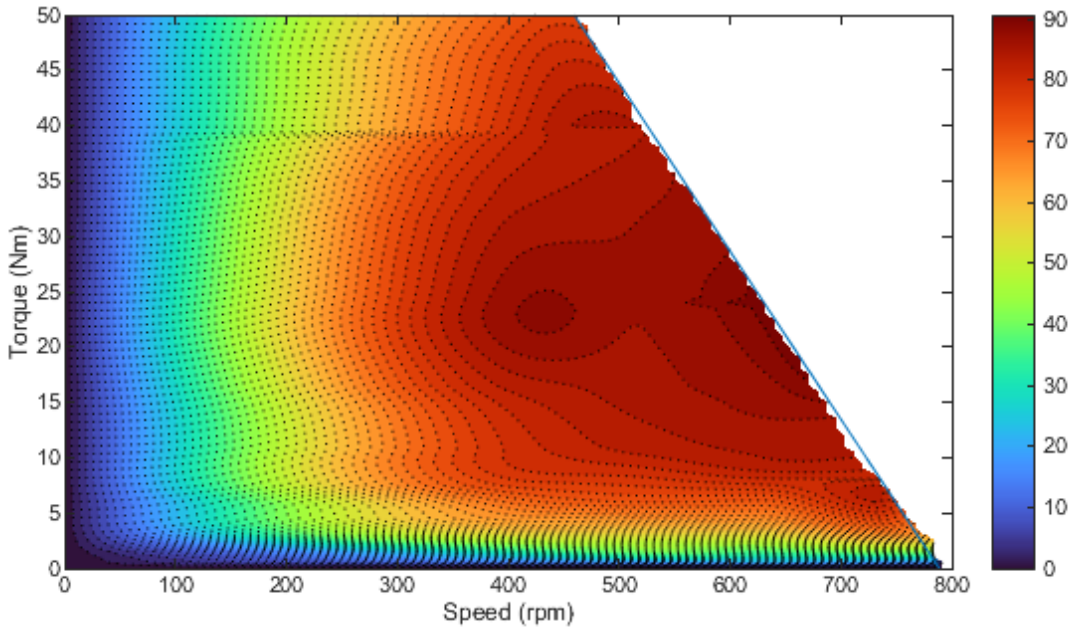

Figure 6-8: Mitsuba M2096-DII efficiency map

6.2.2 Evaluation results

Integrating the available power of solar energy, the output power from the vehicle dynamics, and the input power from the efficiency map, the Mitsuba M2096-DII was run through the drive cycle. The energy evaluation is shown in Figure 6-9. The energy evaluation includes the total accumulation of solar energy, the energy used for propulsion, and the energy balance. Observing the used energy and energy balance waveforms, it is seen that the waveforms tend to have a couple of arc shaped curvatures. These waveforms are due to the simplified route used in the drive cycle. The simplified route, shown in Figure 6-1, has a shallow slope that increases as the road gradient increases. Due to the steep gradient, energy should be stored before the slope can be driven. Energy storage assists in maintaining the energy balance at a positive value. In the circumstance of using an integration method through the pre-defined route and not the simplified route, the energy waveforms will be a linearized waveform.

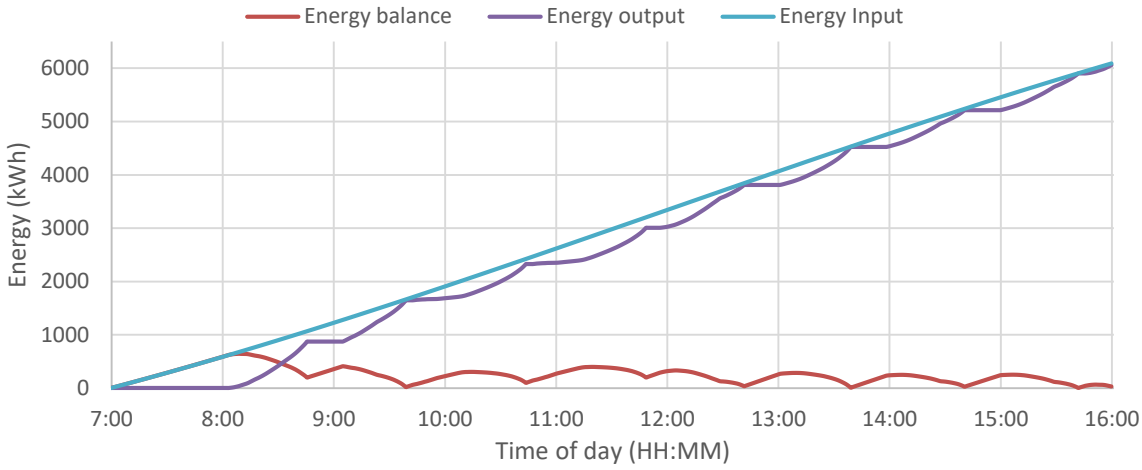

Figure 6-9: The Mitsuba M2096-DII energy usage through the drive cycle

The travelling distance and speed when using the Mitsuba M2096-DII as a traction motor are shown in Figure 6-10. Due to the assumption of average speed for each route section, acceleration and deceleration were excluded from the drive cycle. Therefore, starting each loop in the drive cycle assumed the least amount of power usage i.e., the vehicle propels using gravity. Thus, the average speed through each route section does not show a linearized or smooth waveform, as one would expect. This is because the simplified route was used instead of the pre-defined route, and the average speed chosen during the section differed from one another as acceleration, deceleration and average speed changes was not included into the simplified drive cycle.

The total distance obtained by the traction motor is 398.25 km with an average speed of 52.145 km/h during the evaluation of an eight-hour drive cycle.

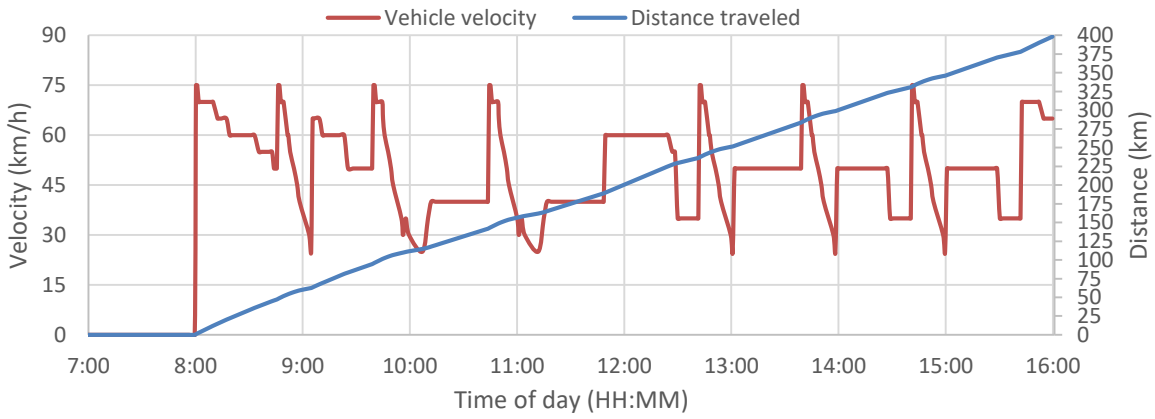

Figure 6-10: The Mitsuba M2096-DII drive distance and speed through the drive cycle

6.2.3 Summary of the Mitsuba M2096-DII

The Mitsuba M2096-DII was evaluated as a traction motor using the drive cycle. Running the vehicle through the simplified route, a travelling distance of 395.25 km was obtained within the operating time of eight-hours. During that time, the total energy usage of the motor was calculated to be 6.06 kWh. The evaluation provided a baseline for the evaluation of an SRM. Thus, the baseline provided a reference on whether an SRM could be considered a viable contender for solar vehicle application.

6.3 The proposed modular switched reluctance motor

The proposed MSRM, designed in chapter 5, consists of a three-phase 12/16 pole configuration. The rated power is 1.84 kW at 550 rpm. The MSRM has 24 coils, with each phase winding connected in series. Chapter 5 provided a comprehensive overview of the proposed MSRM.

6.3.1 Characteristics

Multiple torque-speed characteristic curves were simulated to obtain information over the whole operating range so that an efficiency map could be constructed. The multiple torque-speed characteristics that were simulated are shown in Appendix C.3, Figure C-4, p.179. The simulations for the operating range lower than the rated torque-speed characteristics were performed using lower source voltages and current limits. The overload torque-speed characteristics were simulated using higher source voltages and current limits.

For each of these torque-speed characteristics graphs, an efficiency curve was obtained. The efficiency of each steady-state simulation was calculated by dividing the output power with the input power. Input power is defined as the product of voltage and current. However, the input power equation of an SRM differs from that of AC motors. The input power of an SRM is calculated from the input current and input voltage waveforms during a period (T_s) using equation (56).

Input Power:
$$P_{in} = \frac{q}{T_s} \sum VI\ \Delta t \tag{56}$$

Interpolating between each efficiency curve of the respected torque-speed graph, shown in Appendix C.3, Figure C-4, p.179 was performed to construct an efficiency map. The efficiency map, shown in Figure 6-11 is presented by a colour contour. The efficiency value presented by colour is indicated in the legend, which ranges from a dark blue indicating 0% efficiency to a dark red indicating the maximum efficiency of 80%.

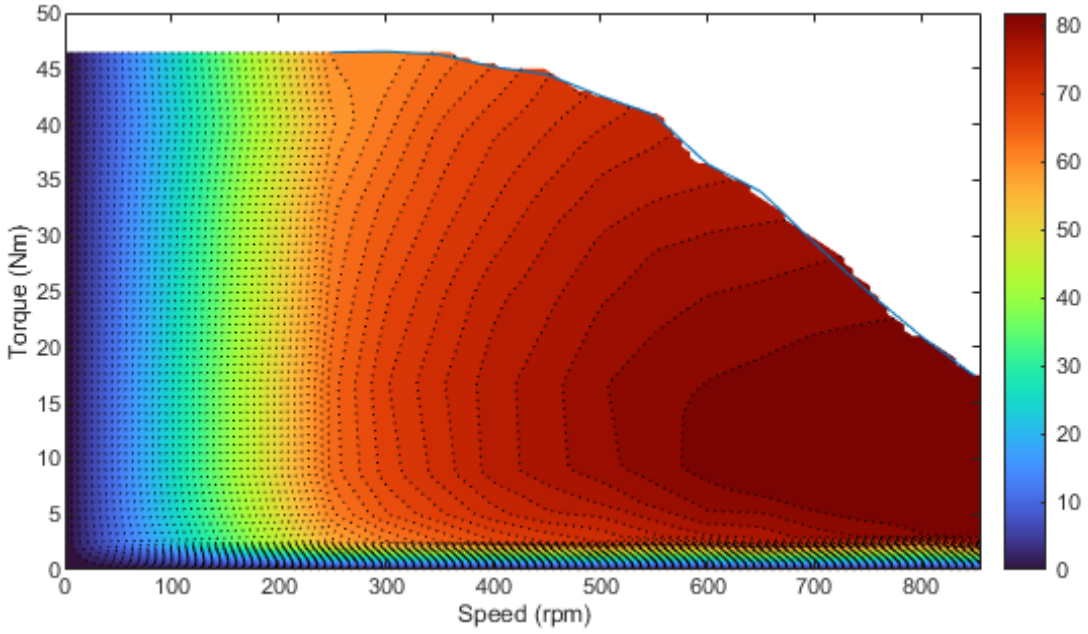

Figure 6-11: Proposed MSRM efficiency map

The efficiency map was constructed from simulated data. Therefore, it should be noted that friction and windage losses were excluded from the efficiency map. Due to manufacturing and financial constraints (§1.5.3, p.10), it is recommended to experimentally evaluate the proposed MSRM, after a comprehensive bearing selection process is finalised and a prototype is manufactured.

6.3.2 Evaluation results

Similar to the Mitsuba M2096-DII (§6.2.2), the proposed MSRM was run through the drive cycle. The energy evaluation of the proposed MSRM, together with the Mitsuba M2096-DII is shown in Figure 6-12. For the evaluation of the proposed MSRM, the following factors have an effect on the results:

- The efficiency map of the proposed MSRM did not account for friction and windage losses. Therefore, the amount of energy used to propel the vehicle in each route section will be higher. Constructing an efficiency map of experimental testing after a prototype is built is recommended.
- The turn-on and turn-off angles (§5.3.3, p.117) were kept constant. Optimising these angles can significantly affect motor performance and efficiency [55]. Thus, using an optimised motor controller will greatly affect the efficiency map and, therefore, driving distance when the MSRM is evaluated.
- The weight difference of the proposed MSRM was not considered in the drive cycle. In the study, the weight of the vehicle was assumed to be the total weight of the vehicle, driver,

and traction motor. However, the difference in weight will affect the torque requirements, as seen by vehicle dynamics (§6.1.1.1, p.126).

- The proposed MSRM was not an optimised design, but was simply an XDM to evaluate future development justifications (§1.5.3, p.10). Therefore, optimising the motor design for efficiency will improve the driving distance when evaluated.

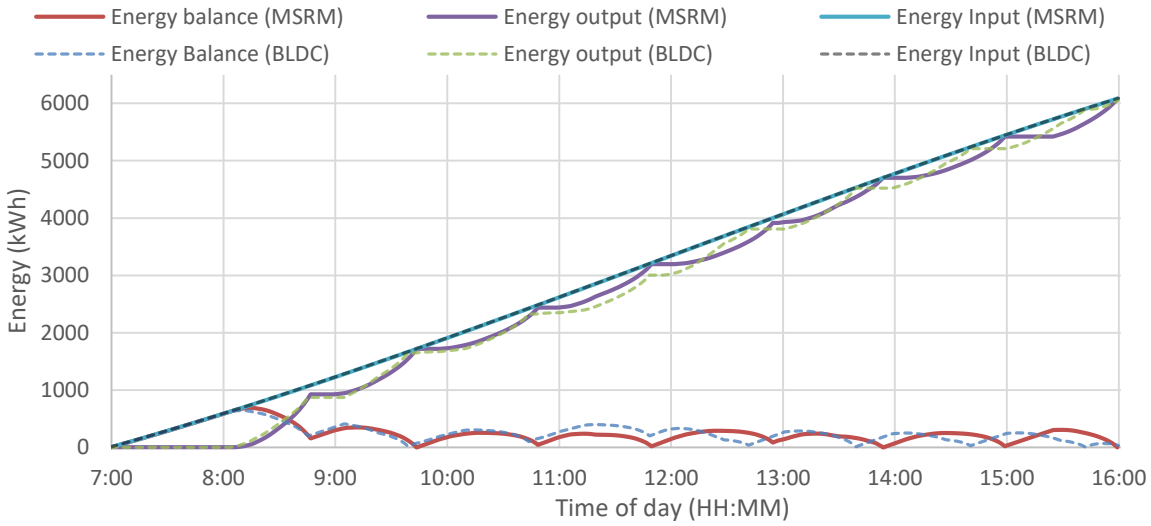

Figure 6-12: The proposed MSRM energy usage through the drive cycle compared to the Mitsuba M2096-DII BLDC

Observing the energy waveforms, the same phenomena occurred as with the evaluation of the Mitsuba M2096-DII (§6.2.2, p.138). Comparing the energy balance in Figure 6-12, it is observed that the energy balance of the proposed MSRM from 12H00 onwards is shaped out of sequence with the Mitsuba M2096-DII. This was due to the propelled speed of the motor not being the same during the two evaluations but merely keeping the energy balance at a positive value while trying to maximise the travelling distance. To maximise the travelling distance, the speed should be maximised. However, the speed was regulated by the usable energy (equations (52), (53) and (55)).

Figure 6-13 shows the travelling distance and speed of the proposed MSRM as the traction motor compared to the Mitsuba M2096-DII BLDC. The total distance obtained was 375.975 km with an average speed of 50.036 km/h during the evaluation of the eight-hour drive cycle.

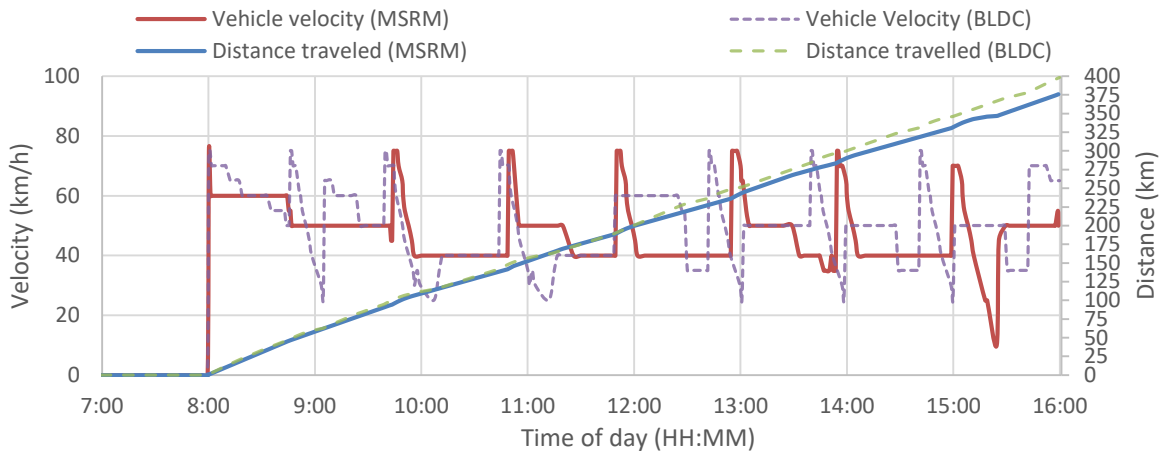

Figure 6-13: The proposed MSRM drive distance and speed through the drive cycle compared to the Mitsuba M2096-DII BLDC

6.3.3 Summary of the proposed modular switched reluctance motor

The proposed MSRM was evaluated as a traction motor using the drive cycle. Running the vehicle through the simplified route, a travelling distance of 375.975 km was obtained within the eight-hour operating time. During that time, the total energy usage of the motor was calculated to be 6.083 kWh. This evaluation provided a good baseline for future design assessments of an SRM.

6.4 Evaluation of the two traction motors

Both Mitsuba M2096-DII and the proposed MSRM were evaluated using the drive cycle, constructed in §6.1.1. The operating torque-speed characteristic points of each motor to propel the vehicle through the drive cycle are shown in Figure 6-14. Figure 6-14 shows the speed-torque characteristic points of each drive cycle evaluation. Also shown was the torque-speed characteristic graph of the proposed MSRM as specified in Table 5-2, p.95 and obtained through the simulation data (§5.4.2, p.120).

For an alternative XDM, it was proposed to change the specified torque-speed characteristics of the proposed MSRM, such that the rated torque is higher and the rated speed is lower. The proposal to change the torque-speed characteristics was to move the highest efficiency region, as shown in Figure 5-23, p122, to the left of the operating points. Moving the highest efficiency contour region to the left would allow more operating points of the proposed MSRM, as shown in the figure below, to operate using lower input power. Thus, higher efficiency is achieved at the operating point, and therefore the driving distance of the proposed MSRM could be extended.

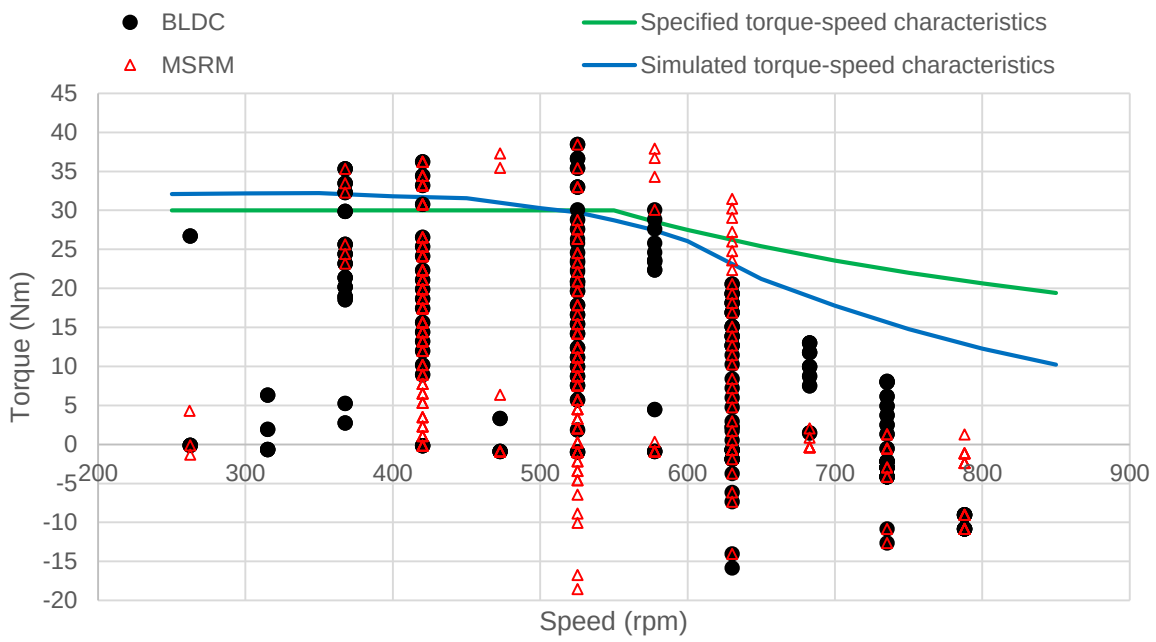

Figure 6-14: Operating torque-speed characteristics through the drive cycle

A new design is needed when changing the torque-speed characteristics. Additionally, changing the torque-speed characteristics for an alternative design will not necessarily provide an improved efficiency map. Therefore, an iterative design process of various MSRMs is required to obtain the most efficient MSRM. Note that an iterative design for optimised motor performance requires ample time, computing power, and simulation accuracy.

6.5 Summary of the traction motor evaluations

The objective of this chapter was to evaluate a traction motor for solar vehicle application. More specifically, to evaluate an SRM for solar vehicle application. To evaluate an SRM, a drive cycle was constructed such that a traction motor has to propel the solar vehicle of the NWU through a pre-defined route using only the energy of the sun. The travelling distance depends on motor performance and energy usage. Thus, by evaluating different motors, the best performing traction motor could be selected from the drive cycle.

Both the proposed MSRM and Mitsuba M2096-DII were evaluated using the drive cycle. The Mitsuba M2096-DII was evaluated to use as a comparative baseline to obtain the motor specifications used to design the proposed MSRM. After the design of the proposed MSRM (chapter 5), the proposed MSRM was evaluated. The driving distance and average speed of the two traction motors are summarised in Table 6-3. Compared to the Mitsuba M2096-DII, the proposed MSRM travelled 23 km less than the Mitsuba M2096-DII within the same operating time of eight hours. This is a 5.59% difference in driving distances.

Table 6-3: Drive cycle comparison

	Mitsuba M2096-DII	Proposed MSRM	Difference (%)
Distance (km)	398.25	375.975	5.59
Average speed (km/h)	52.145	50.036	4.04

After evaluating both traction motors, it was concluded that the proposed MSRM consumed more energy to propel the vehicle. The proposed MSRM consumed more energy, and therefore less travelling distance was achieved by the proposed MSRM. However, it should be noted that the proposed MSRM was not designed for optimal performance and neither was the motor controller. The motor controller used to operate the proposed MSRM in the simulations used constant conduction angles instead of the optimised conduction angles used to improve motor efficiency. If a motor controller was used to operate the proposed MSRM at the most efficient conduction angles for the required torque and speed, the motor would have extended the total travelling distance. However, the detailed effect the conduction angles have on the efficiency map of the proposed MRM is unknown. Thus, a motor controller operating the motor at the conduction angles of optimised efficiency should be used to construct an efficiency map to evaluate the proposed MSRM. Thereafter, a better understanding will be obtained if the change of conduction angles truly have an effect on the motor efficiency.

When an efficiency map is constructed of an optimised MSRM design, a comprehensive selection of bearings, a housing design and friction and windage losses should be included. The friction and windage losses will provide additional losses and therefore decrease the evaluated driving distance. Note that the drive cycle used evaluates the performance of the motors, and does not include the mechanical or structural affects it may have on the evaluated outcomes. A complete mechanical and structural design of the proposed MSRM is recommended as a future study for a complete evaluation of the proposed MSRM. Nevertheless, the proposed MSRM, designed and evaluated as an un-optimised XDM, justify future development of an SRM for solar vehicle application.

CHAPTER 7 CONCLUSION

Since no SRM has been adequately evaluated against a permanent magnet motor, i.e., a BLDC or PMSM in solar vehicle applications, the objective of this study was to evaluate an SRM for solar vehicle application. The process followed in the study is listed below:

1. Literature review.
2. Validating the electromagnetic simulation methods.
3. Design of the proposed modular switched reluctance motor (MSRM).
4. Constructing a drive cycle.
5. Testing and evaluating the Mitsuba M2096-DII BLDC.
6. Evaluating the proposed MSRM for solar vehicle application.

7.1 Literature review

A literature review of the principles and design considerations of an SRM was discussed in chapter 2. From literature it was obtained that an SRM is designed for the specified torque-speed characteristics by considering the aspects of the geometric dimensions, pole configurations, magnetic material properties and winding parameters. Some geometrical variations can be made to improve the efficiency and performance of an SRM. These geometrical variations include the modular, multilayer, hybrid, and transverse constructions of an SRM.

It was concluded that an MSRM offered the best efficiency and performance improvement. MSRMs were found to have many advantages, such as independent flux paths, no flux reversals, larger slot spaces for windings, lower rotor inertia, better heat dissipation, and easy manufacturing. The modular construction of an SRM was found to increase efficiency when an MSRM was compared to conventional SRMs. Thus, an MSRM was an appropriate selection for the design of an SRM.

7.2 Validation of the electromagnetic simulation methods

A literature review of electromagnetic modelling methods was provided in chapter 3. It was found that finite element analysis (FEA) is the most popular method for solving an electromagnetic problem. The FEA software, Ansys® Maxwell, was used in many of the studies found in the literature and was available for use in this study.

The validation of the electromagnetic modelling method was provided in chapter 4. Both the magnetostatic and transient solvers of Ansys® Maxwell were used to create a simulation model of an MSRM. A simulation model of the MSRM designed by Wen Ding *et al.* in [96, 110, 109, 97, 107, 111] was created to compare the simulation results against the simulated results and experimental data of Wen Ding *et al.*

The magnetostatic solver was used to obtain the magnetostatic characteristics, i.e., flux linkage and static torque of the MSRM. A 5% to 13% deviation occurred between the simulated data and experimental data provided by Wen Ding *et al.* Because of the effect the geometric parameters and the magnetic material had on the simulations the modelling method deemed acceptable for the magnetostatic simulations.

The transient solver was used to simulate the steady-state behaviour of the MSRM. The steady-state simulations of the MSRM was performed using a setup that provided the best accuracy for the amount of computing power and time. The simulation data deviated between 13.11% and 12.884% compared to the simulated and experimental data provided by Wen Ding *et al.* For these simulation setups, both the stacking factor and coil resistances were unknown.

The validation of the electromagnetic simulation methods was concluded that the simulations were set up and followed correctly to obtain adequate results compared to the data of Wen Ding *et al.* Thus, it was concluded that the same methods and procedures to set up and analyse an MSRM, designed in chapter 5 could be used.

7.3 Design of the proposed modular switched reluctance motor

An un-optimised exploratory development model of an MSRM, proposed in §2.6, p.45 was designed in chapter 5. The proposed MSRM consists of a radial flux, outer rotor MSRM. The modular structure as the diameter of the motor can be increased for increased torque operations without increasing the losses in the magnetic material. Thus, the modular structure increases efficiency and performance.

An iterative process, involving the geometry design, winding design, flux density observation and the required torque-speed characteristics was followed to design the proposed 12/16 E-core MSRM. .

In conclusion, the proposed MSRM specified to a 355 mm diameter, 100 mm axial length, three-phase, 24 coil motor rated at 1.84 kW, at a speed of 550 rpm. A 3D simulation model in the transient solver was used to simulate the proposed motor at a variety of speeds. Simulations

provided the output torque and input power. Using a set of these simulation results, the torque-speed characteristic graph of the proposed MSRM was constructed.

The efficiency map was constructed from the speed-torque characteristic graphs simulated using different source voltages and current limits. The efficiency map was then used to evaluate the proposed MSRM through the drive cycle.

7.4 Construction of a drive cycle

A method to evaluate a traction motor for solar vehicle applications was necessary. To evaluate the proposed MSRM, it was chosen to construct a drive cycle to simulate the propulsion of the NWU solar vehicle through a route using only the extracted energy of the sun to power the traction motor.

For the vehicle to operate at a certain speed, a certain amount of torque was required from the traction motor. The torque was a function of speed, the vehicle drag coefficient and vehicle mass. Therefore, using an efficiency map of a traction motor, the input power for the calculated output power was determined. In conclusion, using the drive cycle, the travel distance of each traction motor was determined.

7.5 Testing and evaluation of the Mitsuba M2096-DII

The Mitsuba M2096-DII BLDC was tested in the laboratory on a motor test bench. The Mitsuba M2096-DII was tested using the method provided in Appendix A, p.168. The test data was used to construct an efficiency map of the Mitsuba M2096-DII. The efficiency map was then used to evaluate the Mitsuba M2096-DII through the drive cycle.

To propel the vehicle through the drive cycle using the Mitsuba M2096-DII as the traction motor, a total travelling distance of 395.5 km was obtained, with a total energy usage of 6.06 kWh. This evaluation set a reference point of what is expected from the proposed MSRM.

7.6 Evaluation of the modular switched reluctance motor for solar vehicle application

Evaluation of the proposed MSRM for solar vehicle application was presented in chapter 6. The efficiency map constructed of the proposed MSRM was used to evaluate the proposed MSRM through the drive cycle. The proposed MSRM was used to propel the solar vehicle of the NWU through the drive cycle, similar to the evaluation of the Mitsuba M2096-DII.

A total travelling distance of 375.975 km was obtained using the proposed MSRM as the traction motor. For the drive cycle, the total energy consumption was 6.083 kWh. When comparing the

proposed MSRM to the Mitsuba M2096-DII, it is seen that the proposed MSRM obtained a travelling distance of 23 km less than the Mitsuba M2096-DII for roughly the same amount of energy usage. Thus, it was concluded that the proposed MSRM used more energy to drive when considering the average energy used per distance travelled.

Even though the proposed MSRM did not travel further or equal distance compared to the Mitsuba M2096-DII, the proposed MSRM shows some promise as a traction motor in solar vehicle application. Considering that the proposed MSRM is an un-optimised XDM, the proposed MSRM achieved a travelling distance of only 5.59% less than the Mitsuba M2096-DII.

If the design of the proposed MSRM and/ or motor controller is optimised for efficiency, the expectation of extended or equal travelling distance is expected. Future development and optimisation of the proposed MSRM will help to improve motor performance and efficiency and therefore the travelling distance when using the proposed MSRM as a traction motor in the solar vehicle of the NWU.

In conclusion, this study evaluated a switched reluctance motor for solar vehicle application, by adequately evaluating a XDM of the proposed MSRM against a permanent magnet motor, generally used for solar vehicles. The use of an SRM for solar vehicle applications is justified for future development studies to obtain an optimised SRM as a traction motor in a solar vehicle.

7.7 Recommendations for future studies

Additional work or considerations are revealed throughout the study, either due to limitations, literature, or the work performed. This section proposes the recommended studies to further investigate or improve related research. These studies include:

7.7.1 Numerical methods

Ansys® Maxwell was used as the numerical simulation software. Many of the studies discussed in the literature used Ansys® Maxwell to design an SRM. Although Ansys® Maxwell was used in many studies, it is proposed to replicate the design using different numerical simulation software, i.e., JMAG or Altair Flux as listed in §3.1.2, p.49. Using a different software will provide additional validation of the electromagnetic simulation methods.

7.7.2 Alternative motor design considerations

In this study an un-optimised XDM of an MSRM was designed. According to the definition of an XDM, the proposed MSRM designed in chapter 5 has the risk of performing less than optimal. For future design of an MSRM, the following design considerations are recommended.

7.7.2.1 Core shape

In this study, an E-core was chosen for the design based mainly on Xinglong Li [115]. The research question was formed that a core with more poles whilst keeping the axial length and winding turns constant will be more efficient given that flux paths in the core are minimised. A research question formulated in §2.6, p.45 was briefly analysed in §5.2.1.1, p.97. It was found that the core shapes were not directly comparable. Therefore, a future study is proposed to fully evaluate the research question of the efficiency effect when using different core shapes.

For an alternative design of an MSRM, it is proposed to design a C-core and IIII-core with the same torque-speed characteristics, listed in Table 5-2, p.95. Thereafter, the designs can be compared to each other and each motor can be evaluated using the drive cycle to find the most efficient MSRM design.

7.7.2.2 Pole configuration

When comparing a 12/16 MSRM with a 12/20 MSRM, it was found that the 12/16 MSRM produced higher torque. This is contradictory to the literature discussed in §2.3.3, p.31. However, the comparative designs in the literature changed the pole area, embrace, and winding turns, unlike the comparative designs of the 12/16 and 12/20 MSRM in §5.2.1.2, p.101.

The 12/20 MSRM is still an alternative option. However, it is necessary to alter the winding and pole geometry to achieve the same torque-speed characteristics as the 12/16 MSRM. The motor can then be evaluated by comparing the efficiency maps and the drive cycle evaluations. By redesigning the windings and pole geometry, the 12/20 MSRM should produce more torque as more torque is expected based on the conclusive results found in literature (§2.3.3).

7.7.2.3 Pole geometry

The pole geometry of the E-core was arbitrarily chosen for this study, based on the core dimensions found in literature. The pole area and pole embrace were analysed during the design process to find the parameters that produced the most torque within the geometry constraints (Table 5-1, p.90). It is proposed to optimise the pole and core geometry by changing the pole embrace, pole area, and yoke area. However, optimizing the geometry based on these parameters is an extensive process.

7.7.2.4 Winding design

For a three-phase BLDC, the windings can be Wye or series connected. However, this is not the case for an SRM when using an asymmetric half-bridge converter as the motor controller. All the

phase coils of the proposed MSRM are connected in series. It is proposed to connect the coils in a parallel combination and evaluate the performance effects.

Another winding alteration to consider is to use square-shaped conductors. This will improve the fill factor and result in more winding turns around the core. Thus, the same output torque will be produced using less current.

7.7.3 Thermal assessment

Thermal considerations on the coils were provided in §5.2.4, p.112. Predicting coil temperature was done by coupling a magnetostatic simulation to a steady-state thermal analysis. The coils were excited with constant DC while the motor was stationary. Thus, the simulation provided the coil temperatures to ensure that the thermal limitations of the coil insulation were not exceeded.

A comprehensive understanding of thermal behaviour of the proposed MSRM is still required. The use of FEA and CFD are proposed to model the thermal behaviour. Thereafter, experimental testing is proposed to verify the thermal behaviour.

7.7.4 Design optimisation

The design of the proposed MSRM was an un-optimised XDM. As the proposed MSRM is justified, an optimised MSRM is desired. Therefore, it is proposed to optimise the proposed MSRM for efficiency. Optimising the proposed MSRM can be achieved by either the geometrical, material, and winding design or by optimising the conduction angles.

7.7.5 Motor controller design

The design of a motor controller, nor the conduction angles, were included in the scope of this study. However, conduction angles are part of the motor controller and are an important aspect to operate the motor.

The design a motor controller to operate at the optimal conduction angles of the proposed MSRM. Using a motor controller that operate the motor at its most efficient torque-speed characteristics will improve the energy usage of the traction motor. Note that optimising of conduction angles requires some level of sophistication to predict the conduction angles at each torque-speed operating point.

7.7.6 Creating an efficiency map

The efficiency map of the proposed MSRM was constructed using multiple torque-speed characteristic graphs. Each torque-speed characteristic graph was analysed and the efficiency at

the operating points was calculated. After all torque-speed characteristic points were analysed, an efficiency map was constructed. This was a time-consuming process; as multiple simulations had to be run for a single torque-speed characteristic graph, i.e. speeds at 100 rpm to 1000 rpm in steps of 50 rpm.

Ansys® Maxwell offers a unique toolkit in the software that can construct an efficiency map. The toolkit uses the designed motor and the parameters set within the toolkit to construct the efficiency map. Unfortunately, the toolkit is not functional for an SRM with the release of Maxwell 2021R1.

A functional toolkit will provide an easy method to construct an efficiency map. Thus, allowing additional motor designs to be evaluated in less time using the drive cycle. It is proposed to construct an efficiency map of the proposed MSRM and evaluate the proposed MSRM. Evaluation of the MSRM is proposed as the toolkit offers the functionality to construct an efficiency map for the most efficient operating conditions. Thus, evaluation of an efficient motor operation is less time-consuming, as the toolkit automatically sets the conduction angles. Therefore, a study to optimise conduction angles for efficiency is not necessary when the toolkit is used. However, the toolkit must be functional for SRMs.

7.7.7 Prototype manufacturing and experimental testing

Due to financial constraints (§1.5.3, p.10), the proposed MSRM was not manufactured in this study. Therefore, validation of the proposed MSRM using experimental tests was not possible. Manufacturing the proposed MSRM will allow experimental tests of static, dynamic, and thermal characteristics to be performed.

It is proposed to compare the experimental test data with the simulated data to fully validate the efficiency map of the proposed MSRM. This will provide a comparison for the similarity of an efficiency map of a conventional SRM and the proposed MSRM.

Before a prototype of the MSRM is manufactured, additional design aspects should be considered. These additional designs include the motor housing design, bearing selections, and the motor controller. Preferably, the optimised design should be constructed to minimise the financial implications.

7.7.8 Drive cycles for solar races

Chapter 6 presented an analytical evaluation of a traction motor. A traction motor was evaluated using the constructed drive cycle. However, the drive cycle is simplified and uses a lot of assumptions. When two traction motors are compared against each other, these simplifications

and assumptions have little effect on the results when the better traction motor should be selected. However, using the simplified route cannot determine the expected driving distance for a route.

It is proposed to include all variable factors of the road, weather, and vehicles in the drive cycle to allow use of the drive cycle as a prediction tool for solar racing teams. The drive cycle will not only predict the driving distance, but also provide information on the most efficient driving patterns. The driving pattern can then be used to instruct the driver on how to drive and consequently increasing the driving distance.

7.8 Final thoughts

The opinion of Nir Vaks and Nvah Zarate is that an SRM is a potential candidate for the next generation traction motor in EVs. After combining the opinion of Nir Vaks and Nvah Zarate with the use of an electric motor in solar races, the research topic was formulated. The research topic was to evaluate an SRM for solar vehicle application.

This study evaluated an MSRM using a simplified drive cycle. An un-optimised XDM MSRM was designed and evaluated using the drive cycle. Due to financial constraints, no prototype of the proposed MSRM was manufactured. Therefore, a numerical simulation of the proposed MSRM was analysed to construct an efficiency map.

The proposed MSRM was evaluated and is concluded to be justified for future development even though it was concluded that the proposed MSRM was less efficient than the Mitsuba M2096-DII. Future development will improve the proposed MSRM that could lead to the use of an SRM in solar vehicle applications, or in the circumstance of the NWU, solar races such as the Sasol Solar Challenge.

BIBLIOGRAPHY

[1] N. Vaks and N. Zarate, “Next Generation of Electric Vehicle Motors - The Silent Treatment,” in *ANSYS Advantage Issue 1*, Portland, Ansys, 2019, pp. 24-27.

[2] M. PAUL and J. F. T., “Switched Reluctance Motor, the future of Modern Electric Vehicle - A Technical Review,” in *Proceedings of International Conference on Recent Trends in Computing, Communication & Networking Technologies (ICRTCCNT) 2019*, Chennai, Tamilnadu, India, 2019.

[3] P. Gautam, S. Kumar and S. Lokhandwala, “Energy-Aware Intelligence in Megacities,” *Current Developments in Biotechnology and Bioengineering,* pp. 211-238, 11 January 2019.

[4] “United Nations Environment Programme,” [Online]. Available: https://www.unep.org/about-un-environment/sustainability. [Accessed 03 August 2021].

[5] “UNESCO Sustainable Development,” WWW.UNESCO.ORG, [Online]. Available: https://en.unesco.org/themes/education-sustainable-development/what-is-esd/sd. [Accessed 03 August 2021].

[6] M. Evans, “the balance small business,” Dotdash Meredith, 07 July 2020. [Online]. Available: https://www.thebalancesmb.com/what-is-sustainability-3157876. [Accessed 29 February 2022].

[7] N. K. Arora, “Environmental Sustainability—necessary for survival,” *Environmental Sustainability,* vol. 1, no. 1, pp. 1-2, 2018.

[8] P. Sutton, “A Perspective on environmental sustainability?,” Strategy of Green Innovations, Victoria, 2004.

[9] F. Ahjum, C. Godinho, J. Burton, B. McCall and A. Marquard, “A LOW-CARBON TRANSPORT FUTURE FOR SOUTH AFRICA: TECHNICAL, ECONOMIC AND POLICY CONSIDERATIONS,” Climate Transparency, Cape Town, 2020.

[10] “Green Transport Strategy for South Africa: (2018-2050),” Department of Transport: South Africa, Pretoria, 2018.

[11] “European Environment Agency,” European Environment Information and Observation Network, [Online]. Available: https://www.eea.europa.eu/data-and-maps/indicators/transport-emissions-of-greenhouse-gases/transport-emissions-of-greenhouse-gases-12. [Accessed 03 August 2021].

[12] P. Carus, “Roger Bacon (With portraits).,” *The Open Court,* vol. 28, no. 8, p. 1, 1914.

[13] J. McNutt, “The Work of Leonardo da Vinci: From the Mind of a Genius,” *mcnutt2011work,* 2011.

[14] M. Guarnieri, “Looking back to electric cars,” in *2012 Third IEEE HISTory of ELectro-technology CONference (HISTELCON)*, Pavia, Italy, 2013.

[15] R. Matulka, “Energy.Gov,” The U.S. Department of Energy (DOE), [Online]. Available: https://www.energy.gov/articles/history-electric-car. [Accessed 2021 July 05].

[16] D. Dorrel, M. Popescu, A. Knight, L. Evans and D. Staton, “Comparison of different motor design drives for hybrid electric vehicles,” in *Energy Conversion Congress and Exposition (ECCE), 2010 IEEE*, Atlanta, 2010.

[17] D. Sperling and D. Gordon, “Two Billion Cars Transforming a Culture,” in *TR NEWS*, Transportation Research Board Publications Office, 2008, pp. 3-9.

[18] M. Gross, “A planet with two billion cars,” *Current Biology,* vol. 26, no. 8, pp. 307-310, 2016.

[19] “Tesla,” Tesla, 20 April 2020. [Online]. Available: https://www.tesla.com/blog/tesla-roadster-travels-313-miles-single-charge. [Accessed 03 July 2021].

[20] *Tesla Motors,* 2015.

[21] J. A. Arulious, “Design of solar powered electric vehicle,” *Journal of Physics: Conference Series,* pp. 1-8, 2021.

[22] “Tour de Sol: Wikipedia,” Wikimedia Foundation, 20 February 2022. [Online]. Available: https://en.wikipedia.org/wiki/Tour_de_Sol. [Accessed 02 March 2022].

[23] C. Oosthuizen, B. Van Wyk, Y. Hanam and D. Desai, “Solar Electric Vehicle Energy Optimization for the Sasol Solar Challenge 2018,” *IEEE Access,* vol. 7, no. 1, pp. 175143-175158, 2019.

[24] C. Oosthuizen, B. van Wyk and Y. Haman, “Modelling and simulation of the South African designed Sun Chaser II solar vehicle,” in *2017 IEEE AFRICON*, 2017.

[25] “Collinsdictionary.com,” Collins Dictionaries, [Online]. Available: https://www.collinsdictionary.com/submission/20366/traction+motor. [Accessed 05 August 2021].

[26] A. M. Lulhe and T. N. Date, “A technology review paper for drives used in electrical vehicle (EV) & hybrid electrical vehicles (HEV),” in *2015 International Conference on*

Control, Instrumentation, Communication and Computational Technologies (ICCICCT), Kumaracoil, 2015.

[27] W. yan, Y. Tain-ming and R. fei, “The Research of 30kw Electric Vehicle Drive System Based on SRM,” in *IEEE Vehicle Power and Propulsion Conference (VPPC)*, Harbin, 2008.

[28] B. D. Vărăticeanu, P. Minciunescu, S. Ş. Matei and C. Nicolescu, “Optimization and validation of a 10 kW permanent magnet brushless motor for small electric vehicles,” in *2017 Electric Vehicles International Conference (EV)*, Bucharest, 2017.

[29] B. S. Guru and H. R. Hiziroğlu, Electric Machinery and Transformers, New York: Oxford University Press, 2001.

[30] S. Sharifan, S. Ebrahimi, A. Oraee and H. Oraee, “Performance comparison between brushless PM and induction motors for hybrid electric vehicle applications,” in *2015 Intl Aegean Conference on Electrical Machines & Power Electronics (ACEMP), 2015 Intl Conference on Optimization of Electrical & Electronic Equipment (OPTIM) & 2015 Intl Symposium on Advanced Electromechanical Motion Systems (ELECTROMOTION)*, Side, 2015.

[31] N. Hashernnia and A. Behzad, “Comparative Study of Using Different Electric Motors in the Electric Vehicles,” in *International Conference on Electrical Machines*, Vilamoura, 2008.

[32] T. Selvathai, M. A. S., V. L. and R. R., “100 kW Induction Motor for Hybrid Electric Tracked Vehicle - Design Steps and Challenges,” in *2018 8th IEEE India International Conference on Power Electronics (IICPE)*, JAIPUR, 2018.

[33] S. Cui, C. Liang and l. Song, “Study on efficiency calculation model of induction motors for electric vehicles,” in *2008 IEEE Vehicle Power and Propulsion Conference*, Harbin, 2008.

[34] D. Zechmair and K. Steidl, “Why the Induction Motor could be the better choice for your Electric Vehicle Program,” *World Electric Vehicle Journal,* vol. 5, no. 2, pp. 546-549, 2012.

[35] M. Felden, P. Bütterling, P. Jeck, L. Eckstein and K. Hameyer, “Electric vehicle drive trains: From the specification sheet to the drive-train concept,” in *Power Electronics and Motion Control Conference (EPE/PEMC)*, Ohrid, 2010.

[36] A. Krings, A. Mousavi, O. Wallmark and J. Soulard, “Thermal Influence on the Magnetic Properties and Iron Losses in Small Slot-Less Permanent Magnet Synchronous,” in *12th Joint MMM/Intermag Conference*, Denver, 2013.

[37] “Current E,” Current E, 20 July 2017. [Online]. Available: https://current-e.com/blueprints/revealed-m3electro-motor/. [Accessed 05 May 2020].

[38] M. Cheng, L. Sun, G. Buja and L. Song, “Advanced Electrical Machines and Machine-Based Systems for Electric and Hybrid Vehicles,” *Energies,* vol. 8, no. 9, pp. 9541-9564, 2015.

[39] J. F. and F. D., “Axial Flux Interior Permanent Magnet Synchronous Motor for Small Electric Traction Vehicle,” in *International Symposium on Power Electronics Power Electronics, Electrical Drives, Automation and Motion*, Sorrento, 2012.

[40] J. Fan, C. Zhang, Z. Wang, Y. Dong, C. E. Nino, A. R. Tariq and E. G. Strangas, “Thermal Analysis of Permanent Magnet Motor for the Electric Vehicle,” *IEEE Transactions on Magnetics,* vol. 46, no. 6, pp. 2493-2496, 2010.

[41] J. de Santiago, H. Bernhoff, B. Ekergård, S. Eriksson, S. Ferhatovic, R. Waters and M. Leijon, “Electrical Motor Drivelines in Commercial All-Electric Vehicles: A Review,” *IEEE Transactions on Vehicular Technology,* vol. 61, no. 2, pp. 475-484, 2012.

[42] S. P. Nikam, V. Rallabandi and B. Fernandes, “A High-Torque-Density Permanent-Magnet Free Motor for in-Wheel Electric Vehicle Application,” *IEEE Transactions on Idustry Applications,* vol. 48, no. 6, pp. 2287-2295, 2012.

[43] S. Nikam, S. Sau and B. Fernandes, “Design of switched reluctance motor based electric drive-train for intra-campus two wheeler,” in *IECON 2013 - 39th Annual Conference of the IEEE Industrial Electronics Society*, Vienna, 2013.

[44] A. Honda, K. Senda and K. Sadahiro, “Electrical Steel for Motors of Electric and Hybrid Vehicles*,” KAWASAKI STEEL, 2003.

[45] S. Derammelaere, M. Haemers, J. D. Viaene, F. Verbelen and K. Stockman, “A quantative comparison between BLDC, PMSM, brushed DC and stepping motor technologies,” in *2016 19th International Conference on Electrical Machines and Systems (ICEMS)*, Chiba, 2016.

[46] P. Bogusz, “A new method for controlling the switched reluctance motor in the low-speed range,” in *2015 International Conference on Electrical Drives and Power Electronics (EDPE)*, Tatranska, 2015.

[47] L. Teschler, “ElectronicDesign,” Endeavor Business Media, 15 May 2009. [Online]. Available: https://www.electronicdesign.com/tools/learning-resources/basics-of-design/article/21191067/the-switch-to-switched-reluctance. [Accessed 06 September 2022].

[48] C. Ruoff, “A closer look at torque ripple – minimizing its effects on electric machines,” in *Charged electric vehicles magnazine*, ChargedEVs.com, 2015, pp. 22-29.

[49] J. Luo, K. Ohyama, I. Kenshiro, H. Fujii, H. Uehara and Y. Hyakutake, “Trial manufacture of SRM drive system for electric vehicles,” in *2016 IEEE Industrial Electronics and Applications Conference (IEACon)*, Kota Kinabalu, 2016.

[50] M. Yildirim, M. Polat and H. Kürüm, “A survey on comparison of electric motor types and drives used for electric vehicles,” in *2014 16th International Power Electronics and Motion Control Conference and Exposition*, Antalya, 2014.

[51] V. S. De Castro Teixeira, T. A. D. S. Barros, A. B. Moreira and E. R. Filho, “Methodology for the Electromagnetic Design of the Axial-Flux C-Core Switched Reluctance Generator,” *IEEE Access,* vol. 6, pp. 65463-65473, 2018.

[52] A. Labak, “DESIGNING, PROTOTYPING AND INVESTIGATION OF ADVANCED FIVE-PHASE AXIAL FLUX SRM FOR ELECTRIFIED VEHICLE APPLICATION,” University of Windsor, Windsor, Ontario, Canada, 2015.

[53] N. R. Patel, V. A. Shah and M. M. Lokhande, “Design and Performance Analysis of Radial flux C-Core Switched Reluctance Motor for In-Wheel Electrical Vehicle Applications,” in *2016 IEEE Transportation Electrification Conference and Expo (ITEC)*, Dearborn, MI, USA, 2016.

[54] “techopedia,” Janalta Interactive, [Online]. Available: https://www.techopedia.com/definition/16383/exploratory-model#:~:text=The%20exploratory%20model%20is%20an,to%20be%20optimal%20is%20selected.. [Accessed March 19 2022].

[55] B. Bilgin, J. W. Jiang and A. Emandi, Switched Reluctance Motor Drives Fundamentals to Applications, Boca Raton, Florida: CRC Press, 2018.

[56] J. Lin, “External-Rotor 6/10 Switced Reluctance Motor for an electric bicycle,” McMaster University, Hamilton, Ontario, Canada, 2013.

[57] A. Labak, “New design of switched reluctance motor using finite element analysis for hybrid electric vehicle applications,” University of Windsor, Windsor, Ontario, Canada , 2009.

[58] A. Murphy, Design of a Switched Reluctance Machine Drive for Automotive Applications, Dublin: Dublin City University, 2008.

[59] C. S.-H. MAK, “18/12 SWITCHED RELUCTANCE MOTOR DESIGN FOR A MILD-HYBRID ELECTRIC POWERTRAIN APPLICATION,” McMaster University, Hamilton, Ontario, Canada, 2020.

[60] A. E. Fitzgerald, C. J. Kingsley and S. D. Umas, Electric Machinery, New York: McGraw-Hill, 2003.

[61] P. M. T. Lamchich and J.-W. Ahn, “Switched Reluctance Motor,” in *Torque Control*, Shanghai, InTech, 2011, pp. 201-252.

[62] T. Wichert, “Design and Contruction Modifications of Switched Reluctance Machines,” Warsaw University of Technology, Warsaw, 2008.

[63] L. C. Guilera, “Analytical design of a Synchronous Reluctance motor (SRM),” School of Industrial Engineering of Barcelona (ETSEIB), Barcelona, Spain, 2018.

[64] P. Andrada, “SRM Drives for Electric Traction,” Universidad Politécnica de Cataluña, Barcelona, 2019.

[65] P. S. Melo and R. E. Araújo, “Switched Reluctance Motor Modeling and Loss Estimation Review,” in *Modelling and Control of Switched Reluctance Machines*, London, United Kingdom, intechOpen, 2020.

[66] J. Jeffrey, “A closer look at the losses in EV motors,” February 2019. [Online]. Available: https://chargedevs.com/features/a-closer-look-at-the-losses-in-ev-motors/. [Accessed 12 April 2021].

[67] A. Talha, “Design and Analysis of a Switched Reluctance Machine for Traction for Traction in a Hybrid Automotive Application,” Universidad de Oviedo, Oviedo, Asturias, Spain, 2017.

[68] K. Bourchas, “Manufacturing Effects on Iron Losses,” Royal Institute of Technology, Stockholm, Sweden, 2015.

[69] “Motion Control Tips,” WTWH Media, 30 March 2018. [Online]. Available: https://www.motioncontroltips.com/hysteresis-loss/. [Accessed 28 February 2023].

[70] T. H. Syed, “DESIGN OF A SWITCHED RELUCTANCE MOTOR DRIVE FOR AUTOMOTIVE APPLICATIONS,” The University of Nottingham, United Kingdom, 2018.

[71] A. Parsapour, B. M. Dehkordi and M. Moallem, “Predicting core losses and efficiency of SRM in continuous current mode of operation using improved analytical technique,” *Journal of Magnetism and Magnetic Materials,* vol. 378, no. 1, pp. 118-127, 2015.

[72] P. S. Melo and R. E. Araújo, “Switched Reluctance Motor Modeling and Loss Estimation Review,” IntechOpen, 9 September 2020. [Online]. Available: https://www.intechopen.com/chapters/72132. [Accessed 15 September 2022].

[73] H. Xianghui and X. Wang, “Switched Reluctance Motor Loss Optimization Based on Finite Element Method,” in *2016 International Symposium on Computer, Consumer and Control (IS3C)*, Xi'an, China, 2016.

[74] N. R. Patel, V. A. Shah and M. M. Lokhande, “Comparative Analysis of 12/16 Conventional and Proposed C-core Radial Flux SRM Topologies for In-wheel Electric

Vehicle Application," *Majlesi Journal of Electrical Engineering,* vol. 13, no. 2, pp. 57-65, 2019.

[75] N. R. Patel, V. A. Shah and M. M. Lokhan, "A Mathematical and FEM Design of Novel Axial Field Switched Reluctance Motor for Electrical Vehicle (EV) Application," *World Electric Vehicle Journal,* vol. 8, pp. 1-10, 2016.

[76] V. Rallabandi and B. G. Fernandes, "Design procedure of segmented rotor switched reluctance motor for direct drive applications," *IET Electric Power Applications,* vol. 8, no. 3, pp. 77-88, 2013.

[77] A. Labak, "DESIGNING, PROTOTYPING AND INVESTIGATION OF ADVANCED FIVE-PHASE AXIAL FLUX SRM FOR ELECTRIFIED VEHICLE APPLICATION," University of Windsor, Windsor, Ontario, Canada, 2015.

[78] A.-C. Pop, V. Petrus, C. Martis, V. Lancu and J. Gyselinck, "On the Firing Angles Control of a 8/6 Switched Reluctance Machine," *Journal of Electrical and Electronics Engineering ,* vol. 4, no. 1, pp. 189-194, 2011.

[79] R. Madhavan and B. Fernandes, "Comparative Analysis of Axial Flux SRM Topologies for Electric Vehicle Application," in *2012 International Conference on Power Electronics, Drives and Energy Systems*, Bengaluru, India, 2012.

[80] "Magnetic Innovations," Magnetic Innovations, [Online]. Available: https://www.magneticinnovations.com/faq/radial-flux-permanent-magnet-motor/. [Accessed 2022 April 19].

[81] M. Belhadi, G. Krebs, C. Marchand, H. Hannoun and X. Miniger, "Evaluation of axial SRM for electric vehicle application," *Electric Power Systems Research,* vol. 148, pp. 155-161, 2017.

[82] P. Andrada, B. Blanqué, E. Martínez, J. I. Perat, J. A. Sánchez and M. Torret, "Design of a Modular Axial-Flux Double Rotor Switched Reluctance Drive," *Energies,* vol. 13, no. 5, pp. 1-17, 2020.

[83] A. Fraser, "IN-WHEEL ELECTRIC MOTORS The Packaging and Integration Challenges," Protean Electric Ltd, Farnham, United Kingdom, 2018.

[84] Y. Lan , Y. Benomar , K. Deepak, A. Aksoz , M. El Baghdadi , E. Bostanci and O. Hegazy, "Switched Reluctance Motors and Drive Systems for Electric Vehicle Powertrains: State of the Art Analysis and Future Trends," *Energies,* vol. 14, no. 8, pp. 1-29, 2021.

[85] R. Krishnan, "Switched reluctance motor drives: modeling, simulation, analysis, design, and applications," CRC Press LLC, Boca Raton, Florida, 2001.

[86] A. Van den Bossche, H. Bechaouech and M. Ibrahim, “Switched reluctance machine configurations with higher number of rotor poles than stator poles,” in *2nd European Conference on Electrical Engineering & Computer Science*, Bern, 2018.

[87] J. Ye, B. Bilgin and A. Emandi, “Comparative evaluation of power converters for 6/4 and 6/10 switched reluctance machines,” in *2012 IEEE Transportation Electrification Conference and Expo (ITEC)*, Dearborn, MI, USA, 2012.

[88] P. R. Gemin, “Sizing of Switched Reluctance Machines for Automotive Applications,” Ohio State University, Columbus, Ohio, 2003.

[89] K. A. Karim, N. Abdullah, M. N. Othman , S. A. Tarusan, R. Firdaus and N. Z. Zainal, “Effect of Poles Embrace on Switched Reluctance Motor Design,” *Journal of Multidisciplinary Engineering Science Studies,* vol. 3, no. 4, pp. 1661-1664, 2017.

[90] M. Yildirim and H. Kurum, “Influence of Poles Embrace on In-wheel Switched Reluctance Motor Design,” in *IEEE 18th International Power Electronics and Motion Control Conference (PEMC)*, Budapest, 2018.

[91] ArcelorMittal, “ArcelorMittal,” September 2014. [Online]. Available: https://industry.arcelormittal.com/repository2/Automotive_Product%20offer/ArcelorMittal%20iCARe%20technical%20offer%202014.pdf. [Accessed 05 February 2021].

[92] T. s. Europe, “Cogent Power,” 2016. [Online]. Available: https://www.tatasteeleurope.com/sites/default/files/Cogent%20NO%20brochure%202016.pdf. [Accessed 05 February 2021].

[93] thyssenkrupp, “thyssenkrupp,” April 2019. [Online]. Available: https://www.thyssenkrupp-steel.com/media/content_1/publikationen/lieferprogramme/thyssenkrupp_product-range_no-electrical-steel_powercore_steel_en.pdf. [Accessed 05 February 2021].

[94] Y. Sugawara and K. Akatsu, “Characteristics of a Switched Reluctance Motor using Grain-Oriented Electric Steel Sheet,” in *International Conference on Electrical Machines and Systems*, Brusan, Korea, 2013.

[95] L. Szabó, “Modular Switched Reluctance Machines to be Used in Automotive Applications,” Technical University of Cluj-Napoca, Cluj-Napoca, Romania, 2018.

[96] W. Ding, Y. Hu and L. Wu, “Analysis and Development of Novel Three-Phase Hybrid Magnetic Paths Switched Reluctance Motors Using Modular and Segmental Structures for EV Applications,” *IEEE/ASME Transactions on Mechatronics,* vol. 20, no. 5, pp. 2437-2451, 2015.

[97] W. Ding, Y. Hu, H. Fu and Q. Chen, “Analysis and evaluation of modular E-shaped stator switched reluctance machines employing segmented and conventional rotor topologies,” *IET Electric Power Applications,* vol. 10, no. 9, pp. 939-951, 2016.

[98] A. Labak and N. C. Kar, “Outer Rotor Switched Reluctance Motor Design for In-wheel Drive of Electric Bus Applications,” in *2012 XXth International Conference on Electrical Machines*, Marseille, France, 2012.

[99] S.-H. Mao and M.-C. Tsai, “A Novel Switched Reluctance Motor With C-Core Stators,” *IEEE Transactions on Magnetics,* vol. 41, no. 12, pp. 4413-4420, 2005.

[100] M. A. J. Kondelaji, S. A. Ansari, M. Mirsalim and J. S. Moghani, “Modeling and Analysis of a Modular Switched Reluctance Motor for EV Applications,” in *International Conference on Fundamental Research in Electrical Engineering*, Tehan, Iran, 2017.

[101] M. Ruba, I.-A. Viorel and L. Szabó, “Modular stator switched reluctance motor for fault tolerant drive systems,” *IET Power Applications,* vol. 7, no. 3, pp. 159-169, 2013.

[102] S. R. Mousavi-Aghdam, M. R. Feyzi, N. Bianchi and M. Morandin, “Design and Analysis of a Novel High-Torque Stator-Segmented SRM,” *IEEE Transactions on Industrial Electronics,* vol. 63, no. 3, pp. 1458-1466, 2016.

[103] C. Lee, R. Krishnan and N. Lobo, “Novel Two-Phase Switched Reluctance Machine Using Common-Pole E-Core Structure: Concept, Analysis, and Experimental Verification,” *IEEE Transactions on Industry Applications,* vol. 45, no. 2, pp. 703-711, 2009.

[104] H. Zhang, D.-H. Lee and J.-W. Ahn, “A Segmental Rotor Type 12/8 Switched Reluctance Motor: Concept, Design and Analysis,” in *2014 IEEE International Conference on Industrial Technology (ICIT)*, Busan, Korea, 2014.

[105] L. Zeng and H. Yu, “Research on a novel Rotor Structure Switched Reluctance Motor,” in *2012 International Conference on Applied Physics and Industrial Engineering*, Jilin, China, 2012.

[106] N. R. Patel, V. A. Shah and M. M. Lokhande, “A Novel Approach to the Design and Development of 12/15 Radial Field C-Core Switched Reluctance Motor for Implementation in Electric Vehicle Application,” *IEEE Transactions on Vehicular Technology ,* vol. 67, no. 9, pp. 8031-8040, 2018.

[107] W. Ding, Y. Hu, H. Fu and Q. Chen, “Analysis of Novel Segmented E-shaped Stator Switched Reluctance Machines with Segmental and Conventional Rotor Topologies,” in *2016 Eleventh International Conference on Ecological Vehicles and Renewable Energies (EVER)*, Monte-Carlo, Monaco, 2016.

[108] W. Ding, Y. Hu, H. Fu and Q. Chen, “Evaluation of a Segmented-Stator Hybrid Excitation Switched Reluctance Machine with Permanent Magnets for Electric

Vehicles," in *2016 Eleventh International Conference on Ecological Vehicles and Renewable Energies (EVER)*, Monte Carlo, Monaco, 2016.

[109] W. Ding, Y. Hu, Q. Ze, X. Liu and Y. Liu, "A Novel Modular E-Core Stators and Segmental Rotors Switched Reluctance Machine for Electric Vehicles," in *2014 Ninth International Conference on Ecological Vehicles and Renewable Energies (EVER)*, Monte-Carlo, Monaco, 2014.

[110] W. Ding, L. Liu, Y. Hu and Y. Liu, "Modular switched reluctance machine with E-core stators and segmental rotors for high reliability applications," *Electrical Power and Energy Systems,* vol. 62, pp. 496-506, 2014.

[111] W. Ding, Z. Yin, L. Liu, J. Lou, Y. Hu and Y. Liu, "Magnetic circuit model and finite-element analysis of a modular switched reluctance machine with E-core stators and multi-layer common rotors," *IET Electric Power Applications,* vol. 8, no. 8, pp. 296-309, 2014.

[112] Y. Ishihara, H. Ishikawa, M. Sugiura and H. Naitoh, "Improving the Efficiency of Switched Reluctance Motors using a Step-Skewed Rotor," *IEEJ Journal of Industry Applications,* vol. 4, no. 4, pp. 445-453, 2015.

[113] M. M. Bouiabadi, A. D. Aliabad, S. M. Mousavi and E. Amiri, "Design and analysis of E-core PM-assisted switched reluctance motor," *IET Electric Power Applications,* vol. 14, no. 5, pp. 859-864, 2020.

[114] S. Basserrah, "Theoretical and Experimental Investigations of a Permanent Magnet Excited Transverse Flux Machine with a Segmented Stator for In-Wheel Motor Applications," University of Bremen, Bremen, 2014.

[115] X. Li and E. Mendrela, "Optimization of Construction of Linear Switched Reluctance Motor with Transverse Magnetic Flux," in *2008 IEEE Region 5 Conference*, Kansas City, MO, USA, 2008.

[116] "epower-technology," ePower-Motors, [Online]. Available: https://epower-technology.dk/technology/du-srm. [Accessed 12 April 2021].

[117] S. Kachapornkul, R. Pupadubsin, P. Somsiri, P. Jitkreeyarn and K. Tungpimolrut, "Performance Improvement of a Switched Reluctance Motor and Drive System Designed for an Electric Motorcycle," *Energies,* vol. 15, no. 3, pp. 1-17, 2022.

[118] K. Hameyer and R. Belmans, Numerical Modelling and Design of ELECTRICAL MACHINES and DEVICES, Southampton, UK: WIT Press, 1999.

[119] M. KARAKAYA, I. Iskender and H. Ariani, "PERFORMANCE ANALYSIS OF A DISTRIBUTION TRANSFORMER," *International Journal on Technical and Physical Problems of Engineerin,* vol. 12, no. 4, pp. 57-62, 2020.

[120] U. Anderson, “Time-Domain Methods for Maxwell Equations,” Kungliga Tekniska Högskolan Royal Institute of Technology, Stockholm, 2001.

[121] C. Wieners, “A short introduction to Numerical Methods for Maxwell’s Equations,” Karlsruhe Institute of Technology, Karlsruhe, Germany, 2008.

[122] M. A. Musmar, “Analytical and Numerical Treatment of Maxwell's Equations,” An-Najah National University, Nablus, Palestine, 2012.

[123] “Ansys,” Ansys, Inc, [Online]. Available: https://www.ansys.com/products/electronics/ansys-maxwell.

[124] “Altair,” Altair Engineering Inc., [Online]. Available: https://www.altair.com/flux/.

[125] “Siemens,” Siemens, [Online]. Available: https://www.plm.automation.siemens.com/global/en/products/simcenter/magnet.html.

[126] “JMag,” JSOL Corporation, [Online]. Available: https://www.jmag-international.com/.

[127] “COMSOL,” COMSOL, [Online]. Available: https://www.comsol.com/.

[128] “Finite Element Method Magnetics,” WikkaWiki, [Online]. Available: https://www.femm.info/wiki/HomePage.

[129] “Elmer FEM,” Elmer FEM, [Online]. Available: http://www.elmerfem.org/blog/.

[130] M. TÖREN and M. ÇELEBİ, “A Comparison of the Programmes Using Finite Element Software in Electrical Machine Design,” *International Journal of Applied Mathematics, Electronics and Computers,* vol. 4, pp. 391-398, 2016.

[131] K. C. DE MORAIS DE CARVALHO, “Electromagnetic Modeling Approaches of Static Electric Machines,” School of Technology and Management of the Polytechnic Institute of Bragança, Bragança, Portugal, 2020.

[132] S. Li, “MULTI-PHYSICS MODELING AND DESIGN OF SWITCHED RELUCTANCE MACHINES AND LARGE SYNCHRONOUS GENERATORS,” Georgia Institute of Technology, Georgia, 2019.

[133] “Maxwell Help,” Ansys, Canonsburg, Pennsylvania, 2020.

[134] M. Mismar, “Numerical Simulation of Maxwell's Equations,” *IOSR Journal of Engineering (IOSRJEN) ,* vol. 7, no. 3, pp. 2250-3021, 2017.

[135] M. Rosu, P. Zhou, D. Lin, D. Lonel, M. Popescu, F. Blaabjerg, V. Rallabandi and D. Staton, Multiphysics Simulation by design for Electrical Machines, Power Electronics and Dives, Hoboken, New Jersey: John Wiley & Sons, Inc., 2018.

[136] Ł. Skotny, “enterfea,” Enterfea, 7 March 2017. [Online]. Available: https://enterfea.com/correct-mesh-size-quick-guide/. [Accessed 28 April 2022].

[137] *Module 03: Mesh Operations for Rotating Machines,* Ansys, 2019.

[138] “CUEMATH,” CUEMATH, [Online]. Available: https://www.cuemath.com/geometry/tetrahedron/. [Accessed 4 April 2022].

[139] *Lecture 3: Static Magnetic Solvers,* Ansys, 2016.

[140] B. Thacker, S.W.Doebling, F. Hemez, M. Anderson, J. Pepin and E. Rodriguez, “Concepts of Model Verification and Validation,” Los Alamos National Lab, Los Alamos, 2004.

[141] I. The Institute of Electrical and Electronics Engineers, “IEEE Standard for System, Software, and Hardware Verification and Validation,” The Institute of Electrical and Electronics Engineers, Inc., New York, 2016.

[142] “Conformity assessment — General principles and requirements for validation and verification bodies,” International Organization for Standardization and the International Electrotechnical Commission, Vernier, Geneva, 2019.

[143] L. D. Erasmus, “The formulation and evaluation of a neuron model based on biological neurons,” North West University, Potchefstroom, 2007.

[144] D. Inc, “Ansys Quality Assurance,” 30 May 2021. [Online]. Available: https://www.ansys.com/content/dam/company/quality-assurance/2021-2024-ansys-inc-iso-9001-2015-dqs.pdf.

[145] *Workshop 1.2: UDPs,* Ansys, 2019.

[146] M. A. J. Kondelaji, “Design, Simulation, and Prototyping of Novel Modular Switched Reluctance Motors for EV Applications,” Amirkabir University of Technology, Tehran, Iran, 2020.

[147] S. Constantinides, “Arnold magnetic technologies,” October 2008. [Online]. Available: arnoldmagnetics.com/wp-content/uploads/2017/10/Designing-with-Thin-Gauge-presentation-1.pdf. [Accessed 26 August 2021].

[148] S. H. Tirmizi, “DESIGN IF A SWITCHED RELUCTANCE MOTOR DRIVE FOR AUTOMOTIVE APPLICATIONS,” University of Nottingham, Nottingham, United Kingdom, 2018.

[149] K. Cakir and A. Sabanovic, “In-wheel Motor Design for Electric Vehicles,” in *9th IEEE International Workshop on Advanced Motion Control, 2006.*, Istanbul, Turkey, 2006.

[150] A. Lebsir, A. Bentounsi, R. Rebbah, M. Benbouzid and S. Belakehal, “Comparative Study of PMSM and SRM Capabilities,” in *IEEE POWERENG 2013*, Istanbul, Turkey, 2013.

[151] A. Ahmed and D. D. Bhutia, “Propulsion System Design and Sizing of an Electric Vehicle,” *International Journal of Electronics and Electrical Engineering,* vol. 3, no. 1, pp. 14-18, 2015.

[152] W. Ding, Y. Hu, T. Wang and S. Yang, “Comprehensive Research of Modular E-Core Stator Hybrid-Flux Switched Reluctance Motors With Segmented and Nonsegmented Rotors,” *IEEE TRANSACTIONS ON ENERGY CONVERSION,* vol. 32, no. 1, pp. 382-393, 2017.

[153] R. Pohl, “Theory of pulsating-field machines,” *Journal of the Institution of Electrical Engineers - Part II: Power Engineering,* vol. 93, pp. 37-47, 1946.

[154] “Matmatch,” Matmatch GmbH, [Online]. Available: https://matmatch.com/materials/arce0145-en-10106-grade-m235-35a. [Accessed 21 April 2022].

[155] *Cogent Non-oriented electrical steel brochure,* Surahammar: Cogent .

[156] L. Veg, J. Kaska, M. Skalický and R. Pechán, “A Complex Study of Stator Tooth-Coil Winding Thermal Models for PM Synchronous Motors Used in Electric Vehicle Applications,” *Energies,* vol. 14, no. 9, pp. 1-16, 2021.

[157] D. Barater, “Automated Manufacturing of wound components for next generation Electrical machines,” Clean Sky, 2021.

[158] P. Ponomarev, “Tooth-Coil Permanent Magnet Synchronous Machine Design for Special Applications,” Lappeenranta University of Technology (Lappeenranta), Lappeenranta, Finland, 2013.

[159] T. J. Miller, “Optimal design of switched reluctance motors,” *IEEE Transactions on Industrial Electronics,* vol. 49, no. 1, pp. 15-27, 2002.

[160] M. J. Pieterse, “Development of a Thermal Model for an Inner Stator Type Reluctance Motor,” University of Waterloo , Waterloo, Ontario, Canada, 2009.

[161] H. Babaie and H. F. Farahani, “Analysis of Thermal Behaviour of High Frequency Transformers Using Finite Element Method,” *Journal of Electromagnetic Analysis and Applications,* vol. 2, no. 11, pp. 627-632, 2010.

[162] “Car Engineer,” [Online]. Available: https://www.car-engineer.com/the-different-driving-cycles/. [Accessed 20 June 2021].

[163] T. Barlow, S. Latham, I. McCrae and P. Boulter, “A reference book of driving cycles for use in the measurement of road emissions,” TRL Limited, Berkshire, United Kingdom, 2009.

[164] A. Gebisa , G. Gebresenbet, R. Gopal and R. B. Nallamothu, “Driving Cycles for Estimating Vehicle Emission Levels and Energy Consumption,” *Future Transportation,* vol. 1, no. 3, pp. 615-638, 2021.

[165] “plotaroute.com,” plotaroute.com, [Online]. Available: plotaroute.com/routeprofile/1345920. [Accessed 15 August 2020].

[166] “Stack Exchange,” Stack Exchange, Inc., 8 May 2017. [Online]. Available: https://engineering.stackexchange.com/questions/15208/how-to-calculate-the-power-torque-force-needed-to-move-a-4-wheeled-vehicle. [Accessed 13 April 2021].

[167] “Engineering ToolBox,” Engineering ToolBox, 2008. [Online]. Available: https://www.engineeringtoolbox.com/rolling-friction-resistance-d_1303.html. [Accessed 13 April 2021].

[168] A. Mahmoudi, L. S. Soong, G. Pellegrino and E. Armando, “Efficiency Maps of Electrical Machines,” *2015 IEEE Energy Conversion Congress and Exposition (ECCE),* pp. 2791-2799, 2015.

[169] A. Mash, “AndrewMash.com,” [Online]. Available: https://drajmarsh.bitbucket.io/sunpath-on-map.html. [Accessed 1 March 2021].

[170] J. Henderson Jr and T. Miller, Design of brushless permanent-magnet motors, Hillsboro: Magna Pysics Publishing, 1994.

[171] H.-J. Hong, X. Xing and R. Morris, “Torque Ripples in Electric Vehicle Drive Quality in Open and Closed Loop Control Environments,” *SAE Technical Paper.,* 2021.

[172] M. Sumega, S. Zossak, P. Varecha and P. Rafajdus, “Sources of torque ripple and their influence in BLDC motor drives,” *Transportation Research Procedia,* vol. 40, pp. 519-526, 2019.

[173] J. Jenkins, “Charged,” 25 January 2013. [Online]. Available: https://chargedevs.com/features/a-closer-look-at-switched-reluctance-motors/. [Accessed 15 March 2021].

APPENDIX A MOTOR TESTING METHODOLOGY

Electric motors have a bad reputation for being a mix of science and magic. When an electric motor fails to operate, the problem is not immediately obvious. Thus, testing an electrical motor is often done as preventative maintenance to ensure that issues are well known before any visual damage occurs. Visual damage to an electric motor can often be irreversible. In this study, the Mitsuba M2096-DII was tested to verify its motor characteristics and to construct an efficiency map. The methodology to test the motor is described in this section.

A.1 Methodology of motor testing

The Mitsuba M2096-DII are tested in the laboratory to verify motor characteristics and construct its efficiency map. The method to characterise the electric motor by experimental testing is done as follows.

The electric motor is run at full speed under no-load conditions. Once the maximum speed is obtained, the load is gradually increased, effectively increasing the output torque. However, decreasing motor speed is shown in Figure 6-6 and Figure 6-7. Theoretically, the motor would not draw current from the power supply under no-load conditions. As the load increases, the speed of the motor will decrease and the current drawn by the power supply will increase until the motor stalls or the maximum current is drawn [170].

The construction of an efficiency map follows the same procedure as that of a characteristic graph. However, an efficiency map is constructed from various characteristic graphs starting at the no-load speed, and each characteristic graph thereafter starting at a speed lower than the no-load speed.

The methodology followed to experimentally test and characterise the Mitsuba M2096-DII is performed using the prescribed laboratory setup.

A.1.1 Laboratory setup

A diagram of the laboratory setup is shown in Figure A-1, with the laboratory setup consisting of the following equipment:

- A battery used as the power supply
- The Mitsuba M2096C motor controller
- The Mitsuba M2096-DII BLDC motor
- The T40-S2TOS6 torque transducer

- A hydraulic braking system
- The G070 torque-rpm transducer
- The GEN3t portable data recorder
- A personal computer, and
- The Perception software used to control the data recorder and record measurement data

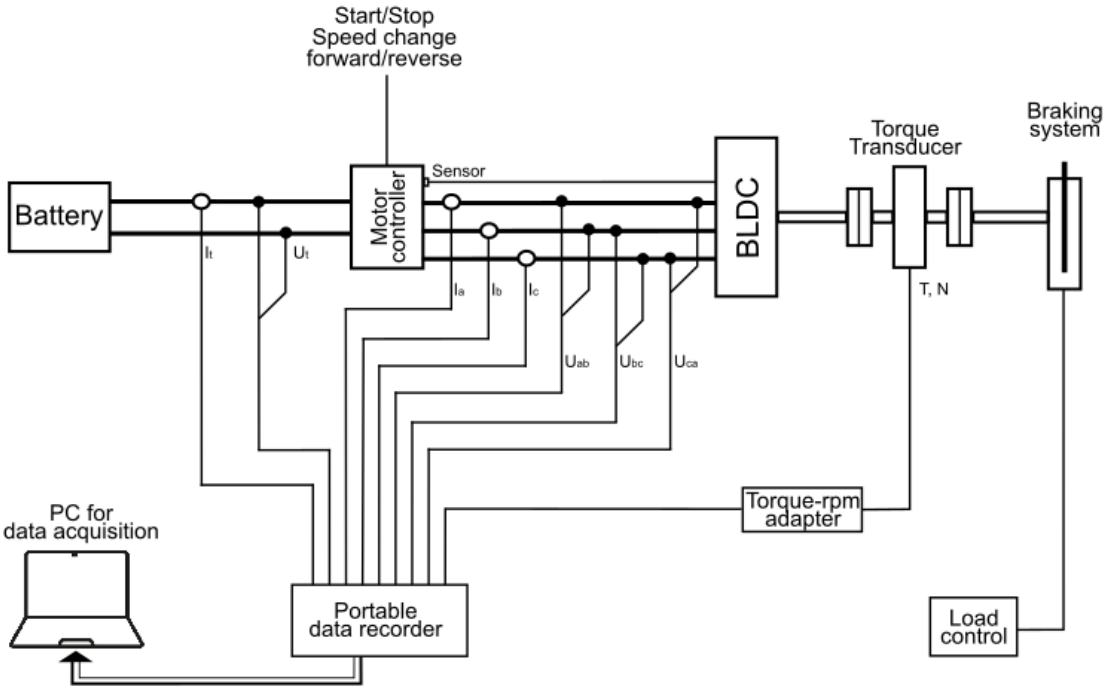

Figure A-1: Motor testing setup in the laboratory

Power measurements consisting of current were obtained using the Chauvin Arnoux E3N clamp meters. The voltages were obtained using test leads. The mechanical torque and speed of the motor were obtained by the torque transducer, while the hydraulic braking system was used to control the load. All the measured signals are transmitted through the data controller to the PC and shown using the required software. Using the software, the measurement data is viewed and recorded after validating that the measured data are correct.

A.1.2 Reliability and validity of the experimental data

Validation of the measurement equipment is necessary to ensure that reliable data is shown and recorded when using the data recorder and the required software. Measurement equipment is validated against other measuring equipment as follows.

- Current and voltage are measured using the Fluke 374 FC digital multimeter.

- Motor speed is measured using a tachometer, and
- Motor torque is validated with a calculation performed by hand. The shaft is locked and a weight is added to a known distance. Thus, the torque is known and compared to the value shown using the software.

Comparing the data obtained by the data recorder with other measuring equipment proved that the data are reliable and sufficient to be recorded for analysis.

A.1.3 Experimental data and analysis

The experimental data are obtained by the portable data recorder and stored on the computer when recorded. Analysis of the measurements shows that the battery voltage decreases as the load is applied to the motor, exceeding the maximum current limits. However, this does not affect motor performance since the input voltage of the motor controller can operate within the range of 45-160V.

Analysis of motor torque shows some torque ripple. Torque ripple is a known phenomenon in electric motors [171, 172]. However, torque ripple measurements are probably exaggerated with the vibration of the test bench under operation. Also, the shaft is not correctly aligned between the electric motor, torque transducer, and braking system. The alignment of the shaft was made by human eye, and the electric motor was run between adjustments until the least amount of torque ripple could be noticed. Another factor that contributes to shaft misalignment and torque ripple is the rubber coupling between the shaft of the torque transducer and the braking system. Ideally, there would be a single shaft between all connected equipment.

Ultimately, experimental data of the Mitsuba M2096-DII are obtained and analysed using the Perception software. When adjusting the load, the speed and torque measurements were taken after stabilisation. The analysed data are exported to Microsoft Excel for the construction of the characteristic graphs.

A.2 Summary of motor tests

The characteristics of the Mitsuba M2096-DII were desirable to validate the motor datasheet (Figure D-1, p.181). Constructing an efficiency map was necessary to evaluate the motor in §6.2.1, p.136 and §6.3.1, p.140. The efficiency map was also important for the NWU when planning drive operations in a solar race. Thus, motor testing holds valuable information about an electric motor and is not only used for preventative maintenance. Following the prescribed methodology, any electric motor intended as a traction motor can be tested for characterisation and construction of an efficiency map when required to evaluate the electric motor.

APPENDIX B VALIDATION OF A MODULAR SWITCHED RELUCTANCE MOTOR

B.1 Two-dimensional validation

Modelling an electric motor in 2D requires an additional amount of input to obtain a model that predicts the characteristics and performance of an actual electric motor. Different correction methodologies compensate for the effects of 2D models. These methodologies allow an accurate representation of an electric motor. However, these methodologies only account for certain electric motors. Thus, in the case of new motor design concepts, a considerable need to accurately predict the electric motor is expected. This is the case of the MSRM, as mentioned in §3.1, p.48.

This section validates the MSRM of Wen Ding *et al.*, found in articles [96, 110, 109, 97, 107, 111]. Validation of a 2D model is compared to 2D FEA data obtained in [110].

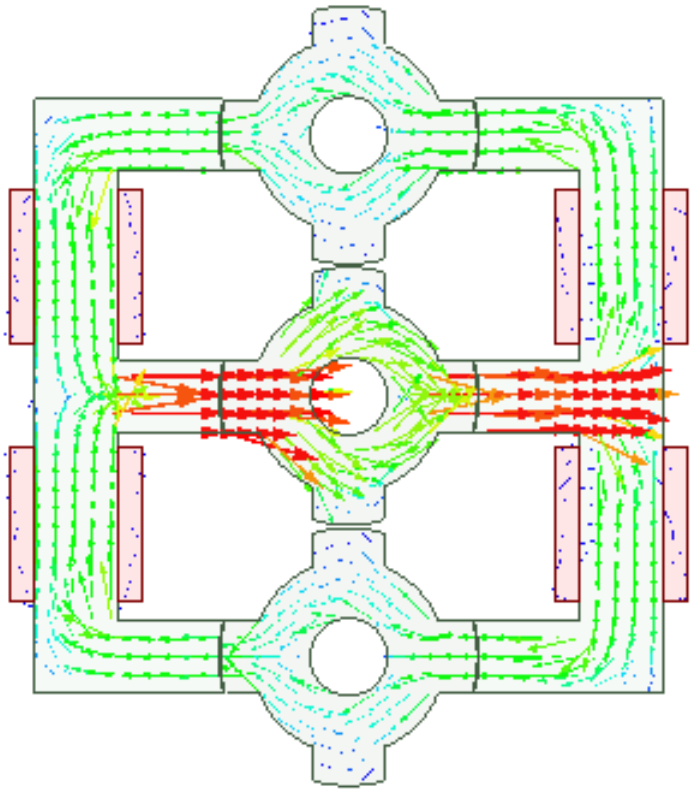

Figure B-1: Flux distribution at an aligned position for a 2D model in Ansys® Maxwell

Figure B-1 shows the magnetic flux paths of the E-core MSRM in a 2D plane. For this validation, both the magnetic characteristics of flux linkage and inductance are validated. The magnetic characteristics are validated using Ansys® Maxwell and FEMM, as shown in Figure B-2.

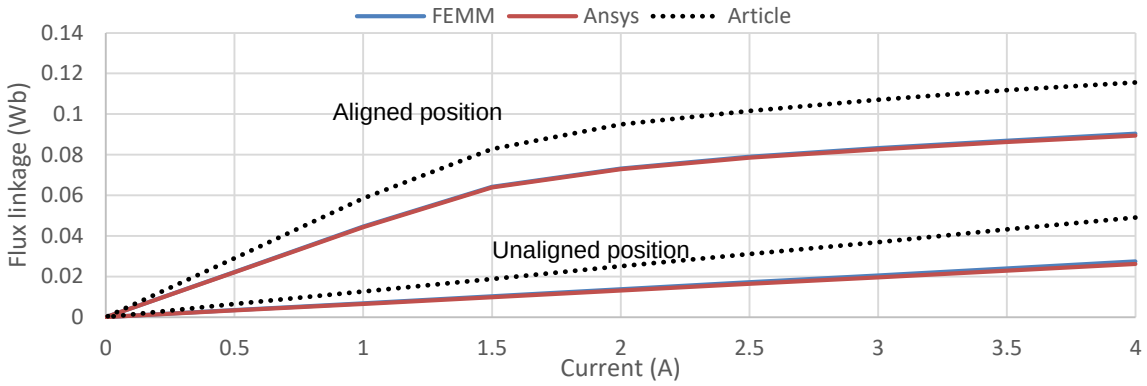

(a)

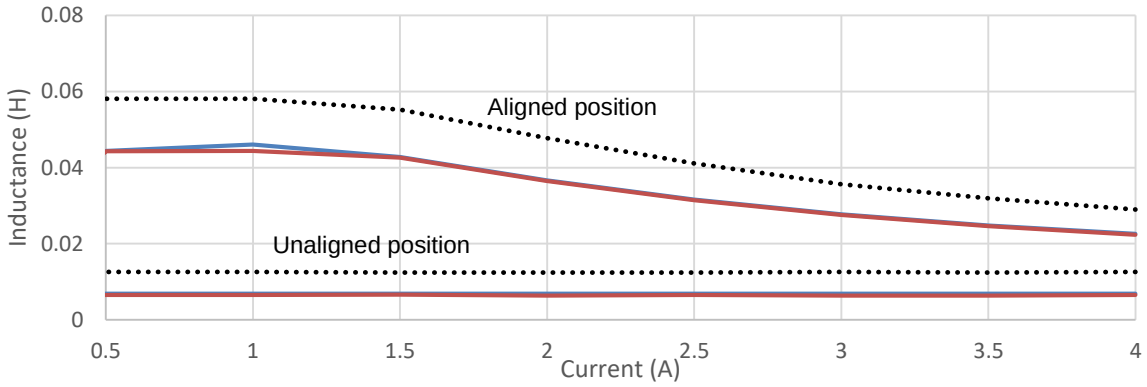

(b)

Figure B-2: Magnetic characteristics of the 2D MSRM model. (a) Flux linkage; (b) Inductance

In Figure B-2 it is observed that the simulated data using both software is fairly far from the FEA data provided by the article. The geometric setup for 2D is not the same as for a 3D model, as only one plane is used as the simulating field plane. Note from the geometry shown in Figure B-1, that a 2D geometry includes a side view of the stator cores, but a top view of the rotor cores. It could well be that the geometry was incorrect from the article, thus the reason for obtaining the difference in simulation data. Otherwise, it was most likely because no correction factor was included in the simulations. Nevertheless, no further analysis is necessary for the difference in 2D MSRM simulations.

B.2 Three-dimensional validation

The magnetic characteristics by *variation of the coil shape* and *variation of the coil fillet* mentioned in §4.4.3, p.81 are included in this section. Following the procedure in §4.4.2, the magnetic characteristics graphs are constructed and compared with the FEA data and the experimental data.

The magnetic characteristics by *variation of the coil shape* are compared in Figure B-3. The shape of the coil is altered from a square to a rectangular shape. A rectangular shape is obtained by minimising opposing coil cross-sectional areas. Analysing the flux linkage, minimal deviation occurs between the simulated, experimental, and FEA data. Observing the static torque graph, it is seen that there is no difference in torque variation, except when compared to the FEA data. Thus, the variation in coil shape does not affect the magnetostatic characteristics of the MSRM.

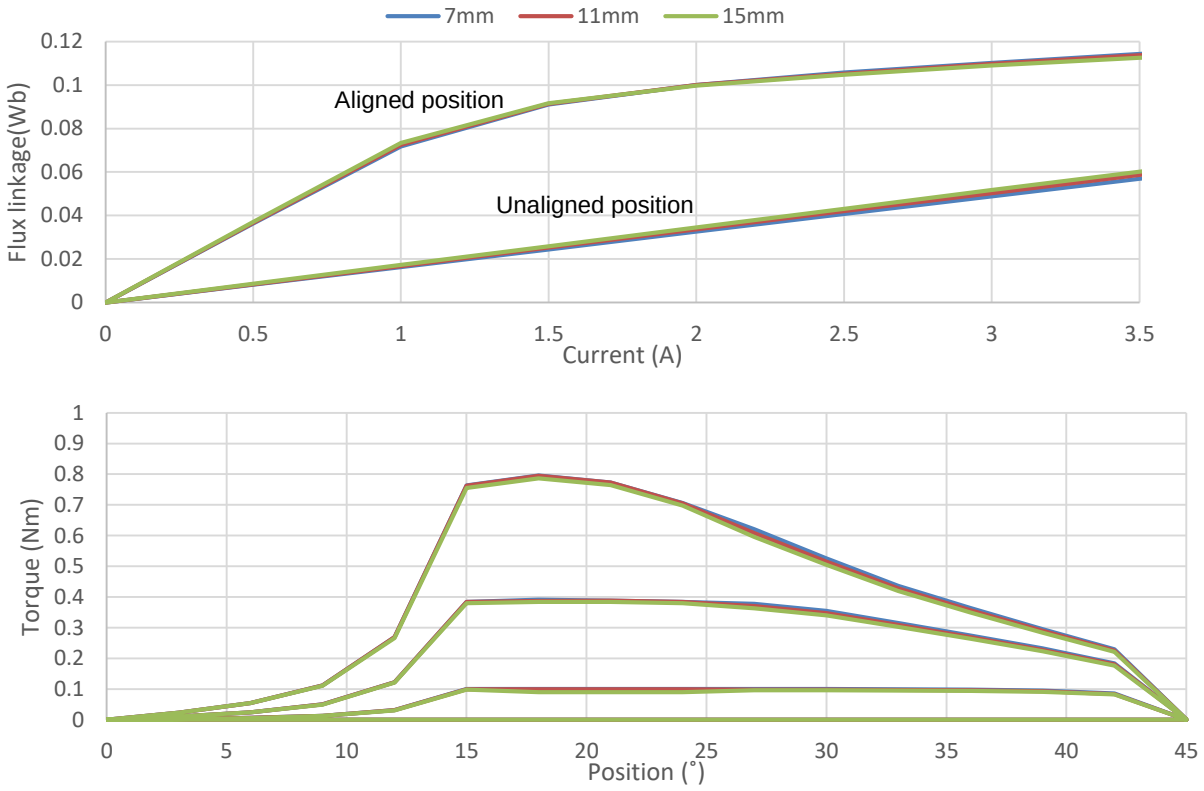

Figure B-3: Magnetic characteristics by variation of the coil shape: (a) Flux linkage; (b) Static torque.

The magnetic characteristics by *variation of the coil fillet* are compared in Figure B-4. The radius of the coil fillet is increased during simulations. Note that all four phase coils are changed to the same coil fillet value. Analysing the flux linkage, minimal deviation occurs between the simulated, experimental, and FEA data. Observing the static torque graph, it is seen that there is no

difference in torque variation, except when compared to the FEA data. Thus, the variation of coil fillets does not affect the magnetostatic characteristics of the MSRM.

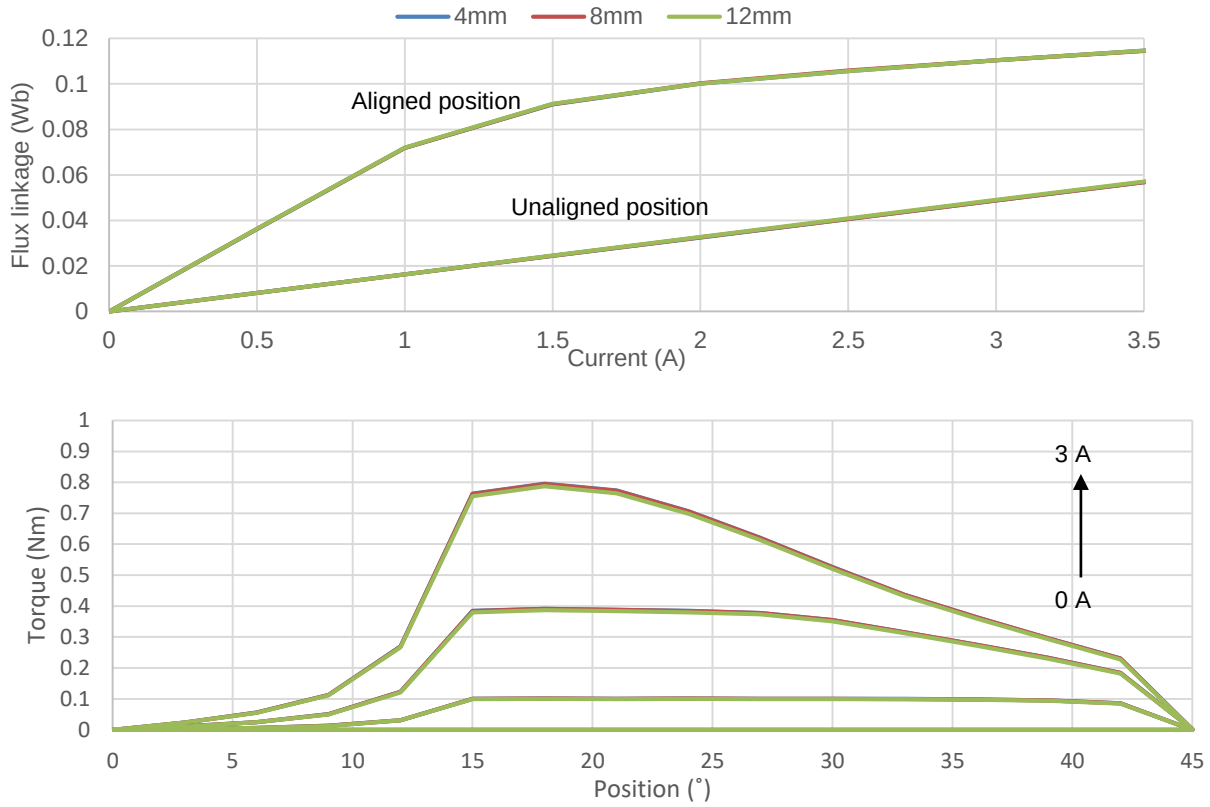

Figure B-4: Magnetic characteristics by variation of the coil fillet: (a) Flux linkage; (b) Static torque.

B.3 Summary of the validation

A 2D model of the MSRM used to validate the numerical methods in chapter 4 was constructed using both FEMM and Maxwell 2D. It was observed that a large difference between the simulation data and the comparative FEA data obtained from article [110] occured. This is likely due to incorrect material, boundary, and geometry settings compared to the simulation data provided by Wen Ding *et al.* in the respective article. Supplementary analysis of a 2D model was not provided, and a transient 2D simulation would not be possible for an MSRM. This is because the magnetic flux is 3D and not 2D as expected for a conventional SRM.

The magnetostatic characteristics, analysed by a parametric sweep of the geometric parameters, were provided in §4.3.3, p.71. In this appendix, the magnetostatic characteristics that do not influence the magnetostatic characteristics were included. These geometric parameters included the coil shape, as the coil was changed from a square to a more rectangular shape, and the coil fillet by increasing the radius of the fillet on the edges of the coil.

APPENDIX C DESIGN OF A MODULAR SWITCHED RELUCTANCE MOTOR

During the analysis of the proposed MSRM, the same numerical modelling methods, demonstrated in chapter 4 was used. This process involved the design and development of an MSRM and analysing its magnetostatic and transient characteristics. This appendix contains the mesh model of the proposed MSRM for transient solutions. Furthermore, the steady-state thermal validation and solution setup are explained, so that the coil temperature during excitation could be obtained, as discussed in §5.2.4, p.112.

C.1 Modular switched reluctance motor transient mesh

A quarter view of the mesh generated by Ansys® Maxwell is shown in Figure C-1. The mesh setup used to simulate the transient solutions of the proposed MSRM in §5.3.2, p.115 consisted of the following mesh selection for each geometric aspect. Refer to §5.2.4, p.112 as a minor difference in the mesh setup occur, compared to the setup used for validation in §4.4.1.3, p.78.

- Band
    - Inside selection length-based mesh of 5 mm
- Rotor core segments
    - Inside selection length-based mesh of 5 mm
- Stator core segment
    - Inside selection mesh of 5 mm
- Coils
    - Inside selection length-based mesh of 4 mm

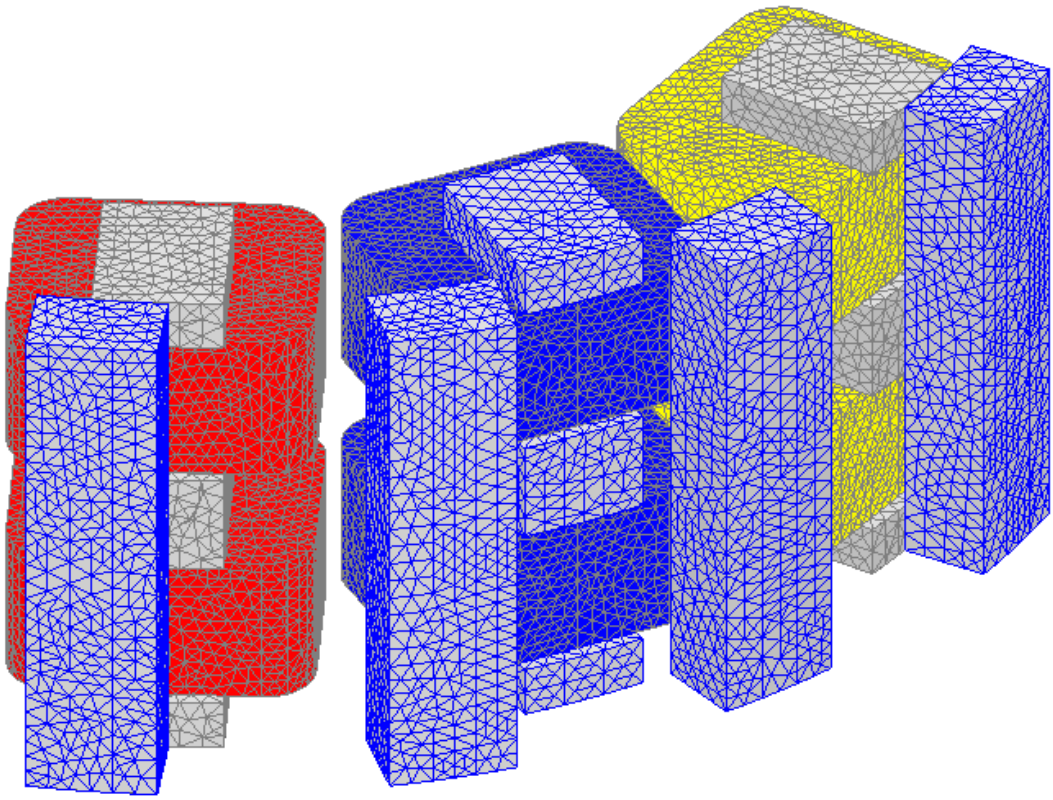

Figure C-1: 3D FEA mesh model of the proposed MSRM

C.2 Thermal validation and analysis

The thermal analysis of the coil windings ensures that an electric machine operates within respectable temperature limits. As discussed in §5.2.4, p.112, the insulation of the coil and magnetic material sets the temperature limit of the proposed motor. To ensure an electric motor operates within its thermal limits is a very complex simulation process. A steady-state thermal analysis of the coil windings was obtained to predict the maximum allowable excitation current.

To ensure that the proper temperature of a coil during simulation was obtained, the validation of a C-core is performed. The C-core was part of an MSRM, designed by Anas Labak, who provided an experimental test point for thermal analysis in [52]. The validation of the coil was compared to the experimental data, which were obtained by keeping the C-core motor stationary and applying a constant DC excitation while measuring the coil temperature. Steady-state coil temperature was reached when the temperature settled on a value.

C.2.1 Thermal validation

The objective of validating thermal analysis on a coil was to ensure that the temperature obtained from the solution was accurate. An accurate temperature solution acknowledged that the correct

simulation setup was followed. For steady-state thermal analysis, a two-way simulation was set up using both Ansys® Maxwell and Ansys® Steady-State Thermal. Both simulations were linked with each other, so that the thermal analysis was conducted from the results of the magnetostatic analysis.

The following setup and process were followed to obtain a steady-state thermal solution. Note that the setup for Ansys® Maxwell is not discussed, as it follows the same setup and procedure discussed in §4.3.1, p.66.

C.2.1.1 Excitation setup

The excitation of the coil is set up in the same way as the magnetostatic simulation setup in Ansys® Maxwell. A single coil wound around the C-core consists of 65 turns. A current excitation of 40 A is applied to the coil.

C.2.1.2 Boundary setup

The boundary setup in Ansys® Maxwell is the same as the magnetostatic simulation setup. However, for Ansys® Steady-State Thermal, the following boundary setup is performed as follows:

- Import the heat-generated load from Ansys® Maxwell.
- Apply a convection film coefficient of 10 W/m^2K to all surfaces. The film coefficient is assumed from the thermal study of an air-cooled transformer [161].
- Set the initial temperature, otherwise known as the ambient temperature, at 22˚C.

C.2.1.3 Solution and analysis setup

The solution and analysis setup in Ansys® Maxwell is the same as the magnetostatic simulation setup. The solution and analysis setup in Ansys® Steady-State Thermal is set to analyse the temperature on the surfaces of the coil. When the solution setup is applied, the temperature distribution on the coil surfaces will be shown.

C.2.2 Thermal procedure

To obtain the temperature distribution of a coil, the following sequence is followed between the simulations.

1. Solve the magnetostatic simulation of the coil and core segment in Ansys® Maxwell.
2. Link the magnetostatic solution to Ansys® Steady-State Thermal setup in Ansys® Workbench. This allows for interaction between the two simulation environments.
3. Set up and solve the thermal analysis of the coil as discussed above.

C.2.3 Thermal analysis results

A series of thermal simulations were completed to obtain a temperature-current graph, shown in Figure 5-17, p113. The graph shows the steady-state temperature of the coil when an excitation current was applied. Following the procedures, the steady-state coil temperature was obtained for both the validated model and the proposed MSRM model.

C.2.4 Thermal distribution of the validated model

The thermal distribution of the coil for the C-core designed by Anas Labak is shown in Figure C-2. The coil was excited with constant current excitation of 40 A. When comparing the coil surface temperature to the experimentally measured temperature in [77], a 10.13% difference was obtained. Thermal analysis of the electric motor was not part of the study, but was simply used as an indication to ensure that the proposed MSRM, designed in chapter 5 operates within respectable temperature limits as described in §5.2.4, p.112.

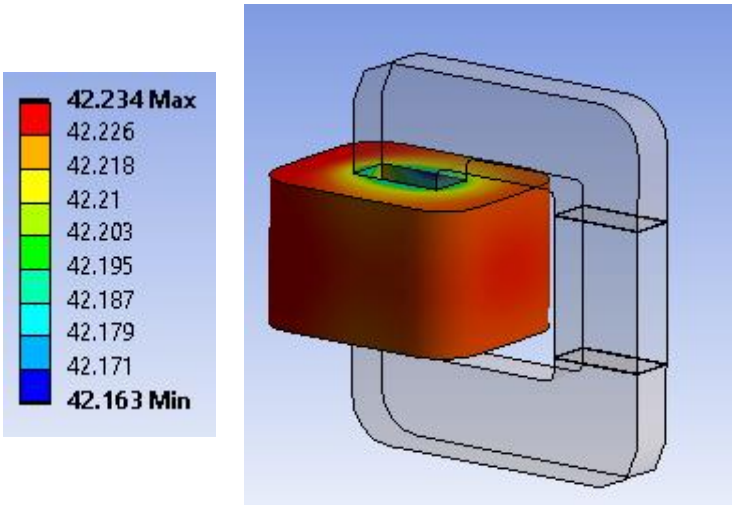

Figure C-2: Temperature distribution of a C-core coil under 40 A excitation

C.2.5 Thermal distribution of the proposed modular switched reluctance motor

The thermal distribution of the coils for the E-core in the proposed MSRM is shown in Figure C-3. The coils were excited with a constant 25 A. The surface temperature obtained by the two-way coupled simulation was around 40˚C. From the temperature distribution on the coil surface, it is observed that the temperature difference was only 0.3˚C. Therefore, the temperature difference shown on the coils was negligible.

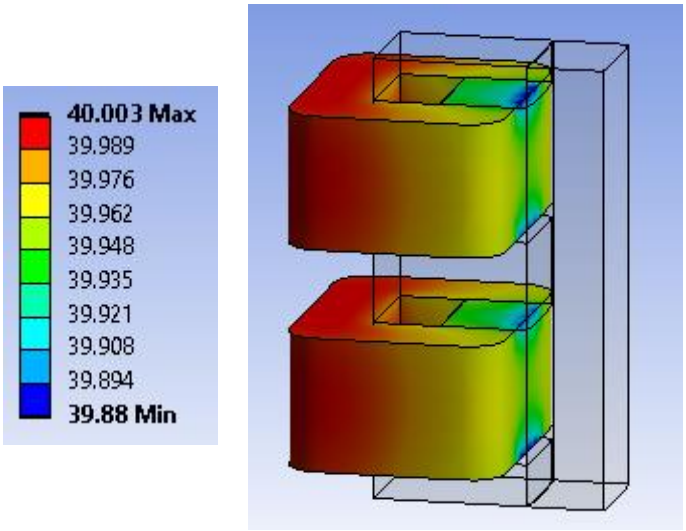

Figure C-3: Temperature distribution of the proposed E-core coils under 20 A excitation

C.3 Torque-speed characteristics

To construct an efficiency map of the proposed MSRM, enough operating points must be simulated. The efficiency map was constructed by interpolating between the efficiency curves obtained from the torque-speed characteristics. Seven torque-speed characteristic graphs were constructed from the simulations, as shown in Figure C-4. Note that the simulations were done only between the speed region of 250 rpm to 850 rpm. Simulations were limited to the region to save simulation time, since the study was limited to computer resources. Furthermore, the expected operating range was expected to occur in that region, based on the operating points of the Mitsuba M2096-DII when operated through the drive cycle (§6.2, p.135).

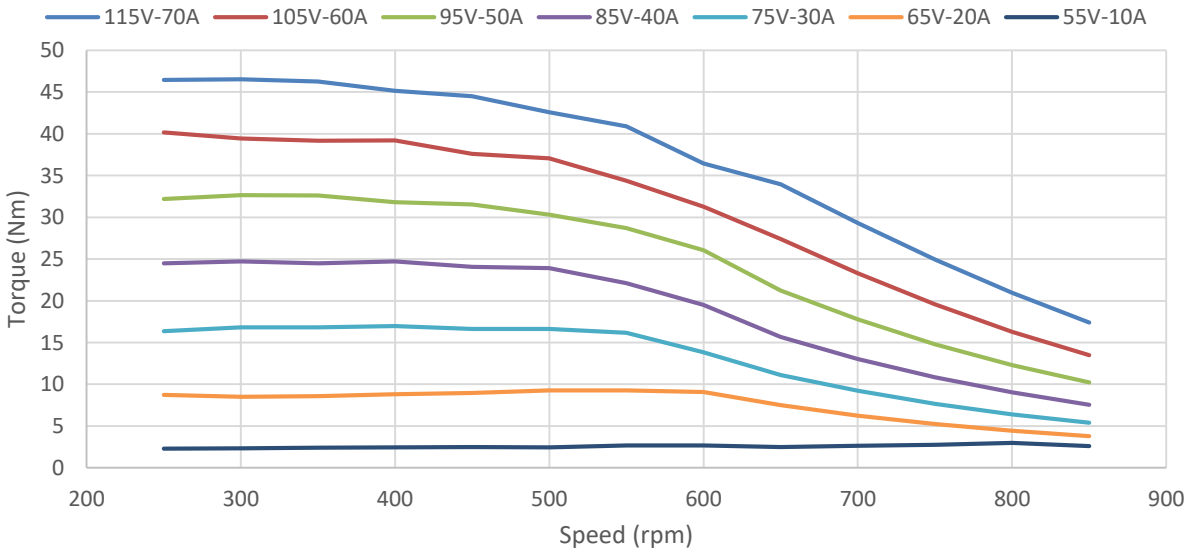

Figure C-4: Torque-speed characteristics of the proposed MSRM

C.4 Summary of the modular switched reluctance motor design

Transient simulations were a vital part of the study. Transient simulations were used to construct torque-speed characteristics of the proposed MSRM, shown in Figure C-4. These torque-speed characteristics were then used to construct efficiency graphs from which the efficiency map was constructed. Thus, the setup of the transient model is significant. The mesh setup of the proposed MSRM is shown in Figure C-1. Note that a quarter of the model was used to minimise computational time and resources. This is possible due to symmetry planes, as discussed in §4.4.1.2, p.78.

Before finalising the design and after the winding design, a thermal analysis of the coils was required. Thermal analysis was required to evaluate the maximum excitation current under the maximum allowable temperature specified by the class of conductor insulation. Refer to §5.2.4, p.112. The validation of a steady-state thermal simulation of a C-core MSRM was provided in §C.2.3. The validation setup and method were used to analyse the coil temperature of the proposed MSRM using a two-way solver coupling between Ansys® Maxwell and Ansys® Steady-State Thermal. The predicted temperature-current graph of the coils is shown in Figure 5-17, p.113.

APPENDIX D EVALUATION

D.1 The Mitsuba M2096-DII

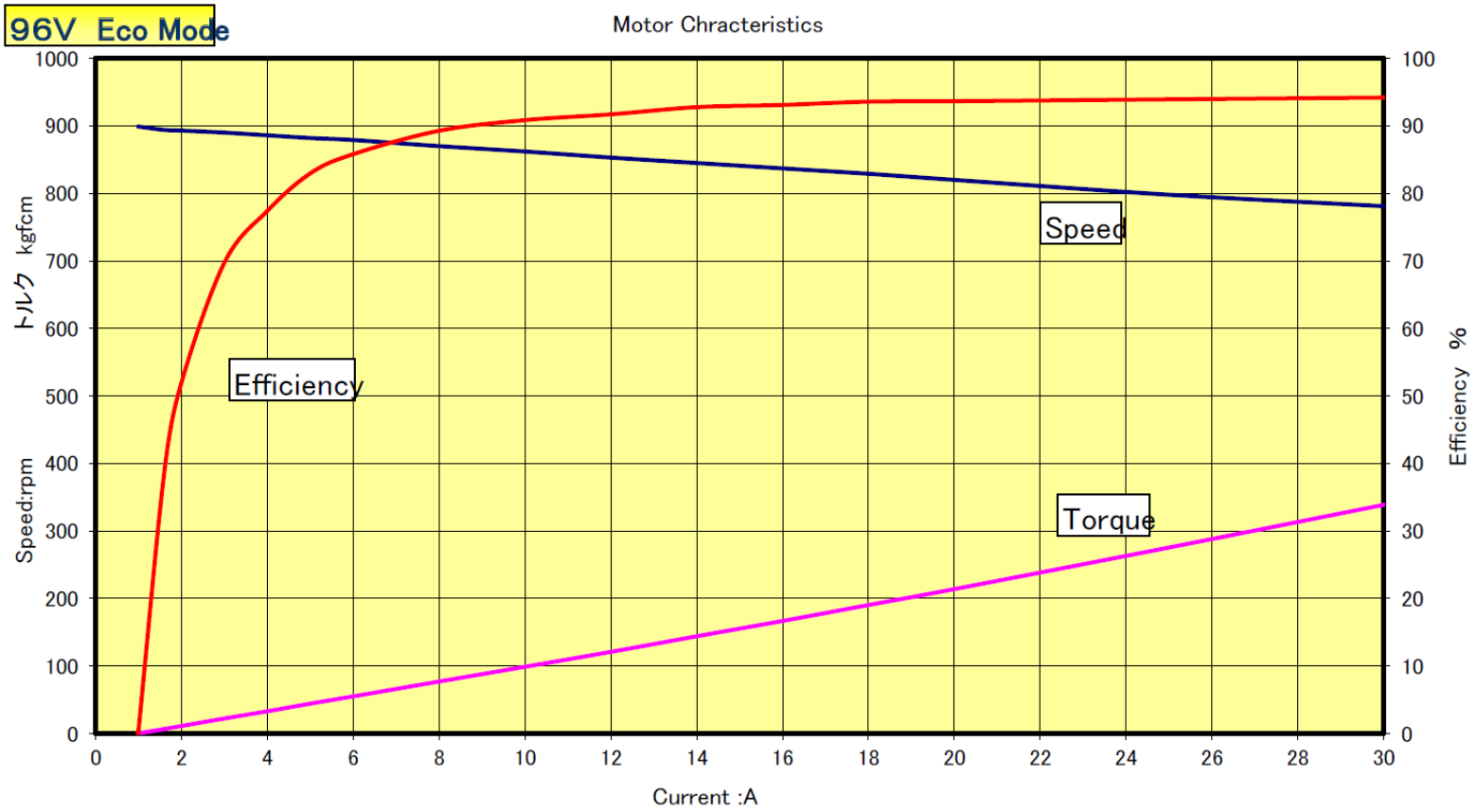

Figure D-1: Mitsuba M2096-DII motor characteristics as from the datasheet

Table D-1: Analytical evaluation of the Mitsuba M2096-DII through the drive cycle

Distance (km)	Speed (km/h)	time taken (H)	Time of day (HH:MM)	Energy used by motor (W)	Energy of the sun as input (W)	Energy balance (W)
0	0	0	7:00	1.6	1.6	1.6
0	0	0	7:03	29.03945	27.43945	29.03945
0	0	0	7:06	56.6566	27.61715	56.6566
0	0	0	7:09	84.44965	27.79305	84.44965
0	0	0	7:12	112.4168	27.96715	112.4168
0	0	0	7:15	140.5563	28.13945	140.5563
0	0	0	7:18	168.8662	28.30995	168.8662
0	0	0	7:21	197.3449	28.47865	197.3449
0	0	0	7:24	225.9904	28.64555	225.9904
0	0	0	7:27	254.8011	28.81065	254.8011
0	0	0	7:30	283.775	28.97395	283.775
0	0	0	7:33	312.9105	29.13545	312.9105
0	0	0	7:36	342.2056	29.29515	342.2056
0	0	0	7:39	371.6587	29.45305	371.6587
0	0	0	7:42	401.2678	29.60915	401.2678
0	0	0	7:45	431.0313	29.76345	431.0313
0	0	0	7:48	460.9472	29.91595	460.9472
0	0	0	7:51	491.0139	30.06665	491.0139
0	0	0	7:54	521.2294	30.21555	521.2294
0	0	0	7:57	551.5921	30.36265	551.5921
0	0	0	8:00	582.1	30.50795	582.1
0.9	75	0.012	8:00	589.4433	7.343329	589.4433
1.8	75	0.012	8:01	596.7949	7.351569	596.7949
2.7	70	0.012857	8:02	604.6807	7.885798	604.6807
3.6	70	0.012857	8:02	612.5759	7.895199	612.5759
4.5	70	0.012857	8:03	620.4805	7.904569	620.4805
6.75	70	0.032143	8:05	640.2827	19.80222	632.2233
7.2	70	0.006429	8:06	644.2501	3.967406	634.1317
8.1	70	0.012857	8:06	652.1918	7.941744	637.0775
9.9	70	0.025714	8:08	668.1029	15.91111	640.5675
11.25	70	0.019286	8:09	680.0603	11.95738	641.8565
12.15	70	0.012857	8:10	688.0433	7.98298	640.1089
14.85	65	0.041538	8:12	713.8964	25.85306	638.6504
15.3	65	0.006923	8:13	718.2143	4.317985	637.8923
16.2	65	0.013846	8:14	726.8581	8.643763	634.9366
17.1	65	0.013846	8:14	735.5122	8.654121	630.1792
20.25	65	0.048462	8:17	765.8827	30.37044	608.442
22.05	60	0.03	8:19	784.7461	18.86338	598.6341
23.4	60	0.0225	8:20	798.9247	14.17868	588.9322
25.2	60	0.03	8:22	817.8709	18.94613	573.9486

27.45	60	0.0375	8:24	841.6192	23.74836	550.0936
31.5	60	0.0675	8:29	884.5479	42.92869	502.7337
34.2	60	0.045	8:31	913.295	28.74705	466.7513
36	60	0.03	8:33	932.5158	19.22079	440.8398
38.25	55	0.040909	8:36	958.7974	26.28167	407.9501
39.6	55	0.024545	8:37	974.6057	15.80824	386.6513
40.5	55	0.016364	8:38	985.1607	10.55504	370.862
41.4	55	0.016364	8:39	995.7286	10.56794	354.1197
41.85	55	0.008182	8:39	1001.017	5.288787	345.181
43.2	55	0.024545	8:41	1016.903	15.88554	314.8189
43.65	55	0.008182	8:41	1022.205	5.301544	303.8193
45	55	0.024545	8:43	1038.128	15.92362	269.0544
45.9	50	0.018	8:44	1049.823	11.69533	243.0015
46.35	50	0.009	8:44	1055.677	5.853347	228.4884
46.8	50	0.009	8:45	1061.534	5.857122	213.307
47.25	50	0.009	8:46	1067.395	5.860886	196.85
48.15	75	0.012	8:46	1075.215	7.820353	204.6704
49.05	75	0.012	8:47	1083.042	7.827002	212.4974
49.95	70	0.012857	8:48	1091.436	8.393424	220.8908
50.85	70	0.012857	8:49	1099.837	8.400997	229.2918
51.75	70	0.012857	8:49	1108.245	8.40854	237.7003
54	60	0.0375	8:52	1132.813	24.56771	262.268
54.45	60	0.0075	8:52	1137.734	4.921143	267.1892
55.35	55	0.016364	8:53	1148.48	10.74578	277.935
57.15	50	0.036	8:55	1172.162	23.68263	301.6176
58.5	45	0.03	8:57	1191.942	19.77915	321.3967
59.4	40	0.0225	8:58	1206.802	14.86014	336.2569
62.1	30	0.09	9:04	1266.46	59.65808	395.915
62.55	25	0.018	9:05	1278.433	11.97277	407.8877
63.45	65	0.013846	9:06	1287.652	9.219026	405.5074
64.35	65	0.013846	9:06	1296.879	9.226988	401.3228
67.5	65	0.048462	9:09	1329.235	32.35661	381.5717
69.3	60	0.03	9:11	1349.313	20.07821	372.9787
70.65	60	0.0225	9:13	1364.396	15.08243	364.1805
72.45	60	0.03	9:14	1384.537	20.14128	350.3921
74.7	60	0.0375	9:17	1409.764	25.22648	328.0152
78.75	60	0.0675	9:21	1455.309	45.54503	283.2717
81.45	60	0.045	9:23	1485.768	30.45965	249.0018
83.25	50	0.036	9:25	1510.19	24.42215	232.0941
85.5	50	0.045	9:28	1540.785	30.59462	206.8551
86.85	50	0.027	9:30	1559.177	18.39196	189.5445
87.75	50	0.018	9:31	1571.453	12.2758	176.7193
88.65	50	0.018	9:32	1583.74	12.28729	162.7987
89.1	50	0.009	9:32	1589.888	6.14793	155.0153
90.45	50	0.027	9:34	1608.349	18.4608	129.1583

90.9	50	0.009	9:35	1614.508	6.159234	119.6914
92.25	50	0.027	9:36	1633.002	18.49446	89.17164
93.15	50	0.018	9:37	1645.346	12.3435	63.76695
93.6	50	0.009	9:38	1651.522	6.175876	49.57638
94.05	50	0.009	9:38	1657.7	6.178613	34.71642
94.5	50	0.009	9:39	1663.882	6.181339	18.5799
95.4	75	0.012	9:40	1672.128	8.246008	26.82591
96.3	75	0.012	9:40	1680.379	8.250812	35.07672
97.2	70	0.012857	9:41	1689.224	8.845457	43.92218
98.1	70	0.012857	9:42	1698.075	8.850912	52.77309
99	70	0.012857	9:43	1706.931	8.856336	61.62943
101.25	70	0.032143	9:45	1729.096	22.16437	75.73444
101.7	65	0.006923	9:45	1733.874	4.778231	79.02759
102.6	60	0.015	9:46	1744.232	10.3581	87.18323
104.4	55	0.032727	9:48	1766.856	22.6243	105.3573
105.75	50	0.027	9:50	1785.547	18.69037	122.2125
106.65	45	0.02	9:51	1799.406	13.8593	132.7466
109.35	35	0.077143	9:55	1852.977	53.5713	183.5638
109.8	30	0.015	9:56	1863.415	10.4373	192.0756
110.7	35	0.025714	9:58	1881.322	17.90786	204.7576
111.6	30	0.03	10:00	1902.239	20.91672	219.3662
114.75	25	0.126	10:07	1990.366	88.12652	280.7877
116.55	35	0.051429	10:10	2026.459	36.09372	298.3312
117.9	40	0.03	10:12	2047.546	21.08658	301.3566
119.7	40	0.04	10:14	2075.697	28.15119	303.3557
121.95	40	0.05	10:17	2110.942	35.24515	300.3447
126	40	0.09	10:23	2174.535	63.59308	290.1555
128.7	40	0.06	10:26	2217.035	42.4995	278.6128
130.5	40	0.04	10:29	2245.412	28.37745	268.8376
132.75	40	0.05	10:32	2280.933	35.5202	251.6173
134.1	40	0.03	10:34	2302.27	21.33724	239.8108
135	40	0.02	10:35	2316.505	14.23505	230.4385
135.9	40	0.02	10:36	2330.748	14.24309	220.0417
136.35	40	0.01	10:37	2337.872	7.124528	214.0418
137.7	40	0.03	10:38	2359.258	21.38534	193.3656
138.15	40	0.01	10:39	2366.39	7.132315	185.5859
139.5	40	0.03	10:41	2387.798	21.40835	160.4508
140.4	40	0.02	10:42	2402.08	14.28159	138.1264
140.85	40	0.01	10:43	2409.224	7.143562	125.6983
141.3	40	0.01	10:43	2416.369	7.145386	112.2745
141.75	40	0.01	10:44	2423.516	7.147196	97.85549
142.65	75	0.012	10:45	2432.095	8.579003	106.4345
143.55	75	0.012	10:45	2440.677	8.581564	115.0161
144.45	70	0.012857	10:46	2449.874	9.197346	124.2134
145.35	70	0.012857	10:47	2459.074	9.200226	133.4136

146.25	70	0.012857	10:48	2468.277	9.203075	142.6167
148.5	70	0.032143	10:50	2491.297	23.01995	157.5773
148.95	65	0.006923	10:50	2496.258	4.960404	161.0526
149.85	60	0.015	10:51	2507.008	10.75025	169.6004
151.65	55	0.032727	10:53	2530.476	23.46773	188.6179
153	50	0.027	10:54	2549.849	19.37364	206.1564
153.9	45	0.02	10:56	2564.207	14.3581	217.1893
156.6	35	0.077143	11:00	2619.644	55.4369	269.872
157.05	30	0.015	11:01	2630.434	10.78929	278.7359
157.95	35	0.025714	11:03	2648.937	18.50312	292.0132
158.85	30	0.03	11:05	2670.535	21.59818	307.3032
162	25	0.126	11:12	2761.371	90.83555	371.4337
163.8	35	0.051429	11:15	2798.499	37.12839	390.0119
165.15	40	0.03	11:17	2820.17	21.67111	393.6218
166.95	40	0.04	11:19	2849.079	28.90875	396.3785
169.2	40	0.05	11:22	2885.236	36.15706	394.2794
173.25	40	0.09	11:28	2950.372	65.13639	385.6335
175.95	40	0.06	11:31	2993.831	43.45829	375.0496
177.75	40	0.04	11:34	3022.816	28.98549	365.8824
180	40	0.05	11:37	3059.061	36.24521	349.3871
181.35	40	0.03	11:39	3080.815	21.75355	337.997
182.25	40	0.02	11:40	3095.32	14.5048	328.8944
183.15	40	0.02	11:41	3109.826	14.50662	318.7611
183.6	40	0.01	11:42	3117.08	7.253953	312.8906
184.95	40	0.03	11:43	3138.844	21.76427	292.5934
185.4	40	0.01	11:44	3146.1	7.255509	284.9369
186.75	40	0.03	11:46	3167.868	21.76859	260.1621
187.65	40	0.02	11:47	3182.382	14.51396	238.07
188.1	40	0.01	11:48	3189.64	7.257411	225.7557
188.55	40	0.01	11:48	3196.898	7.257678	212.4442
189	40	0.01	11:49	3204.155	7.25793	198.136
189.9	60	0.015	11:50	3215.043	10.88734	209.0233
190.8	60	0.015	11:51	3225.931	10.88782	219.9111
191.7	60	0.015	11:51	3236.819	10.88826	230.7994
192.6	60	0.015	11:52	3247.708	10.88865	241.688
193.5	60	0.015	11:53	3258.597	10.88899	252.577
195.75	60	0.0375	11:56	3285.82	27.22365	279.8007
196.2	60	0.0075	11:56	3291.265	5.444881	285.2455
197.1	60	0.015	11:57	3302.155	10.88987	293.9329
198.9	60	0.03	11:59	3323.935	21.77998	307.8081
200.25	60	0.0225	12:00	3340.27	16.335	316.2391
201.15	60	0.015	12:01	3351.16	10.88992	320.4056
203.85	60	0.045	12:04	3383.829	32.66885	328.8747
204.3	60	0.0075	12:04	3389.273	5.44461	329.8058
205.2	60	0.015	12:05	3400.162	10.88899	330.5059

206.1	60	0.015	12:06	3411.051	10.88865	329.6098
209.25	60	0.0525	12:09	3449.158	38.10691	321.2869
211.05	60	0.03	12:11	3470.93	21.77244	314.3881
212.4	60	0.0225	12:12	3487.258	16.32763	306.8351
214.2	60	0.03	12:14	3509.026	21.7676	294.673
216.45	60	0.0375	12:16	3536.23	27.2048	274.2744
220.5	60	0.0675	12:20	3585.184	48.95322	232.9391
223.2	60	0.045	12:23	3617.806	32.62263	200.8322
225	60	0.03	12:25	3639.548	21.74194	177.4419
227.25	55	0.040909	12:27	3669.187	29.63895	147.9095
228.6	55	0.024545	12:29	3686.965	17.77793	128.5804
229.5	35	0.025714	12:30	3705.585	18.61984	124.8659
230.4	35	0.025714	12:32	3724.2	18.61483	120.2066
230.85	35	0.012857	12:33	3733.505	9.305458	117.1382
232.2	35	0.038571	12:35	3761.413	27.90819	105.4662
232.65	35	0.012857	12:36	3770.713	9.299899	100.6308
234	35	0.038571	12:38	3798.604	27.89077	84.20768
234.9	35	0.025714	12:39	3817.19	18.58611	67.40528
235.35	35	0.012857	12:40	3826.481	9.290641	57.63389
235.8	35	0.012857	12:41	3835.77	9.288991	46.74254
236.25	35	0.012857	12:42	3845.057	9.28731	34.77099
237.15	75	0.012	12:43	3853.724	8.666612	43.4376
238.05	75	0.012	12:43	3862.389	8.665097	52.1027
238.95	70	0.012857	12:44	3871.671	9.282322	61.38502
239.85	70	0.012857	12:45	3880.952	9.280523	70.66555
240.75	70	0.012857	12:46	3890.23	9.278694	79.94424
243	60	0.0375	12:48	3917.282	27.05212	106.9964
243.45	60	0.0075	12:48	3922.691	5.408458	112.4048
244.35	55	0.016364	12:49	3934.489	11.79794	124.2028
246.15	50	0.036	12:51	3960.433	25.94394	150.1467
247.5	45	0.03	12:53	3982.04	21.60745	171.7541
248.4	40	0.0225	12:55	3998.238	16.19788	187.952
251.1	30	0.09	13:00	4062.96	64.72198	252.674
251.55	25	0.018	13:01	4075.89	12.93044	265.6044
252.45	50	0.018	13:02	4088.816	12.92559	270.9813
253.35	50	0.018	13:03	4101.737	12.92065	274.3718
256.5	50	0.063	13:07	4146.919	45.18223	282.15
258.3	50	0.036	13:09	4172.708	25.78943	284.0403
259.65	50	0.027	13:11	4192.036	19.32773	283.9101
261.45	50	0.036	13:13	4217.787	25.75064	280.772
263.7	50	0.045	13:16	4249.942	32.15575	272.27
267.75	50	0.081	13:20	4307.728	57.78524	249.5209
270.45	50	0.054	13:24	4346.18	38.4524	230.9921
272.25	50	0.036	13:26	4371.782	25.60201	215.2643
274.5	50	0.045	13:29	4403.746	31.96429	191.3949

275.85	50	0.027	13:30	4422.904	19.15769	174.85
276.75	50	0.018	13:31	4435.667	12.76291	162.5119
277.65	50	0.018	13:32	4448.423	12.75571	149.0598
278.1	50	0.009	13:33	4454.798	6.37513	141.5036
279.45	50	0.027	13:35	4473.912	19.11436	116.3002
279.9	50	0.009	13:35	4480.28	6.367741	107.0417
281.25	50	0.027	13:37	4499.372	19.09194	77.11949
282.15	50	0.018	13:38	4512.09	12.71845	52.08975
282.6	50	0.009	13:38	4518.447	6.356341	38.07964
283.05	50	0.009	13:39	4524.801	6.354405	23.39548
283.5	50	0.009	13:39	4531.154	6.352457	7.430074
284.4	75	0.012	13:40	4539.62	8.466896	15.89697
285.3	75	0.012	13:41	4548.084	8.463391	24.36036
286.2	70	0.012857	13:42	4557.148	9.064001	33.42436
287.1	70	0.012857	13:42	4566.208	9.059918	42.48428
288	70	0.012857	13:43	4575.264	9.055805	51.54009
290.25	60	0.0375	13:45	4601.653	26.38898	77.92907
290.7	60	0.0075	13:46	4606.926	5.273499	83.20257
291.6	55	0.016364	13:47	4618.427	11.50079	94.70335
293.4	50	0.036	13:49	4643.704	25.27718	119.9805
294.75	45	0.03	13:51	4664.742	21.03814	141.0187
295.65	40	0.0225	13:52	4680.505	15.76274	156.7814
298.35	30	0.09	13:58	4743.416	62.91146	219.6929
298.8	25	0.018	13:59	4755.971	12.5549	232.2478
299.7	50	0.018	14:00	4768.517	12.54558	237.2446
300.6	50	0.018	14:01	4781.053	12.53617	240.2507
303.75	50	0.063	14:05	4824.854	43.80128	246.6479
305.55	50	0.036	14:07	4849.83	24.9757	247.7245
306.9	50	0.027	14:08	4868.536	18.70568	246.9722
308.7	50	0.036	14:10	4893.441	24.90557	242.989
310.95	50	0.045	14:13	4924.515	31.07424	233.4056
315	50	0.081	14:18	4980.283	55.76801	208.6392
317.7	50	0.054	14:21	5017.341	37.05723	188.7153
319.5	50	0.036	14:23	5041.99	24.64951	172.0349
321.75	50	0.045	14:26	5072.739	30.74849	146.9497
323.1	50	0.027	14:28	5091.154	18.41478	129.662
324	35	0.025714	14:29	5108.667	17.51364	124.8413
324.9	35	0.025714	14:31	5126.157	17.48973	119.0569
325.35	35	0.012857	14:32	5134.893	8.735826	115.4188
326.7	35	0.038571	14:34	5161.064	26.17095	102.0096
327.15	35	0.012857	14:35	5169.775	8.711371	96.58562
328.5	35	0.038571	14:37	5195.872	26.09685	78.36861
329.4	35	0.025714	14:39	5213.238	17.36654	60.34665
329.85	35	0.012857	14:39	5221.912	8.673771	49.95839
330.3	35	0.012857	14:40	5230.58	8.667397	38.44544

330.75	35	0.012857	14:41	5239.241	8.660992	25.84757
331.65	75	0.012	14:42	5247.318	8.077787	33.92536
332.55	75	0.012	14:42	5255.391	8.072157	41.99752
333.45	70	0.012857	14:43	5264.033	8.642463	50.63998
334.35	70	0.012857	14:44	5272.669	8.63594	59.27592
335.25	70	0.012857	14:45	5281.298	8.629387	67.90531
337.5	60	0.0375	14:47	5306.43	25.13133	93.03663
337.95	60	0.0075	14:47	5311.449	5.019477	98.05611
338.85	55	0.016364	14:48	5322.393	10.94368	108.9998
340.65	50	0.036	14:50	5346.43	24.03762	133.0374
342	45	0.03	14:52	5366.421	19.99056	153.028
342.9	40	0.0225	14:54	5381.389	14.96834	167.9963
345.6	30	0.09	14:59	5441.048	59.65914	227.6554
346.05	25	0.018	15:00	5452.939	11.89009	239.5455
346.95	50	0.018	15:01	5464.815	11.87598	243.8728
347.85	50	0.018	15:02	5476.676	11.86179	246.2045
351	50	0.063	15:06	5518.08	41.4033	250.2037
352.8	50	0.036	15:08	5541.659	23.57913	249.8837
354.15	50	0.027	15:10	5559.304	17.6457	248.0715
355.95	50	0.036	15:12	5582.78	23.47552	242.6582
358.2	50	0.045	15:15	5612.04	29.25977	231.2603
362.25	50	0.081	15:20	5664.466	52.42665	203.1526
364.95	50	0.054	15:23	5699.242	34.77586	180.9473
366.75	50	0.036	15:25	5722.347	23.10469	162.7221
369	50	0.045	15:28	5751.137	28.79056	135.679
370.35	50	0.027	15:29	5768.363	17.22567	117.2021
371.25	35	0.025714	15:31	5784.734	16.37115	111.2389
372.15	35	0.025714	15:32	5801.072	16.33749	104.3023
372.6	35	0.012857	15:33	5809.228	8.156043	100.0844
373.95	35	0.038571	15:35	5833.645	24.41696	84.92126
374.4	35	0.012857	15:36	5841.767	8.121829	78.90772
375.75	35	0.038571	15:39	5866.08	24.31358	58.90744
376.65	35	0.025714	15:40	5882.246	16.1655	39.68443
377.1	35	0.012857	15:41	5890.315	8.069589	28.69199
377.55	35	0.012857	15:42	5898.376	8.060775	16.57242
378	35	0.012857	15:42	5906.428	8.05193	3.365494
378.9	70	0.012857	15:43	5914.471	8.043055	11.40855
379.8	70	0.012857	15:44	5922.505	8.03415	19.4427
380.7	70	0.012857	15:45	5930.53	8.025213	27.46791
381.6	70	0.012857	15:45	5938.547	8.016247	35.48416
382.5	70	0.012857	15:46	5946.554	8.007249	43.49141
384.75	70	0.032143	15:48	5966.532	19.97856	55.41061
385.2	70	0.006429	15:49	5970.521	3.988899	57.34043
386.1	70	0.012857	15:49	5978.492	7.970953	60.31553
387.9	70	0.025714	15:51	5994.407	15.91442	63.80878

389.25	70	0.019286	15:52	6006.318	11.91165	65.05211
390.15	70	0.012857	15:53	6014.248	7.929535	63.25108
392.85	65	0.041538	15:55	6039.803	25.55486	61.49429
393.3	65	0.006923	15:56	6044.052	4.249646	60.66784
394.2	65	0.013846	15:57	6052.544	8.491108	57.55956
395.1	65	0.013846	15:57	6061.024	8.480164	52.62815
398.25	65	0.048462	16:00	6090.618	29.59384	30.11435

D.2 The proposed modular switched reluctance motor

Table D-2: Analytical evaluation of the proposed MSRM through the drive cycle

Distance (km)	Speed (km/h)	time taken (H)	Time of day (HH:MM)	Energy used by motor (W)	Energy gain by the sun as input (W)	Energy balance (W)
0	0	0	7:00	0	1.6	1.6
0	0	0	7:03	0	27.43945	29.03945
0	0	0	7:06	0	27.61715	56.6566
0	0	0	7:09	0	27.79305	84.44965
0	0	0	7:12	0	27.96715	112.4168
0	0	0	7:15	0	28.13945	140.5563
0	0	0	7:18	0	28.30995	168.8662
0	0	0	7:21	0	28.47865	197.3449
0	0	0	7:24	0	28.64555	225.9904
0	0	0	7:27	0	28.81065	254.8011
0	0	0	7:30	0	28.97395	283.775
0	0	0	7:33	0	29.13545	312.9105
0	0	0	7:36	0	29.29515	342.2056
0	0	0	7:39	0	29.45305	371.6587
0	0	0	7:42	0	29.60915	401.2678
0	0	0	7:45	0	29.76345	431.0313
0	0	0	7:48	0	29.91595	460.9472
0	0	0	7:51	0	30.06665	491.0139
0	0	0	7:54	0	30.21555	521.2294
0	0	0	7:57	0	30.36265	551.5921
0	0	0	8:00	0	30.50795	582.1
0.9	75	0.012	8:00	0	7.343329	589.4433
1.8	60	0.015	8:01	0	9.190746	598.6341
2.7	60	0.015	8:02	0	9.203574	607.8376
3.6	60	0.015	8:03	0	9.216353	617.054
4.5	60	0.015	8:04	0	9.229083	626.2831
6.75	60	0.0375	8:06	0	23.12808	649.4112
7.2	60	0.0075	8:07	0	4.635061	654.0462
8.1	60	0.015	8:07	3.393159	9.279518	659.9326

9.9	60	0.03	8:09	9.814659	18.59645	672.1075
11.25	60	0.0225	8:11	15.47666	13.97988	680.4254
12.15	60	0.015	8:11	21.42343	9.335329	683.814
14.85	60	0.045	8:14	43.3587	28.0794	689.9581
15.3	60	0.0075	8:15	47.69932	4.690543	690.308
16.2	60	0.015	8:16	57.78328	9.390155	689.6142
17.1	60	0.015	8:16	70.02634	9.402205	686.7734
20.25	60	0.0525	8:20	117.9828	33.00191	671.8188
22.05	60	0.03	8:21	148.3219	18.92344	660.4032
23.4	60	0.0225	8:23	173.2883	14.2234	649.6601
25.2	60	0.03	8:25	209.552	19.00532	632.4018
27.45	60	0.0375	8:27	260.5411	23.82165	605.2343
31.5	60	0.0675	8:31	359.1743	43.05868	549.6598
34.2	60	0.045	8:34	429.4745	28.83233	508.192
36	60	0.03	8:35	479.4323	19.27702	477.5111
38.25	60	0.0375	8:38	547.7702	24.158	433.3313
39.6	60	0.0225	8:39	591.2336	14.52743	404.3954
40.5	60	0.015	8:40	621.7876	9.698444	383.5397
41.4	60	0.015	8:41	654.008	9.709182	361.0286
41.85	60	0.0075	8:41	670.9148	4.858602	348.9803
43.2	60	0.0225	8:43	725.406	14.59178	309.0809
43.65	60	0.0075	8:43	744.4059	4.869231	294.9502
45	60	0.0225	8:44	804.0641	14.62352	249.9156
45.9	55	0.016364	8:45	848.2877	10.65013	216.3421
46.35	55	0.008182	8:46	872.2151	5.329728	197.7444
46.8	55	0.008182	8:46	896.9909	5.332826	178.3014
47.25	50	0.009	8:47	922.4708	5.869679	158.6912
48.15	50	0.018	8:48	922.4708	11.75053	170.4418
49.05	50	0.018	8:49	922.4708	11.76537	182.2072
49.95	50	0.018	8:50	922.4708	11.78012	193.9873
50.85	50	0.018	8:51	922.4708	11.79478	205.7821
51.75	50	0.018	8:52	922.4708	11.80937	217.5914
54	50	0.045	8:55	922.4708	29.58666	247.1781
54.45	50	0.009	8:55	922.4708	5.92809	253.1062
55.35	50	0.018	8:57	922.4708	11.86685	264.973
57.15	50	0.036	8:59	922.4708	23.77611	288.7491
58.5	50	0.027	9:00	925.9753	17.86885	303.1135
59.4	50	0.018	9:01	929.5168	11.92992	311.5019
62.1	50	0.054	9:05	942.5723	35.87213	334.3185
62.55	50	0.009	9:05	945.4894	5.99059	337.392
63.45	50	0.018	9:06	952.7729	11.99129	342.0998
64.35	50	0.018	9:07	962.1709	12.00469	344.7065
67.5	50	0.063	9:11	999.9905	42.12079	349.0077
69.3	50	0.036	9:13	1024.459	24.14091	348.6802
70.65	50	0.027	9:15	1045.043	18.13947	346.236

72.45	50	0.036	9:17	1075.451	24.23049	340.0583
74.7	50	0.045	9:20	1119.019	30.35871	326.8486
78.75	50	0.081	9:25	1204.09	54.83942	296.6173
81.45	50	0.054	9:28	1265.279	36.69484	272.1233
83.25	50	0.036	9:30	1309.172	24.522	252.752
85.5	50	0.045	9:33	1369.829	30.71744	222.8124
86.85	50	0.027	9:34	1408.7	18.46459	202.4055
87.75	50	0.018	9:35	1436.196	12.32377	187.2343
88.65	50	0.018	9:37	1465.319	12.33491	170.4454
89.1	50	0.009	9:37	1480.683	6.171607	161.2529
90.45	50	0.027	9:39	1530.494	18.5313	129.9734
90.9	50	0.009	9:39	1547.915	6.182556	118.7354
92.25	50	0.027	9:41	1602.723	18.56389	82.49061
93.15	50	0.018	9:42	1645.401	12.38935	52.20266
93.6	50	0.009	9:42	1668.556	6.198666	35.24628
94.05	45	0.01	9:43	1692.216	6.890512	18.47627
94.5	45	0.01	9:44	1717.299	6.893767	0.287544
95.4	75	0.012	9:44	1717.299	8.276796	8.56434
96.3	75	0.012	9:45	1717.299	8.281438	16.84578
97.2	75	0.012	9:46	1717.299	8.286055	25.13183
98.1	75	0.012	9:47	1717.299	8.290646	33.42248
99	70	0.012857	9:47	1717.299	8.887903	42.31038
101.25	65	0.034615	9:49	1717.299	23.95479	66.26517
101.7	60	0.0075	9:50	1717.299	5.195125	71.4603
102.6	55	0.016364	9:51	1717.299	11.34085	82.80114
104.4	50	0.036	9:53	1717.299	24.9787	107.7798
105.75	45	0.03	9:55	1717.299	20.84548	128.6253
106.65	40	0.0225	9:56	1717.299	15.65169	144.277
109.35	40	0.0675	10:00	1728.459	47.04377	180.1604
109.8	40	0.01125	10:01	1730.187	7.853346	186.2861
110.7	40	0.0225	10:02	1735.043	15.71741	197.147
111.6	40	0.0225	10:04	1742.137	15.73156	205.7848
114.75	40	0.07875	10:08	1772.236	55.16954	230.8557
116.55	40	0.045	10:11	1792.379	31.59968	242.3119
117.9	40	0.03375	10:13	1809.686	23.73418	248.7394
119.7	40	0.045	10:16	1835.91	31.69042	254.2057
121.95	40	0.05625	10:19	1874.494	39.68325	255.3051
126	40	0.10125	10:25	1951.165	71.61873	250.2525
128.7	40	0.0675	10:29	2006.832	47.87458	242.4602
130.5	40	0.045	10:32	2047.161	31.97102	234.1019
132.75	40	0.05625	10:35	2103.377	40.02293	217.9096
134.1	40	0.03375	10:37	2139.512	24.04432	205.8186
135	40	0.0225	10:39	2165.307	16.04194	196.066
135.9	40	0.0225	10:40	2192.766	16.05166	184.6585
136.35	40	0.01125	10:41	2207.305	8.029427	178.1482

137.7	40	0.03375	10:43	2254.665	24.10242	154.8914
138.15	40	0.01125	10:43	2271.367	8.038782	146.2274
139.5	40	0.03375	10:45	2323.886	24.12999	117.8386
140.4	40	0.0225	10:47	2365.445	16.09782	92.37783
140.85	40	0.01125	10:47	2388.057	8.052198	77.81786
141.3	40	0.01125	10:48	2411.549	8.054363	62.38056
141.75	40	0.01125	10:49	2436.6	8.056506	45.38586
142.65	75	0.012	10:49	2436.6	8.595947	53.98181
143.55	75	0.012	10:50	2436.6	8.598338	62.58015
144.45	75	0.012	10:51	2436.6	8.600704	71.18085
145.35	75	0.012	10:52	2436.6	8.603045	79.78389
146.25	70	0.012857	10:52	2436.6	9.220118	89.00401
148.5	50	0.045	10:55	2436.6	32.29091	121.2949
148.95	50	0.009	10:56	2436.6	6.46193	127.7569
149.85	50	0.018	10:57	2436.6	12.92753	140.6844
151.65	50	0.036	10:59	2436.6	25.86941	166.5538
153	50	0.027	11:01	2440.104	19.4143	182.4636
153.9	50	0.018	11:02	2443.646	12.94853	191.8706
156.6	50	0.054	11:05	2456.701	38.8719	217.687
157.05	50	0.009	11:05	2459.618	6.482373	221.2522
157.95	50	0.018	11:06	2466.902	12.96784	226.9366
158.85	50	0.018	11:08	2476.3	12.9719	230.5106
162	50	0.063	11:11	2514.12	45.43242	238.1234
163.8	50	0.036	11:13	2538.588	25.98187	239.6368
165.15	50	0.027	11:15	2559.172	19.49566	238.5489
166.95	50	0.036	11:17	2589.58	26.00602	234.1467
169.2	50	0.045	11:20	2633.148	32.52557	223.1038
173.25	40	0.10125	11:26	2709.82	73.24931	219.6817
175.95	40	0.0675	11:30	2765.486	48.87841	212.8932
177.75	40	0.045	11:33	2805.816	32.60324	205.1672
180	40	0.05625	11:36	2862.031	40.77159	189.7236
181.35	40	0.03375	11:38	2898.166	24.47133	178.0596
182.25	40	0.0225	11:40	2923.961	16.31736	168.5824
183.15	40	0.0225	11:41	2951.42	16.31969	157.4429
183.6	40	0.01125	11:42	2965.96	8.160664	151.0638
184.95	40	0.03375	11:44	3013.319	24.48503	128.1896
185.4	40	0.01125	11:44	3030.022	8.16262	119.6495
186.75	40	0.03375	11:46	3082.541	24.49041	91.62107
187.65	40	0.0225	11:48	3124.099	16.32885	66.39137
188.1	40	0.01125	11:48	3146.711	8.164939	51.94413
188.55	40	0.01125	11:49	3170.203	8.165254	36.61773
189	40	0.01125	11:50	3195.254	8.165548	19.73207
189.9	75	0.012	11:50	3195.254	8.710219	28.44229
190.8	75	0.012	11:51	3195.254	8.710506	37.15279
191.7	75	0.012	11:52	3195.254	8.710768	45.86356

192.6	75	0.012	11:53	3195.254	8.711004	54.57456
193.5	70	0.012857	11:53	3195.254	9.333453	63.90802
195.75	65	0.034615	11:55	3195.254	25.1295	89.03752
196.2	60	0.0075	11:56	3195.254	5.44487	94.48239
197.1	55	0.016364	11:57	3195.254	11.87984	106.3622
198.9	50	0.036	11:59	3195.254	26.13598	132.4982
200.25	45	0.03	12:01	3195.254	21.77994	154.2781
201.15	40	0.0225	12:02	3195.254	16.33468	170.6128
203.85	40	0.0675	12:06	3206.415	49.00085	208.4533
204.3	40	0.01125	12:07	3208.142	8.16613	214.8918
205.2	40	0.0225	12:08	3212.999	16.33149	226.3668
206.1	40	0.0225	12:10	3220.092	16.33033	235.6034
209.25	40	0.07875	12:14	3250.191	57.14468	262.6493
211.05	40	0.045	12:17	3270.335	32.64412	275.15
212.4	40	0.03375	12:19	3287.641	24.47733	282.3207
214.2	40	0.045	12:22	3313.865	32.62769	288.7243
216.45	40	0.05625	12:25	3352.449	40.76872	290.9091
220.5	40	0.10125	12:31	3429.121	73.33143	287.5692
223.2	40	0.0675	12:35	3484.788	48.84414	280.7464
225	40	0.045	12:38	3525.117	32.54084	272.958
227.25	40	0.05625	12:41	3581.332	40.64908	257.3918
228.6	40	0.03375	12:43	3617.467	24.37408	245.6306
229.5	40	0.0225	12:45	3643.262	16.24264	236.0787
230.4	40	0.0225	12:46	3670.721	16.23706	224.8566
230.85	40	0.01125	12:47	3685.261	8.116382	218.4332
232.2	40	0.03375	12:49	3732.62	24.34032	195.4143
232.65	40	0.01125	12:49	3749.323	8.110426	186.822
234	40	0.03375	12:51	3801.842	24.32196	158.6251
234.9	40	0.0225	12:53	3843.4	16.20666	133.2732
235.35	40	0.01125	12:53	3866.012	8.100877	118.7619
235.8	40	0.01125	12:54	3889.504	8.099214	103.3695
236.25	40	0.01125	12:55	3914.555	8.09753	86.4158
237.15	75	0.012	12:56	3914.555	8.635486	95.05129
238.05	75	0.012	12:56	3914.555	8.633522	103.6848
238.95	75	0.012	12:57	3914.555	8.631534	112.3163
239.85	75	0.012	12:58	3914.555	8.62952	120.9459
240.75	75	0.012	12:58	3917.863	8.627481	126.2657
243	70	0.032143	13:00	3926.49	23.09909	140.7375
243.45	65	0.006923	13:01	3927.978	4.973204	144.2231
244.35	65	0.013846	13:02	3931.317	9.944263	150.828
246.15	55	0.032727	13:04	3935.714	23.49305	169.9242
247.5	50	0.027	13:05	3939.218	19.36924	185.7889
248.4	50	0.018	13:06	3942.76	12.90638	195.1538
251.1	50	0.054	13:09	3955.815	38.6873	220.7856
251.55	50	0.009	13:10	3958.733	6.443128	224.3116

252.45	50	0.018	13:11	3966.016	12.88209	229.9102
253.35	50	0.018	13:12	3975.414	12.87646	233.3887
256.5	50	0.063	13:16	4013.234	45.02204	240.5911
258.3	50	0.036	13:18	4037.702	25.69407	241.8168
259.65	50	0.027	13:20	4058.286	19.25437	240.4875
261.45	50	0.036	13:22	4088.694	25.65039	235.7297
263.7	50	0.045	13:25	4132.262	32.02652	224.1878
267.75	50	0.081	13:29	4217.333	57.54164	196.6587
270.45	40	0.0675	13:33	4273	47.84251	188.8343
272.25	40	0.045	13:36	4313.329	31.83768	180.3427
274.5	40	0.05625	13:40	4369.544	39.7303	163.8578
275.85	40	0.03375	13:42	4405.68	23.80157	151.524
276.75	40	0.0225	13:43	4431.474	15.85211	141.5816
277.65	40	0.0225	13:44	4458.934	15.83945	129.9619
278.1	40	0.01125	13:45	4473.473	7.914921	123.337
279.45	35	0.038571	13:47	4520.621	27.11224	103.3017
279.9	35	0.012857	13:48	4537.204	9.028835	95.74749
281.25	35	0.038571	13:50	4589.641	27.06035	70.37057
282.15	40	0.0225	13:52	4631.2	15.76684	44.57885
282.6	35	0.012857	13:52	4653.865	9.003466	30.91748
283.05	35	0.012857	13:53	4677.521	8.99895	16.25949
283.5	35	0.012857	13:54	4702.66	8.994404	0.115587
284.4	75	0.012	13:55	4702.66	8.390649	8.506236
285.3	75	0.012	13:55	4702.66	8.386637	16.89287
286.2	70	0.012857	13:56	4702.66	8.981203	25.87408
287.1	70	0.012857	13:57	4702.66	8.976539	34.85061
288	70	0.012857	13:58	4702.66	8.971844	43.82246
290.25	65	0.034615	14:00	4702.66	24.13139	67.95385
290.7	60	0.0075	14:00	4702.66	5.223895	73.17774
291.6	55	0.016364	14:01	4702.66	11.39188	84.56962
293.4	50	0.036	14:03	4702.66	25.03431	109.6039
294.75	45	0.03	14:05	4702.66	20.83231	130.4362
295.65	40	0.0225	14:07	4702.66	15.60631	146.0425
298.35	40	0.0675	14:11	4713.82	46.72501	181.6072
298.8	40	0.01125	14:11	4715.548	7.77359	187.6531
299.7	40	0.0225	14:13	4720.404	15.53507	198.3317
300.6	40	0.0225	14:14	4727.498	15.51879	206.7568
303.75	40	0.07875	14:19	4757.597	54.18518	230.8432
305.55	40	0.045	14:21	4777.74	30.8698	241.5695
306.9	40	0.03375	14:23	4795.047	23.10689	247.3698
308.7	40	0.045	14:26	4821.271	30.74751	251.8932
310.95	40	0.05625	14:30	4859.855	38.33342	251.6428
315	40	0.10125	14:36	4936.526	68.70971	243.6811
317.7	40	0.0675	14:40	4992.193	45.59286	233.607
319.5	40	0.045	14:42	5032.522	30.2977	223.5755

321.75	40	0.05625	14:46	5088.738	37.76009	205.1203
323.1	40	0.03375	14:48	5124.873	22.59532	191.5803
324	40	0.0225	14:49	5150.668	15.0379	180.8237
324.9	40	0.0225	14:50	5178.127	15.01719	168.3817
325.35	40	0.01125	14:51	5192.666	7.500776	161.3427
326.7	40	0.03375	14:53	5240.026	22.47081	136.4543
327.15	40	0.01125	14:54	5256.728	7.479697	127.2312
328.5	40	0.03375	14:56	5309.247	22.40708	97.11951
329.4	40	0.0225	14:57	5350.806	14.91118	70.47213
329.85	40	0.01125	14:58	5373.418	7.447463	55.30742
330.3	40	0.01125	14:59	5396.91	7.442019	39.25778
330.75	40	0.01125	14:59	5421.961	7.436554	21.64313
331.65	70	0.012857	15:00	5421.961	8.492201	30.13533
332.55	70	0.012857	15:01	5421.961	8.485006	38.62034
333.45	70	0.012857	15:02	5421.961	8.477781	47.09812
334.35	70	0.012857	15:02	5421.961	8.470525	55.56864
335.25	70	0.012857	15:03	5421.961	8.463238	64.03188
337.5	65	0.034615	15:05	5421.961	22.74919	86.78107
337.95	60	0.0075	15:06	5421.961	4.921941	91.70301
338.85	55	0.016364	15:07	5421.961	10.73001	102.433
340.65	50	0.036	15:09	5421.961	23.56342	125.9964
342	45	0.03	15:11	5421.961	19.59104	145.5875
342.9	40	0.0225	15:12	5421.961	14.6661	160.2536
345.6	25	0.108	15:18	5421.961	70.06755	230.3211
346.05	25	0.018	15:19	5421.961	11.62405	241.9452
346.95	10	0.09	15:25	5421.961	57.88436	299.8296
347.85	45	0.02	15:26	5430.201	12.80912	304.3985
351	50	0.063	15:30	5468.021	40.21804	306.7969
352.8	50	0.036	15:32	5492.489	22.89164	305.2202
354.15	50	0.027	15:34	5513.073	17.12522	301.7618
355.95	50	0.036	15:36	5543.481	22.77507	294.1286
358.2	50	0.045	15:39	5587.049	28.37378	278.934
362.25	50	0.081	15:43	5672.12	50.80269	244.6659
364.95	50	0.054	15:47	5733.309	33.67237	217.1495
366.75	50	0.036	15:49	5777.202	22.35977	195.6159
369	50	0.045	15:51	5837.859	27.84898	162.8079
370.35	50	0.027	15:53	5876.731	16.65517	140.5916
371.25	50	0.018	15:54	5904.226	11.08068	124.1772
372.15	50	0.018	15:55	5933.349	11.06237	106.1158
372.6	50	0.009	15:56	5948.714	5.52429	96.27599
373.95	50	0.027	15:57	5998.524	16.54517	63.01039
374.4	50	0.009	15:58	6015.945	5.505788	51.09565
375.75	55	0.024545	15:59	6072.892	14.99211	9.141073
375.975	50	16:00	6083.561	2.744785	1.216534	16:00

This page intentionally left blank